Universidad de Málaga
Facultad de Ciencias

UNIVERSIDAD
DE MÁLAGA

DEVELOPMENT OF INTEGRATED DEVICES FOR BOTH PHOTOELECTRIC CONVERSION AND ENERGY STORAGE

TESIS DOCTORAL

Química y Tecnologías Químicas. Materiales y Nanotecnología
2018

Directores: José Ramón Ramos Barrado
Francisco de Paula Martín Jiménez

Daniel Solís Cortés

AUTOR: Daniel Solís Cortés

http://orcid.org/0000-0003-3820-4562

EDITA: Publicaciones y Divulgación Científica. Universidad de Málaga

UNIVERSIDAD DE MÁLAGA

DEPARTAMENTO DE FÍSICA APLICADA I

UNIVERSIDAD
DE MÁLAGA

DEVELOPMENT OF INTEGRATED DEVICES FOR BOTH PHOTOELECTRIC CONVERSION AND ENERGY STORAGE

TESIS DOCTORAL

Daniel Solís Cortés

Directores:

José Ramón Ramos Barrado

Francisco de Paula Martín Jiménez

Málaga, 2018

DEVELOPMENT OF INTEGRATED DEVICES FOR BOTH PHOTOELECTRIC CONVERSION AND ENERGY STORAGE

Memoria presentada por el Ingeniero Químico Daniel Solís Cortés en cumplimiento de los requisitos para optar al grado de Doctor por la Universidad de Málaga.

Thesis submitted by chemical engineer Daniel Solís Cortés in partial fulfillment of the requirements for the degree of Doctor of the Universidad de Málaga.

Daniel Solís Cortés

Málaga, de Diciembre de 2018

El presente trabajo ha sido llevado a cabo con el apoyo de la Junta de Andalucía a través del proyecto RNM1399 y a través del grupo de investigación FQM-192.

The present work has been carried out with the support of the Junta de Andalucía through the project RNM1399 and through the research group FQM-192.

UNIVERSIDAD DE MÁLAGA

D. José Ramón Ramos Barrado, Catedrático de Universidad del Departamento de Física Aplicada I, de la Universidad de Málaga, y **D. Francisco de Paula Martín Jiménez**, Catedrático de Universidad del Departamento de Ingeniería Química de la Universidad de Málaga,

CERTIFICAN:

Que la memoria presentada por el Ingeniero Químico Daniel Solís Cortés, bajo el título "DEVELOPMENT OF INTEGRATED DEVICES FOR BOTH PHOTOELECTRIC CONVERSION AND ENERGY STORAGE", ha sido realizada bajo nuestra dirección en los laboratorios del Departamento de Física Aplicada I de la Universidad de Málaga, reuniendo a nuestro juicio los requisitos necesarios para optar al grado de Doctor por la Universidad de Málaga, por lo que autorizamos su presentación.

Y para que así conste, firmamos el presente certificado en Málaga, a de diciembre de 2018.

Fdo.: José Ramón Ramos Barrado
Catedrático de Universidad de Física Aplicada
Universidad de Málaga

Fdo.: Francisco de Paula Martín Jiménez
Catedrático de Universidad de Ingeniería Química
Universidad de Málaga

UNIVERSIDAD DE MÁLAGA

D. José Ramón Ramos Barrado, Catedrático de Universidad, Director del Departamento de Física Aplicada I y Coordinador del Programa de Doctorado *Química y Tecnologías Químicas. Materiales y Nanotecnología*, de la Universidad de Málaga,

CERTIFICA:

Que la Tesis Doctoral, titulada "DEVELOPMENT OF INTEGRATED DEVICES FOR BOTH PHOTOELECTRIC CONVERSION AND ENERGY STORAGE", constituye la memoria que presenta D. Daniel Solís Cortés para optar al título de Doctor por la Universidad de Málaga, y que ha sido realizada bajo mi dirección y la del Catedrático Francisco de Paula Martín Jiménez, en el Departamento de Física Aplicada I de la Universidad de Málaga.

Y para que así conste, firmo el presente certificado en Málaga, a de diciembre de 2018.

Fdo.: José Ramón Ramos Barrado

AGRADECIMIENTOS

En primer lugar, me gustaría agradecer a mis directores de tesis, José Ramón Ramos Barrado y Francisco de Paula Martín Jiménez por brindarme la oportunidad de realizar esta investigación, por confiar en mí desde el principio y estar dispuestos en todo momento a guiarme y apoyarme durante este camino. Quiero agradecer también al resto de componentes del grupo de investigación, concretamente a Dietmar y a David Marrero por su ayuda con los hornos y todas sus aportaciones. También agradezco al resto de profesores del departamento su amabilidad y explicaciones durante la docencia en laboratorio, Félix, Juanjo, Antonio, José Antonio y Javier.

Quiero agradecer especialmente al profesor Enrique Dalchiele, quién considero como mi tercer director en la distancia, gracias por tu capacidad de trabajo, por tu simpatía y por haberme enseñado tanto durante mi estancia en Uruguay, me sentí como un uruguayo más en tu tierra.

Gracias a los miembros del personal técnico del SCAI que siempre han estado dispuestos amablemente para la caracterización de las muestras. Especialmente a Rocío y Ana por buscarme siempre un hueco casi imposible para mis medidas, por su profesionalidad y sus sabias palabras. Además a Laura, Cristina, Valle, Adolfo y Shanti por su buen hacer en el análisis de muestras.

A mis queridos compañeros de departamento e investigación, a Elena por su ayuda inestimable desde el inicio, por estar siempre dispuesta a resolver mis dudas con el *sputtering* y por supuesto gracias por tu último trabajo. Gracias a David por hacer grupo, por sus ideas y por ser un auténtico artista técnico, haciendo que la experimentación parezca fácil con tus inventos. A Ali y Juanjo por trabajar juntos día a día y mano a mano en el laboratorio, por vuestra ayuda y por hacerme muy amena la vida investigadora. A Dani Vallejo por su eficiente trabajo y su simpatía, y a Efraín por sus consejos y por acordarse de mí para la solicitud de este proyecto.

Durante estos 3 años de tesis también he podido conocer grandes investigadores en los intercambios realizados con universidades latinoamericanas. Quisiera agradecer a Marcelo, por sus conocimientos de electroquímica, por acogerme tan bien en Chile y por los buenos momentos compartidos tanto aquí como allí, sabes que eres mi amigo chileno. A Andrés por ser un tío chévere y llevarnos a comer una bandeja paisa colombiana. A Rodrigo por su infinita sabiduría, su ayuda paciente y ser tan grande. También quiero agradecer a todos mis compañeros de laboratorio en la Universidad de La República, Guillermo, Andrés, Daniel Gau y Javier, gracias por hacerme muy fácil la vida allí, por vuestra ayuda y por el buen ambiente generado.

Por supuesto, no me olvido de todos mis amigos que siguen apoyándome en mi camino, por las risas, los buenos momentos, las grandes conversaciones y sobre todo porque pase lo que pase sé que siempre estaréis ahí.

A mi familia, a mi madre y a mi hermano por ser piezas clave en mi vida, por animarme y preocuparse por mí, por su gran apoyo moral durante la realización de esta tesis y por toda la energía que me transmiten cada día. A mi padre porque con su sonrisa me enseñó a ser una persona alegre, optimista y luchadora, porque desde ahí arriba, estará orgulloso de mí. Soy como soy gracias a vosotros.

A mi Vane, por acompañarme en este viaje de la vida, por su apoyo incondicional, por su sonrisa, su serenidad y porque su luz ha hecho iluminar mis momentos de oscuridad. Parte de este trabajo es tuyo también, juntos lo hemos conseguido. Gracias.

A mi familia

RESUMEN

En la presente Tesis, se describen y presentan los resultados obtenidos para el desarrollo de un dispositivo generador y almacenador de energía eléctrica a partir de energía solar. Se ha diseñado, fabricado y optimizado cada uno de los elementos que forman parte del fotocondensador. Dicho dispositivo está formado por el fotoánodo como parte generadora de energía combinado con un supercondensador como parte almacenadora de energía. El fotoánodo del primer tipo de dispositivo está compuesto por nanohilos de ZnO sensibilizados con *quantum dots* (QDs) de Ag_2S y recubiertos por una capa pasivante de sulfuro de zinc (ZnS), crecido sobre un electrodo transparente conductor, habiéndose usado FTO comercial para el primer dispositivo y una capa delgada de GIZO sintetizada en nuestro laboratorio para el segundo fotocondensador. Ambos dispositivos se han combinado con el supercondensador compuesto por un electrolito iónico conductor ([HEMIm][BF_4]/PVP) y electrodos de polímero conductor de PEDOT. El fotoánodo del segundo tipo de dispositivo se compone de una capa delgada de dióxido de titanio (TiO_2) crecida sobre ITO comercial y la parte almacenadora está compuesta por un electrolito ion gel y una capa de $LiFeO_2$ como cátodo.

Se ha sintetizado un óxido transparente conductor con elevada movilidad electrónica, conductividad y alta densidad de portadores, compuesto por Galio, Indio, Zinc y Oxígeno (GIZO).

Se ha desarrollado y optimizado la parte fotoactiva de generación eléctrica habiéndose realizado medidas fotoelectroquímicas para estudiar la influencia de los distintos parámetros de crecimiento de los QDs sobre la eficiencia de fotorrespuesta.

Se ha obtenido y caracterizado un supercondensador simétrico con electrolito transparente. Se ha estudiado la influencia del espesor de PEDOT sobre las propiedades del dispositivo. Finalmente, el ensamblaje de fotoánodo y supercondensador en un solo dispositivo forma el fotosupercondensador cuyo estudio pormenorizado y resultados son presentados de forma comparativa para los dos tipos de fotocondensador desarrollados.

ABSTRACT

In the present Thesis, the results obtained for the development of a device to generate and store electrical energy from solar energy are described and presented. Each of the elements that form part of the photocapacitor has been designed, manufactured and optimized. This device consists of the photoanode as part of the energy generator combined with a supercapacitor as part of the energy storage. The photoanode of the first type of device is composed of ZnO nanowires sensitized with quantum dots (QDs) of Ag_2S and covered by a passivating layer of zinc sulphide (ZnS), grown on a conductive transparent electrode, having used commercial FTO for the first device and a thin layer of GIZO synthesized in our laboratory for the second photocapacitor. Both devices have been combined with the super capacitor composed of a conductive ionic electrolyte ([HEMIm][BF_4]/PVP) and PEDOT conductive polymer electrodes. The photoanode of the second type of device consists of a thin layer of titanium dioxide (TiO_2) grown on commercial ITO and the storage part consists of an ion gel electrolyte and a layer of $LiFeO_2$ as cathode.

A conductive transparent oxide with high electronic mobility, conductivity and high carrier density has been synthesized, composed of Gallium, Indium, Zinc and Oxygen (GIZO).

The photoactive part of electrical generation has been developed and optimized, having carried out photoelectrochemical measurements to study the influence of the different growth parameters of the QDs on the efficiency of the photoresponse.

A symmetrical supercapacitor with transparent electrolyte has been obtained and characterized. The influence of the PEDOT thickness on the properties of the device has been studied.

Finally, the assembly of photoanode and supercapacitor in a single device forms the photocapacitor whose detailed study and results are presented in a comparative way for the two types of photocapacitor developed.

LIST OF ACRONYMS AND SYMBOLS

Acronym	Description
AFM	Atomic Force Microscopy
XRD	X-Ray Diffraction
AM1.5g	Air Mass 1.5 global spectrum
CV	Cyclic Voltammetry
DSSC	Dye Sensitized Solar Cell
ECD	Electrochemical Deposition
EDX	Energy Dispersive X-Ray
EIS	Electrochemical Impedance Spectroscopy
FTIR	Fourier Transformed Infrared Spectroscopy
FTO	Fluorine Tin Oxide
GCD	Galvanostatic Charge Discharge
GZO	Gallium Zinc Oxide
GIZO	Gallium Indium Zinc Oxide
ITO	Indium Tin Oxide
PEDOT	Poly(3,4-ethylenedioxythiophene)
QDSSC	Quantum dot sensitized solar cell
RF	Radiofrequency
SC	Supercapacitor
SSSCs	Semiconductor Sensitized Solar Cells
FESEM	Field Emission Scanning Electron Microscopy
FOM	Figure of Merit
HRTEM	High Resolution Transmission Electron Microscopy
TCO	Transparent Conducting Oxide
UV	Ultraviolet
PV	Photovoltaic
PSC	Photosupercapacitor
XPS	X-Ray Photoelectron Spectroscopy

Symbol	Description	Units
μ	Carrier Mobility	$cm^2V^{-1}s^{-1}$
A	Area	
C	Capacitance	F
E	Energy	eV
Eg	Band gap	eV
FF	Fill Factor	%
h	Planck constant	J.s ($6.6261*10^{-34}$)
i	Current	A
I_{sc}	short circuit current	A
J	current density	A m^{-2}
J_{sc}	short circuit current density	A m^{-2}
n	refractive index	
k	extinction coefficient	
ε	dielectric function	
R_{sh}	Sheet resistance	Ω/sq
R	Resistance	Ω
T	Temperature	^oC
t	time	s
P	Power	W
V	Potential	V
V_{oc}	Open circuit voltage	V
Z	Impedance	Ω
λ	Wavelength	nm
n_e	Charge carrier density	cm^{-3}
σ	Electrical conductivity	$S.cm^{-1}$
q	charge	C
η	Efficiency	%

TABLE OF CONTENTS

I

INTRODUCTION

A. ENERGY STORAGE AND SOLAR HARVESTING DEVICES

In recent decades, the growing global energy demand and the fact that fossil fuels are limited has encouraged the development and research of renewable energies in many fields, such as solar energy, fuel cells, energy storage or wind power. However, in the case of solar cells, the latest discoveries in nanostructured solar cells have not been commercialized on a large scale, due to the high cost of materials and underdeveloped manufacturing and fabrication industrial techniques.

On the other hand, a good power generation from these photovoltaic systems must be combined with an adequate energy storage and distribution of the electricity. In fact, energy storage is a crucial factor in the integration of renewable sources, playing a significant role in maintaining a reliable modern electricity system. This system should avoid power fluctuations, enable storage and enhance the electric system flexibility allowing the supply of energy[1].

There is a variety of types of energy storage systems, including mechanical, electrical, thermal or electrochemical systems. Electrochemical supercapacitors, fuel cells and batteries are three types of the most important electrochemical energy storage devices used nowadays. Concretely for photovoltaic systems, the most common types of electrochemical storage devices are batteries, such as, Nickel-Cadmium, Sodium-Nickel chloride, Lead-Acid or Lithium ion. Apart from that, among the electrical storage devices is found the electrochemical supercapacitor (also known as supercapacitor), with a high power density and energy density. There exists three types of supercapacitors such as double-layer capacitors, pseudocapacitors and hybrid capacitors, whose difference is the charge storage mechanism.

Nowadays, most solar cells sold on the market are made of silicon wafers, known as “first generation” solar cell technology. Due to the Shockley-Queisser limit for single-bandgap devices[2], this technology has achieved

record lab efficiencies of 26.7% for mono-crystalline silicon wafer-based technology[3].

Finally, since there exists a thermodynamic limit on the conversion of sunlight to electricity of 93%, a new emerging and less expensive photovoltaic cell (PV) called "third generation", is expected to overcome the efficiencies of the previous solar cells. Between these solar cells, it is possible to find nanostructured solar cells where the photoactive semiconductor is supported on it. Depending on the semiconductor the different types of this generation of solar cells are Dye Sensitized Solar Cells (DSSC), Quantum-Dot Sensitized Solar Cells (QDSSC), Organic Photovoltaic (OPV) and Perovskite Solar Cells[4,5].

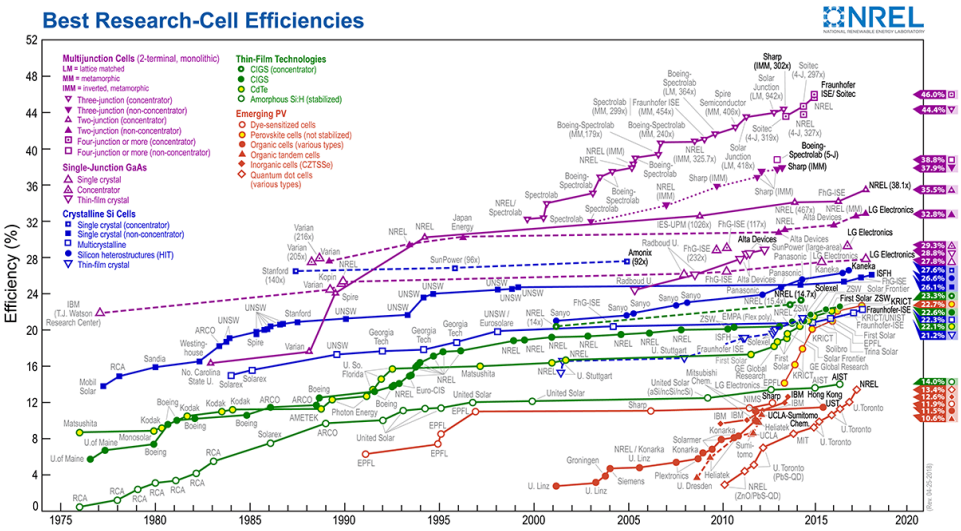

Figure 1.1. Best research cell efficiencies from 1975 to 2017. (NREL 2017)

In this Thesis, the chosen solar cell has been the "Quantum-Dot Sensitized Solar Cells" due to its many advantages as it will be explained in Chapter III dedicated to the photo-anode. Figure 1.1 shows the best research cell efficiencies of PV cells in the evolution since 1975 until nowadays, where the QDSSC (orange circles) efficiencies are experiencing a high linear growth since their first fabrication in 2010.

A common element to both parts of generation and storage energy is the transparent conductive oxide (TCO). This element is essential and work as substrate being fundamental for the success of the device.

The combination of a solar cell with a supercapacitor in a single device is known as photo-supercapacitor, receiving more and more interest in the last years because of their multiple applications in future portable and wearable devices. This device is capable of generate and store electricity at the same time from solar energy.

B. BACKGROUND MOTIVATION

The conversion of solar energy and the storage of electricity produced are becoming key strategies for solving the problems of the energy crisis and its sustainable use. Currently, the conceptual and experimental framework of the problem is the need for self-sufficient buildings, which leads to the use of incident sunlight on windows by converting it into electricity and the need to storage that energy to be used afterwards. The thin film transparent in the visible region solar cell meets the first mission and the batteries or supercapacitor device meets the second mission. A fundamental part of this problem is the possibility to combine photogeneration with energy storage of an effective way. There are some designs developed to combine both functions, solar energy conversion and electrical energy storage into a single transparent device for smart windows[6,7].

Energy saving can be addressed by the use of devices with lower energy consumption, but the increase in population compensates for the reduction effects by this route. The ideal goal is the reduction of energy consumption through energy self-sufficiency. The decrease of energy consumption can and must be achieved through different lines of action. The use of incident solar radiation on building windows by converting it into electric energy and regulating the energy flowing through windows are two ways to save energy.

In order to be self-sufficient, a building has to generate its own energy, which requires systems that can take advantage of incident solar radiation. If the devices are going to be integrated into the glazed surfaces, they must be transparent or semi-transparent. Ideally, they should be transparent in the visible region and the perceived color neutral, unless it is desired a color because of the aesthetics of the building.

Achieving stable devices begins with a proper selection and optimization of the elements that make them up. Thus, all the active devices mentioned, photo generators, storage and energy regulators, need transparent conductors for their electrical contacts and for the electrodes that are part of any of the devices. Therefore, the key materials in the development of this type of devices are transparent conductors and transparent polymer electrolytes. Transparent conducting oxides (TCO) comprise a class of materials that can be considered as materials that conjugate properties of technological interest such as electrical conductivity and transparency [4].

Secondary lithium-ion batteries are one of the most widely used batteries in consumer electronics. They lack a "memory effect" and show good cyclability and high capacity [6]. The multi-billion dollar market for these devices has led to an intensification of research into these batteries aimed at improving safety and power-to-weight ratio. In addition to the high values of the specific capacity developed, they do not give rise to safety problems because they do not use metallic lithium. On the other hand, the use of a solid ion electrolyte also contributes to battery safety. Sony sold the first rechargeable lithium-ion battery in 1991. Since then, research in this area has been very extensive. An alternative device to solar cells and batteries is the photocapacitor[7], since it is built of both in a single device. A photo-capacitor is a device capable of generating energy from solar radiation and storing it for a sufficient time afterwards. Ideally, the advantages of the capacitor are the possibility of building windows integration, fast charging (photo-response), stability and increased cyclability.

C. OBJECTIVE

The overall objective of the present Thesis is, to design, develop and characterize a transparent photo-supercapacitor capable of capturing the solar energy, to transform it into electricity and to store it in an efficient way.

In order to achieve this goal, the following strategies were proposed:

1) To identify and to develop a transparent conducting oxide (TCO) with appropiate opto-electronic properties to be part of the photoanode of the final photocapacitor device.
2) To prepare new architectures of nanostructured semiconductive materials in a wide range of morphologies, seeking the synergistic combination of properties as photoanode electrode.
3) To synthesize conducting polymers by electrodeposition and to obtain transparent ionic conductive electrolytes based on commercial ionic liquids to build a supercapacitor.
4) To assembly and to characterize the photocapacitor device from the above elements.

D. THESIS OUTLINE

This doctoral Thesis contains five chapters; this first introduction explains in general terms the energetic current situation of the world and gives a general vision of the importance of energy efficiency nowadays.

An emerging and home-made transparent conducting oxide (TCO) named Gallium Indium Zinc Oxide is presented in Chapter II. This thin film has been developed and characterized for their use as transparent photoanode.

The third chapter deals with a third generation (3G) solar cell, focusing on the fabrication and characterization of quantum dot sensitized solar cells and zinc oxide nanowires. Moreover, results on photoelectrochemical characterization are presented.

Chapter IV is devoted to the development of the storage part of the whole device, concretely the supercapacitor. Main results, materials and methodology are discussed in this chapter.

The final photo-supercapacitors are presented in the fifth chapter, having combined the previous individual devices such as solar cell and supercapacitor to form two different types of photo-supercapacitor.

Finally, a brief description of the characterization techniques used throughout the project can be found on Appendix A, along with the mandatory Spanish summary on Appendix B.

II

TRANSPARENT CONDUCTING OXIDES: GIZO

A. INTRODUCTION

Transparent conductive oxides (TCOs) are a very important part in many optoelectronic devices such as solar cells and also in new relevant devices for energy harvesting and storage [8–10] as the photo-supercapacitors, which are novel and promising devices that will allow to produce energy from the sunlight and store it in the same device [11,12]. Obtaining efficient solar cells and photo-supercapacitors requires a careful design of all its parts and, undoubtedly, transparent electrodes play an important role as an active part in the development of these devices. The main advantage of these compounds is that they can be obtained by various methods such as spray pyrolysis[13,14] electrodeposition[15–17] or magnetron sputtering[18] with good optical and electrical properties. ZnO doped with Al[19] or Ga[20], and more recently with In[21], are materials that can fulfill the requirements for optoelectronic devices. An opportunity to get better TCO materials is using ZnO compounds doped with Ga and In [22], i.e. Indium–gallium–zinc oxide (GIZO). When properly doped, zinc atoms are substituted by trivalents atoms (X^{3+}, where X = Al, In, Ga). The extrinsic donors due to dopant are more stable than the intrinsic donors due to native defects. However, they present a limitation in the improvement of conductivity when increasing the dopant content, Al, Ga or In, above a certain value, since the conductivity and transparency decrease. This saturation in the doping of ZnO by Al or Ga is possibly due to the conduction mechanisms in these compounds [23]. There is evidence that saturation in doping with Ga is reached at about 2 at%[24,25]. For higher values of Ga doping, the conductivity decreases probably due to the degradation of the crystallinity of the film because of the difference in ionic radius between the Ga^{3+} (0.062 nm) and Zn^{2+} (0.074 nm). The resulting effect would be the loss of charge carrier mobility[26]. Another possible reason would be that the increase of dopant atoms produces neutral defects that do not contribute to the conductivity. In addition, the neutral atoms can be segregated at the grain boundaries increasing carriers scattering[27]. The charge carrier density and their mobility determine the conductivity and to obtain significant improvements it is necessary to combine both adequately. GIZO can improve its optoelectronic properties

with respect to Ga: ZnO or Al: ZnO. Kimizuka and Mohri[28] synthesized GIZO for the first time in 1985, and Shunpei Yamazaki[29] discovered that various GIZO crystal morphologies are formed in addition to amorphous and single-crystal. The discovered c-axis-aligned crystalline GIZO and nanocrystalline GIZO morphologies showed significant differences from single-crystal and polycrystalline structures. Nanocrystalline GIZO (nc-GIZO) exhibited nanometer-sized crystals that were oriented in random directions[30].

In general, there no exists in bibliography several works based on an optimal and statistical methodology to carry out the laboratory experiments to grow thin films. Therefore, in this Thesis, it has been chosen an experimental design for the growth of GIZO thin films.

The experimental response surface designs, which are the most suitable for the optimization of one or several responses, are limited to three factors by a principle of economy in the experimental effort. If it is suspected that more than three factors may have significant effects, then it is appropriate to select three of them and fix the rest at a value that is considered adequate. For this reason, and although it is obvious that the variation in the amount of Ga will influence the final properties of GIZO films, it was decided to select three sputtering parameters and the Ga/Zn ratio was set at 2% based on previous work of our group and others found in bibliography [18,24]. Therefore, to achieve GIZO films with optimal electrical conductivity and transparency, a Box-Behnken experimental design of response surface has been employed to evaluate the effects of three factors: power applied to the In_2O_3 target, substrate temperature, and deposition time. The goal is to establish their influence on GIZO films properties such as charge carrier density, mobility, crystallinity, etc. The aim of this work is then to obtain GIZO films with a good compromise between transparency and conductivity to be used as transparent electrodes. With this objective new figures of merit (FOM) have been defined for the first time as a modification of other well known FOMs, proposed by other authors. The new FOMs have been comparatively applied to the obtained GIZO films.

B. MATERIALS AND METHODS

1) GROWTH OF GIZO THIN FILMS BY MAGNETRON SPUTTERING

For the growth of GIZO thin films, it was chosen a physical vapor deposition process, that is, Radio-Frequency (RF) magnetron sputtering. The main advantage of this method is the possibility to control the growth of pure and dense films varying several parameters such as, temperature, time, RF-power of the targets, gases flux into the main chamber or deposition pressure.

Sputtering is a technique used to deposit thin films of a material onto a substrate. The first step is the creation of a gaseous plasma and after that the acceleration of the ions from this plasma into some source material (target). When the acceleration of the ions towards the cathode occurs, interaction with the surface of the material produces a transfer of the kinetic momentum causing the pulverization of the target. After that, the atoms from the target are expelled upon and coat the substrate material. Magnetron sputtering equipment incorporates electromagnet or permanent magnets below the target, so the electrons are confined close to the cathode. Hence, there is a flux of electrons moving from north pole to the south-oriented magnet, improving the plasma density. Therefore, the resulting coating layer possesses improved conformation coverage, better coating rate and film adhesion.

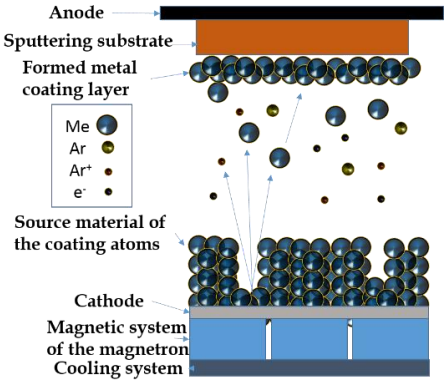

Figure 2.1. Scheme of magnetron sputtering process.

In this Thesis, GIZO thin films electrodes have been deposited by RF magnetron sputtering in co-sputtering mode on 1 and 2 cm^2 glass substrates after the proper wet-chemical cleaning in ultrasonic baths of isopropanol (10 min), deionized water (10 min), acetone (10 min) and, dried finally under nitrogen flow. Two types of ceramics targets from AJA International, Inc were employed: Ga_2O_3 (2%) - doped ZnO target (98%) and In_2O_3 (99.99%). The 150 W applied power to the Ga:ZnO target selected in base of previous studies[18], and the obtained Ga:ZnO film has been considered as corresponding to ratio zero for the In/Zn ratio.

A Box-Behnken response surface factorial design has been used to organize the experimentation and identify the effects of three magnetron sputtering parameters such as In_2O_3 target power (P), deposition time (t) and substrate temperature (T) on the properties of the GIZO films and the potential interactions between these three factors. The films were prepared in random order to include unidentified sources of variability in the experimental error. The three levels used for the factors are shown in Table 2.1, being the power applied to the In_2O_3 target of 80 W, 110W and 140 W, and 150, 250 and 350 ^oC the substrate temperatures. The films were deposited during 20, 40 and 60 min. The full experimental design is show in Table 2.2. The working pressure into the vacuum chamber was kept constant at $1.4 \cdot 10^{-2}$ mbar, and high purity (5N) Ar gas stream, regulated by a mass flow controller at 12 sccm was used.

Table 2.1. Factors and levels used for the Box-Behnken response surface experimental design, and identification of the sample.

Level (symbolic)	**Factor**		
	In_2O_3 applied power (W)	**Substrate temperature (^oC)**	**Deposition time (min)**
-1	80	150	20
0	110	250	40
+1	140	350	60
Identification of the film: GIZO_ Power_Temperature_time			

Table 2.2. Box-Behnken design. Symbolic and real values of the factors.

	Symbolic values			Real values		
Exp. Nº	**Power**	**Temperature**	**Time**	**Power (W)**	**Temperature (ºC)**	**Time (min)**
1	0	0	0	110	250	40
2	-1	0	-1	80	250	20
3	1	0	-1	140	250	20
4	-1	0	1	80	250	60
5	1	0	1	140	250	60
6	-1	-1	0	80	150	40
7	1	-1	0	140	150	40
8	0	0	0	110	250	40
9	-1	1	0	80	350	40
10	1	1	0	140	350	40
11	0	-1	-1	110	150	20
12	0	-1	1	110	150	60
13	0	1	-1	110	350	20
14	0	1	1	110	350	60
15	0	0	0	110	250	40

C. RESULTS AND DISCUSSION

1) STRUCTURAL, COMPOSITIONAL AND MORPHOLOGICAL PROPERTIES OF GIZO THIN FILMS.

From the analysis of the Box-Behnken design the applied power was found to be the main significant effect, positive, on the In/Zn atomic ratio, which means that there is a linear dependence, positive slope, between In_2O_3 target power and In/Zn ratio, as seen in Fig. 2.1(a). There is also a smaller positive effect of the deposition time on the In/Zn ratio. The Ga/Zn ratio remained near constant with median 0.021 and standard deviation $3.7x10^{-3}$ as seen in the values of the atomic Ga/Zn ratio, and Ga/(Zn+In+Ga) shown in Table 2.3. However, the main significant effect on the thickness is the deposition time, being less significant the effect due to the applied power. This means, as expected, that the thickness increases linearly with deposition time as shown in Fig. 2.1(b), and additionally by the increase in the amount of deposited In (Fig. 2.1(a)). The Pareto graph of the effects for both responses are shown in Fig. 2.2 (a, b).

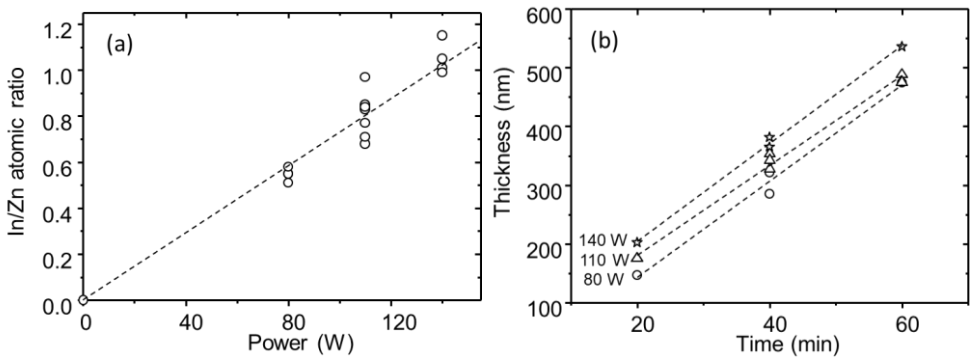

Figure 2.1. **(a)** In/Zn atomic ratio versus applied power to the In_2O_3 target **(b)** Thickness versus deposition time.

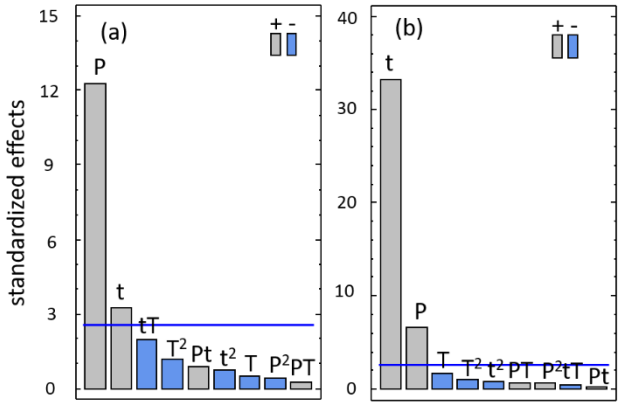

Figure 2.2. Pareto graph of the effects. Factors: "P" applied power, "t" deposition time, "T" substrate temperature. **(a)** Response: In/Zn atomic ratio. **(b)** Response: Thickness.

Table 2.3. Atomic percentages and ratios.

Exp. Nº	%Zn*	%Ga*	%In*	In/Zn ratio	Ga/Zn ratio	Ga/(In+Zn+Ga) ratio
1	23.84	0.44	20.18	0.85	0.018	0.010
2	20.25	0.35	10.39	0.51	0.017	0.011
3	17.09	0.37	17.27	1.01	0.022	0.011
4	30.45	0.66	16.66	0.55	0.022	0.014
5	21.93	0.41	23.1	1.05	0.019	0.009
6	28.48	0.77	15.82	0.56	0.027	0.017
7	22.2	0.47	22.04	0.99	0.021	0.011
8	21.87	0.41	18.34	0.84	0.019	0.010
9	27.21	0.64	15.96	0.59	0.024	0.015
10	20.45	0.62	23.39	1.14	0.030	0.014
11	19.51	0.46	13.33	0.68	0.024	0.014
12	25.02	0.42	19.32	0.77	0.017	0.009
13	19.65	0.36	13.87	0.71	0.018	0.011
14	22.97	0.48	22.28	0.97	0.021	0.010
15	23.94	0.46	20.32	0.85	0.019	0.010

Figure 2.3 shows XRD diffraction patterns. The GIZO films grew hexagonal, c-axis textured with a main diffraction peak around 2θ=31º corresponding to (0 0 n) crystallographic planes. This peak does not appear at a fixed 2θ angle because 2θ changes with the In/Zn ratio. Fig. 2.3(a-c) shows the XRD patterns for samples obtained at 80, 110 and 140 W applied to the In_2O_3 target. Increasing the power increases the In/Zn ratio, and it was found that the crystal size of the films decreases with increasing In/Zn atomic ratio (Fig. 2.4). It has been reported that crystalline films are generally obtained for low In/Zn atomic ratio. When In/Zn is higher amorphous films are obtained[31]. The amorphization in In-rich IZO films is probably due to In atoms would locate in or near grain boundary regions [32][33]. The reason could be also attributed to the presence of In^{3+} that produces crystalline defects, which due to the cubic structure of InO_2^- are not incorporated into the GIZO structure[34]. G.H. Kim *et al*. reported that as the indium concentration increases, the activation energy for crystallization increases too [35]. When Ga is incorporated to the IZO (GIZO) then the transition to amorphous phase happens in a wider range of In/Zn ratios[36].

By the ANOVA analysis of the Box-Behnken design, the main positive effect on the crystal size is due to the substrate temperature. This is clearly shown in Fig. 2.3(b-c). The applied power shows a negative effect (Fig. 2.3(a-c)), the films are less crystalline when the power is increased, which is linked to the In/Zn ratio evolution as mentioned and shown in Fig. 2.4. Figure 2.3(d) shows the effect of time on samples obtained at 80 W and 250º C. These films showed the main peak at 2θ= 31.7º, and, additionally, two peaks at 2θ= 45.1º and 2θ = 58.8º of lower intensity corresponding to, (0 0 12), (1 0 8) and (1 0 12) crystallographic planes respectively (JCPDS 98-016-2451).

Figure 2.3(e), shows comparatively the XRD patterns for the hexagonal Ga:ZnO (2% Ga), IZO_140_250_30, a GIZO sample, and cubic In_2O_3, all obtained by magnetron sputtering. Fig 2.3(e-f) show as the position of the (0 0 n) peaks for the obtained GIZO films change between from 2θ =34.4º (0 0 2) for hexagonal 2% Ga:ZnO (ZnO JCPDS 98-016-3383) to 30.3º for cubic In_2O_3 (2 2 2) (JCPDS 98-064-0179).

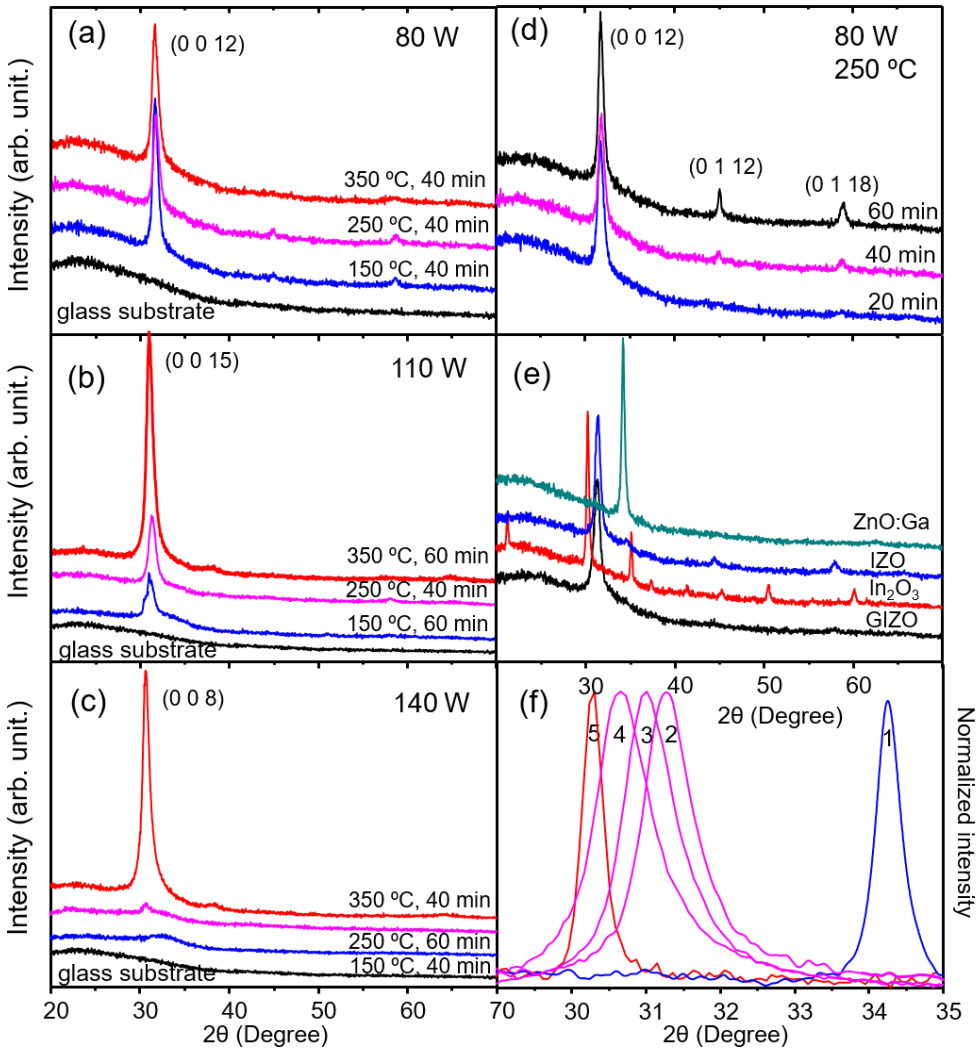

Figure 2.3. XRD patterns of samples obtained at (a) 80 W (b) 110 W (c) 140 W at different temperatures. XRD spectra of the samples obtained at 8W, 250ºC and different times. And the XRD spectra of the ZnO:Ga, In_2O_3 and a GIZO sample. (f) Normalized XRD spectra of (1) ZnO.Ga, (2-4) GIZO at 40 min, 350ºC and 80, 110, 140 W respectively; (5) In_2O_3.

Comparatively, in Fig. 2.4 the position of the c-axis peak (0 0 n) around 31º corresponding to three GIZO JCPDS standards is presented. 2θ changes from 32.01º corresponding to $In_2Zn_4O_7$, crystal plane (0 0 12), In/Zn=0.5 (JCPDS 98-016-2451); to $In_2Zn_3O_6$, 31.56º plane (0 0 15), In/Zn= 0.66 (JCPDS 98-016-2450), and $In_2Zn_2O_5$, 30.98º (0 0 8), In/Zn=1 (JCPDS 00-020-1442). In Fig. 2.4,

2θ for Ga:ZnO (2% Ga) (In/Zn =0), and the peak (2 2 2) for cubic In_2O_3 (In/Zn = ∞), together the 2θ values for the GIZO samples as function of the In/Zn atomic ratio have been represented too. K. Tominaga *et al*. [36] have found a similar evolution when the In/Zn ratio increases. They have also found that the addition of gallium drifts this transition of the 2θ angle to lower values of In/Zn ratio. This change in the value of the 2θ angle, or planar distance, means changes in the crystallographic a, c parameters of the hexagonal structure. To discard a potential drift of the position of the 2θ angle of the peak due to a fault of alignment of the substrate with the goniometer of the XRD device, the planar distances were corroborated by HRTEM, FTT and SAED.

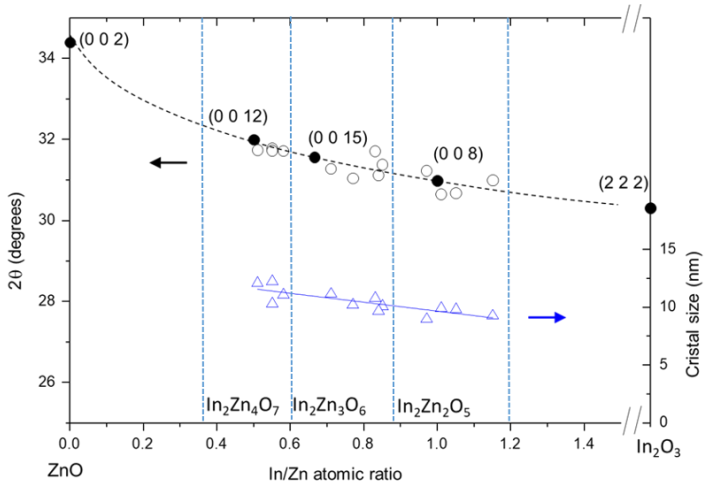

Figure 2.4. 2θ Position of the plane (0 0 n) versus the In/Zn atomic ratio: (filled circles) JCPDS standards, (open circles) GIZO samples. Crystal size versus the In/Zn atomic ratio (triangles).

Additional crystalline planes that were not identified by routine XRD were analyzed by HRTEM (Fig. 2.5-2.6). Figure 2.5(a) shows the HRTEM image of a particle obtained by scratching of the surface of the GIZO_80_250_60 (In/Zn = 0.55). This film is crystalline as shown by SAED (Fig. 2.5(b)) and exhibits an hexagonal structure with the crystallographic parameters estimated as a=3.34 Å and c= 33.72 Å closed to the values of the JCPDS standard 98-016-2451 (a=3.336 Å and c=33.526 Å, $In_2O_7Zn_4$). Figures 2.5(c-f) show the zoom image of two areas of this film and the corresponding FFT.

Figures 2.5 (g-h) show the HRTEM image of a particle of the GIZO_140_150_60 film, with In/Zn =0.99 closed to the JCPDS 00-020-1442 (a=3.376 Å, b=23.154 Å, $In_2O_5Zn_2$), and the corresponding SAED (Fig. 2.5(h)). The SAED (Fig. 2.5(h)) shows a diffuse ring characteristic of a practically amorphous film. By Scherrer (XRD), the crystal size for this GIZO film was estimated as 2 nm.

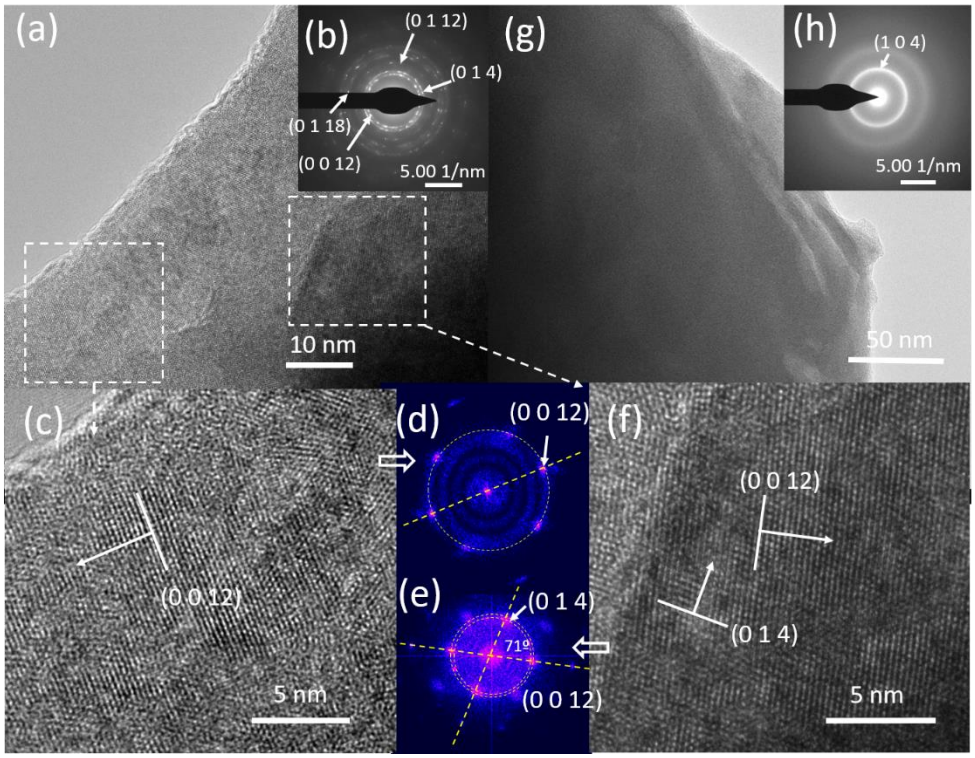

Figure 2.5. HRTEM image of (a) a particle of GIZO obtained at 80 W, 60 min, 250ºC. (b) SAED, (c, f) Zoom of a partial areas of the particle, (e, f) FFT of the zoomed areas. (d, e). HRTEM image of the particle obtained at 140 W, 40 min, 150 ºC (g) and the corresponding SAED (h).

Figures 2.6 shows the EDS (Fig. 2.6(a-c)) and the HRTEM images of the cross section of the GIZO_140_350_40 (In/Zn = 1.05). The film is c-axis textured, with the plane (0 0 8) parallel to the substrate (JCPDS 00-020-1442). The HRTEM images of the cross section of the GIZO film (Fig. 2.6(d)) suggest an initial growth of 3D islands following the Volmer-Weber model, followed by a layer-by-layer growth according the Fran-van de Merwe model. In the first

step (Volmer-Weber) the film adatoms are more strongly bound to each other than to the substrate surface, leading to a slow diffusion of the adatoms which form 3D islands. The islands are not necessarily c-axis oriented, as shown in Fig. 2.6(d, f), and by the FFT (Fig. 2.6e). In the second step of growth (layer-by layer), the crystals are c-axis oriented as shown by the FFT (Fig. 2.6(g)). Nevertheless, crystal grains would be connected to each other and no clear grain boundary are observed in the cross section. The formation of this crystalline morphology, c-axis aligned crystal, was discussed and computer modeled by Shunpei Yamazaki *et al.* [29].

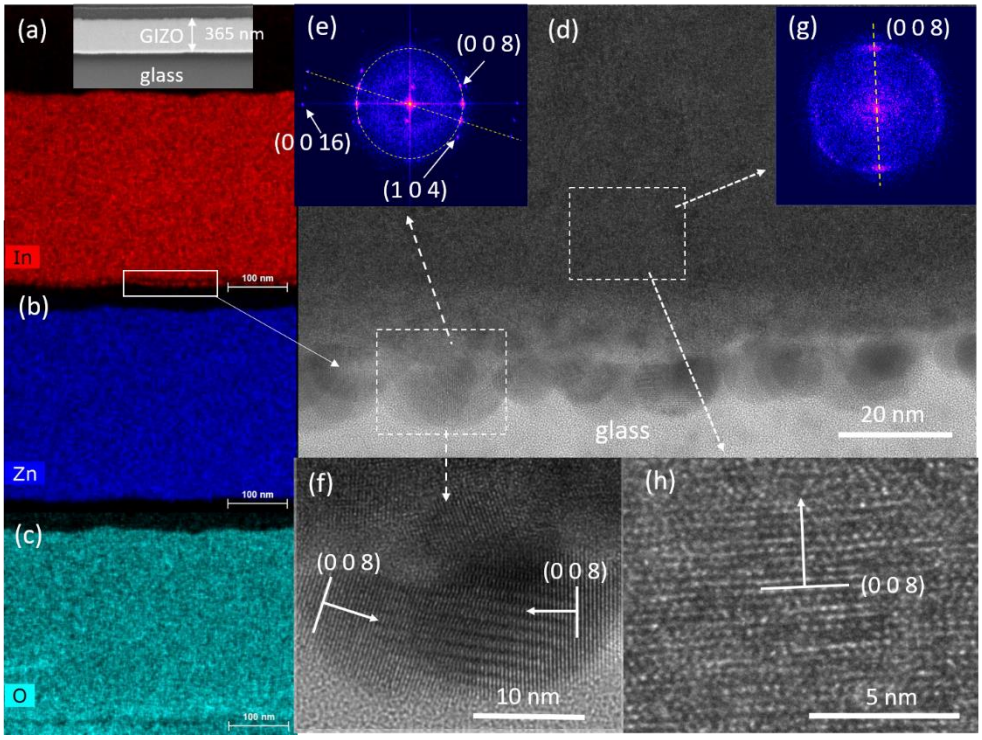

Figure 2.6. (a-c) EDS images of the cross section of the GIZO film obtained at 140 W, 40 min, 350 ºC; **(d)** HRTEM image of the cross section; **(e, f)** HRTEM images of the zoomed areas of the cross section **(g, h)** FFT of the zoomed areas.

Figure 2.7 shows the FESEM images of GIZO films obtained at different values of applied power to the target, time and temperature. In general, the obtained films are very smooth and the roughness decreases with the temperature and with the applied power. By AFM, GIZO films show a

surface Rms roughness of 4 nm for the amorphous GIZO and 11 nm for the crystalline GIZO. The GIZO grains do not exhibit marked sharp edges at the highest power.

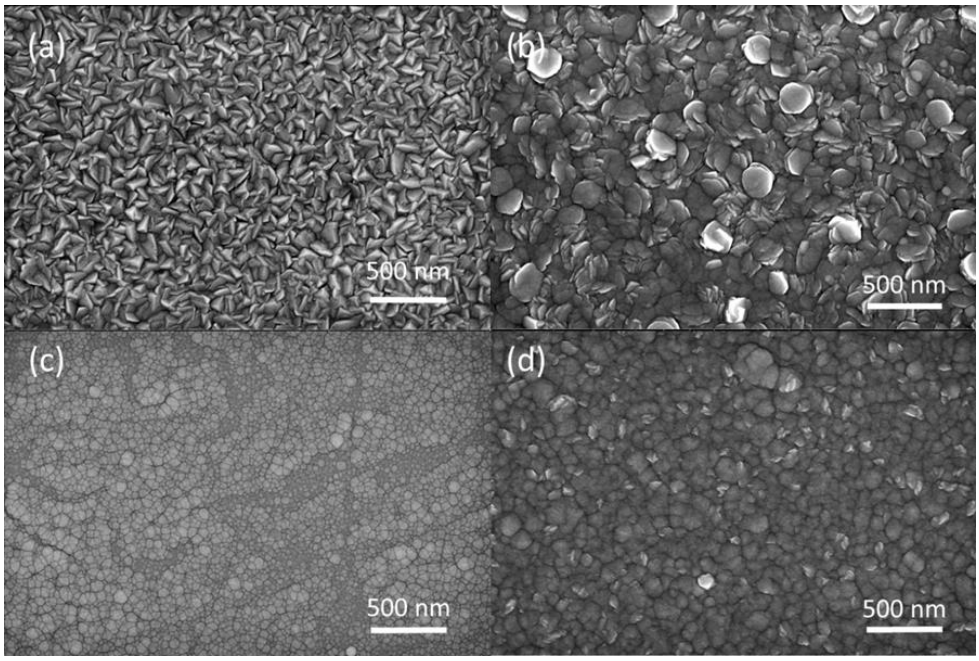

Figure 2.7. FE-SEM micrographs surface images of the samples obtained at (a) 80 W, 60 min, 250ºC (b) 110 W, 60 min, 150ºC (c) 140 W, 40 min, 150 ºC (d) 140 W, 40 min, 350 ºC.

2) OPTICAL PROPERTIES OF GIZO THIN FILMS.

When the GIZO films are used as TCO, and depending on the purpose of the device, the optical behavior influences the efficiency of the device, like for example when used as electrode in solar cells or photocapacitors. From the ANOVA analysis of the Box-Behnken design, the main negative effect on the visible and solar transmittances (Eq. 2.1-2.2) is the deposition time.

$$T_{vis} = \frac{\int_{370}^{780} D_{65}(\lambda)\, V(\lambda)\, T(\lambda)\, d\lambda}{\int_{370}^{780} D_{65}(\lambda)\; V(\lambda)\, d\lambda} \tag{2.1}$$

where, $D_{65}(\lambda)$ is the spectral power distribution of CIE standard illuminant D_{65}, $V(\lambda)$ is the photopic spectral sensitivity function for human vision [37], $T(\lambda)$ is the spectral transmittance of the sample, glass/IGZO film. $T(\lambda)$ is substituted by $R(\lambda)$ for visible reflectance. Solar transmittance and reflectance (T_{solar}, and R_{solar} respectively) were calculated using the Eq 2.2.

$$T_{solar} = \frac{\int_{300}^{2500} I_{AM1.5}(\lambda)\, T(\lambda)\, d\lambda}{\int_{300}^{2500} I_{AM1.5}(\lambda) d\lambda} \tag{2.2}$$

where $I_{AM1.5}$ is the standard spectrum distribution of solar energy for 1.5 atmosphere thickness, corresponding to a solar zenith angle of 48.2°. Solar reflectance can be obtained using $R(\lambda)$ instead of $T(\lambda)$.

This negative effect of the deposition time on the visible transmittance, as is shown in Fig. 2.8(a), is related with the increase of the thickness due to the Beer–Lambert effect. The absorption is proportional to the optical density, product of film thickness t and the absorption coefficient α_λ. Figure 2.8(a) shows also the solar transmittance, the visible, solar reflectances, and the spectral absorptance is calculated as $A(\lambda)= 1- R(\lambda)- T(\lambda)$ and solar absorptance α_{solar} as:

$$\alpha_{solar} = \frac{\int_{300}^{2500} I_{AM1.5}\left(1-R(\lambda)-T(\lambda)\right) d\lambda}{\int_{300}^{2500} I_{AM1.5}\, d\lambda} \tag{2.3}$$

Figure 2.8(b) shows the relationship between solar absorptance of the GIZO films and the charge carrier density. The solar absorptance for the glass

substrate was 8.8 10^{-3}. The solar absorptance increases with the increase of the charge carrier density.

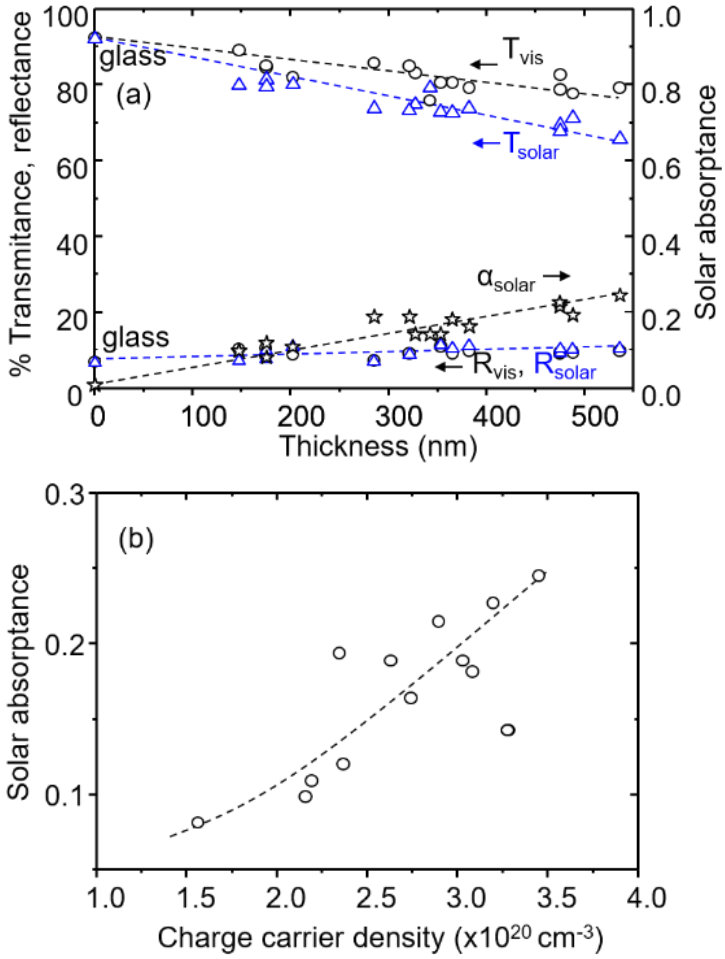

Figure 2.8. (a) Visible and solar transmittance and reflectance, and solar absorptance, versus film thickness **(b)** solar absorptance versus carrier density.

The decay in the transmittance and the rising in the reflectance in the NIR region, as shown in Fig. 2.9 for four GIZO samples with different thicknesses and carrier densities n_e (calculated in next section 3 of present Chapter), would be linked with the charge carrier density, as it will be discussed in section 3. Figure 2.9 shows also the curve of sensitivity of the human eye, and the solar AM1.5 spectral irradiance spectrum.

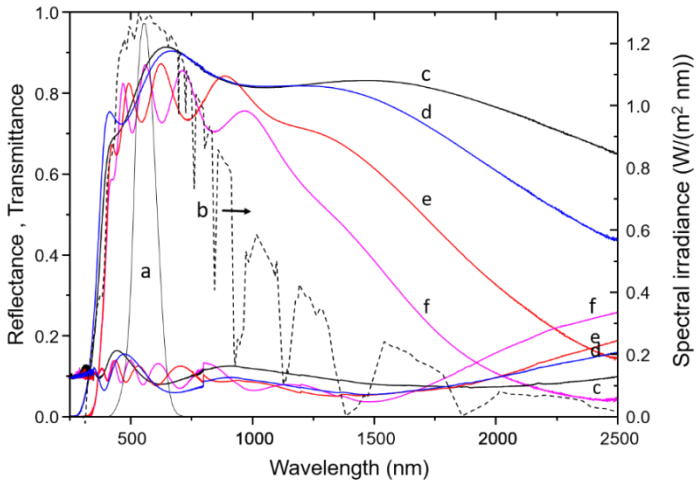

Figure 2.9: (a) Curve of sensitivity of the human eye, **(b)** AM1.5 spectral irradiance. Transmittance and reflectance spectra for GIZO films: **(c)** GIZO_110_150_20, In/Zn= 0.68, t=175 nm, $n_e = 1.56\ 10^{20}$ cm^{-3} ; **(d)** GIZO_140_250_20, In/Zn=1.01, t= 202 nm, $n_e = 2.19\ 10^{20}$ cm^{-3}; **(e)** GIZO_110_150_60, In/Zn=0.97 t= 488 nm, $n_e = 2.35\ 10^{20}$ cm^{-3}; **(f)** GIZO_140_250_60; In/Zn= 1.15, t= 536 nm, $n_e = 3.45\ 10^{20}$ cm^{-3}.

According to Abeles, the relationship between the transmission at a certain wavelength λ, T_λ, the reflection R_λ. and the coefficient of absorption α_λ is:

$$\alpha_\lambda = \frac{1}{t}\ln\left(\frac{(1-R(\lambda))^2}{T(\lambda)}\right) \tag{2.4}$$

where *t* is the film thickness, and α_λ t is de optical density. The coefficient of absorption α_λ has been calculated using the Abeles formula, and estimated from the coefficient of extinction k as obtained from the optical model fitting. The real and imaginary parts of the complex refraction index, n and k respectively, have been obtained by simultaneous fitting of the measured transmittance and reflectance spectra of the films by using an optical multilayer stack model GIZO film/glass substrate, susceptibility optical models, and the Fresnel relationships. The total susceptibility χ can be obtained by adding various contributions (χi) from several susceptibility models. That way, the frequency dependent dielectric function of the glass substrate was previously obtained by using a sum of Brendel's oscillators and a dielectric background. The GIZO film was optically modeled by using

a dielectric function model with the O'Leary–Johnson–Lim model [38], an alternative to the classical Lorentz oscillator, to describe the optical spectra in the region of the band gap, and the extended Drude model for free charge carriers contribution. The classical Drude model (see Eq (2.5)) has been used to describe the interaction of free charge carriers, such as electrons or holes.

$$\chi = -\frac{\omega_p^2}{\omega^2-\Gamma^2} + i\,\frac{\Gamma\,\omega_p^2}{\omega^3+\,\omega\,\Gamma^2} \tag{2.5}$$

where ω is the frequency, ω_p the plasma frequency and Γ the damping constant.

This model of the susceptibility has two parameters, the plasma frequency (ω_p), and the damping constant Γ [39,40] which is inversely proportional to the relaxation time. ω_p is a characteristic frequency at which the material changes from a metallic to a dielectric response. The plasma frequency ω_p is proportional to the charge carrier density n_e by

$$\omega_p^2 = \frac{n_e\,e^2}{m^*\,\varepsilon_0} \tag{2.6}$$

where e is the electron elementary charge, ε_0 is the permittivity of the free space and m^* the effective mass of the charge carriers which is proportional to m_e, the free electron mass, $m^* = n\,m_e$. In spite of effective mass of the conduction electrons varies with the carrier concentration, most of the theoretical analyses assume the effective mass as a constant. We have estimated the effective mass m* for the GIZO films to be approximately 0.32 m_e. This value is coherent with expected values for this kind of conductive n type oxides [41], and identical to the obtained by Takagi *et al*. [42], for single-crystalline GIZO films, and the same authors have reported 0.34 m_e for amorphous GIZO. Other authors have reported values for m* of around 0.2 m_e [43].

The damping constant Γ is related to the charge mobility μ_e by

$$\mu_e = \frac{e}{m^*\,\Gamma} \tag{2.7}$$

In the classical Drude model, the damping constant does not depend on frequency ω. In the extend Drude model (Eq. 8) the damping constant Γ

changes smoothly from a constant at low frequencies Γ_L to another constant level at high frequency Γ_H.

$$\Gamma = \Gamma_L - \frac{\Gamma_L - \Gamma_H}{\pi}\left[\arctan\left(\frac{\omega - \omega_C}{\omega_W}\right) + \frac{\pi}{2}\right] \quad (2.8)$$

where, Γ_L, Γ at low frequencies; Γ_H, Γ at high frequency. The transition region is defined by the crossover frequency ω_c and the width parameter ω_W, width of the transition region.

Figure 2.10 shows the obtained real and the imaginary parts of the complex refraction index (n, k) and the complex dielectric function (ε_1, ε_2), for Ga:ZnO, and three GIZO films. Around plasma frequencies, the contribution due to k becomes important and ε_1 becomes negative for frequencies below ω_p, and the free-electron gas has a metallic response with high reflectivity and absorption. For frequencies higher than ω_p, the free electrons cannot follow the oscillating electric field, and therefore, the film is transparent being ε_1>o and k <n. When ε_1<0, k> n the reflectance is higher (Fig.2.9 and Fig. 2.10b). As n_e increases, the plasma wavelength shifts to shorter wavelengths. The plasma frequencies for the four GIZO films showed in Fig. 2.9 , from the lower to higher n_e, 6621 cm^{-1}, 7844 cm^{-1}, 8114 cm^{-1}, 9837cm^{-1}, and the corresponding estimated wavelength for the minima reflectivity λ_{min}, 1307 nm, 1104 nm, 1067 nm and 880 nm. λ_{min} was estimated from[43]:

$$\lambda_p = \lambda_{min}\sqrt{\frac{\varepsilon_\infty}{\varepsilon_{\infty-1}}} \quad (2.9)$$

being λ_p, the wavelength corresponding to the plasma frequency, ε_∞ the high frequency dielectric constant, which was taken as 4.

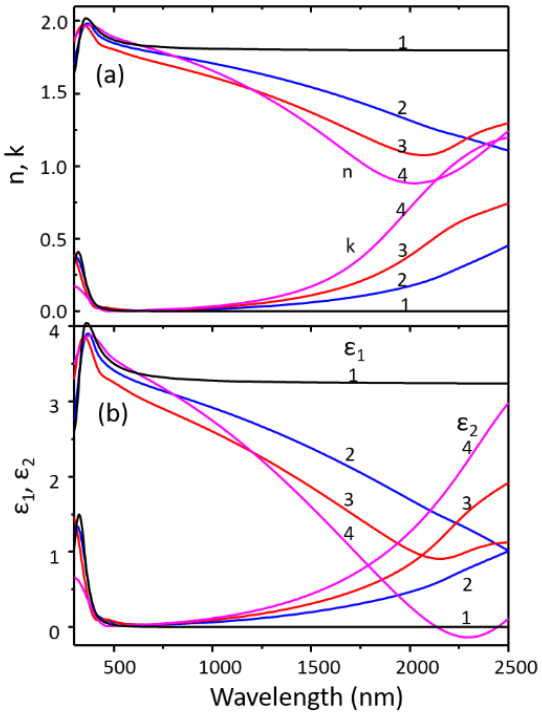

Figure 2.10. Real and imaginary parts of the complex refraction index (a) and the dielectric constant (b) for the samples: (1) Ga:ZnO (2% Ga), (2) GIZO_110_150_20, (3) GIZO_140_250_20 , (4) GIZO_140_250_60.

Fig. 2.11 shows the spectral absorptance for these four GIZO films.

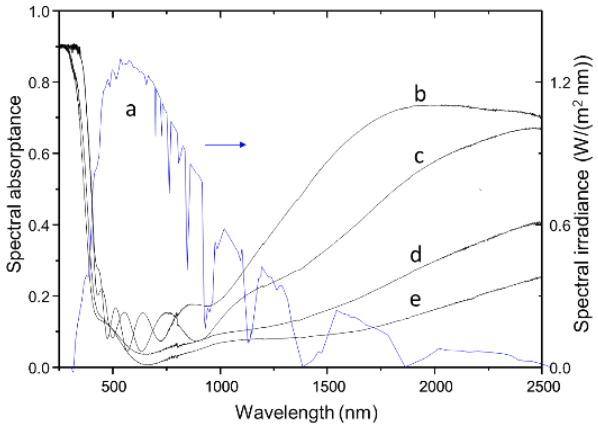

Figure 2.11. (a) AM1.5 spectral irradiance. Transmittance and reflectance spectra for IGZO films: (b) GIZO_110_150_20 (c) GIZO_140_250_20, (e) GIZO_110_150_60 (f) GIZO_140_250_60.

Tauc's equation expresses the relationship between the absorption coefficient α_λ (cm^{-1}), the photon energy (hν) (eV), and the energy of the optical band gap E_g (eV):

$$(\alpha_\lambda h\nu) = c\,(h\nu - E_g)^n \tag{2.10}$$

where $h\nu$ is the energy of the incident photon and c is the absorption edge width parameter. The values of E_g can be determined by extrapolating the linear region of the Tauc plot to hν = 0. The obtained values of the band for GIZO were between 3.4 eV obtained for Ga:ZnO and 3.7 eV for pure cubic In_2O_3 as can be seen in Figure 2.12.

The optical band gap of doped TCO films undergoes a blue shift by the well-known Burstein-Moss (BM) effect or redshift caused by electronic band gap renormalization [44]. The estimated Burstein-Moss blueshift λE_{BM} may differ also of the experimental data due to the variation of electron effective mass, which is dependent on the charge carrier density. λE_{BM} can be estimated by the bandgap widening in n-type semiconductor with parabolic band by the following equation:

$$\Delta E_{BM} = \frac{h^2}{8\,\pi^2 m^*}\,(3\,\pi^2\,n_e)^{\frac{2}{3}} \tag{2.11}$$

where, h is the Planck's constant. In our case, the bandgap shift was estimated as depending on $n_e^{2/3}$. Additionally to the Burstein-Moss effect, there may be other subordinate effects or types of imperfections [44]. Moreover, lattice compression could increase the band gap [45]. A clear relationship between the atomic ratio In/Zn or the crystal size with the band gap is not found in the present work, the band gap seems to grow with the ratio (In/Zn) and the decreasing of crystal size. Kumar *et al*. [46] found a decrease in the band gap with the increase of the amount of In.

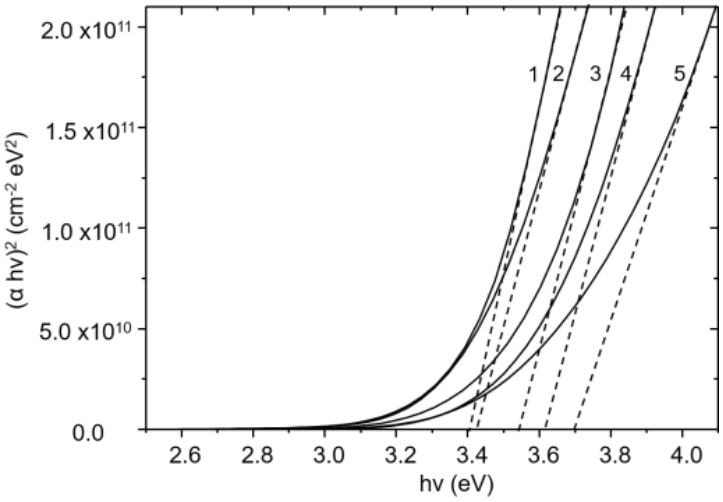

Figure 2.12. Tauc's plots for films **(1)** Ga:ZnO (2% Ga) and GIZO **(2)** GIZO_110_150_20, **(3)** GIZO 110_150_60, **(4)** GIZO_140_350_40, **(5)** GIZO_110_350_60.

3) ELECTRICAL PROPERTIES OF GIZO THIN FILMS.

One of the fundamental relationships describing electrical conduction is

$$\mu_e = \frac{1}{n_e\, e\, \rho_e} \tag{2.12}$$

where μ_e is the charge carrier (electron) mobility, ρ_e (Ω cm) is the electrical resistivity, which is obtained from the sheet resistance R_{sq} (Ω/sq) as $\rho_e = R_{sq}\, t$ (measured by four point probe, see Appendix A). The electrical conductivity σ is the inverse of the electrical resistivity. From the ANOVA analysis the applied power to the In_2O_3 target was the only factor with a significant effect on the conductivity, this means that there is a linear dependence with the applied power as shown in Figure 2.13.

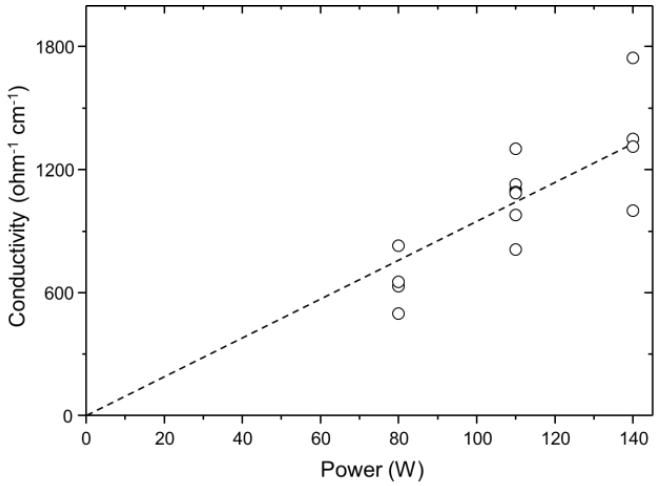

Figure 2.13. Conductivity versus applied power to the In_2O_3 target.

However, as shown in Fig. 2.14(a), the relationship between conductivity and the In/Zn atomic ratio is no lineal. It has been proposed that the increase in dopant atoms would produce some neutral defects, which do not contribute to the conductivity, or to ionized impurities and neutral atoms, which can be segregated at the edges of the grains increasing the scattering of the carriers [47].

Applied power has the largest positive linear effect on the mobility, while the deposition time and substrate temperature have linear negative effects on the electronic mobility with a slight contribution of a positive quadratic effect of the temperature. This means that the increase of the In/Zn ratio increases the mobility, as shown in Fig 2.14(b). A higher Indium concentration in GIZO films produces higher mobility, like other works in bibliography confirm [35,48]. Increasing temperature and time of deposition decreases the mobility, which would be related with the crystalline structure of the film, increasing substrate temperature and deposition time increase the crystallinity as shown in Fig. 2.3. The effect of the annealing temperature on the mobility was studied by Makise *et al.*[49], finding a mobility that decreased when the film changed from amorphous to polycrystalline. This would be the explanation for the dispersion of some points in Fig. 2.14. (b).

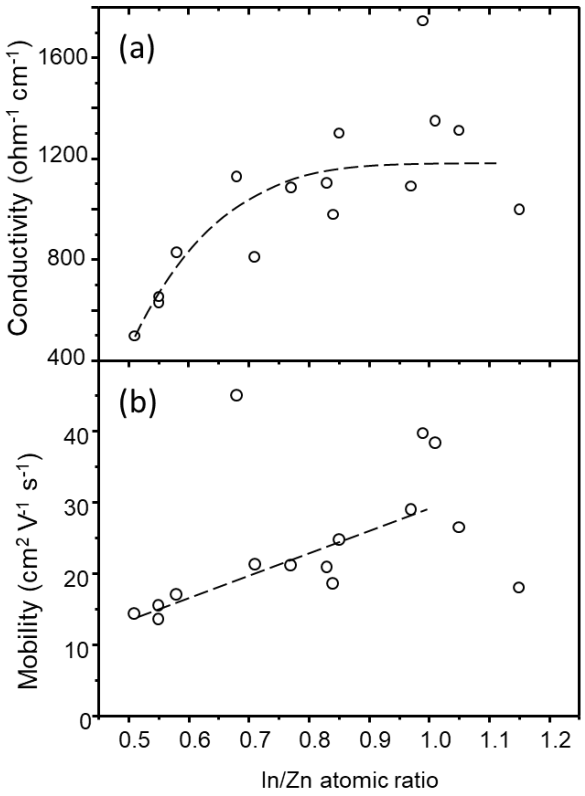

Figure 2.14. **(a)** Conductivity and **(b)** carrier mobility, versus In/Zn atomic ratio.

From the ANOVA analysis, it was found that there are not linear effects on the charge carrier density, being the quadratic effect of the deposition time the most important (Fig.2.15(a)). The effects due to interaction between power and time, and a quadratic effect of the substrate temperature (Fig. 2.16), both positive, were less significant. This means that larger charge carrier density should be obtained at higher tested time (Fig. 2.15(a)) and temperature, as shown in Fig. 2.16-2.17. A higher In/Zn ratio should lead to larger charge carrier density (Fig. 2.14(a)) and hence higher conductivities, in agreement with the study of Pham *et al.*[26], and the same trend was obtained by Kumar *et al.*[43] for undoped amorphous IZO. The charge carrier density found by these authors ranges from 1.26 10^{20} cm^3 (In/Zn = 0.52) to 3.73 10^{20} cm^3 (In/Zn =0.86), and are similar to those found in this work, where the charge carrier density obtained ranges from 1.56 10^{20} (In/Zn =0.68) to 3.45 10^{20} cm^3 (In/Zn = 1.15) Table 2.4. However, as shown in Fig.

2.15(b), the charge carrier density increases for each applied power with the In/Zn ratio, but this evolution segregate in three groups as shown in Fig. 2.15(b). This separation into three groups could be related with the crystallographic structure, undergoing a decreasing in the charge carrier density due to changes in the crystalline parameters of the hexagonal structure with further increasing the In/Zn ratio, as commented in section 1. The maximum values for each group in Fig. 2.15(b) are achieved for the optima combination of temperature and time, Fig. 2.17. Takeda *et al*. [50] reported an increase in mobility when the charge carrier density increased.

Table 2.4. Values of conductivity, carrier density and mobility

Exp. Nº	**Conductivity (Ω^{-1} cm^{-1})**	**Carrier density (cm^{-3})**	**Mobility (cm^2 V^{-1} s^{-1})**
1	1301	3.28 10^{20}	25
2	497	2.16 10^{20}	14
3	1349	2.20 10^{20}	38
4	630	2.90 10^{20}	14
5	998	3.45 10^{20}	18
6	653	2.63 10^{20}	16
7	1745	2.74 10^{20}	40
8	1102	3.29 10^{20}	21
9	828	3.03 10^{20}	17
10	1311	3.08 10^{20}	27
11	1129	1.56 10^{20}	45
12	1090	2.35 10^{20}	29
13	809	2.37 10^{20}	21
14	1085	3.20 10^{20}	21
15	978	3.28 10^{20}	19

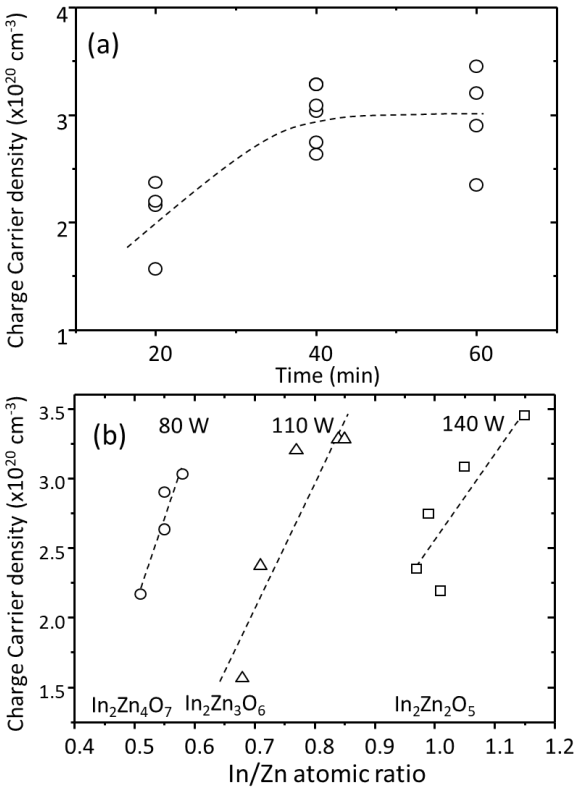

Figure 2.15. Charge carrier density versus **(a)** time **(b)** In/Zn atomic ratio.

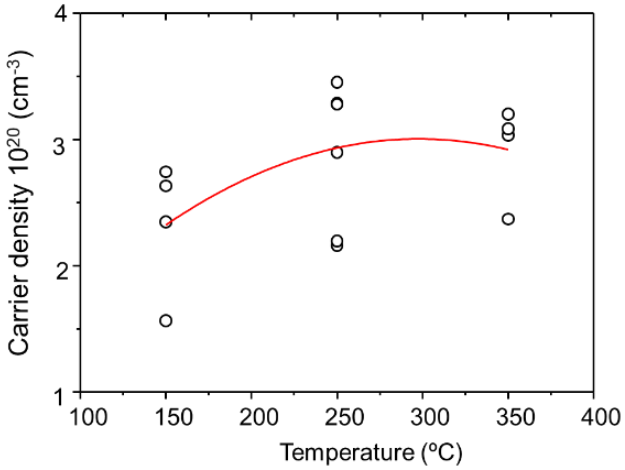

Figure 2.16. Carrier density versus substrate temperature.

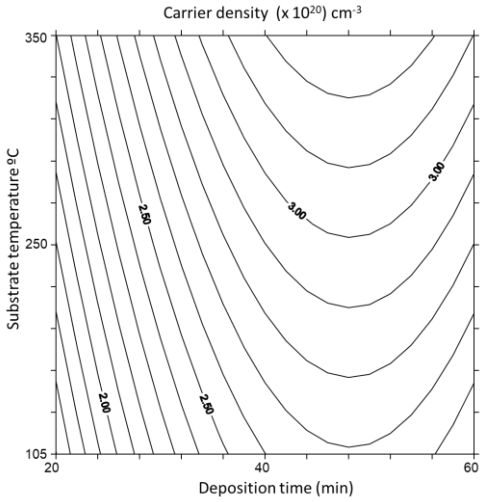

Figure 2.17. Surface response of carrier density as function of deposition time and substrate temperature.

For the optimization of TCOs a compromise between conductivity and transparency is necessary, and for this purpose different figures of merit (FOM) have been defined. Fraser and Cook [51] proposed using the ratio of transmission at a given wavelength and the sheet resistance to characterize the TCO films. Haacke [52] suggested the figure of merit

$$\Phi_{TC} = T_{550}^{10} / R_{sq} = \sigma\, t \exp(-10\, \alpha_\lambda\, t) \qquad (2.13)$$

where R_{sq} is the sheet resistance. T is the optical transmission (scale 0-1) at 550 nm. This merit functions uses the exponent 10 with the intention of reducing the excessive weight of the sheet resistance in Φ_{TC}. Gordon[53] suggested using the conductivity/absorption coefficient ratio, σ/α_λ. Fernández *et al.*[54] proposed;

$$\Phi_F = -1/\rho \ln (T) = \sigma\ \alpha_\lambda\ t \qquad (2.14)$$

There are other proposals [55], and more recently, Hu *et al*. [56] proposed a modified form of the Haacke:

$$\Phi_H = \frac{\left(\frac{Q_A}{Q_T}\right)^{10}}{R_{sq}} \qquad (2.15)$$

where Q_A and Q_T are the numerator and denominator of the Eq. 2.2, respectively. Therefore, Q_A/Q_T is the solar transmittance T_{solar}, corrected by a specific external quantum function for each kind of solar cells in which the TCO is used, and limiting the range of wavelength to the absorbable waveband of the specific solar cell. However, Hu *et al*. did not define the figure of merit Φ_H for the visible region. Transparency in the visible range is important for several applications in transparent electronics or smart windows. We propose to replace the solar spectra irradiance AM1.5 by theoretical illuminant $D_{65}(\lambda)$, as proposed by CIE [37], and the specific external quantum function by $V(\lambda)$ for the visible region. Here $V(\lambda)$ plays the same role as the external quantum function, and the ratio Q_A/Q_T of the Eq. 2.15 converts in the visible transmittance T_{vis}, resulting the modified forms of Φ_{TC}.

$$\Phi_{TCMvis} = T_{vis}{}^{10}/R_{sq} \tag{2.16}$$

and

$$\Phi_{Hsolar} = T_{solar}{}^{10}/R_{sq} \tag{2.17}$$

where Φ_{Hsolar} is Φ_H without the specific external quantum function. Both FOMs are shown in Figure 2.18(a).

In the same way, we have also modified the FOMs proposed by Fernández *et al.* (Eq.2.14)

$$\Phi_{FMvis} = -1/\rho \ln (T_{vis}) \tag{2.18}$$

$$\Phi_{FMsolar} = -1/\rho \ln (T_{solar}) \tag{2.19}$$

and the Gordon's FOM, α_{solar}, as calculated by Eq. 3,

$$\Phi_{GMsolar} = \sigma/\alpha_{solar} \tag{2.20}$$

These FOMs are represented in Fig. 2.18(c-d). We have also defined for the first time, two new FOMs for the visible region and solar region:

$$\Phi_{Mvis} = T_{vis}/\rho \tag{2.21}$$

$$\Phi_{Msolar} = T_{solar}/\rho \tag{2.22}$$

where ρ is the electrical resistivity (Ω cm). We consider resistivity more suitable that sheet resistance because ρ considers the film thickness t, $\rho = R_{sq}$ t. Both FOMs show similar behavior (Fig. 2.18(b)).

All the FOMs were fitted by a second-degree polynomial. In our case, we were interested in selecting the optimum In/Zn atomic ratio based on the best balance between conductivity and transparency. It has been found that for our GIZO films, Φ_{Hsolar} behaves well to find the In/Zn ratio that provides the best balance for the solar region (Fig. 2.18(a)), but Φ_{TCMvis} does not. Φ_{Hsolar} shows a maximum for In/Zn= 0.89, while Φ_{TCMvis} increases. The opposite behavior happened with Φ_{FMvis} and $\Phi_{FMsolar}$ (Fig. 2.18 (d)). Figure 2.18 (c) shows $\Phi_{GMsolar}$ with a maximum for In/Zn=0.86. Φ_{Mvis} and Φ_{Msolar} show maximums around In/Zn= 0.95 and In/Zn = 0.93 respectively. Φ_{Mvis} and Φ_{Msolar} show a similar evolution with the In/Zn ratio in contrast with the other FOMs (Fig. 2.18).

The best values of electrical conductivity were obtained for GIZO films with In/Zn ratio ≥ 1, being the best reached value of conductivity 1.75 10^3 Ω^{-1} cm^{-1}, and improving the conductivity of pure ZnO, Gallium Zinc Oxide (GZO) [57] and another GIZO films deposited by sputtering method [58,59], the visible and solar transmittances were below 0.8. It is accepted that visible transmittance should not be below 80% for a TCO. In spite of these individual maximum values of conductivity, it should be expected that the best balance of conductivity and transparency should be obtained for the In/Zn ratio corresponding to the maximum values of the FOMs. Therefore, GIZO films with the nearest ratios to the maximum values of the FOMs, around 0.9. In/Zn 0.83, 0.85 have conductivities of 1102, 1300 $\Omega^{-1}cm^{-1}$, visible transmittances of 81%, 83%, and solar transmittances of 73%, 75% respectively (glass/GIZO films). The measured transmittances of the glass substrate were 92.5% and 92.2% for T_{vis} and T_{solar} respectively. The losses of 7.5% and 7.8% in visible and solar light transmission are due to reflection of the glass substrate. We can conclude that In/Zn ratios between 0.85-0.90 are optimal for GIZO films (2% Ga/Zn) as TCOs for visible and solar applications.

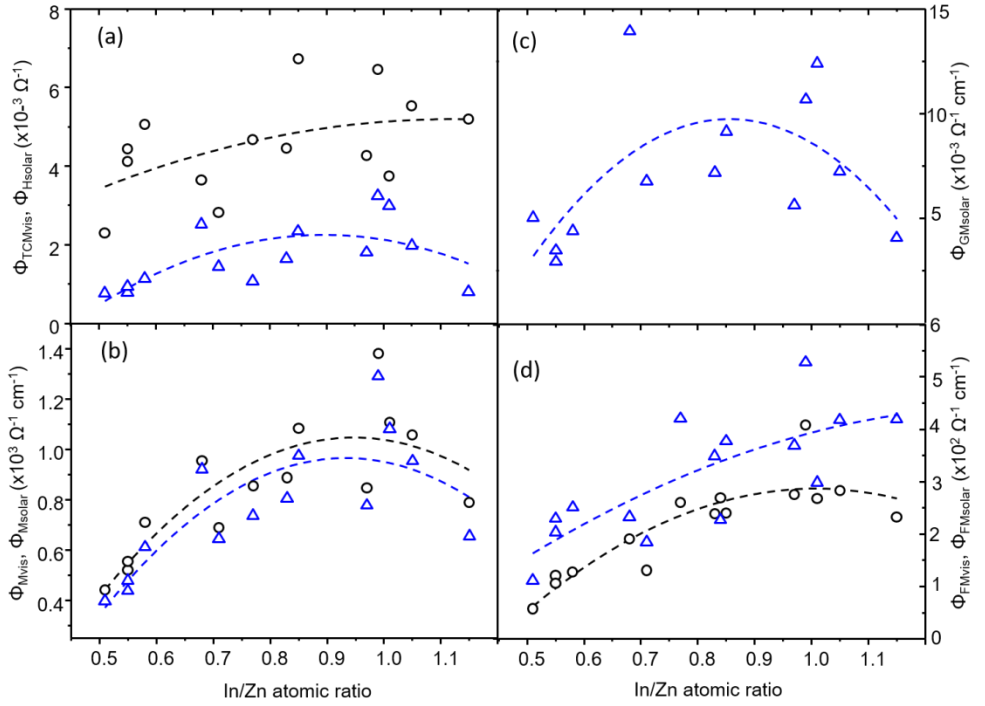

Figure 2.18. FOMs versus In/Zn atomic ratio: **(a)** Φ_{Hsolar} (triangles), Φ_{TCMvis} (circles) **(b)** Φ_{Msolar} (triangles), Φ_{Mvis} (circles) **(c)** $\Phi_{GMsolar}$ **(d)** Φ_{FMvis} (circles), $\Phi_{FMsolar}$ (triangles).

4) ELECTROCHEMICAL PROPERTIES OF GIZO THIN FILMS.

The selection of an appropriate substrate is an important preliminary step in accurately evaluating electrochemically active materials including electrocatalysts, photoelectrodes, electrochromic devices and electrochemical capacitors[60,61]. Then, the electrochemical reactivity of GIZO substrate is a key criterion which is particularly important when choosing a substrate for electrochemical applications. In most cases, an inert substrate that exhibits no electrochemical activity under the testing conditions is preferred. In general, the electrochemical (or potential) windows (that is, the ranges of potentials over which the electrodes are stable) of different materials can be limited because of (i) oxidation/ reduction (decomposition) of the solvent or (ii) oxidation/reduction (decomposition or change in surface properties) of the electrode surface itself[60,61]. The electrochemical stability of GIZO thin films is of great importance in the various application fields above mentioned. Their electrochemical properties directly affect the electrochemical stability of the involved systems. Moreover, the performance of TCO materials used in electrochemical applications is primarily determined by electron-transfer kinetics. So, understanding the electron transfer properties of a TCO substrate is essential for exploring its application as an electrode material. While the electrochemical behavior (stability and electron transfer properties), of many individual TCO substrate materials such as ITO and FTO has been extensively studied [60,62–65], to the best of our knowledge, there has been no comprehensive and systematic experimental study of the electrochemical behavior of GIZO thin films.

Here, the electrochemical behavior (stability and electron transfer properties), and photoelectrochemical characteristics of synthesized RF magnetron sputtered transparent and conducting GIZO thin film samples has been examined. These results provide useful insights into the behavior of this TCO material and serve as a starting point for the selection of appropriate substrate materials for their use as photoelectrodes in the final photocapacitor, since this thin film allow the electrodeposition of ZnO nanowires with no need of a seed layer.

The electrochemical behavior of GIZO thin films were evaluated by cyclic voltammetry (CV) curves, carried out at room temperature with a Biologic VSP potentiostat. The experiments were performed in a conventional three-electrode electrochemical cell with the GIZO or a Pt sheet as the working electrode, a platinum sheet as the counter electrode and a saturated calomel electrode (SCE) as the reference one. The electrolyte solution was saturated with pure molecular nitrogen by bubbling for 15 min prior to start each measurement and continuously during the process over the solution. In this research, the surface characterization of GIZO was performed with 1N H_2SO_4 , and the electrochemical kinetics properties was evaluated employing a redox couple of 10 mM $Fe(CN)_6^{3-/4-}$. For comparison, another commercial TCOs such as ITO and FTO were also measured in 1N H_2SO_4 in the same conditions.

4.1 ELECTROCHEMICAL STABILITY OF THE GIZO THIN FILMS

The electrochemical stability behavior of the synthesized RF magnetron sputtered GIZO thin film samples (electrical resistivity 0.92 mΩ.cm), has been examined by using cyclic voltammetry technique in acidic aqueous electrolyte (0.5M H_2SO_4 solution) and results are presented in Fig. 2.19. For comparison, two transparent commercial conducting oxide substrates on glass substrates (i.e.: ITO and FTO), have also been evaluated (see Fig. 2.19). In line to previous studies[66], the resulting cyclic voltammograms have been separated for purpose of discussion, into three main regions: double layer region (I), the cathodic region (II, II'), and the oxide region (III). Region I for these oxide films are bounded at positive potentials (region III) by oxygen evolution and at negative potentials (region II) by oxide reduction to a lower valence state of the metal, hydrogen evolution and/or reduction of surface to the metallic state (region II'). For all oxide films, the charge on the electrode changes monotonically throughout region I, indicating a wide potential window available for carrying out redox reactions. This current is attributed to the charging and discharging of positive surface states[67]. The distinction between region I and II is made to indicate the small Faradic current which possibly involves the surface and appears to occur at

potentials in region II'[66]. GIZO and ITO thin films present the same potential window for this redox reactions (ca. 2.2 V), unlike FTO with a lower available potential (ca. 2.0 V). Region III is the oxygen evolution region, being very similar between them, as metals of these oxides are presents in their highest oxidation state of the metal. In the voltammogram obtained for an GIZO thin film sample, it can be seen that during the potential scan towards the cathodic potentials, a very intense and broad well-defined large reduction peak at -1.12 V and a small peak at -1.3 V appeared, characteristics of reduction reactions. Moving to more cathodic potentials (-1.5 V), a monotone current increase in the potential characteristic of the evolution of hydrogen, can be seen. In the reverse scan, two anodic peaks at -0.98 V and -0.47 V can be appreciated, these oxidation current features can be attributed, in a similar way to the FTO case, to formation of hydrous indium-zinc oxide/hydroxide in the film[61].

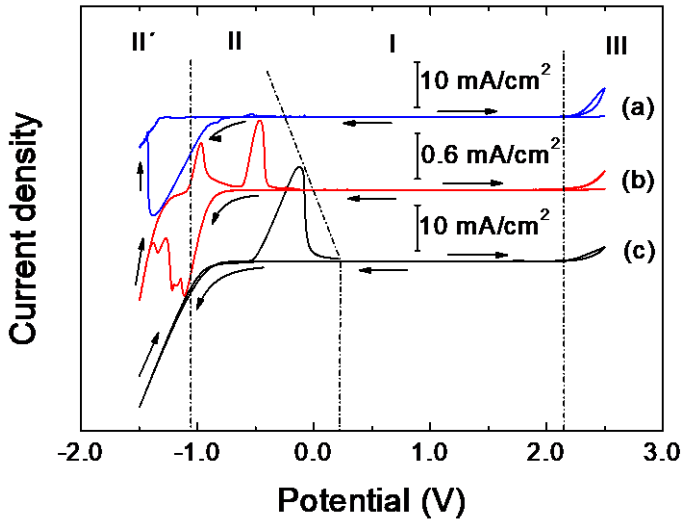

Figure 2.19. Cyclic voltammograms for: (a) commercial ITO transparent conducting oxide on glass substrate; (b) a typical RF magnetron sputtered GIZO thin film sample onto a glass substrate, and (c) commercial FTO transparent conducting oxide onto a glass substrate. Electrolytic bath solution: 1N H_2SO_4 aqueous media. Scan rate: 100 mV s^{-1}. The black line arrows indicate the potential scan direction.

4.2 ELECTRON TRANSFER PROPERTIES OF THE GIZO THIN FILMS

The electrochemical performance of the GIZO thin films in electron-transfer reactions has been assessed using the common redox probe ferrocyanide ($Fe(CN)_6^{4-/3-}$). This redox probe has been chosen because the fact that its electrochemical behavior at a variety of electrode materials is well documented and understood. In fact, the ferro/ferricyanide redox complex has been extensively characterized in the past and several studies have shown that it is sensitive to the surface structure of electrode materials [68]. Moreover, redox probe ferrocyanide termed surface sensitive in that heterogeneous electron transfer (HET) rate is strongly influenced by the state of the electrode surface (surface chemistry and microstructure) via specific electro-catalytic interactions[69]. The redox electrochemistry on GIZO has been studied in a comparative manner with Pt electrodes in an aqueous electrolyte, in order to investigate the electron-transfer properties. GIZO thin films with different resistivity values (see Table 2.5) have been compared to a Pt electrode in order to assess their possible use as electrodes in optoelectronic devices, and check the electrical resistance effect on the electrochemical properties. Thus, the electrochemical properties of the GIZO thin films have been done through a study of their performances in cyclic voltammetry towards that redox probe reaction, at different scan rates. This is a simple and traditional experiment whereas providing valuable information about electrochemical reversibility, diffusion coefficient and electron transfer kinetics[70].

Table 2.5. Different properties of the studied GIZO thin film samples.

Sample name	In/Zn atomic ratio	Electrical resistivity (mΩ.cm)
Z	0.55	1.30
H	0.71	1.26
X	0.77	0.92
C	1.05	0.83

Figure 2.20 shows cyclic voltammograms (CVs) at different potential scan rates (ranging from 10 to 200 mV/s), for a Pt electrode in a 10 mM $Fe(CN)_6^{4-}$ + 1 M KNO_3 electrolytic solution. The effect of the scan rate (v) on the appearance of the CVs is clearly seen in this Figure 2.20. As described by Randless-Sevcik equation [71], both anodic peak current (i_{pa}) and cathodic peak current (i_{pc}) increase with $v^{1/2}$, as is depicted in the inset of Figure 2.20 (where linear fittings have been done), indicating that the process is diffusion-controlled.

Furthermore, the separation of the peak potentials (i.e.: $\Delta E_{pp}=E_{pa}-E_{pc}$, where E_{pa} and E_{pc} are the anodic and cathodic peak potentials in the cyclic voltammogram, respectively) of ca. 77-135 mV is close to the theoretical value of 59 mV (where the deviation is explained by an IR-drop in the solution). These results are independent of v (within the measurement uncertainties), indicating a reversible electrochemical process, with anodic and cathodic current peak ratio of approximately one. Relevant parameters from these data are assembled in Table 2.6.

At this point it must be pointed out that through ΔE_{pp} values, qualitative and quantitative info about electron transfer rate constant and resistance to electron transfer can be obtained[71]. For instance, smaller ΔE_{pp} values represent an increased reversibility in the electrochemistry at the redox probe utilized, and thus faster HET kinetics at the given electrode material, which is generally beneficial in numerous instances.

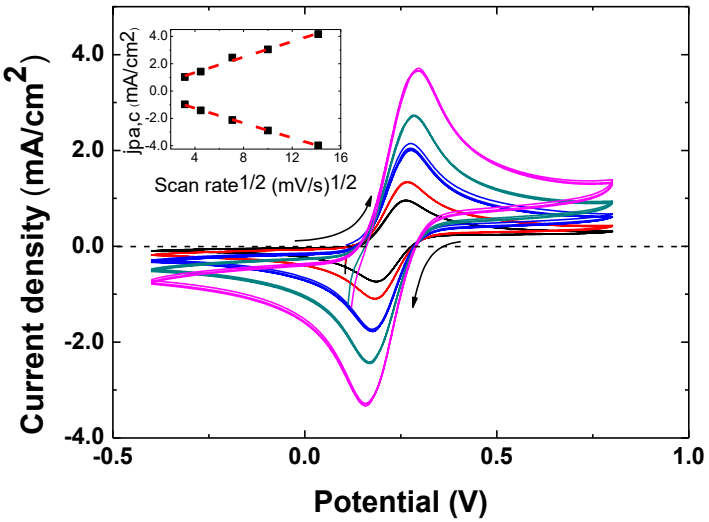

Figure 2.20. Cyclic voltammograms of a Pt electrode in 10 mM $Fe(CN)_6^{4-}$ + 1 M KNO_3 at different potential scan rates (10 mV/s (black line curve), 20 mV/s (red line curve), 50 mV/s (blue line curve), 100 mV/s (dark cyan line curve) and 200 mV/s (magenta line curve)). Inset: Anodic and cathodic peak currents versus square root of potential scan rate. Red dashed lines correspond to the linear curve fitting of these data.

Figures 2.21 and 2.22 show the cyclic voltammetric profiles at different scan rates (ranging from 10 to 200 mV/s), for both the lowest (more conductive) and the highest (less conductive) electrical resistivity GIZO samples, samples C and Z, respectively.

In each case, ΔE_{pp} strongly increases with the potential scan rate, a trend consistent with a quasi-reversible behavior. Moreover, and more important, ΔE_{pp} for the GIZO case is always much higher than for Pt electrode, see Table 2.6, demonstrating the inefficacy of charge transfer at that oxide electrode surface (ΔE_{pp} is as high as 1.189 V for sample Z at v=200 mV/s).

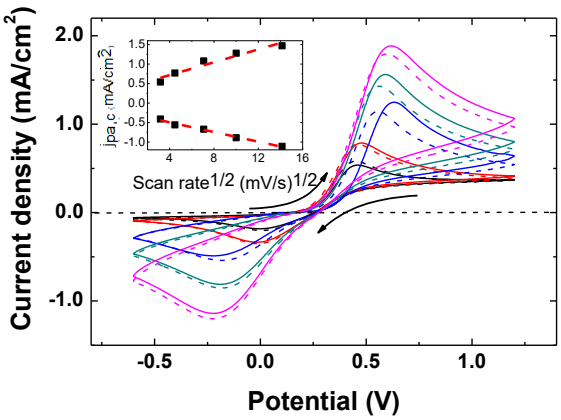

Figure 2.21. Cyclic voltammograms of an GIZO thin film sample electrode (electrical resistivity: 0.83 mΩ.cm) in 10 mM $Fe(CN)_6^{4-}$ + 1 M KNO_3 at different potential scan rates (10 mV/s (black line curve), 20 mV/s (red line curve), 50 mV/s (blue line curve), 100 mV/s (dark cyan line curve) and 200 mV/s (magenta line curve)). Inset: Anodic and cathodic peak currents versus square root of potential scan rate. Red dashed lines correspond to the linear curve fitting of these data.

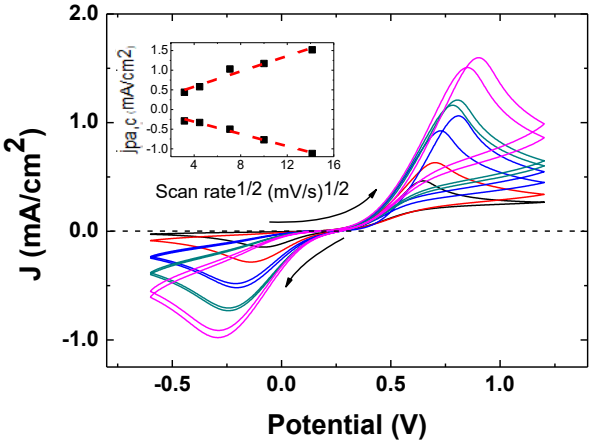

Figure 2.22. Cyclic voltammograms of an GIZO thin film sample electrode (electrical resistivity: 1.30 mΩ.cm) in 10 mM $Fe(CN)_6^{4-}$ + 1 M KNO_3 at different potential scan rates (10 mV/s (black line curve), 20 mV/s (red line curve), 50 mV/s (blue line curve), 100 mV/s (dark cyan line curve) and 200 mV/s (magenta line curve)). Inset: Anodic and cathodic peak currents versus square root of potential scan rate. Red dashed lines correspond to the linear curve fitting of these data.

Table 2.6. Cyclic voltammetry data for Pt and GIZO electrodes in 10 mM $Fe(CN)_6^{4-}$ + 1 M KNO_3, and resulting electrochemical kinetics.

Pt	**Scan rate v (mV/s)**	**ΔE_{pp} (mV)**	**i_{pa}/i_{pc}**	**α**
	10	77	1.0	0.50
	20	86	1.0	
	50	100	1.1	
	100	115	1.0	
	200	135	1.0	
GIZO (sample C, ρ=0.83 mΩ.cm)	**Scan rate v (mV/s)**	**ΔE_{pp} (mV)**	**i_{pa}/i_{pc}**	**α**
	10	460	1.3	0.54
	20	497	1.4	
	50	736	1.6	
	100	782	1.4	
	200	841	1.3	
GIZO (sample Z, ρ=1.30 mΩ.cm)	**Scan rate v (mV/s)**	**ΔE_{pp} (mV)**	**i_{pa}/i_{pc}**	**α**
	10	731	1.5	0.70
	20	843	1.7	
	50	1017	2.0	
	100	1048	1.5	
	200	1189	1.4	

To further evaluate the electrochemical behavior of the redox probe ferrocyanide onto the different GIZO surfaces, the influence of scan rate on the anodic peak potential has been analyzed. The variation of E_{pa} with the logarithm of scan rate, ln v, for the different GIZO substrates under study is shown in Fig. 2.23.

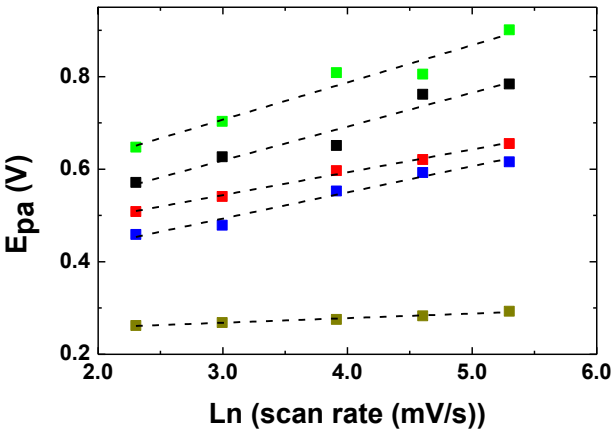

Figure 2.23. Anodic peak potential versus logarithm of potential scan rate for a Pt electrode (dark yellow symbols), and for GIZO thin film sample electrodes with different electrical resistivity values: 1.30 mΩ.cm (green symbols),1.26 mΩ.cm (black symbols), 0.92 mΩ.cm (red symbols) and 0.83 mΩ.cm (blue symbols). Black dashed lines correspond to the linear curve fitting of these data. Cyclic voltammograms of these electrodes carried out in 10 mM $Fe(CN)_6^{4-}$ + 1 M KNO_3.

It can be observed that: i) for the Pt case the anodic peak potentials remain nearly constant irrespective of the potential scan rate (indicating again its reversible behavior), and ii) for the case of GIZO surface the anodic peak potentials shift to more anodic potentials when the potential scan rate increases, and that this effect is similar for all GIZO samples under study. The value of αn (where α is the transfer coefficient and n is the number of electrons transferred for the oxidation/reduction process) can be determined through the Laviron's approach. According to Laviron's expression for an electrochemical process [71,72], E_{pa} is governed by:

$$E_{pa} = E^o + \frac{2.303RT}{(1-\alpha)nF} log \frac{(RTk^o)}{(1-\alpha)nF} + \frac{(2.303RT)}{(1-\alpha)nF} logv \qquad (2.23)$$

where v is the scan rate, n is the number of electrons transferred, α is the transfer coefficient, E^o is the formal standard redox potential and k^o is the standard heterogeneous rate constant of the reaction, and the other symbols have their usual meaning. The value of αn can be calculated from the slope of the E_{pa} vs. log v plot. Thus, from the slopes of plots depicted in Fig. 2.23, and with a n value equal to 1, values of α have been calculated and are assembled in Table 2.6.

Taking into account the separation of the peak potentials (ΔE_{pp}) measured, the reversibility of redox processes at cyclic voltammetries can be directly related to the electrical resistivity data presented on Table 2.5 for the different GIZO samples under study. In this way, the film quality from the point of view of their use as electrodes can be related with their electrical properties.

4.3. PHOTOELECTROCHEMICAL BEHAVIOR OF THE GIZO THIN FILMS

In order to explore the photoresponse and to evaluate the photolectrochemical properties of the GIZO thin films, potentiodynamic j/E profiles of these GIZO samples as working electrodes in 0.1 M Na_2S + 0.1 M Na_2SO_3 aqueous electrolyte, and under chopped white light illumination have been carried out (see Fig. 2.24a). In this way, both the dark current and photocurrent can be recorded during a single scan. The onset of photocurrent can be located at ca. -0.8 V (potential region not shown in the plot of Fig. 2.24.a). All of the GIZO thin film samples demonstrate a typical anodic photocurrent response confirming their n-type conductivity behavior. In fact, it is known from earlier reports that IZO films are semiconductors exhibiting n-type electrical conductivity [73,74]. A very high anodic current under dark conditions can be appreciated, probably owing to the oxidation of GIZO itself or due to a capacitive behavior of GIZO. This GIZO thin film sample electrode exhibits an anodic photocurrent (hole current) of about 2 $\mu A/cm^2$ in the -0.1 to 0.1 potential range (see inset of Fig. 2.24a). During illumination the photogenerated holes are scavenged by S^{2-}. The influence of bias voltage on the transient photoresponse has also been studied (at -0.5 V, 0 V and 0.2 V bias potential), and is illustrated by the data in Fig. 2.24b. Depending on the photoelectrode potential the photoelectrical transient response of the electrode varies significantly. At a bias of -0.5 V the photoresponse exhibited a characteristic decay from a 'spike' to a steady state during the illumination period, followed by an overshoot in the opposite direction and decay back to zero during the dark period. The anodic overshoots and their subsequent decay towards a steady state value could indicate a significant accumulation of holes at the electrode surface under

white illumination [75–78] or the existence of a recombination of electrons with holes. Upon closing the shutter, the cathodic overshoot current that has been observed before the dark value was reached, can be attributed to the recombination of surface-trapped holes with electrons from the conduction band of GIZO semiconductor material [75,77–79]. At more anodic bias potentials of 0 V and 0.2 V (see Fig. 2.24b), it can be seen that the initial current increase with increasing anodic potential as expected but more important, both the anodic current decay and the cathodic current flow decrease at higher anodic potentials. Thus, the transients disappear as the photocurrent approaches its saturation value with more positive potentials. The basis for this behavior is simply that the interface is deleted of majority carriers at these potentials such that back reduction of the oxidized redox species and the oxidized state is inhibited [80].

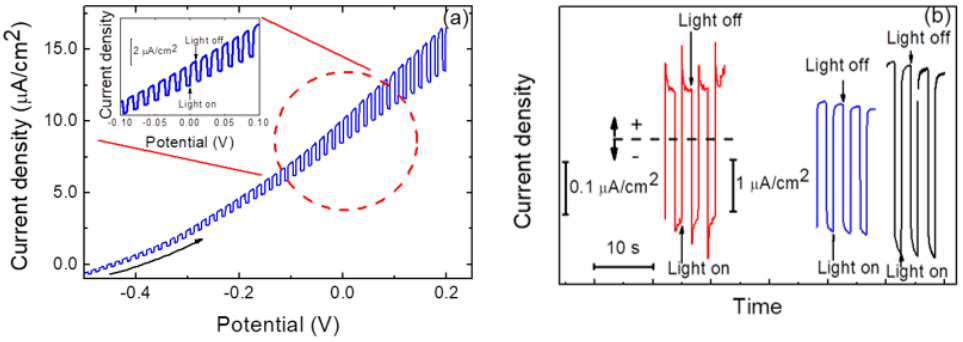

Figure 2.24. (a) Linear scan voltammetry of a typical GIZO thin film electrode under chopped light illumination condition. These curves have been recorded at a potential scan rate of 0.025 Vs^{-1}, under white illumination. Inset: magnified view of the circled region from -0.10 V to 0.10 V. (b) Transient photoresponse of a typical GIZO thin film electrode for three different electrode bias potentials: -0.5 V (red line curve), 0.0 V (blue line curve) and 0.2 V (black line curve) under white illumination. Currents in the case of applied bias of 0.0 V and 0.2 V, are both anodic, whereas at -0.5 the current sign is indicated. Both type of experiments carried out in 0.1 M Na_2S + 0.1 M Na_2SO_3 electrolytic aqueous solution, and under white illumination from a solar simulator: 100 mW/cm^2, AM 1.5.

D. CONCLUSIONS

Conductive and transparent GIZO films were successfully deposited on glass substrates with a fixed Ga /Zn ratio of 0.02. The best values of electrical conductivity were obtained for GIZO films with In/Zn ratio ≥ 1, being the best reached value of conductivity 1.75 10^3 Ω^{-1} cm^{-1}, and improving the conductivity of pure ZnO, Gallium Zinc Oxide (GZO) and another GIZO films deposited by sputtering method. By means of a Box-Behnken experimental design approach the effects of the magnetron sputtering parameters, namely, power applied to the In_2O_3 target, substrate temperature and deposition time, on the structural, optical and electrical properties of the GIZO films were determined. The thickness increases linearly with the deposition time and the power applied to the In_2O_3 target, and the In/Zn ratio increases with the applied power too. The crystalline parameters of the hexagonal structure change with the In/Zn ratio and the charge carrier density is linked to those changes, and therefore to the GIZO stoichiometry. The GIZO films grew c-axis oriented after an initial island step. The small percentage of Ga introduces early amorphization, which leads to an increase of the carrier mobility and conductivity. The increase of the solar absorptance, due to the increase in the spectral absorptance in the NIR region, is related to the plasma frequency, and therefore to the charge carrier density. New FOMs have been proposed for the first time that use integrated values, weighted by functions for visible and solar, instead of individual of average values for the transmitted radiation or the absorption coefficient. The defined figures of merit indicate that the best balance between conductivity and transparency for visible and solar applications of the GIZO films (2% Ga/Zn) as TCOs are in the In/Zn of 0.85-0.90 range.

With regard to electrochemical properties, GIZO possess a good stability in the electrochemical conditions used due to their high potential window (ca. 2.2 V) similar to ITO films and higher than FTO films (ca. 2.0 V). GIZO thin films demonstrate a typical anodic photocurrent response whose value depend on the applied potential bias, confirming their n-type conductivity behavior. The reversibility of redox processes can be directly related to the electrical resistivity of GIZO samples under study.

III

PHOTOANODE

A. INTRODUCTION

QUANTUM DOT SENSITIZED SOLAR CELLS (QDSSC)

Sensitized Solar Cells have emerged in solar energy field in the last two decades as a very promising "third-generation" photovoltaic device [81]. Among them, we can find the Dye-Sensitized Solar Cells (DSSCs) and the Quantum Dot-Sensitized Solar Cells (QDSSCs). In the DSSCs, an organic and/or metalorganic molecular dye is the light absorbing material while the QDSSCs use an inorganic semiconductor quantum dot (QD) to act as light harvesting material. Initially, O´Regan and Grätzel were the pioneer proposing a DSSC in 1991 employing a Ruthenium-based dye molecule[82]. However, these devices have the disadvantage of high cost due to the expensive synthesis procedures of molecular dyes. Later on, QDSSCs appear as a new concept of SSCs, because of their advantages such as low cost, the possibility to realize light absorption in wide solar spectrum regions, easy fabrication and the multiple-exciton generation leading a theoretical efficiency up to 44%[83]. In this Thesis, it has been developed a QDSSC as a generation part of a photo-supercapacitor.

QDs are defined as a group of semiconductors with a narrow bandgap being quasi-zero-dimensional nanoparticles characterized by their unique quantum confinement effect. This phenomenon occurs when the diameter of QD is less than the Bohr radium. These characteristics make QDs to possess tunable band gaps [84], multiple exciton generation (MEG) [85] and higher absorption coefficients than dye molecules[86].

The working principle of QDSSCs (see Figure 3.1) is initially to generate a light irradiation to produce a photo excitation of the semiconductor nanocrystals leading a separation of the exciton (electron-hole pairs) from the Valence Band (VB) to the Conduction Band (CB). Consequently, the electrons are injected into the wide bandgap semiconductor, and the holes are driven to the hole transporting material (HTM), to finally been collected into their respective contacts. In general, this mechanism of separation

(Reaction 3.1) and recombination (Reaction 3.2) of QD, can be demonstrated with the following reactions[87]:

$$QD + h\nu \rightarrow QD(e_p + h_p) \rightarrow QD(e_s + h_s) \quad (3.1)$$

$$QD(e_s + h_s) \rightarrow QD + h\nu' \quad (3.2)$$

where e_p and h_p symbolize the higher electronic states of the electrons (e) and holes (h) and e_s, h_s symbolize the lower electronic states.

In this process, it is crucial to avoid the recombination between electron-hole pair to increase the efficiency of the solar cell [88,89].

The scheme of the structure and working principle of typical QDSSCs is:

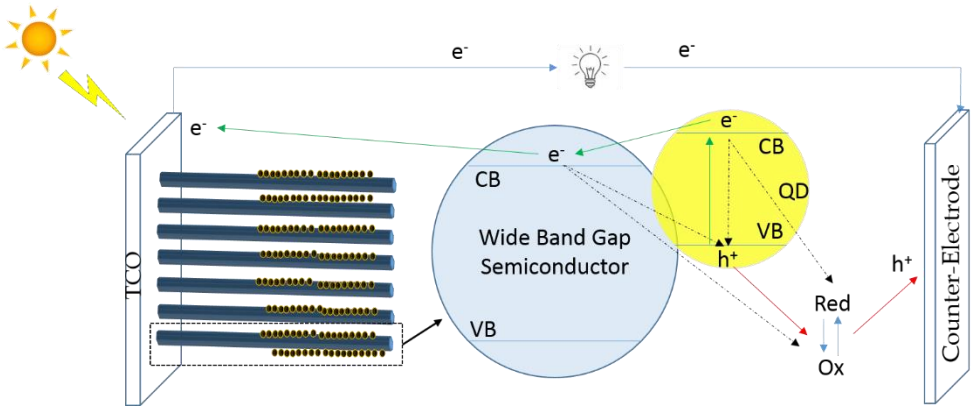

Figure 3.1. Schematic illustration of structure and working of QDSSCs. Solid green and blue lines represent electrons and holes transportation to external load, respectively. Different relaxation and recombination losses in QDSSC are shown by dashed black lines.

Although the majority of researches in QDSSC field have been done using TiO_2 as wide band gap semiconductor sensitized with QDs of CdS[90], CdSe[91], PbSe[92], PbS[93] or Sb_2S_3[94]. In this Thesis it has been employed ZnO as wide band gap semiconductor since it has higher electron mobility than TiO_2. Moreover, Ag_2S QDs have been chosen due to their narrow band gap (1.1 eV) that is very near to the optimal Eg of 1.13 eV of a single junction photovoltaic device and their negligible toxicity[95].

B. MATERIALS AND METHODS

1) SUBSTRATES

The substrates used in this photoanode consisted in conductive GIZO/glass and commercial FTO/glass with a sheet resistance of 10 Ω/□. GIZO film was grown on glass substrates by sputtering as described below (see Chapter II). The size of the samples was 2 cm x 1 cm. All the substrates were properly cleaned before their first use. For this purpose, they were immersed 15 minutes in acetone, 15 min in 2-propanol and 15 min in deionized water in an ultrasonic bath. After that, substrates were dried with N_2 gas.

2) ZINC OXIDE SEED LAYER

2.1) SPIN COATING METHOD

The effect of a ZnO seed layer (SL) on the growth of ZnO nanowires have been widely studied by several researchers[96,97]. The deposition of a seed layer increases the number of nucleation centers for the growth of nanorods, increasing their density. Furthermore, seed layer contributes to smaller mean diameter and length than those grown onto untreated FTO/glass substrate. On the other hand, the degree of orientation is improved by the presence of ZnO seed layer, obtaining c-axis orientation of electrochemically grown ZnO nanorod arrays (NRAs)[19]. The deposition of ZnO seed layer has only been carried out onto FTO substrates since under assumption that GIZO films is mainly composed of ZnO would not need a seed layer.

Spin coating has been used for several decades for the application of thin films. A typical process consists of a dispense step in which a certain volume of a fluid compound is deposited onto the center of a substrate and then spinning the substrate at high speed (typically from 1500 to 6000 rpm).

Spin coating was employed to deposit a ZnO seed layer thin film onto FTO substrates. Zinc acetate was dissolved in methanol (10 mM) and a volume of 1 ml of this solution was dripped over the substrate. An angular velocity of 2000 rpm was applied for 40 seconds. Then, the sample was introduced in an oven at 105˚C during 10 minutes to evaporate the solvent. This process is repeated four times and after that, a thermal treatment is carried out to the sample in a furnace at 350ºC during 20 minutes with a 10ºC/min heating rate. This procedure was done twice over each sample in order to achieve an optimal seed layer for the growth of a good density of nanowires with a mean diameter of 35 nm [98].

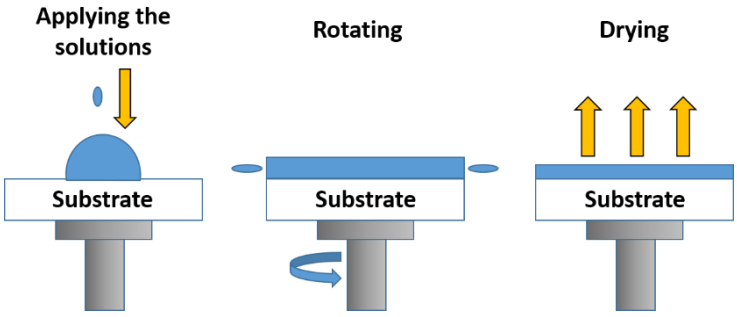

Figure 3.2. Scheme of Spin coating deposition process.

3) ZINC OXIDE (ZnO) NANOWIRES

3.1) ELECTROCHEMICAL DEPOSITION

ZnO has been extensively studied during decades due to its optimal optoelectronic properties and its unique ability to form a variety of nanostructures such as nanowires (NWs), nanobelts, nanospheres, nanofibers or nanoribbons. The interest in ZnO is stimulated by its variety of properties, including high transparency[99], piezoelectricity[100], ferroelectricity[101], wide band gap (3.37 eV)[102], conductivity from metallic to insulating (including n-type and p-type conductivity)[103], magneto-optical[104] and it is inexpensiveness and environment-

friendly[105]. Among all nanostructures, nanowires or nanorods have attracted special attention due to the ordered and vertically arranged ZnO nanowires are expected to enhance performance of the third generation of solar cells[106].

There exist several techniques for the preparation of ZnO, such as chemical vapor deposition[107], radio frequency magnetron sputtering[108], spray pyrolysis[99], hydrothermal[109] or electrochemical deposition[110]. Electrodeposition provides advantages in comparison with other methods, like large-scale deposition, low cost and possibility of morphology control of resultant films.

In order to synthetize ZnO nanowires, a potentiostatic electrochemical deposition has been used. This technique consists on the application of a constant potential obtaining at the same time the current response as a function of time (chronoamperometry).

This useful technique leads to obtain the initial information about nucleation and growth mechanism in a studied system. Additionally, the amount of electricity for deposition can be determined. Also, this method can be applied for the determination of a nucleation rate constant and an adsorption isotherm. With the chronoamperometry, the current is measured versus time as a response to a (sequence of) potential pulse.

A fundamental reaction in electrodeposition of ZnO nanowires is based on reduction of an oxygen precursor to OH^-, followed by reaction with Zn^{2+} ions, according to the following mechanism:

$$O_2 + 2H_2O + 4\,e^- \rightarrow 4\,0H^- \tag{3.3}$$

$$Zn^{2+} + 20H^- \leftrightarrow Zn(OH)_2 \tag{3.4}$$

The zinc hydroxide formed in this reversible reaction is transformed at elevated temperature into zinc oxide:

$$Zn(OH)_2 \xrightarrow{Heat} ZnO + H_2O \tag{3.5}$$

In this Thesis, it was employed for the growth of ZnO nanowires (NWs) by electrochemical deposition (ECD) onto FTO/ZnO SL, a Box-Behnken experimental design. In order to study the influence of deposition parameters such as deposition time (30, 60, 90 min), solution temperature (60, 70, 80 ^{o}C) and solution concentration (0.1, 1, 1.9 mM), over the properties of ZnO nanostructures, was elaborated. The three levels used for the factors are shown in Table 3.1. An aqueous solution of Zinc acetate ($ZnAc_2$) dehydrate and Sodium acetate (NaAc) 0.1 M as supporting electrolyte (pH=6.76) was employed as precursor.

The full experimental design consisting of 15 samples (see Table 3.2) was carried out using the double seed layer (SL) of ZnO/FTO/glass as substrate. Furthermore, ZnO NW´s were grown on FTO/glass without a SL using the optimal condition found for the electrodeposition for comparison. On the other hand, ZnO nanowires were electrodeposited onto GIZO/glass without seed layer to obtain a photoanode for the subsequent photocapacitor.

Electrochemical deposition was made in a conventional electrochemical cell of three electrodes, where ZnO SL/FTO and GIZO were used as working electrode; platinum (Pt) sheet as Counter electrode and a saturated calomel electrode (SCE) as a Reference electrode. Chronoamperometry was carried out at a potential of -1.0 V with respect to SCE. The influence of electrodeposition potential is related to the necessary potential for oxygen reduction, leading to generate more hydroxide ions, and in the meantime, zinc ions in the electrolyte easily diffused to or absorbed on the cathode surfaces due to the stronger electric field intensity. All this would promote the electrodeposition proceeding, and the growth rate of the electrodeposition of ZnO would increase. Guo *et al*.[111] demonstrated the best electrodeposition potential for the ZnO nanowires growth resulted to be -1.0 V according to the highest density, lowest average diameter and highest length of nanowires. Electrolyte was saturated bubbling O_2 about 20 min prior to ECD and during the process. After the ECD, the samples of ZnO NW´s were rinsed with deionized water to remove impure ion and un-reacted products from the surface of ZnO nanostructures and dried in air.

Table 3.1: Factors and levels used for the Box-Behnken response surface experimental design, and identification of the sample.

Level (symbolic)	Factor		
	Solution concentration (mM)	Solution temperature (ºC)	Deposition time (s)
-1	0.1	60	1800
0	1.0	70	3600
+1	1.9	80	5400

Table 3.2. Box-Behnken design. Symbolic and real values of the factors.

	Symbolic values			Real values		
Exp. Nº	Solution concentration	Temperature	Time	Solution concentration (mM)	Temperature (ºC)	Time (s)
1	0	1	1	**1**	**80**	**5400**
2	0	0	0	**1**	**70**	**3600**
3	1	1	0	**1.9**	**80**	**3600**
4	-1	0	-1	**0.1**	**70**	**1800**
5	1	0	1	**1.9**	**70**	**5400**
6	0	0	0	**1**	**70**	**3600**
7	0	-1	-1	**1**	**60**	**1800**
8	-1	-1	0	**0.1**	**60**	**3600**
9	0	-1	1	**1**	**60**	**5400**
10	1	-1	0	**1.9**	**60**	**3600**
11	0	1	-1	**1**	**80**	**1800**
12	0	0	0	**1**	**70**	**3600**
13	-1	1	0	**0.1**	**80**	**3600**
14	-1	0	1	**0.1**	**70**	**5400**
15	1	0	-1	**1.9**	**70**	**1800**

4) Silver Sulphide (Ag_2S) Quantum Dots as Sensitizers for ZnO Nanowires

4.1) SUCCESSIVE IONIC LAYER ADSORPTION AND REACTION (SILAR)

Thin films for electronic applications have been grown by solution-phase techniques for many years, due to their advantages such as simple setups, low price and low temperature. The successive ionic layer adsorption and reaction (SILAR) technique can be regarded as a modification of Chemical Bath Deposition (CBD). SILAR method was first described by Nicolau in 1985 [112]. The main advantage for the QDs growth is the tunable band gap due to the changeable QDs size.

Film or nanoparticles growth in the SILAR technique proceeds by alternate immersion of the substrate in the cationic and anionic precursor solutions, with an intermediate rinsing of the substrate. These four steps mean one growth cycle and it can be seen in Figure 3.3.

The first step consists of an immersion of the substrate in the cation solution, the ions of the precursor solution will be adsorbed onto the surface of the substrate. Once immersed in this cationic solution, a double layer is formed where cations form an inner layer and the anions of the cation precursor provide a charge-balancing outer layer. The second step is the rinsing of the substrate with deionized water or another organic solvent, to immobilize the double layer and remains on the substrate surface. The following reaction step, the substrate is immersed in the anionic precursor solution. The anions of the solution diffuse into the surface and react with the adsorbed cations of the inner layer. In this moment, it has been formed the first solid nanoparticles layer on the substrate surface. The final step is the rinsing of substrate to remove the ions from the diffusion layer. The global reaction occurring during one SILAR cycle can be presented as follows:

$$mM^{n+}(aq) + nA^{m-}(aq) \rightarrow M_mA_n(s) \qquad (3.5)$$

There are several factors affecting thin film or QDs size in the SILAR method such as, temperature, concentrations, solubility, pH and counter-ions of the precursor solutions.

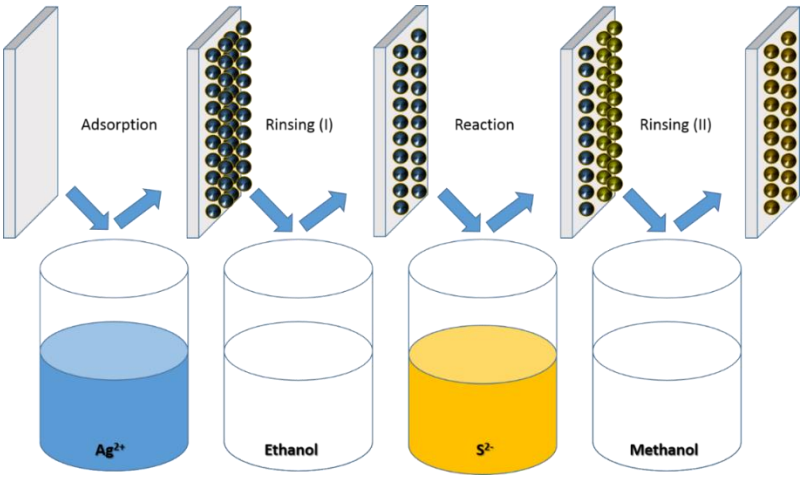

Figure 3.3. Scheme of SILAR process for Ag_2S QDs.

In our laboratory, we have used a homemade SILAR equipment controlled by computer allowing the movement of the substrate in the "xy" axis. The equipment also allows controlling the up and downing velocity, acceleration, distance and immersed time until five different positions.

Silver sulphide (Ag_2S) QDs were synthesized over ZnO nanowires using the SILAR method. It was employed five different precursor concentration of $AgNO_3$ in ethanol and Na_2S in methanol (0.001, 0.01, 0.05, 0.10 and 0.15 M), being the dipping time 1 min and the number of SILAR cycles varied from 3,6,9 and 12. ZnO NW´s were selected under the best condition found from the experimental design previously studied. ZnO NW´s were dipped into the Ag^+ cationic solution for 1 min, washed with ethanol for 20 s, then dipped into S^{2-} for 1 min and finally washed with methanol. The two-step procedure forms one SILAR cycle.

5) THERMAL TREATMENT

A thermal treatment is necessary to improve the crystallinity of the nanostructures. In this Thesis, the electrode was annealed in an oven, during 1 hour at 400ºC with 2ºC/min of ramp up in N_2 atmosphere.

6) ZINC SULPHIDE (ZnS) PASSIVATION LAYER

One of the most extended post-treatments used for improving the efficiency of QDSSC consists of the deposition of ZnS over the photoanode. It has been demonstrated that a ZnS coating on QDs improve the efficiency observed[113,114]. This strategy was pioneered by Yang *et al.* in 2002 [115]. They proved that a ZnS layer grown over PbS/CdS QDs prevented chalcogenide photocorrosion and enhanced the output parameters of the cell.

Previously the studies of Guijarro *et al.* [116] showed the role of the ZnS treatment in the performance of QDSSC. On the one hand it exists a blockage of the ZnO nanowire surface, reducing the leakage of electrons injected into the oxide toward the electrolyte. From another hand, the passivation of Ag_2S QDs avoid the recombination and prevent electron trapping.

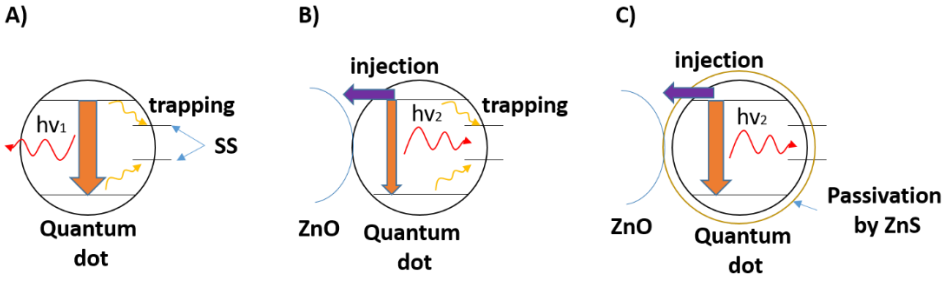

Figure 3.4. Routes of radiative recombination and trapping in surface/interfacial states (SS), for carriers photogenerated in Ag_2S QDs: in colloidal dispersion (A), after attachment to ZnO nanowires (B) and followed by ZnS treatment (C). The arrow width qualitatively indicates the number of carriers involved in the corresponding pathway.

In this work, the deposition of ZnS was carried out by 2, 4, 5 and 6 cycles of SILAR method to study the effect on photoelectrochemical results for comparison. The photoelectrode was alternatively dipped in 0.5 M of Zinc acetate ($Zn(CH_3COO)_2$) as cationic solution and 0.5 M of sodium sulphide (Na_2S) as anionic aqueous solutions for 1 min, rinsing with distillated water between both to remove the non-adsorbed/unreacted ions.

7) PEDOT AS HOLE TRANSPORTING MATERIAL

Choosing an adequate Hole Transporting Material (HTM) is crucial to obtain good photocurrents from the QDSSC. In this way, several types of HTM have been used for these devices, being the most common redox couple employed the polysulfide (S^{2-}/S_n^{2-}), generally in an aqueous solution [117]. In addition, there are inorganic and organic p-type semiconductor used as HTM, such as CuSCN [118], spiro OMeTAD [119], PEDOT[120] or P3HT[121], respectively.

In this case, we have used poly(3,4-ethylenedioxythiophene) (PEDOT) as HTM due to their optimal properties[122]. PEDOT is a great interesting conducting polymer owing its excellent characteristics, including high chemical stability, reversible doping states, regular structure, low band-gap and electrochemical properties.

PEDOT was synthetized by electropolymerization of EDOT over the photoanode nanostructure formed previously of FTO-GIZO/ZnO NWs/Ag_2S QDs/ZnS. It was used a three electrodes cell, employing a Pt sheet as counter electrode, a SCE as reference electrode and the photoanode substrate as working electrode. The electrodeposition was carried out at room temperature and the aqueous solution composition were 3mM EDOT + 0.2 M $LiClO_4$. Nitrogen gas was bubbled into the solution before the electrodeposition to remove the oxygen dissolved and after that, the nitrogen was flushed over the solution during the electropolymerization. The cyclic voltammetry was carried out from -0.8 to 2 V at 75 mV/s, during 5 cycles. Further details of electropolymerization process are showed in Chapter V.

C. RESULTS AND DISCUSSION

1) ZINC OXIDE (ZnO) SEED LAYER

1.1) STRUCTURAL AND MORPHOLOGICAL PROPERTIES.

The morphological properties of the ZnO seed layer grown onto the FTO/glass substrates have been characterized by FE-SEM and AFM images. Figure 3.5 (a) and (b) shows top views of pure FTO/glass substrates and ZnO seed layer, respectively, and Fig. 3.5 (c) and (d) shows tilted views of pure FTO/glass substrates and ZnO seed layer for comparison. FE-SEM micrograph images have been used to evaluate the deposition homogeneity on the substrate, the grain size and the shape of the seed layer. In this Fig. 3.5 can be seen the change of surface morphology between pure FTO and ZnO seed layer grown onto it. It can be appreciated that the ZnO seed layer is polycrystalline composed of ZnO nanoparticles with a spherical cap like shape, which covers in a uniform way the whole FTO surface. The size of the seeds is approximately 20 nm, being crucial for the morphological characteristics of the nanowire growth, such as, diameter, density and orientation degree. Moreover, the seed layer works as electron blocking layer avoiding the direct contact between the hole transporter PEDOT with the FTO substrate diminishing the electron recombination at this interface.

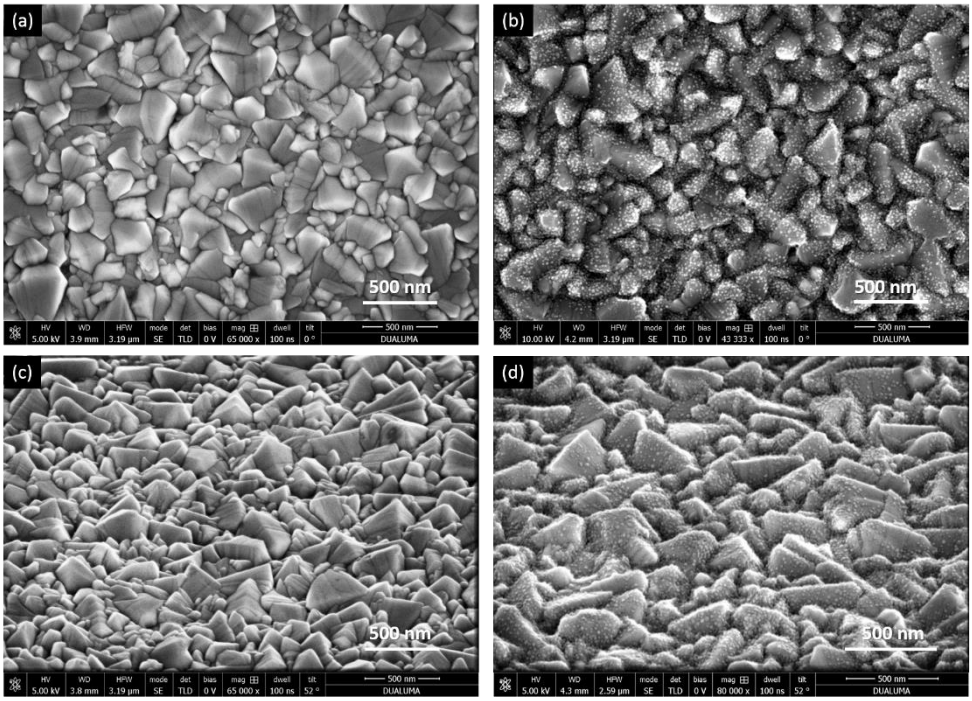

Figure 3.5. FESEM micrographs of top view of **(a)** FTO bare **(b)** ZnO SL and tilted view of **(c)** bare FTO and **(d)** ZnO SL.

Figure 3.6 (a) and (b) shows AFM images of the bare FTO and ZnO seed layer respectively. The seed layer deposition produces a small increment in the RMS roughness of FTO/ZnO seed layer, experiencing a rise from 19.2 nm to 26.7 nm. The bare FTO substrate exhibits a very rough surface similar to wedges with polyhedral pyramidal grains and very marked sharp edges (see Fig. 3.6(a)). After the deposition, FTO grain edges are rounded by the nanoparticles of the ZnO seed layer (see Fig. 3.6 (b)), increasing the nucleation sites for the subsequent nanowire growth. In Figure 3.6 (c) and (d) can be seen the difference between phase images of pure FTO and ZnO seed layer. In Fig. 3.6 (d) it is possible to observe clearly the density and spherical nanoparticle shape of ZnO covering the FTO substrate. It can be concluded that ZnO seed layer has been successfully deposited onto FTO substrates by Spin Coating.

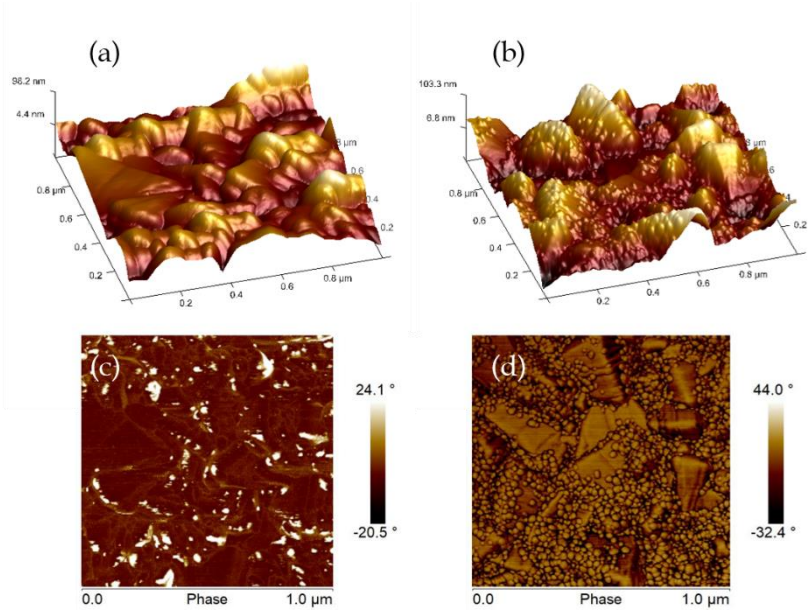

Figure 3.6. AFM topography of (a) bare FTO, (b) ZnO SL, (c) Phase bare FTO, (d) Phase ZnO SL.

1.2) ELECTRICAL PROPERTIES

A further characterization of ZnO seed layer consists in measuring the open circuit voltage in the same solution used to grow ZnO nanowires just before the beginning of the electrodeposition process. This technique provides in situ information of the correct seed layer deposition over FTO substrates. As can be seen in Figure 3.7, the open circuit voltage has been measured during 1 hour for pure FTO (Fig. 3.7 (a) red line) and ZnO seed layer deposited onto FTO substrates (Fig. 3.7 (b) black line). Open circuit voltage of pure FTO exhibits a nearly constant and positive value of about 30 mV while the voltage of ZnO seed layer exhibit a negative value of approximately -80 mV. In this way, it is possible to be sure the adequate ZnO seed layer deposition.

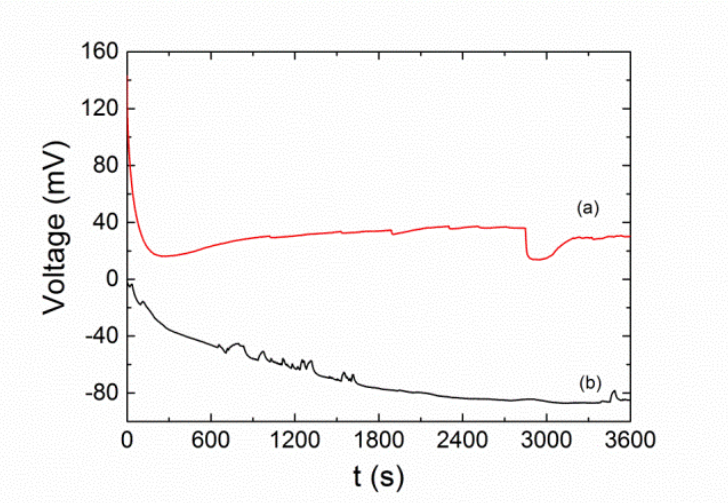

Figure 3.7. Open Circuit Potential of (a) bare FTO and (b) ZnO SL.

2) ZINC OXIDE (ZnO) NANOWIRES

2.1) STRUCTURAL AND MORPHOLOGICAL PROPERTIES.

Figure 3.8 shows a typical X-ray diffraction pattern of ZnO nanowire arrays (NWAs) obtained by electrodeposition onto a naked FTO/glass substrate (Fig. 3.8 (a), red line), ZnO seed layer (Fig. 3.8 (a), blue line) and onto GIZO/glass substrate (Fig. 3.8 (b)), for comparison. The diffractogram of Fig. 3.8 (a) can be indexed to the hexagonal wurtzite ZnO structure (JCPDS file No. 05-0664) and to the SnO_2 phase corresponding to FTO substrate. There are seven diffraction peaks corresponding to the (0002), (10$\underline{1}$0), (10$\underline{1}$1), (10$\underline{1}$2), (11$\underline{2}$0), (10$\underline{1}$3) and (11$\underline{2}$2) planes of the ZnO hexagonal wurtzite structure which can be clearly identified. The large (0002) ZnO diffraction peak height confirms that ZnO nanowires grown on seed layer are highly crystalline with a hexagonal structure and indicates a preferential growth of the ZnO NW's perpendicular to the substrate, as confirmed as well by the FE-SEM images in Fig. 3.12. The main difference regarding the diffractogram of the nanowires grown onto naked FTO is the lower intensity of the (0002)

peak, indicating that there is not a preferential growth of these nanowires, being they much more tilted with respect to the substrate. The diffractogram of Fig. 3.8 (b) also shows the same peaks as before, including in this case the only peak of crystalline GIZO (008 plane) as substrate, being overlapped with (10$\underline{1}$0) ZnO plane.

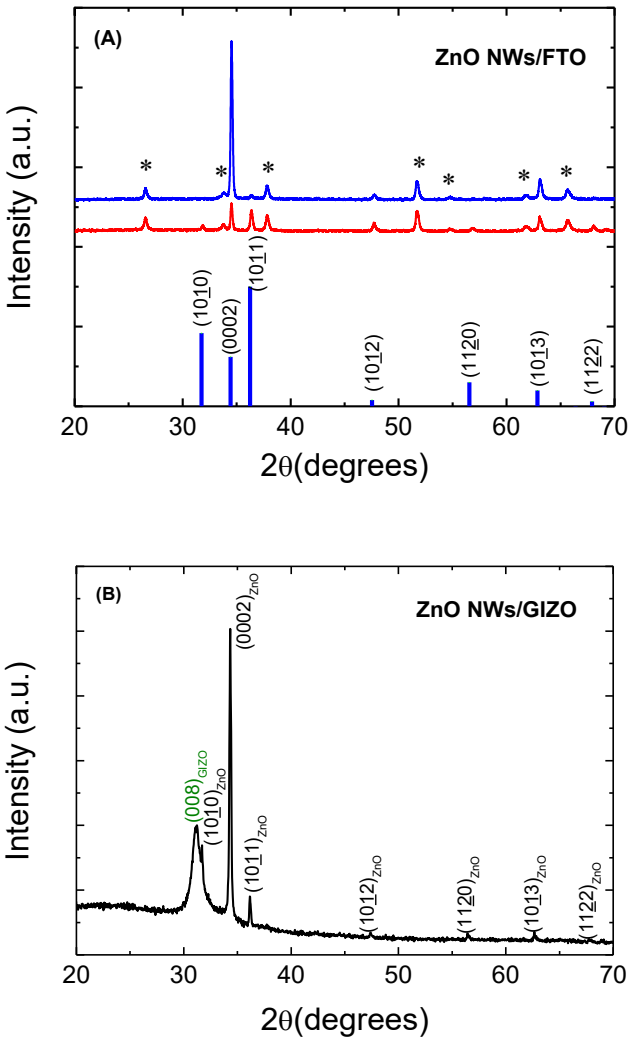

Figure 3.8. X-ray diffraction pattern of ZnO nanowires grown on (a) FTO with ZnO SL (blue line) and onto bare FTO (red line) (b) GIZO (*, indicates the peaks originated from the SnO_2:F substrate and blue bars indicate ZnO planes from JCPDS 05-0664).

2.1.1) ANALYSIS OF THE BOX-BHENKEN EXPERIMENTAL DESIGN.

The objective of the experimental design was to study the effective factors, the influence and optimization of electrodeposition parameters (deposition time, solution temperature and Zinc Acetate concentration) on the ZnO Nanowire growth.

The response variables such as Dv (crystallite size), σ (degree of orientation) and Diameter were measured and studied to evaluate the electrochemical parameters influence on the nanowires. Table 3.4 shows the factors and response values obtained from the 15 experiments.

Table 3.4: Factors and response values obtained from the experimental design.

Factors and levels			**Response values**		
time (s)	**T (ºC)**	**Concentration (mM)**	**Diameter (nm)**	***σ***	**Dv (nm)**
5400	80	1	60.1	2.12	216.4
3600	70	1	74.6	2.37	209.0
3600	80	1.9	63.7	1.81	204.1
1800	70	0.1	44.3	1.09	9.8
5400	70	1.9	130.1	2.10	287.1
3600	70	1	64.7	2.16	201.5
1800	60	1	70.1	1.81	180.1
3600	60	0.1	0	0.87	6.5
5400	60	1	225.9	2.39	293.0
3600	60	1.9	145.3	1.41	222.4
1800	80	1	45.2	1.82	182.7
3600	70	1	66.3	2.38	224.4
3600	80	0.1	45.2	1.23	185.1
5400	70	0.1	54.2	0.92	104.6
1800	70	1.9	76.1	1.93	155.1

Analysis of variance (ANOVA) for **Diameter** results indicate that the only statistically significant factor over the diameter is the solution concentration due to its p-value lower than 0.05. It has a positive linear effect regarding

diameter, this is, diameter increase with increasing concentration, as it can be seen in Figure 3.9. The rest of parameters and interactions do not have a significant effect on diameter. Determination coefficient (R^2=0.8786) shows the quality of the polynomial model for the ZnO nanowire diameter.

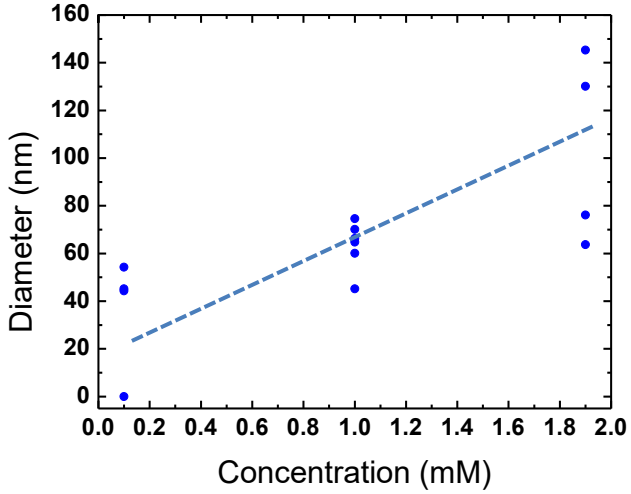

Figure 3.9: Diameter nanowire versus precursor concentration. Dash line shows the tendency between diameter and concentration.

An increase of ZnO nanowire diameter, as a function of the precursor concentration, has been also reported by Elias *et al.*[123], employing $ZnCl_2$ as precursor solution with concentration between 5 x 10^{-5} and 1 x 10^{-3} M. An increment of particle size is generally expected in solution techniques, when the precursor concentration increases[124]. Establishing the optimal diameter for the nanowires is crucial for the final photocapacitor device, since the entire coating of Ag_2S QDs on the nanowires will depend on their surface area and the space between them so that the QDs can cover their entire length. In this study, the 0.1 mM concentration produce very thin nanowires of mean diameter 47.9 nm and the 1.9 mM concentration lead to very thick nanowires of mean diameter 103.8 nm, without enough space to introduce QDs. For this reason, the optimal solution precursor concentration [$ZnAc_2$] for the nanowires growth is 1 mM since produce diameters of 63.5 nm.

The **degree of preferential orientation** (σ), indicates the preferential orientation of nanowires in the c-axis and was calculated from XRD diffraction pattern using the equation 3.1:

$$\sigma = \left(\frac{\sum_N (Ci - \overline{Ci})^2}{N}\right)^{0.5} \quad (3.1)$$

where N is the number of the reflections that are considered; Ci is the texture coefficient; $\overline{Ci}$ is the average of Ci values.

Texture coefficient (Ci) gives a measure of the orientation of reflection i in comparison to a completely random sample and σ is used to compare the degree of orientation between different nanowire arrays (σ =0 indicates a completely random oriented sample)[125]. When comparing two nanostructures, the sample with the higher value of σ will be the most verticality oriented.

Texture coefficient (Ci) is calculated by means of the following equation:

$$Ci = \frac{I_{(hkl)}/I_{0_{(hkl)}}}{\left(\frac{1}{N}\right)\sum_N I_{(hkl)}/I_{0_{(hkl)}}} \quad (3.2)$$

where I is the measured intensity of (hkl) plane and I_0 is the intensity of the reference powder. In this case, seven crystalline planes, namely $(10\bar{1}0)$, (0002), $(10\bar{1}1)$, $(10\bar{1}2)$, $(11\bar{2}0)$,$(10\bar{1}3)$ and $(11\bar{2}2)$ were considered in the analysis due to their high intensity.

From ANOVA results of **degree of preferential orientation** (σ), it can be concluded that the most significant effect over the degree of orientation (σ) is the positive linear and quadratic effect of solution concentration, as can be seen in Figure 3.10.

A high determination coefficient (R^2=0.9101) shows the quality of the model. Figure 3.10 shows the relation between σ and precursor concentration [$ZnAc_2$], finding maximum values for the 1 mM concentration. These results were also corroborated by other authors[123] when using 1 mM concentration. For this reason, it is possible to confirm again that 1 mM was the optimal solution concentration chosen for the ZnO nanowire growth.

Employing this value, the degree of orientation of nanowires in the [0002] direction is maximized.

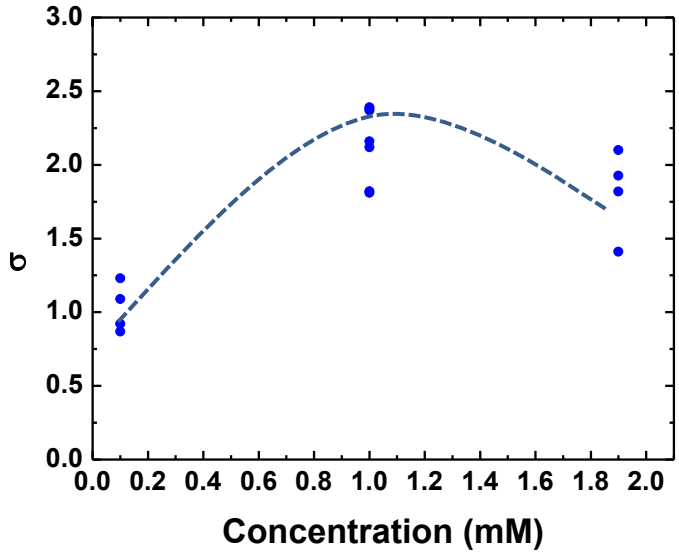

Figure 3.10. Degree of orientation "σ " versus solution concentration. Dash line shows the parabolic tendency of the results.

The last studied parameter of ZnO nanowires was the crystallite size (Dv), this parameter was calculated from XRD diffraction patterns through Debye Scherrer equation as follows:

$$D_{hkl} = \frac{0{,}95\ \lambda}{\beta_{hkl} \cos\theta_{hkl}} \tag{3.3}$$

where D_{hkl} is the crystallite size, λ is the wavelength used (1.54 Å), β_{hkl} is the corrected angular line width at half-maximum intensity in radians, and θ_{hkl} is Bragg's angle. The β_{hkl} parameter was corrected using the following formula:

$$\beta_{hkl} = \sqrt{\beta_{exp}^2 - \beta_{ins}^2} \tag{3.4}$$

where β_{exp} corresponds to the experimentally determined full width at half of the maximum intensity, FWHM, of the peak. The instrumental width was

determined as β_{ins} = 0.07º by using a standard lanthanum hexaboride (LaB_6) powder pattern.

From analysis of variance for **crystallite size** (Dv), it can be concluded that the most significant effect over the crystallite size is the positive linear effect of time and concentration and a negative quadratic effect of solution concentration.

Figure 3.11 depicts a contour graph where it is shown the relation between Dv with regard to concentration and time. In this graph, each area represents the conditions of time and concentration to grow nanowires whose crystallite size is shown in the legend white box. The darkest green area indicates the condition for the maximum values of crystallite size, thus, from 1 to 1.9 mM and from 4500 to 5400 seconds, the electrodeposition of nanowires with highest crystallite sizes is possible.

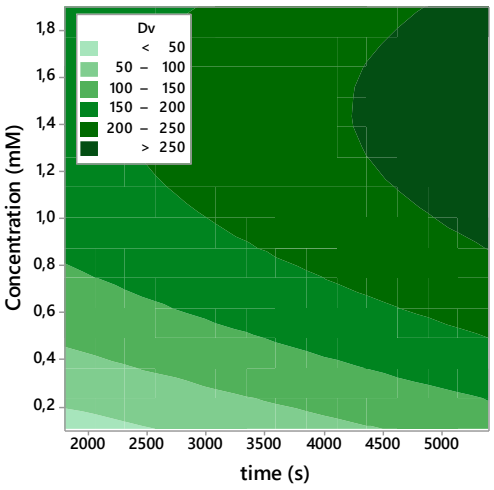

Figure 3.11. Contour graphs of crystallite size as a function of concentration and time.

Figure 3.12 (a) shows FE-SEM images of some examples of ZnO NWs obtained from experimental design onto naked FTO/glass substrate and Fig. 3.12 (b), (c) and (d) onto ZnO seed layer grown at different precursor concentration. In Figure 3.12 (a) the ZnO NRAs electrodeposited onto a bare FTO/glass substrate can be seen and the hexagonal cross-section with planar

top ends and hexagonal faceted with smooth surfaces can be appreciated. On the other hand, the majority of the nanowires grown onto ZnO seed layer are vertically oriented to the substrate plane and the axial direction is aligned with the c-axis of the hexagonal ZnO crystal structure. However, ZnO NWs grown onto bare FTO do not present a preferential alignment but exhibit a random orientation (see Fig. 3.12(a)). The main difference between ZnO NWs grown onto naked FTO (Fig.3.12 (a)) and onto ZnO SL (Fig. 3.12 (b), (c) and (d)) is the higher diameter, lower density and lower degree of orientation of the nanorods grown onto naked FTO than the nanowires grown onto ZnO SL. The diameter of the ZnO NWs grown onto naked FTO is about 350 nm, while the values for the samples grown onto ZnO SL at 0.1 mM, 1 mM and 1,9 mM varies from 45 nm, 70 nm and 140 nm, respectively, as can be seen in Fig. 3.12 (b), (c) and (d) and confirmed from ANOVA results explained previously (see Table 3.4).

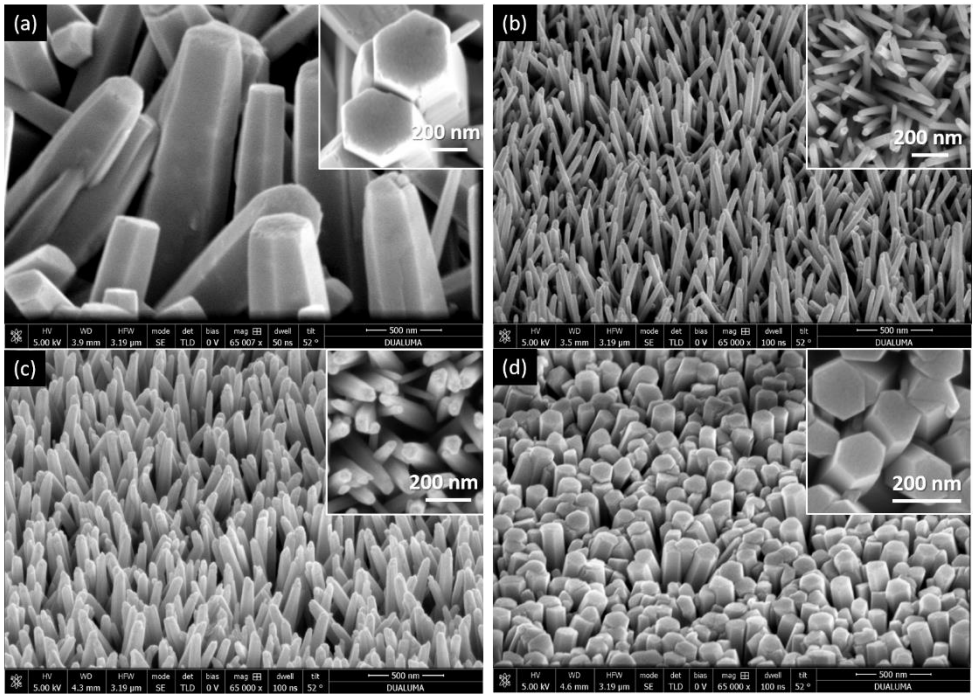

Figure 3.12. Tilted FESEM Micrographs of **(a)** ZnO NWs grown on bare FTO ([$ZnAc_2$]=1 mM), **(b**) ZnO NWs grown on SL ([$ZnAc_2$]=0,1 mM, **(c)** ZnO NWs grown on SL ([$ZnAc_2$]= 1 mM, **(d)** ZnO NWs grown on SL ([$ZnAc_2$]= 1,9 mM. Inset shows top view of corresponding nanowires.

Considering that the **length** of ZnO nanowires mainly depends on the electrodeposition time, three samples grown at three different times were studied, being 30 minutes, 1 hour and 1.5 hours. Figure 3.13 shows the mapping and cross sectional micrograph images. The average height of nanowires varies from 900 nm for 30 min growth, 1.4 μm for 1 hour and 2 μm for 1.5 hours. The nanowire length may also affect the device performance of photoanode due to the electron transport time. This is, the device based on longer NWs need relatively long time to transport the photogenerated electrons to the collector electrode[126].

Theoretically, photoanode with longer NWs offer more surface area for QD deposition and this should result in higher short cirtuit current density (*Jsc)* and efficiency (η). However, Zhang *et al.*[127] demonstrated that longest NWs did not show the best performance, due to longer electron transport time were obtained for the longest NW photoanodes. Thus, the longer transport time increases the option for recombination of photogenerated charges before reaching the contacts. In our case, the deposition time chosen has been 1 hour owing to the nanowires length is about 1.4 μm being also the optimal length found by that author.

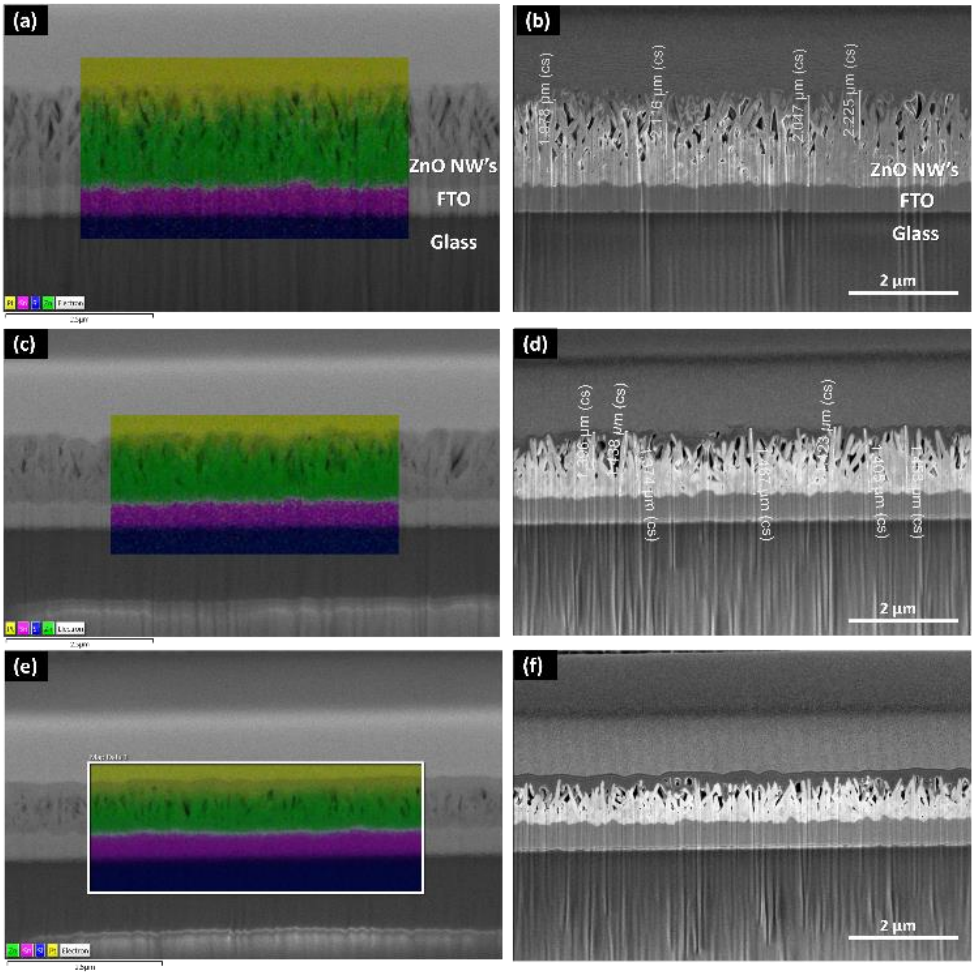

Figure 3.13: EDX elemental mapping images of ZnO NWs cross section grown during (a and b) 1h 30min, (c and d) 1h, (e and f) 30 min. Blue color symbolize Si element of glass, pink for Sn (FTO) and green for Zn (ZnO NW's).

Since the electrodeposition temperature does not have an important effect or influence on the studied parameters conditions, it has been set to a constant temperature of 70ºC for the nanowires growth in this Thesis. This temperature is optimal for the dehydration reaction of $Zn(OH)_2$ to ZnO finding an equilibrium according to diameter, length and density of nanowires[111].

From the results evaluated above, it can be concluded that the best conditions for the nanowires growths for the subsequent quantum dots

deposition are a concentration of 1 mM, temperature of 70ºC and time of 3600 s.

Finally, in Figure 3.14 can be seen the ZnO nanowires grown onto conductive and crystalline GIZO prepared and explained in Chapter II at three different precursor concentrations without the deposition of a ZnO seed layer. It has been employed the same temperature and electrodeposition time as before, to evaluate the influence of concentrations and to observe the morphology of ZnO nanowires grown onto GIZO thin films. As can be seen in Fig. 3.14 (a) and (b), nanowires grown at 1 mM exhibits a very high diameter and random orientation, in addition, the shape of the top face is not completely hexagonal. Figure 3.14 (c) and (d) shows ZnO NWs grown at 0.5 mM and it can be clearly observed the hexagonal structure of wurtzite ZnO. There is a high density of nanowires with a high degree of vertical orientation. The diameter of these nanowires was approximately 150 nm. Figure 3.14 (e) and (f) shows ZnO NWs grown onto the same GIZO thin films at 0.3 mM to evaluate the influence of concentration. In this case, the density of nanowires is lower as can be seen in Fig. 3.14 (e), however the degree of orientation in (002) plane continues to be strong. This is because the ZnO nanowire growth begins in the same plane of the GIZO films, since GIZO is based on ZnO.

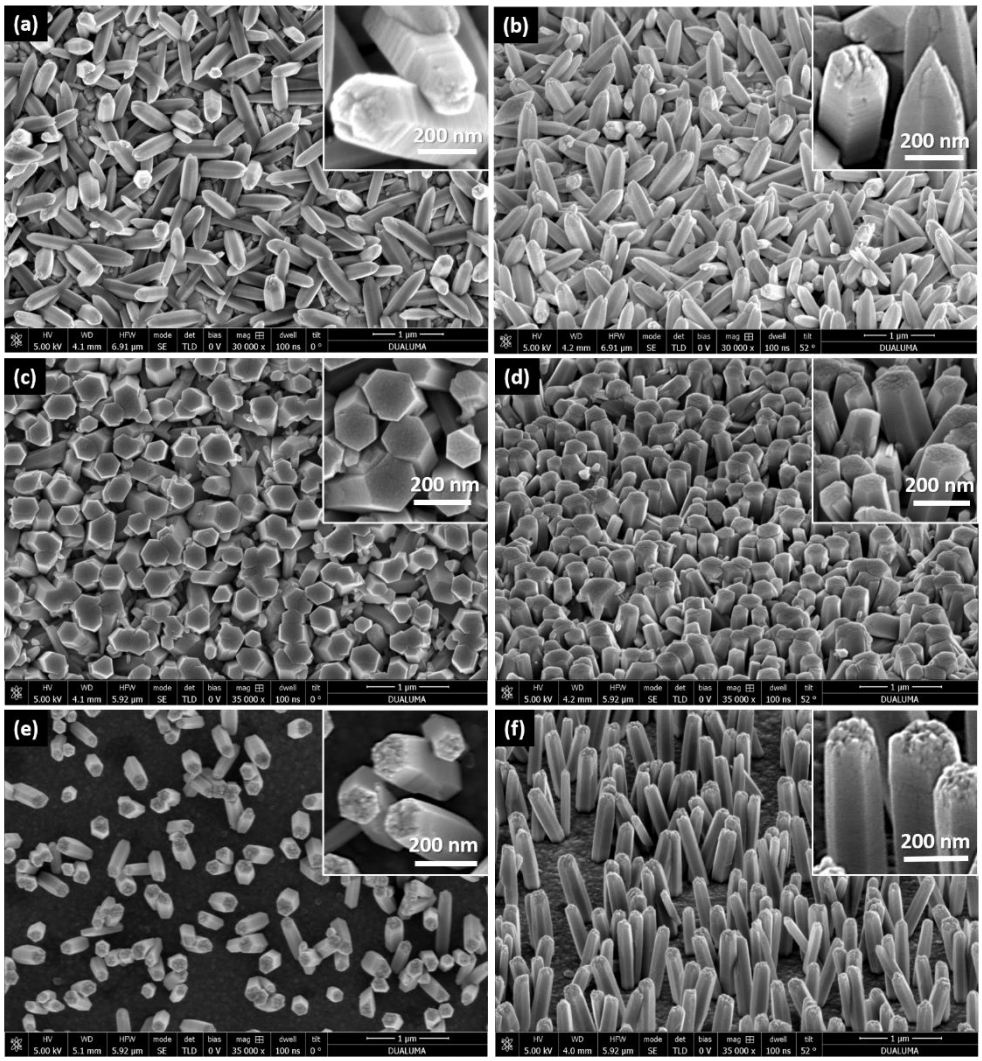

Figure 3.14. FESEM Micrographs **(a)** Top view and **(b**) Tilted view of ZnO NWs grown on crystalline GIZO ([$ZnAc_2$]=1 mM), **(c)** Top view and **(d)** Tilted view of ZnO NWs grown on crystalline GIZO ([$ZnAc_2$]=0.5 mM). Micrographs **(e)** Top view and **(f**) Tilted view of ZnO NWs grown on crystalline GIZO ([$ZnAc_2$]=0.3 mM. Inset shows a high magnification of corresponding nanowires.

In Figure 3.15, a high resolution cross section transmission electron micrograph of ZnO nanorods grown onto GIZO/substrates can be seen. In this image it is demonstrated how the growth of nanorods begin at the same GIZO structure, due to their composition based on ZnO that allow a continuous growth.

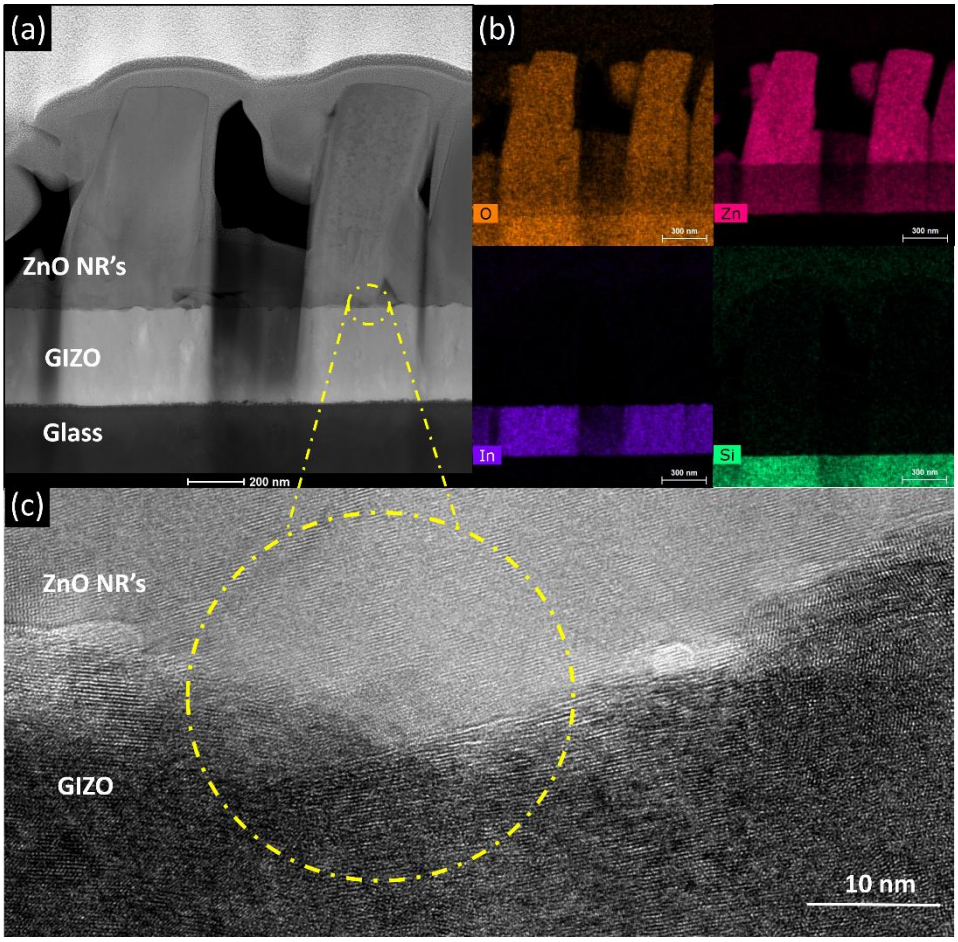

Figure 3.15. **(a)** Transmission electron micrograph of ZnO nanorods grown onto GIZO/glass substrates, **(b**) the corresponding EDX elemental mapping of O (orange), Zn (magenta), In (blue) and Si (green) and **(c)** the corresponding zoomed area of the interface between GIZO and ZnO nanorods.

From this result, it can be concluded that the best electrochemical conditions are 0.5 mM of concentration at 70 ºC during 3600 s for the nanowires growth onto GIZO thin films.

3) SILVER SULPHIDE (Ag_2S) QUANTUM DOTS AS SENSITIZERS FOR ZnO NANOWIRES

3.1) STRUCTURAL AND MORPHOLOGICAL PROPERTIES.

As explained before, Ag_2S QDs have been chosen due to their very low toxicity and their narrow band gap (1.1 eV). Figure 3.16 shows a typical X-ray diffraction pattern of ZnO nanowire arrays (blue line) and ZnO nanowires covered with Ag_2S QDs (red line) for comparison. The X-ray diffraction peaks can be indexed as monoclinic Ag_2S structure (JCPDS file No. 00-014-0072). It can be appreciated that the obtained Ag_2S QDs/ZnO nanowires arrays share the structural characters of both ZnO and Ag_2S because no any other diffraction peaks besides SnO_2 which comes from the FTO substrate were detected.

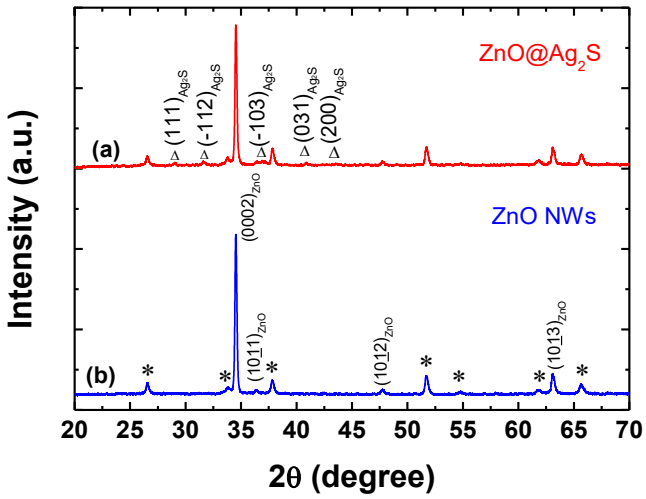

Figure 3.16 X-ray diffraction pattern of **(a)** ZnO sensitized Ag_2S QDs (JCPDS 14-0072) and **(b)** ZnO nanowire. Diffraction planes are indicated for ZnO and Ag_2S. (*, indicates the peaks originated from the SnO_2:F substrate).

On the other hand, five diffraction peaks at 29º, 31.5º, 37.7º, 40.7º and 43.3º corresponding to the (111), (-112), (-103), (031) and (200) planes respectively, of the acanthite crystal of Ag_2S, can be appreciated. The diffraction peak

intensity of ZnO shows a little decrease after depositing Ag_2S QDs due to the ZnO NWs were completely covered with Ag_2S.

3.1.1) Influence of Precursor Concentration

Figure 3.17 shows five micrographs in order to evaluate the size and morphology of Ag_2S QDs according to the precursor concentration $[Ag^+]=[S^{2-}]$. In this figure can be observed the morphologic differences between QDs grown at different concentration such as 0.15 M, 0.10 M, 0.05 M, 0.01 M and 0.001 M. It can be seen how the size of the nanoparticles decrease according to the decrease of precursor concentration $[Ag^+]=[S^{2-}]$.

At 0.15 M, there exists big amounts of Ag_2S deposited on top of nanowires and they do not cover the entire nanowire, in this case, it is not possible to say that they are QDs due to their high size. At 0.10 M there are less amount of Ag_2S on the surface of nanowire. For 0.05 M begin to appear nanoparticles with spherical shape and it is possible to differentiate the nanowires and the nanoparticles. When the concentration is 0.01 M is possible to see the QDs covering completely the nanowires and finally for the 0.001 M the amounts of Ag_2S on the surface of nanowires is minimum being possible to differentiate perfectly the ZnO nanowire structure with the QDs on it.

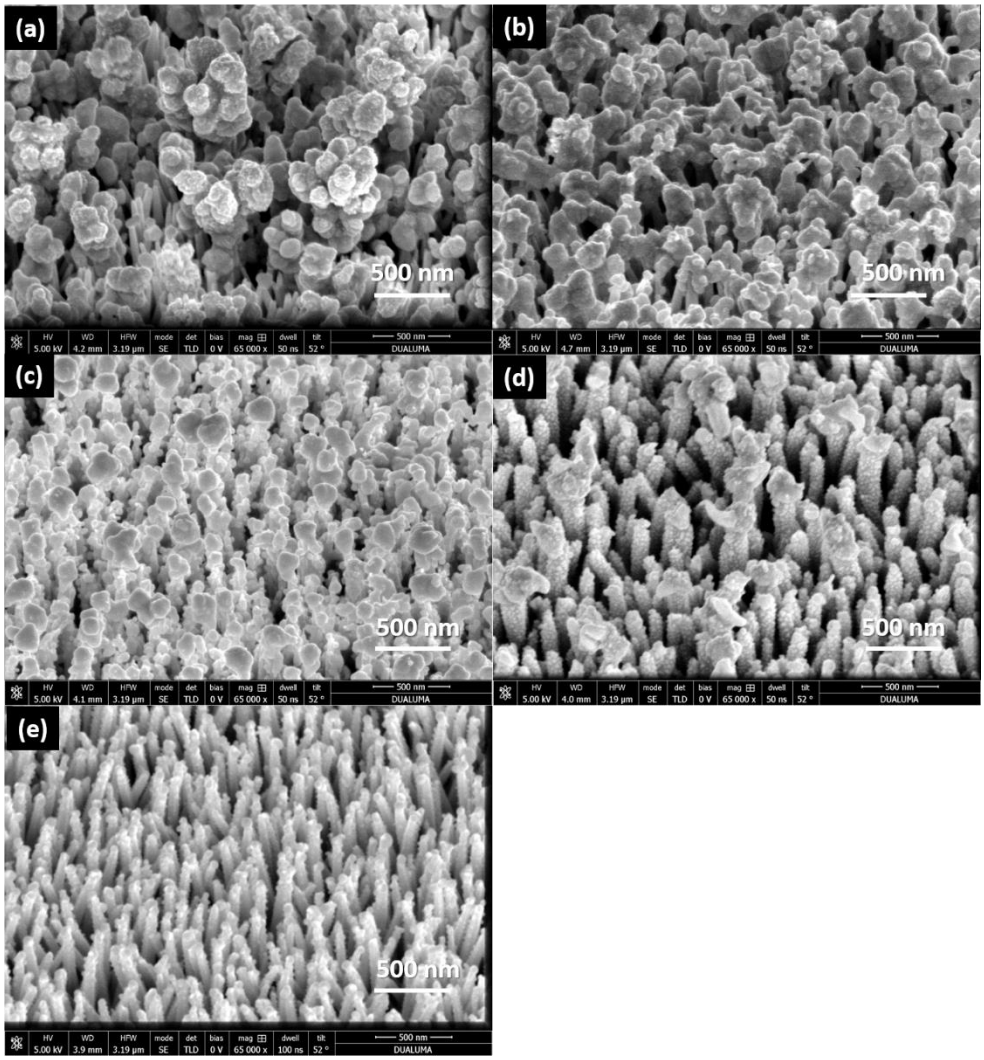

Figure 3.17. FESEM micrographs of Ag_2S QDs/ZnO NWs grown at 9 SILAR cycles at different precursor concentration: (a) $[Ag^+]=[S^{2-}]=0.15$ M, (b) $[Ag^+]=[S^{2-}]=0.10$ M, (c) $[Ag^+]=[S^{2-}]=0.05$ M, (d) $[Ag^+]=[S^{2-}]=0.01$ M and (e) $[Ag^+]=[S^{2-}]=0.001$ M .

3.1.2) INFLUENCE OF CYCLES NUMBER

Figure 3.18 shows the field emission scanning electron microscopy images of ZnO@Ag_2S core-shell NWAs grown at four different cycles number.

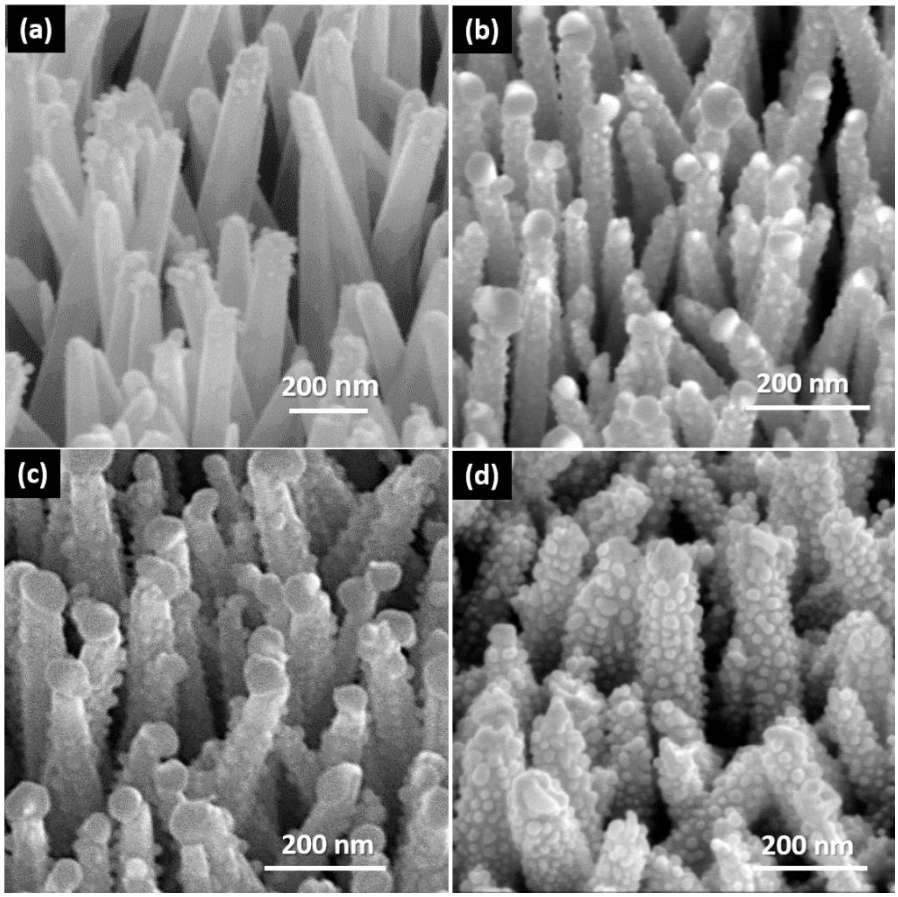

Figure 3.18. FESEM micrographs of Ag_2S QDs/ZnO NWs grown at $[Ag^+]=[S^{2-}]=$ 0.001 M at different SILAR cycles: (a) 3 cycles, (b) 6 cycles, (c) 9 cycles and (d) 12 cycles.

It can be appreciated the morphological change of QDs coating according the number of SILAR cycles. After decoration, the NWs surface became rough and grainy, being clearly visible the presence of spherical nanoparticles rounded of them. The quantity and the size of QDs increase as a function of SILAR cycles. For the 3 cycles, there are a scarcity of QDs and they are only

deposited on the NWs top. From 6 cycles, the QDs cover all the nanowire surface with increasing the QDs from 6 to 9 cycles. When 12 cycles are carried out, it exists a saturation and a bigger size of QDs, leading to a loss of quantum confinement effect and a diminishing of the generation of electron-hole pairs. The morphology of ZnO nanowires before and after QDs deposition is similar, what indicates that the NW structure does not change during Ag_2S QDs growth on the ZnO NWs. These results suggest that Ag_2S QDs could be successfully deposited onto the surface of the ZnO nanowires along their entire length, forming a ZnO/Ag_2S core-shell structure.

The finer details of microstructure and chemical composition of the Ag_2S@ZnO NWAs core-shell were further investigated by high resolution transmission electron microscopy (HRTEM), being illustrated in Figure 3.19. Figure 3.19(a) shows a HRTEM image of a single Ag_2S QD/ZnO NR detached from the ZnO seed layer substrate. It can be appreciated the large amount of QDs deposited onto the entire NR surface. Fig 3.19(b) shows the EDX elemental mapping, revealing the presence of Ag and S elements in the shell part, Zn and O in the core part. Fig 3.19(c) and (d) shows the HRTEM image of various QDs deposited onto the ZnO nanowire surface. It can be appreciated that the Ag_2S QDs have a spherical shape with a mean diameter in the range of 10 nm-20 nm.

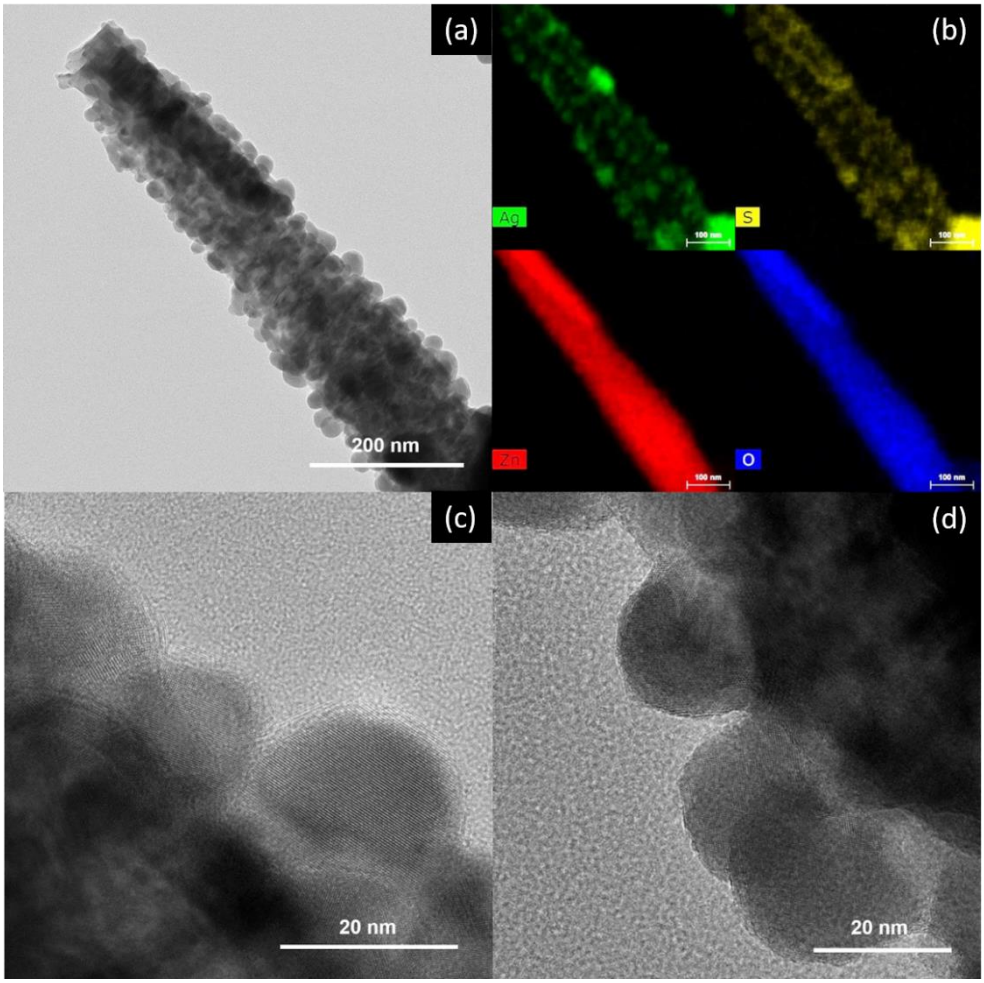

Figure 3.19. (a) Transmission electron micrograph of a single Ag_2S QDs/ZnO nanowire heterostructure detached from the FTO/glass substrate, and **(b)** the corresponding EDX elemental mapping of Ag (green), S (yellow), Zn (red) and O (blue). **(c)** HRTEM micrograph of a ZnO nanowire densely coated with Ag_2S nanocrystals. **(d)** Higher magnification HRTEM micrograph of several Ag_2S nanocrystals (indicated by dashed circles), revealing its single crystalline character. Insets of **(c)** and **(d)** show the corresponding FFT patterns. (Samples prepared using 9 coating cycles).

3.2) OPTICAL PROPERTIES.

Figure 3.20 (a) and 3.20 (b) show the Total transmittance (TT) and Diffuse transmittance (DT) spectra for the ZnO nanowires and for the ZnO nanowires sensitized with Ag_2S QDs, respectively. For ZnO NWs (see Fig. 3.20 (a)) a structure located ca. 380 nm (abrupt growth of the TT) is observed due to the absorption edge of the ZnO located at 3.287 eV. For ZnO sensitized with Ag_2S QDs (Fig 3.20 (b)) can be observed a structure identified with the absorption edge of Ag_2S QDs located at ca. 530 nm, corresponding to a band gap of 2.272 eV. Furthermore, there exist another absorption edge of lower energy (ca. 1.65 eV). In the insets of both figures can be seen the Tauc plot for the determination of band gap (E_g). On the other hand, for ZnO/Ag_2S there exists another absorption edge of lower energy (ca. 1.65 eV). From the comparison of the TT of both samples, a drastic decrease of the TT for lower wavelengths than the corresponding to the absorption edge of the Ag_2S QDs can be observed; this decrease is a consequence of the absorption of the QDs[128,129].

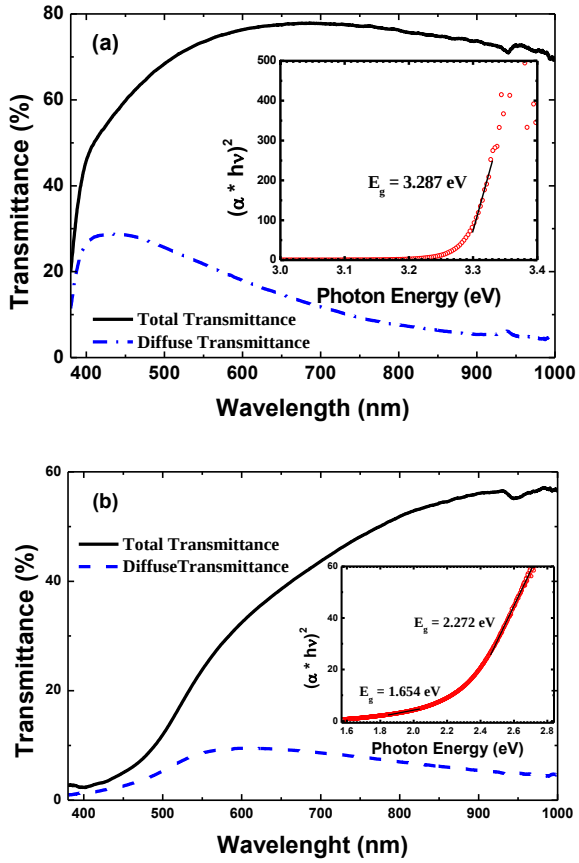

Figure 3.20. Total transmittance (black solid line) and Diffuse transmittance (blue dash line) spectra of **(a)** ZnO NWs and **(b)** ZnO NWs sensitized with Ag_2S QDs. Inset shows corresponding Tauc plot.

The morphology of the NWs (radius, length, etc.) compared to the wavelength determines the optical dispersion capacity of the sample [130–132]. As for DT, for ZnO NWs the structure associated with absorption edge is observed, at longer wavelengths a well-defined peak is observed and then the decrease of DT towards near infrared (NIR) (Fig. 3.20(a)). For sensitized NWs there is a mild growth of DT (due to light absorption), a wide peak and the subsequent decrease of DT towards the NIR (Fig. 3.20(b)). It is interesting to note that the DT spectra for both samples coincide towards the NIR. This may be a consequence of the fact that the sensitization process does not significantly alter the morphology of the NWs, suggesting that in the area of

transparency the light scattering capacity would be determined mainly by the NWs. Fig. 3.21 shows the Haze transmittance (Ht), calculated from the DT and TT according to the expression Ht = DT/TT.

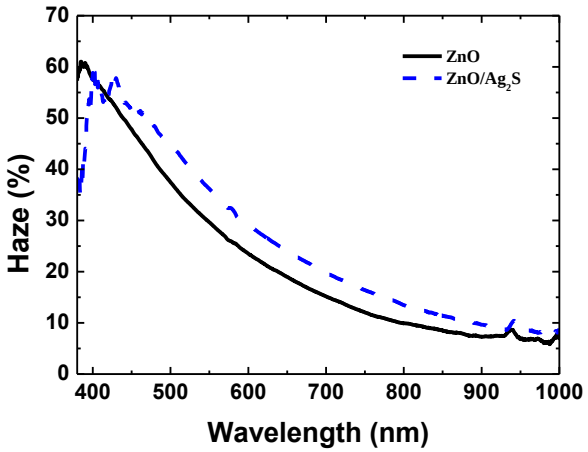

Figure 3.21. Haze spectra of ZnO nanowires (black solid line) and ZnO nanowires sensitized with Ag_2S QDs (blue dash line).

The Ht measures the quantity of light transmitted in diffuse form with respect to the total light transmitted, presenting a very similar shape for both samples, however, there is a shift in the peak of the Ht after sensitization. This may be due to the location of the absorption edge of the QDs and the high absorption at low wavelength, once the absorption edge of the QDs is exceeded the sample becomes transparent and the Ht retains the shape obtained for the NWs, indicating the same light scattering dynamics in both structures.

Finally, the sensitization of nanowires with Ag_2S QDs leads to an increase in optical absorption in the visible region. The fact that the light scattering properties are not significantly altered in the transparency area suggests that the sensitization process under these conditions does not significantly alter the morphology of the samples.

3.3) PHOTOELECTROCHEMICAL PROPERTIES.

In order to evaluate the photovoltaic performance of the sensitized ZnO nanowires decorated by Ag_2S QDs was employed a photoelectrochemical (PEC) system. An adequate redox couple composed of Na_2S+Na_2SO_3 in an electrolyte solution was used as the electron or hole transporting material instead of a semiconductor or metal contact. This PEC system was carried out due to their several advantages for using a liquid electrical contact to form a junction with the semiconductor under study. These advantages are a complete contact between the liquid and the solar cell making it very suitable for nanostructured QDSSC, also is important the facility by which this contact can be made and removed[133].

Photoelectrochemical (PEC) studies of bare ZnO NWs and Ag_2S QDs sensitized ZnO nanowire arrays were carried out in a conventional three-electrode rectangular quartz cell using a Pt sheet as counter electrode, a saturated calomel electrode (SCE) as reference electrode, and the ZnO NWs and Ag_2S QDs/ZnO NWs heterostructure samples as the working photoelectrode. These photoelectrochemical measurements have been performed in a 0.1 M Na_2S + 0.1 M Na_2SO_3 aqueous solution. The electrolyte solution was purged with argon for 30 min prior to each experimental series and then kept under flowing argon during the analysis. The J-V curves were recorded at the scan rate of 20 mV s^{-1} using a Teq_01 potentiostat, the illumination was provided by a Xe lamp employing a light intensity of 100 mW/cm^2 (1 sun). The illuminated area on the electrode surface was about 1.0 cm^2.

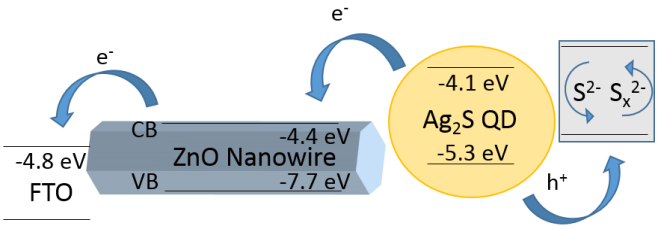

Figure 3.22. Schematic energy level and carrier transport diagram in the photoanode.

A scheme of the energy levels and the carrier transport diagram which takes place in the photoanode is shown in Figure 3.22.

Figure 3.23. shows the photocurrent density-voltage (J-V) curves of bare ZnO NW´s, Ag_2S QDs/ZnO NW´s, ZnS/Ag_2S QDs/ZnO NW´s and ZnS/Ag_2S QDs/ZnO NW´s after Thermal Treatment grown at the same conditions under light illumination. In this figure can be observed that all the electrodes show photoresponse, exhibiting anodic photocurrent under applied electrochemical bias, confirming the n-type behavior of the bare ZnO nanowires and the primary role of the type-II heterostructure between ZnO and Ag_2S in dictating the overall PEC behavior. Nevertheless, the anodic photocurrent in the case of bare ZnO nanowires is very negligible. This low photocurrent is due to the limited absorption of visible light (in fact ZnO exhibits a wide band-gap of 3.3 eV). On the other hand, it is clearly seen the photocurrent increase according to the Ag_2S QDs deposition, followed by ZnS film deposition and finally with the thermal treatment of the complete photoelectrode. The improvement of photocurrent with Ag_2S QDs deposition has an explanation due to the increment of visible light absorption by the Ag_2S nanocrystals. Furthermore, the type-II alignment between ZnO and Ag_2S is another significant factor that contributes to the observed enhanced photoelectrochemical results. The presence of ZnS films produce an improvement in the photocurrent due to the passivation of QDs avoiding the recombination of electron-holes pairs. Finally, the best efficiency (η=0.1 %) is obtained when the heterojunction ZnS/Ag_2S/ZnO is thermal treated since improves the crystallinity favoring the compaction of the nanostructures. This result is near to the obtained for other authors which employ ZnO nanowires sensitized with Ag_2S QDs[127] with the difference that in that case Zhang *et al.* fabricated a solid state solar cell with P3HT as hole conducting material. The results of Jsc, Voc, FF and efficiency for each photoanode can be seen in the Table 3.6.

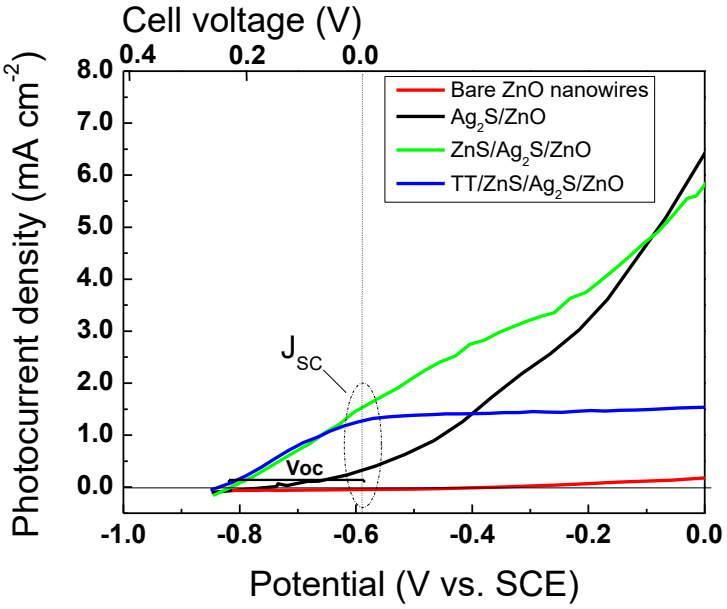

Figure 3.23. Photocurrent density – voltage curves of **(a)** ZnO NRs (red line); **(b)** Ag_2S/ZnO (black line); **(c)** ZnS/Ag_2S/ZnO (green line); and **(d)** TT/ZnS/Ag_2S/ZnO (blue line), obtained at the scan rate of 20 mV s^{-1} at the applied potentials from -0.85 V to +0.20 V under illumination intensity (100 mW cm^{-2}) in 0.1 M Na_2S and 0.1 M Na_2SO_3 electrolyte system.

Table 3.6. Photocurrent-voltage characteristic parameters of photoanode based on QDSSC.

Photoanode	Jsc (mA cm^{-2})	Voc (V)	FF	η (%)
ZnO bare	0	0	0	0
ZnO/Ag_2S	0.31	0.17	0.20	0.01
ZnO/Ag_2S/ZnS	1.54	0.22	0.22	0.07
ZnO/Ag_2S/ZnS/ TT	1.26	0.25	0.31	0.10

3.3.1) INFLUENCE OF PRECURSOR CONCENTRATION

The precursor concentration of silver nitrate and sodium sulphide is crucial for the final shape and size of the Ag_2S quantum dots, as can be seen in above Figure 3.17. This size has an influence in the photoelectrochemical properties and it should be studied adequately. The results of photocurrent has been measured from 0.15M, 0.1M, 0.05M, 0.01M, 0.001M of precursor concentration $[S^{2-}]=[Ag^{2+}]$. Figure 3.24 shows how the photocurrent increase from 0.001M until a maximum value of short circuit photocurrent density (J_{sc}) found for the concentration of 0.05 M, when begin to decrease for higher concentrations.

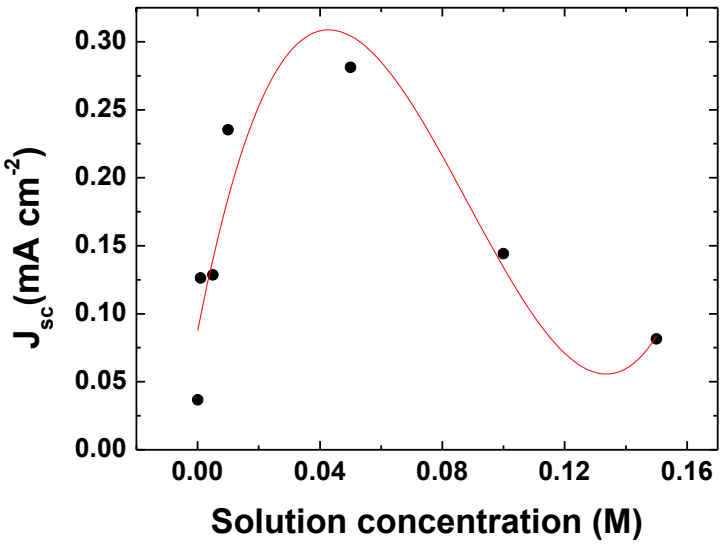

Figure 3.24: Photocurrent density as a function of precursor concentration obtained at the scan rate of 20 mV s^{-1} at the applied potentials from -0.85 V to +0.20 V under illumination intensity (100 mW cm^{-2}) in 0.1 M Na_2S and 0.1 M Na_2SO_3 electrolyte system. Solid red line indicates the followed tendency.

These results indicate that the best precursor concentration to obtain a maximum photocurrent is 0.05 M, for this reason, this has been the chosen concentration for the Ag_2S QDs growth in the photoanode.

3.3.2) INFLUENCE OF Ag_2S SILAR CYCLES

The number of SILAR cycles for the Ag_2S quantum dots deposition have an influence in the number and size of nanoparticles deposited over the nanowire, for this reason is important to evaluate their influence on the PEC properties. Figure 3.25 shows the results of photocurrent for 3, 6, 9 and 12 SILAR cycles, finding the maximum photocurrent for 9 SILAR cycles. This is due to the fact that increased amounts of QDs on ZnO nanowire increases the light absorption and thereby increases the number of photogenerated charges. However, further increases in QDs amount, the performance of the cells begin to decrease and the possible reason is that the additional QDs deposition leads to the formation of larger aggregates around ZnO nanowire (see Fig. 3.18) which are less efficient in transferring electrons although they absorb a wider region of the visible spectrum.

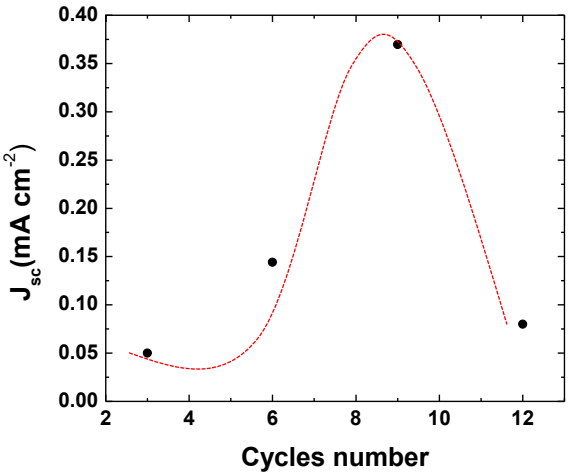

Figure 3.25. Photocurrent density as a function of number of cycles concentration obtained at the scan rate of 20 mV s^{-1} at the applied potentials from -0.85 V to +0.20 V under illumination intensity (100 mW cm^{-2}) in 0.1 M Na_2S and 0.1 M Na_2SO_3 electrolyte system. Dash red line indicates the followed tendency.

This result is in agreement with another studies that obtain maximum values of efficiencies when the number of SILAR cycles is 8[127]. In that case, efficiency increase from 2 to 8 cycles and after that begin to decrease for higher SILAR cycles. On the other hand, for the study of Kang *et al.*[134] the

maximum efficiency for a Ag_2S quantum dot sensitized zinc oxide photoanode was obtained for 6 SILAR cycles of Ag_2S QD deposited.

3.3.3) INFLUENCE OF ZnS COATING CYCLES

In order to study the influence of passivation ZnS layer coating cycles on photocurrent density, a different number of SILAR cycles was grown onto the same growth condition of ZnO nanowires/Ag_2S QDs, from 2 to 6 cycles. Figure 3.26 shows the photocurrent density as a function of voltage curves for 2, 4, 5 and 6 ZnS coating cycles. There is a maximum value of short circuit density of 0.84 mA cm^{-2} when ZnS film is grown during 4 SILAR cycles. The lowest value of Jsc is resulted to be 0.28 mA cm^{-2} for 2 SILAR coating cycles.

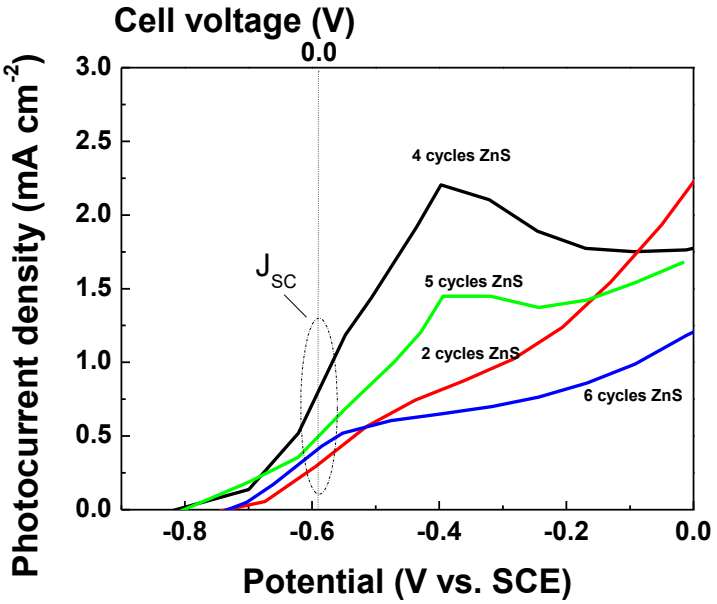

Figure 3.26. Photocurrent density – voltage curves of ZnO/Ag_2S/ZnS with 2 SILAR cycles of ZnS (red line), 4 SILAR cycles of ZnS (black line), 5 SILAR cycles (green line) and 6 SILAR cycles of ZnS (blue line).

Finally, from photoelectrochemical results exposed above, it can be concluded that the best conditions for the growth of Ag_2S QDs and ZnS

passivation layer are: 9 SILAR cycles and 0.05 M of precursor concentration for Ag_2S QDs and 4 coating cycles of passivation ZnS layer. For this reason, these have been the conditions established for the fabrication of photoanode for the photosupercapacitor.

4) PEDOT/ZnS/Ag_2S QDs/ZnO NWs

4.1) STRUCTURAL AND MORPHOLOGICAL PROPERTIES.

Figure 3.27 (a) and (c) shows a tilted and top view of the nanostructures without PEDOT, respectively. In Fig 3.27 (b) and (d) appears the same sample after covering with electrodeposited PEDOT. It can be seen how the PEDOT covers the surface of nanowires forming an uniform film.

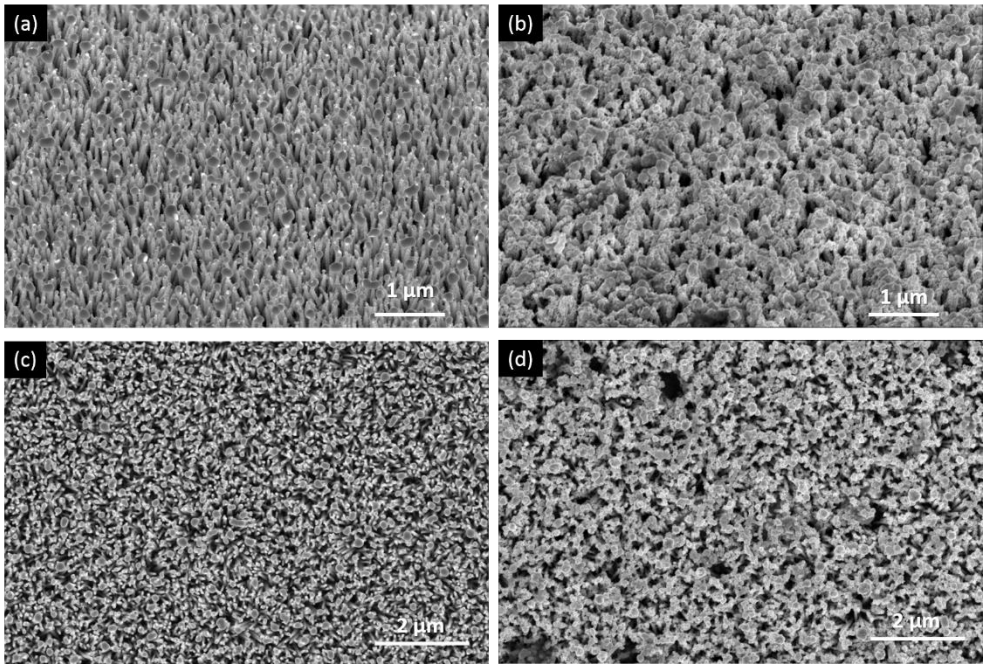

Figure 3.27. FE-SEM micrographs of **(a)** and **(c)** tilted and top images of Ag_2S QDs@ZnO NWs, respectively and **(b)**, **(d)** tilted and top images of PEDOT grown onto Ag_2S QDs@ZnO NWs, respectively.

Figure 3.28 shows the Raman spectrum of PEDOT electrodeposited onto FTO (Fig. 3.28(a)), and the spectrum of PEDOT grown onto nanostructures of QDs/ZnO NWs (Fig. 3.28(b)), for comparison. In the table 3.6 are listed the wavenumbers of the Raman peaks carried out at 532 nm, the comparison with another studies and their assignments of the bands based on the research of Snyder *et al.*[135] and Louarn *et al.* [136]

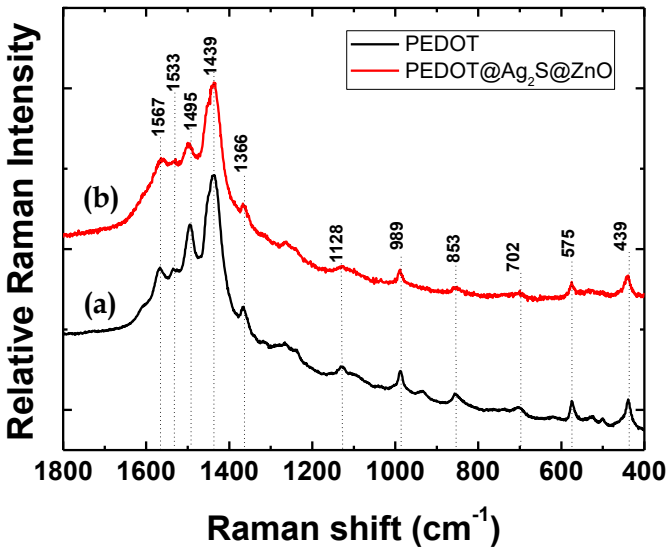

Figure 3.28. Raman spectrum (532 nm excitation) of **(a)** electrochemically prepared PEDOT and **(b)** electrochemically prepared PEDOT over Ag_2S QDs@ZnO NWs.

By examination of the Raman spectra of both samples, it can be confirmed the conducting polymer PEDOT cover the entire surface of the nanostructures, due to the exact coincidence of the main peaks in both Raman curves.

Table 3.6. Summary of vibrations in PEDOT in the Raman spectra at three different excitation wavelength (532 nm, 785 nm and 1064 nm).

Excitation wave length			Approximative description of vibrational modes
532 nm (cm^{-1}) (this work)	785 nm (cm^{-1})[137]	1064 nm (cm^{-1})[138]	
1533	1516	1520	Asymmetric C_α=C_β stretching
1439	1414	1431	Symmetric C_α=C_β (-O) stretching
1366	1370	1369	$C_\beta - C_\beta$ stretching
1266	1252	1226/1270	C_α–$C_{\alpha'}$ (inter-ring) stretching
1128	1097	1111	C–O–C deformation
989	990	991	Oxyethylene ring deformation
702	699	692	Symmetric C–S–C deformation
575	578	571	Oxyethylene ring deformation

D. CONCLUSIONS

The photoanode composed of QDSSC have been designed, fabricated and optimized. Initially a double ZnO seed layer has been deposited on the FTO substrate demonstrating the improvement of the nucleation sites for the nanowires. ZnO nanowires have been successfully grown onto FTO and transparent conductive GIZO substrates. The electrodeposition parameters of the ZnO nanowires have been optimized, finding the optimal temperature conditions in 70ºC, 1 hour of growth time and a concentration of 1 mM solution, according to the degree of orientation in the plane (0002), diameter, length and density of the nanowires. In a second step, the parameters of the SILAR method for the growth of Ag_2S quantum dots (solution concentration and number of cycles) and ZnS layers were successfully optimized according to the photoelectrochemical properties of the photoanode. The best growth conditions of the quantum dots resulted to be 0.05 M for the precursor concentration during 9 SILAR cycles. For the ZnS passivation layer, the 4-cycles growth of SILAR proved to be the highest photo-response. The PEDOT polymer film has been successfully electro-deposited onto the nanostructures explained above to form the final photoanode of the final photosupercapacitor.

IV

SUPERCAPACITOR

A. INTRODUCTION

The development and large-scale implementation of renewable energies are closely related to the possibility of having electricity available at any time of the day, without depending on fluctuations due to weather changes, such as the arrival of the night or variations in the wind velocity. For this reason, the need to develop efficient energy storage devices is crucial to harvest the intermittent energy coming from clean energy sources. Electrochemical supercapacitors, fuel cells and batteries are three examples of the most important electrochemical energy storage devices used nowadays. To evaluate the quality of an electrochemical energy device, beside the cycle-life, energy density and power density are the two most important properties to take into account. Figure 4.1 shows the Ragone plots for several electrochemical energy storage devices, where the supercapacitors are located between the conventional dielectric capacitors and batteries/fuel cells. Supercacitors can have much higher power densities than batteries/fuel cells, but they have much lower energy density.

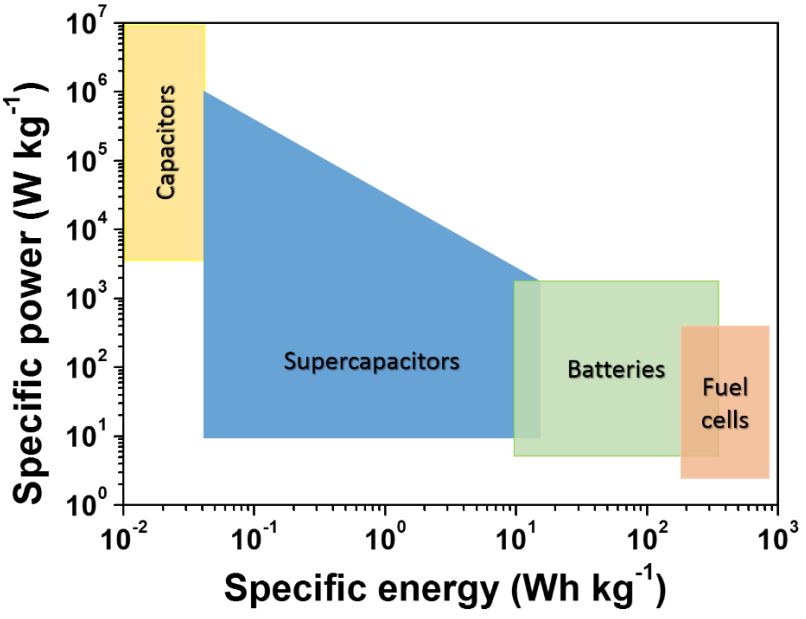

Figure 4.1. Ragone plot for capacitors, batteries and supercapacitors.

For this reason, this makes them promising for applications in current stabilization when accessing intermittent renewable energy sources.

In this regard, the electrochemical supercapacitor or also known as supercapacitor has attracted marked interest in this storage field because of their remarkable advantages such as long cycle life (>100 000 cycles), simple principle, high power density and fast charging/discharging rate if it is compared to batteries and fuel cells. These features make this device has multiple interesting applications in an electric or hybrid electric vehicles, tools, portable electronic and smart grids.

In general, a supercapacitor is a kind of capacitor that possesses different properties with respect to the classical electrostatic capacitors (Fig. 4.2 (A)) related to the charge storage mechanism, the electrode materials, electrolyte and the device structure.

Supercapacitors can be classified into three types depending on the charge storage mechanism, in this way, it is possible to find electrochemical double-layer capacitors (EDLCs), pseudocapacitors and hybrid capacitors.

- EDLCs is a supercapacitor based on a capacitance produced by the electrostatic charge separation at the interface between the electrode and the electrolyte. Normally, this kind of supercapacitor is constituted by carbon electrode materials to maximize the surface area and, therefore, the storage capacity (Fig. 4.2 (B)).
- Pseudocapacitors store the charges from the fast and reversible faradaic redox reactions (Fig 4.2 (C)).
- Hybrid capacitors are those that benefit from double layer and faradaic mechanisms to store charges (Fig. 4.2 (D)).

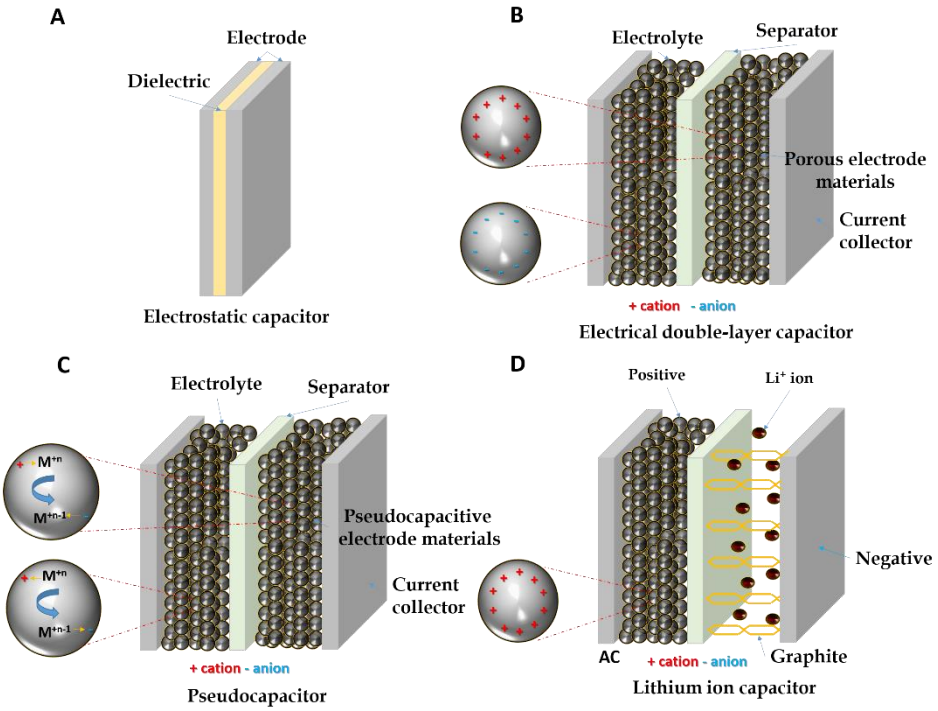

Figure 4.2. Schematic diagram of A) electrostatic capacitor, B) electric double-layer capacitor, C) pseudocapacitor, D) hybrid-capacitor.

This device is composed of two electrodes (anode and cathode), and an intermediate electrolyte. The electrolyte plays a critical role in the final properties of the supercacapitor and it has been the subject of study by numerous researchers over the last few years[139]. One of the most investigated aspects is the increment of cell voltage (V) to improve the energy density (E) of the device as can be seen in the equation $E = \frac{1}{2} C \cdot V^2$ where C is the capacitance.

Depending on their chemical composition it is possible to find several electrolytes that provide different voltage window such as:

- Aqueous solution electrolyte: It has an operating potential window of about (1.0 – 1.3 V).

- Organic electrolyte: It possess a potential window of 2.5 – 2.7 V
- Ionic liquid electrolyte: Is has a potential window of 3.5 – 4.0 V.
- Redox-type electrolytes.
- Solid or semi-solid electrolytes.

The different characteristics that a good electrolyte must fulfill are: a wide potential window; high transport numbers, low flammability, environmentally friendly; high chemical and electrochemical stability; high ionic conductivity; wide operating temperature range and low cost[140].

In this Thesis, a symmetric supercapacitor as storage device composed of a polymer conductor (PEDOT) as electrodes and an ionic-liquid as electrolyte, has been studied and developed (see Figure 4.3).

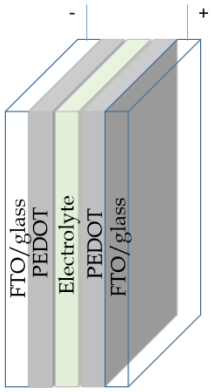

Figure 4.3. Scheme of the structure of the symmetric supercapacitor.

B. MATERIALS AND METHODS

1) SYNTHESIS OF PEDOT/FTO ELECTRODES

In a first step, PEDOT was synthetized by electropolymerization of EDOT over commercial FTO/glass substrates after the proper ultrasonically cleaning (10 min ethanol, 10 min deionized water and 10 min acetone). A three electrodes configuration electrochemical cell was used, employing a Pt sheet as counter electrode, a saturated calomel electrode (SCE) as reference electrode and a FTO-coated glass substrate as working electrode (WE). The electrodeposition was carried out at room temperature by immersion of the WE in a 3 mM monomer 3,4-Ethylenedioxythiophene (EDOT) + 0.2 M $LiClO_4$ aqueous solution. MilliQ water with a nominal resistivity of 18.3 MΩ was used to prepare all solutions. Nitrogen gas was bubbled into the solution before the electrodeposition in order to remove oxygen dissolved and after that, the nitrogen was flushed over the solution during the electropolymerization.

PEDOT thin film was electrodeposited by cyclic voltammetry scanning from -0.8 to 2 V at 75 mV/s by using a Biologic VSP potentiostat, during 5 cycles and 10 cycles to obtain two different supercapacitors and to evaluate them for comparison. The electropolymerization process consists of the oxidation of EDOT at the electrode surface and its subsequent polymerization, according to the following chemical reactions[141,142]:

$$nEDOT(sol) \rightarrow nEDOT^{+\cdot} + ne^{-} \quad (4.1)$$

$$nEDOT^{+\cdot} + zClO_4^{-} \rightarrow (n-z)H + \left[(EDOT_n)^{z+}ClO_4^{-}{}_z\right] \quad (4.2)$$

where ne^{-} are n-electrons, $nEDOT$ are n-monomers of 3,4-ethylenedioxythiophene, $nEDOT^{+\cdot}$ are n-radical cations of EDOT and z is a measure of the doping level of polymer.

2) PREPARATION OF [HEMIm][BF_4]/PVP ELECTROLYTE AND SUPERCAPACITOR ASSEMBLY.

The ionic liquid polymer electrolyte was synthesized as follows.

Initially, 8 g of Polyvinilpirrolidone (PVP, Mw 1,300,000) were dissolved in 15 ml of CH_3OH. Additionally, the rest of 8 g of PVP until 16 g and the rest volume of methanol until 40 ml were slowly added at the same time in small amounts. When this solution was homogeneus and almost solid, the total 9 g of ionic liquid 1-hexyl-3-methylimidazolium [HEMIm][BF_4] was added under stirring. Finally, the final composition was 15% wt of ionic liquid.

Once the Ionic Liquid-PVP solid polymer was prepared, it was deposited over PEDOT/FTO substrates by the dip-coating method at a withdrawal speed of 10 mm/min. Between each of the 2 dipping cycles, samples were dried for 10 min using an halogen lamp.

Finally, the freshly prepared glass/FTO/PEDOT/Ionic Liquid-PVP sample was placed over the glass/FTO/PEDOT electrode by simple hand pressure, employing a polymer film separator between them (Meltonix, 25 µm, from Solaronix). The whole device was heated at 50ºC in a hot plate during 5 min to achieve the sealing of the separator with the two electrodes.

3) CHARACTERIZATION OF [HEMIm][BF_4]/PVP ELECTROLYTE.

The specific ionic conductivity (σ) of the Ionic Liquid-PVP was measured by means of electrochemical impedance spectroscopy (EIS). The liquid electrolyte was spilled in a liquid parallel plate sample cell from *Novocontrol Technologies*, employing a Teflon o-ring to avoid the contacts between the copper disk electrodes. The impedance data were collected by using an AC impedance technique with FRA Solartron 1256 and a BDC from Novocontrol, where the AC frequency was scanned from 0.01 Hz to 1 MHz

at an applied potential bias of 0.0V in the temperature range from 278 to 323 K. The ionic conductivity (σ, S cm^{-1}) of the electrolyte can be calculated by the following equation[143]:

$$\sigma = \frac{l}{(R_b \cdot A)} \tag{4.3}$$

where l (cm) is the distance between the two gold (Au) electrodes, R_b (Ω) is the bulk resistance and A (cm^2) is the contact area of the Ionic Liquid-PVP with the golden electrodes.

4) SUPERCAPACITOR PERFORMANCE STUDY.

The performance of the resulting supercapacitor device was evaluated by galvanostatic charge-discharge (GCD) curves, cyclic voltammetry (CV) and electrochemical impedance spectroscopy (EIS) measurements, all carried out with a Biologic VSP Potentiostat. The impedance measurements were carried out in the frequency range from 0.01 Hz to 1 MHz at a signal level of 20 mV at different applied potential bias.

From GCD curves, the gravimetric specific capacitance C of supercapacitor can be determined through the following equation[144,145]:

$$C = \frac{2 \cdot i \cdot t}{m \cdot \Delta V} \tag{4.4}$$

where C is the areal specific capacitante (F/g), i is the discharge current (A), t is the discharge time (s), m is the mass of active materials on electrode and ΔV is the scanning potential window (V).

Based on the CV curves, the gravimetric specific capacitance of device can be calculated through the equation:

$$C = \frac{\int i dV}{m \cdot \Delta V \cdot v} \tag{4.5}$$

where $\int idV$ is the integrated area of CV curve, v is the scan rate (V s^{-1}), the rest of parameters have the usual meaning as stated before.

The specific energy density and power density can be obtained according to the following equations:

$$E = \frac{\frac{1}{2}C \cdot \Delta V^2}{3600} \tag{4.6}$$

$$P = \frac{3600 \cdot E}{t} \tag{4.7}$$

where E is the gravimetric specific energy density (Wh g^{-1}), P is the specific power density (W g^{-1}) and t is the discharge time (s).

The coulombic efficiency was evaluated using the next relation:

$$\eta = \frac{t_D}{t_C} \cdot 100\% \tag{4.8}$$

where t_C and t_D are the charging and discharging times, respectively.

C. RESULTS AND DISCUSSION

1. CHARACTERIZATION OF PEDOT/FTO ELECTRODES

PEDOT thin film electrodes have been obtained by electropolymerization of the EDOT monomer in $LiClO_4$ aqueous solution. Once PEDOT was electrodeposited onto FTO, it exhibited a dark blue color, it was uniform with no visible defects and it had good adhesion to the FTO surface. The number of cycles allows controlling the thickness of PEDOT films, being an important parameter that influences in the final performance of the supercapacitor. The thickness of PEDOT film was measured by cross section images of field emission-scanning electron microscopy. After 5 cycles, the thickness of PEDOT film was 60.5 nm and after 10 cycles the thickness resulted to be 151.4 nm. FE-SEM micrographs of the PEDOT films deposited onto FTO substrates by potentiostatic polymerization method are presented in Figure 4.4(a). The low magnification image shows a uniform and continuous film, without cracks or pinholes. Inset image depicts a higher magnification of the film showing a dense and rough granular layer of round-shaped particles of about 200 nm in diameter.

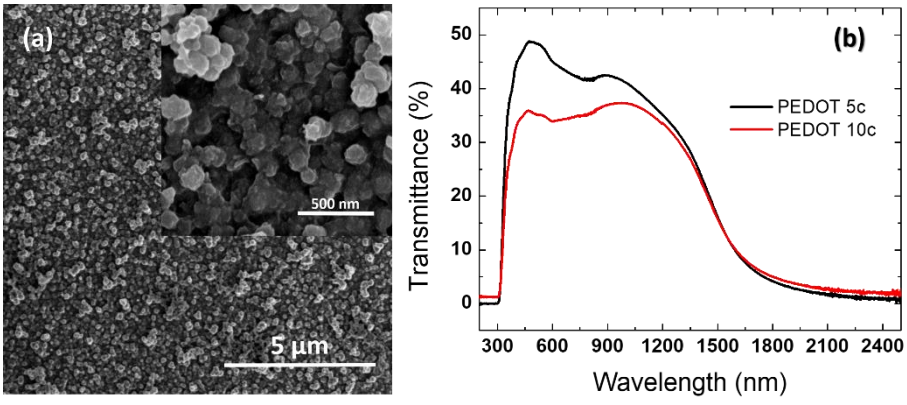

Figure 4.4. **(a)** Top view FE-SEM image of PEDOT. Inset shows a magnification of the film and **(b)** Transmittance spectra of 5c PEDOT (black line) and 10c PEDOT (red line) films.

Figure 4.4(b) shows the optical transmittance measurements of PEDOT film grown during 5 and 10 polymerization cycles, in order to investigate the transparency properties of the film. The spectra of 5 cycles PEDOT reveals a maximum optical transmittance nearly 50% in the visible region. However, the transmittance decrease with the increase of electropolymerization cycles obtaining a maximum of 35% in the visible region. The roughness of PEDOT electrodes grown at 5 cycles and 10 cycles was measured through AFM, being 40.4 nm and 144 nm, respectively. Figure 4.5 shows the AFM images for PEDOT taking an area of 1 μm^2.

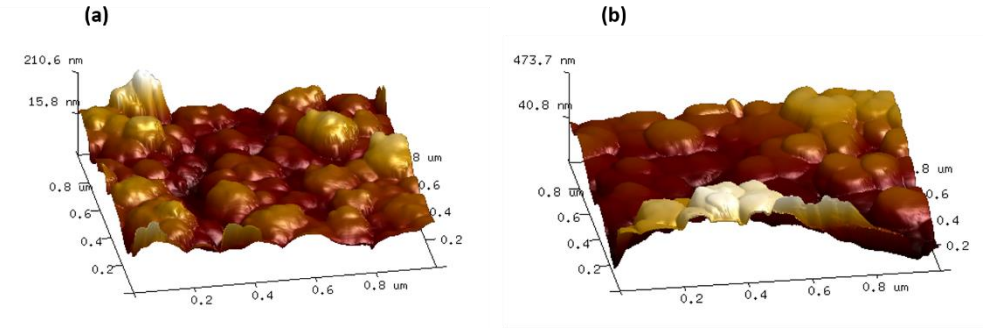

Figure 4.5. AFM image of electrochemically prepared PEDOT during **(a)** 5 cycles and **(b)** 10 cycles.

In order to confirm that the electrodeposited thin film was PEDOT, Raman spectroscopy analysis were carried out. Figure 4.6 shows Raman spectra in the wavenumber region 1800-400 cm^{-1} of a typical PEDOT thin film. As mentioned before, in Table 4.1. are listed the wavenumbers of the eleven Raman peaks found, the comparison with another studies of undoped PEDOT and their assignments of the bands based on the research of Snyder *et al*.[135] and Louarn *et al*.[136]. The Raman spectrum in Fig. 4.6 shows a consistent match of all peaks with corresponding Raman spectrum of the chemically synthesized PEDOT[138]. The shift of position of doped PEDOT peaks with regard to undoped PEDOT is related to the level of doping in the conducting polymer.

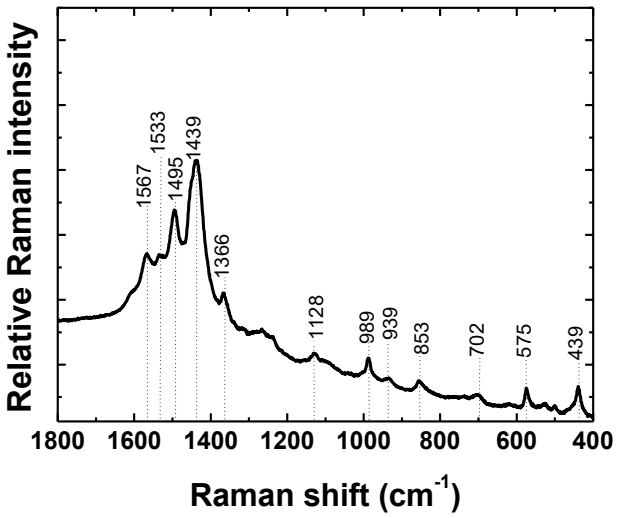

Figure 4.6. Raman spectrum (532 nm excitation) of electrochemically prepared PEDOT.

In Fig. 4.6 the most intense peak is observed at 1439 cm^{-1} and it is attributed to the symmetric stretching vibrational modes $C_\alpha=C_\beta(-O)$. The asymmetric $C_\alpha=C_\beta$ stretching modes are identified by peaks at 1495 and 1533 cm^{-1}. This indicates that in the electropolymerization process, PEDOT film formation involves long-chain linkage by α–β couplings. Therefore, the linkages at the β-position become feasible via progressive delocalization of the unpaired electrons[146]. The position of Raman peaks corresponding to $C_\beta - C_\beta$ stretching and C_α–$C_{\alpha'}$ inter-ring stretching modes at 1366 and 1266 cm^{-1} suggests that the cation radical association is also by the linkage at α–α′ (5, 5′) position which indicates short-chain PEDOT oligomers wherein the molecular structure is dominantly in the *trans* configuration with highly regiochemical order [147]. The Raman peaks corresponding to the ClO_4^- ion conjugation during PEDOT growth is revealed by broad peak at 939 cm^{-1} based on the Raman peaks of free ClO_4^- at 934 cm^{-1} and ion pairs, $[Li^+ClO_4^-]$ at 948 cm^{-1}[148]. The anion (ClO_4^-) association in the growing chain network is caused by the positive charge in the molecular subunits of the chain creating the doped state of PEDOT.

Table 4.1. Summary of PEDOT Raman vibrations at three different excitation wavelengths (532 nm, 785 nm and 1064 nm).

Excitation wavelength			Approximate description of vibrational modes
532 nm (cm^{-1}) Doped PEDOT (This work)	785 nm (cm^{-1})[137] Undoped PEDOT	1064 nm (cm^{-1})[138] Undoped PEDOT	
1533	1516	1520	Asymmetric C_α=C_β stretching
1439	1414	1431	Symmetric C_α=C_β (-O) stretching
1366	1370	1369	$C_\beta - C_\beta$ stretching
1266	1252	1226/1270	C_α–$C_{\alpha'}$ (inter-ring) stretching
1128	1097	1111	C–O–C deformation
989	990	991	Oxyethylene ring deformation
702	699	692	Symmetric C–S–C deformation
575	578	571	Oxyethylene ring deformation

Finally, by examination of the Raman spectrum, it can be concluded that conducting polymer doped PEDOT has been successfully electrodeposited onto FTO substrates.

2. CHARACTERIZATION OF THE [HEMIM][BF_4]/PVP ELECTROLYTE.

The ionic conductivity of electrolytes depends on the number of mobile charge species and their mobility along with polymer chain mobility. The room-temperature ionic conductivity of [HEMIm][BF_4]/PVP electrolyte is $\sigma = 1.5\ 10^{-3}$ S cm^{-1}, which is comparable to the neat [HEMIm][BF_4] ionic liquid that is $4.6\ 10^{-3}$ S cm^{-1} at 25 ^{o}C[149,150]. However, pure PVP is highly resistive with $\sigma < 10^{-9}$ S cm^{-1}[151].

The dependence between temperature and ionic conductivity is represented in Fig. 4.7. As can be observed in Fig. 4.7 (a), the ionic conductivity increases exponentially with temperature. This behavior is similar for other ionic

liquids studied in literature[152]. Figure 4.7 (b) shows the natural logarithm of σ versus the inverse of absolute temperature, i.e., ln σ versus 1/T. If the electrolyte under study would follow a Vogel-Tamman-Fulcher (VTF) type equation, the data of Fig. 4.7 (b) had to form a curvature[153,154]. However, lnσ has a linear relationship with reciprocal temperature, following an Arrhenius relation, which can be written as[155]:

$$\sigma = \sigma_0 \exp\left[-\frac{Ea}{k_B T}\right] \tag{4.9}$$

where , σ_0 is the maximum electrical conductivity (that it would have at infinite temperature), E_a is the activation energy for electrical conduction, that indicates the energy needed for an ion to hop to a free hole, k_B is the Boltzmann constant and T is the absolute temperature.

The increment of conductivity according to the temperature may be due to the reduction of viscosity and enhancement mobility of polymer chains. This linear behavior between conductivity and temperature is in agreement with the J. Tang *et al*. [156]research and it can be explained due to the free volume and the hopping of charge carriers between localized sites[157]. The crystallinity of the polymer at low temperatures is high and this succeed hinders the motion of ions, producing a decrease in the overall ionic conductivity. As the temperature rises, the amorphicity of the polymer increases gradually provoking a segmental mobility of the polymer chains[158,159]. This amorphicity can promote inter and intra-chain ion hopping movements, leading to an increase in ionic conductivity[160].

Red lines in Fig. 4.7 shows the best fitting, and from the linear fitting (Fig. 4.7 (b)) has been obtained the parameters of Arrhenius equation; σ_0 = 110.38 S cm^{-1} and E_a=0.28 eV. This low value of activation energy for ionic conduction is desirable for supercapacitor applications[161].

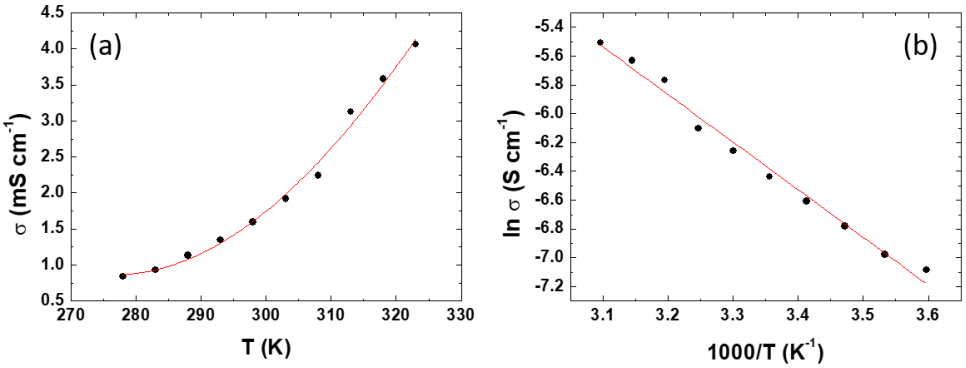

Figure 4.7. **(a)** Ionic conductivity, σ, as a function of absolute temperature and **(b)** Logarithm of the ionic conductivity versus the inverse of the absolute temperature for the PVP/[HEMIm][BF_4] electrolyte. Red lines are the best fit of the data.

Figure 4.8. shows the optical transmittance spectra from 2500 to 200 nm of the polymer electrolyte. It can be seen that the optical transmittance reaches a maximum constant value of 90% in the visible region from 370 to 770 nm. An important property for the use of a supercapacitor in optoelectronic devices, is the transparency of its electrolyte. For this reason, our ionic liquid polymer electrolyte fulfill the requirements necessaries having a high transparency in the visible range.

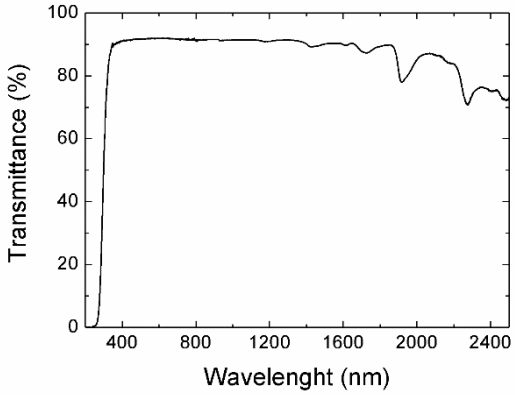

Figure 4.8. Optical transmittance spectra of the PVP/[HEMIm][BF_4] electrolyte.

3. PERFORMANCE STUDIES OF SOLID-STATE SUPERCAPACITOR.

The capacitive behavior of the supercapacitor has been evaluated by cyclic voltammetry (CV) curves in ambient conditions at different scan rate from 25 to 200 mV s^{-1}, in the potential window of -2.0 to 2.0 V. Figure 4.9(a) shows typical cyclic voltammograms of the supercapacitor grown during 5 cycles (5c) PEDOT at various scan rates. These curves exhibit a shape with obvious redox peaks, which indicates Faradaic redox reactions as storage mechanism of the device. Three redox peaks can be observed in each curve. In the case of double-layer capacitors, the shape of CV curves are nearly rectangular, however, for Faradaic redox reactions, large redox current peaks are present. In our case, these results indicate that the capacitance characteristics are mainly due to Faradaic redox reactions. This is because the use of electronically conducting polymers (PEDOT in our case) has been employed to make the electrodes, being a redox active material. For this reason, this device behaves with a certain degree of deviation from an ideal capacitor[162]. The anodic and cathodic peaks are observed to be symmetric, suggesting that the quasi-reversibility of the process in the electrode materials.

From CV curves depicted in Fig. 4.9 (a) and through Eq.(4.5), the specific capacitances were calculated to be 21.04, 18.91, 17.76, 16.85, 15.65 and 14.90 mF g^{-1} at scan rates of 25, 50, 75, 100, 150 and 200 mVs^{-1} ,respectively. Specific capacitances decreases gradually with increasing scan rate, (Fig. 4.9 (b)), this can be attributed to electrolytic ions diffusing and migrating into the active materials at low scan rates. At high scan rates, the diffusion effect, limiting the migration of the electrolytic ions, causes some active surface areas to become inaccessible for charge storage.

On the other hand, the energy density and power density are two important parameters that characterize the electrochemical performance of an electrochemical capacitor. Figure 4.9 (b) shows the capacitances and energy density obtained versus CV sweep scan rates. The maximum value of energy density obtained was 0.046 mWh/g with a maximum power density of 59.28 mW/g.

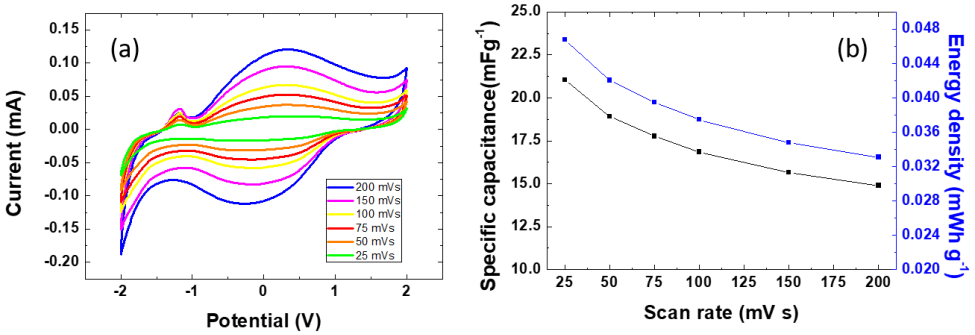

Figure 4.9. **(a)** Cyclic voltammograms for 5c PEDOT supercapacitor at different scan rates and **(b)** Specific capacitance and energy density as a function of scan rate.

Cyclic voltammetries curves for 10 cycles PEDOT supercapacitor are showed in Figure 4.10(a) while the specific capacitances and energy densities obtained from these curves are showed in Fig. 4.10(b). In this case, cyclic voltammograms do not have a redox peak at -1.2 V, as the previous 5 cycles supercapacitor. Values of specific capacitance and energy density follow a similar decreasing tendency, however the results obtained are lower than for 5 cycles PEDOT supercapacitor. For this supercapacitor, specific capacitances were resulted to be 14.10, 11.74, 10.42, 9.56, 8.42 and 8.05 mF g^{-1} at scan rates of 25, 50, 75, 100, 150 and 200 mVs^{-1} ,respectively. The maximum value of energy density obtained has been 0.031 mWh g^{-1} and the maximum power density is 39.74 mW g^{-1}.

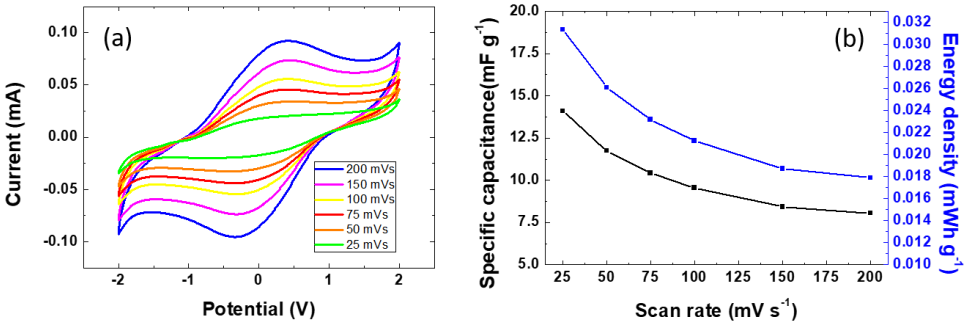

Figure 4.10. (a) Cyclic voltammograms for 10c PEDOT supercapacitor at different scan rates and **(b)** Specific capacitance and energy density as a function of scan rate.

Figure 4.11 depicts a comparative study between a supercapacitor of 5 cycles and 10 cycles of PEDOT. Figure 4.11(a) shows the difference in the shape and area of cyclic voltammogram curves. The area of 5c PEDOT is bigger than 10c PEDOT, this means better specific capacitances for this device as can be seen in Fig. 4.11(b).

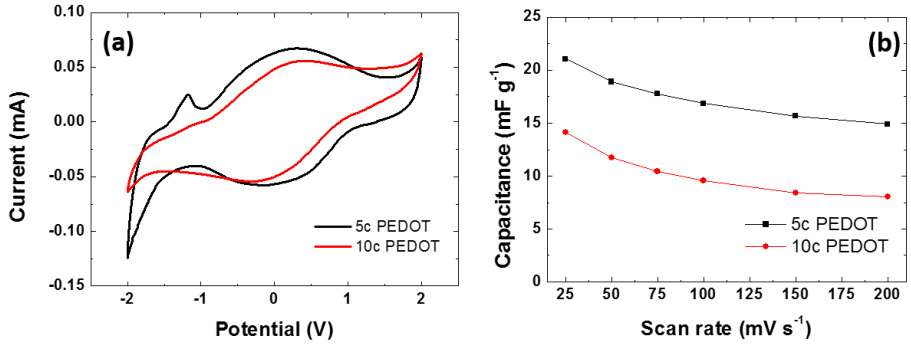

Figure 4.11. (a) Cyclic voltammograms at 100 mVs^{-1} and **(b)** Specific capacitance as a function of scan rate for 5c PEDOT (black line) and 10c PEDOT (red line) supercapacitor.

Figure 4.12 shows the galvanostatic charge-discharge (GCD) curves of both supercapacitors cell tested at different constant current density in the potential range of (0-2) V. The shape of the GCD curves at low current densities (5, 10 $\mu A/cm^2$) is different from linear curves of a typical double-layer supercapacitor (Fig. 4.12 (a)), in other words, they are not triangular and this means there exists a quasi-reversible Faradaic reaction in the electrode. This could be related with a redox reaction of PEDOT since the ion liquid electrolyte does not suffer this type of reaction.

On the other hand, if the current density is increased (100 $\mu A/cm^2$) for the charging and discharging process, the device experiments a typical supercapacitor behavior with a triangular shape of the GCD curves. The symmetry of this curve indicates high charge/discharge coulombic efficiency "η" with a value of 94.5%. There is a low IR drop, what indicates that the internal resistance of the device is quite low. This information is of great importance in energy storing devices due to less energy will be wasted to produce undesirable heat during the charge-discharge process. The

discharge time decreases according to the increment of galvanostatic current applied. The GCD curves of the supercapacitor of 10c PEDOT (Fig. 4.12 (b)) follows a similar behavior with a clear difference in the charge-discharge time at any current, being these higher than the 5c PEDOT device. The asymmetry in these curves indicates low charge/discharge coulombic efficiency for this supercapacitor.

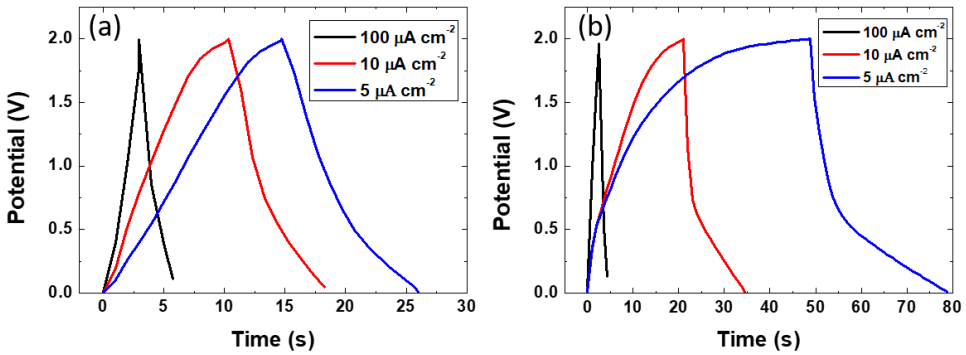

Figure 4.12. Galvanostatic charge-discharge curves of **(a)** PEDOT 5c and **(b)** 10c PEDOT at different constant current density.

From CV curves and GCD curves, it can be concluded that 5c PEDOT supercapacitor possess better performance characteristics than 10c PEDOT, being fundamental the number of cycles or thickness of PEDOT electrode for their use in a final device. For this reason, EIS measurements have been carried out for 5c PEDOT supercapacitor, showing Nyquist and Bode plots in Fig. 4.13 (a) and (b), respectively.

There is always a double electric layer at the interface between an electrode and its surrounding electrolyte. This double layer is composed of ions and other charged species from the electrolyte that "adhere" to the surface of the electrode. This is the double layer capacitance.

Usually, the double-layer parameter measured is typically not an ideal capacitor, since some heterogeneity should be expected due to the porosity of solid electrodes, electrode material, atomic-scale inhomogeneity, applied voltage and current distribution; this implies that the capacitor of the equivalent circuit is replaced by a constant phase element, as it is our case. This element decreases slowly with the applied voltage, it could be for an

increase of the double layer thickness. The presented equivalent circuit model (inset Fig. 4.13(a)) has been applied to simulate the cell response using ZView software. In this model, R_s represents the series resistance, C_d is the double layer capacitance, R_p is the parallel resistance, R_{ct} is the charge transfer resistance and Q is the constant phase element with power of *n* (with no physical meaning). The estimated values of the elements in the model are listed in Table 4.2 for each applied potential bias.

When an interface is disturbed from its equilibrium by means of an external electric field, a flow of charge and matter occurs. This flow can be due to a gradient of electrochemical potential that produces a transport of active species between the electrolyte and the interface or there are electrochemical reactions that allow the transfer of charge between the electrode, metal or semiconductor, and the charges of the electrolyte ions. Electrode reaction may be composed of charge transfer, adsorption and desorption and, also, mass transport. These processes are controlled by the charge transfer resistance that is related to the activation energy and the distance between the species and the electrode. This is a "Faradaic" process in which the transfer of electrons to the electroactive species or viceversa occurs in the medium that is near the electrode surface in the double layer. The charge transfer resistance dominates the total impedance response at low frequencies of Hz and mHz regions and at DC.

The charge transfer resistance is well defined only when the polarization depends on the electrochemical charge transfer current. If there is no electron transfer, the resistance to charge transfer R_{CT} will be very large, and the electrode is polarizable with a poorly defined potential. If there is an electron transfer reaction, R_{CT} becomes smaller. The values obtained for Rct in our device are high and decrease with the applied voltage but up to 1 V, then increase.

The resistance R_p represents the resistance to the leakage currents in the supercapacitor. A high value of R_p supposes a low leakage current and therefore a very low electronic conductivity of the capacitor electrolyte. In our device, the value of R_p decreases by a power law very slowly from a maximum value for a zero applied voltage.

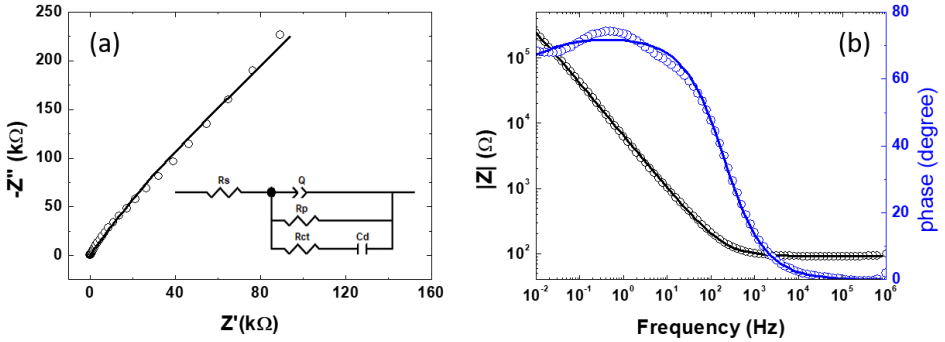

Figure 4.13. (a) Nyquist and **(b)** Bode plots recorded for the supercapacitor device under study at an applied bias potential of 0.0 V. The symbols (open circle shapes) stand for experimental data; the solid lines are fitting with electrical circuit model depicted in the inset of (a).

Figure 4.14 shows Nyquist plot at different applied bias voltage from 0.0 to 1.2 V.

Table 4.2. Comparison at different applied potential of impedance parameters.

Applied potential (V)	**Rs (ohm)**	**Cd (F)**	**Rp(ohm)**	**Rct(ohm)**	**Q(S sec^n)**	**n**
0	91	1.91×10^{-5}	5.72×10^{7}	1.99×10^{6}	3.52×10^{-5}	0.806
0.2	106	1.70×10^{-5}	1.36×10^{7}	8.13×10^{5}	3.15×10^{-5}	0.81
0.4	102	1.94×10^{-5}	3.53×10^{6}	4.98×10^{5}	2.82×10^{-5}	0.81
0.6	99	2.34×10^{-5}	2.07×10^{6}	3.80×10^{5}	2.51×10^{-5}	0.82
0.8	72	2.13×10^{-5}	8.91×10^{5}	1.74×10^{5}	2.41×10^{-5}	0.84
1.0	74	1.44×10^{-5}	7.35×10^{5}	3.01×10^{5}	2.10×10^{-5}	0.86
1.2	70	6.51×10^{-4}	4.88×10^{5}	7.34×10^{5}	1.88×10^{-5}	0.86

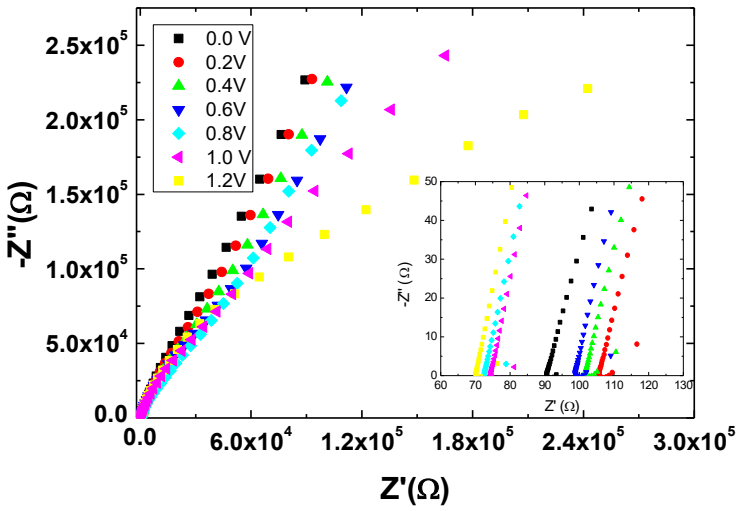

Figure 4.14. Nyquist plots of symmetrical solid state supercapacitor cell at different bias voltages. Inset shows the high frequency region.

D. CONCLUSIONS

A symmetric supercapacitor using electrodeposited PEDOT as electrodes and [HEMIm][BF_4]/PVP ionic liquid polymer as electrolyte, has been successfully synthetized. Good ionic conductivity was found to be $\sigma = 1.5\ 10^{-3}$ S cm^{-1} for the ionic liquid polymer electrolyte. The energy storage in this device is accomplished by charges storage through the reversible Faradaic redox reactions due to the doping and de-doping process at the PEDOT electrode. The influence of the PEDOT-film thickness in the overall specific capacitance of supercapacitor, has been studied, finding that the 5 cycles PEDOT supercapacitor showed better electrochemical properties than 10 cycles PEDOT supercapacitor. The highest gravimetric specific capacitance was 21.04 mF g^{-1} based on the CV data at low scan rates. Energy density and power density resulted to be 0.046 mWh/g and 59.28 mW/g, respectively.

V

PHOTO-SUPERCAPACITOR

A. INTRODUCTION

As discussed in the previous chapters, the fluctuation of the output power from solar cells due to the intermittent sunlight and the requirement of proper energy storage devices makes necessary the obtention of a new and promising device. Photosupercapacitor is an innovative energy device that combines the photoelectric conversion function of a solar cell with the energy storage capability of a supercapacitor. The possibility of generate and storage energy simultaneously in a single device have attracted intensive research attention in the past few years. Since Miyasaka *et al*.[11] fabricated a photo-supercapacitor for the first time in 2004, combining a DSSC and a supercapacitor, this research field have been developing rapidly in the last 14 years as can be seen in Figure 5.1. Two and three electrodes configurations of dye-sensitized solar cells in the beginning to continues with other solar cells based on polymer, Quantum dots and perovskite nowadays.

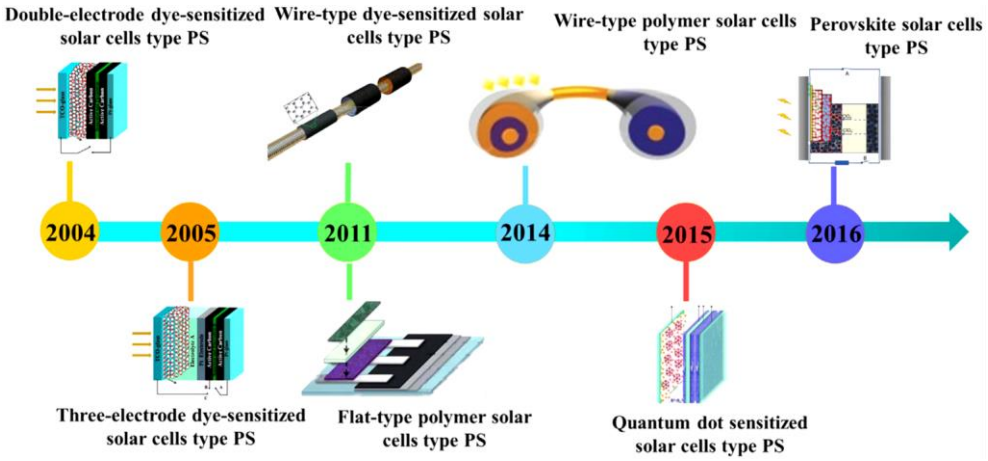

Figure 5.1. Chronology of the development of photosupercapacitors[163].

In this Thesis, it has been chosen as a first configuration a Quantum dot sensitized solar cells configuration for photoanode part for photosupercapacitor which was reported in 2015 for the first time[164]. Therefore, it is considered a novel and emerging type of photosupercapacitor.

1. Types of configuration

On one hand, depending on the number of electrodes, there are configurations of two or three electrodes as can be seen in Figure 5.2.(a) and (b) respectively. This image shows a typical configuration of two and three electrodes based on a Dye Sensitized Solar Cell as photoanode part and active carbon as storage part. These first configurations of photosupercapacitors were reported by Miyasaka and Murakami in 2004[11] and 2005[165]. Initially, it was reported a photocapacitor of two-electrode integrated planar device comprising a DSSC and a symmetric supercapacitor based on active carbon. This device was constructed on a multilayer photoelectrode composed of dye-sensitized TiO_2/hole-trapping layer/activated carbon in contact with an organic electrolyte solution, as shown in Figure 5.2 (a). Upon illumination, generated electrons are injected into the conduction band of TiO_2 and they are collected by the anode flowing into the external part to the counter-electrode. The photoinduced positive and negative charges in solar cells are accumulated on the microporous surface of the activated carbon. However, the internal resistance during the discharge process was relatively large because the electrons passed through the Schottky barrier in the TiO_2 layer. Later, the same authors reported a three-electrode configuration to overcome this problem, introducing an internal bifunctional electrode of platinum between working and counter electrodes, to conduct redox electron transfer on one side and charge storage on the other side simultaneously (Fig. 5.2 (b)). In this improved device, the electrons moved to the active carbon more efficiently on the internal electrode without the potential barrier.

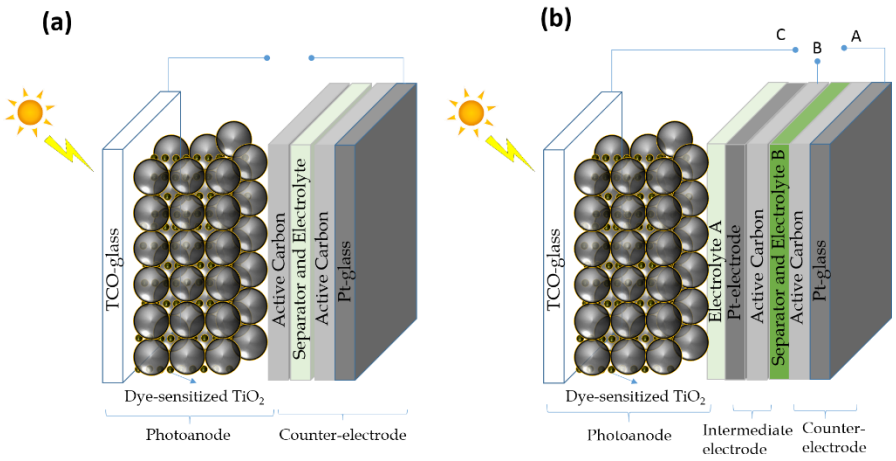

Figure 5.2. Schematic image of the first reported photosupercapacitor of **(a)** two electrodes structure[11,163] and **(b)** three electrodes structure[163,165].

Generally speaking, in a three-electrode photocapacitor system the working principle is the following; when photocapacitor is under illumination, photoanode and counter-electrode are short-circuited by closing the junctions A and C, and opening the junction B. The generated photocurrent flow to counter-electrode and it is accumulated at the surface of the active carbon as a double-layer negative charge. Once the photocapacitor is charged, it occurs the galvanostatic discharging process through the external circuit combining the intermediate electrode and counter-electrode by connecting the junction A and B. Now, the intermediate electrode and the counter-electrode work as positive and negative charged electrodes, respectively.

On the other hand, apart from the traditional planar structure explained before, it exists a newly emerging fiber-shaped integrated photocapacitor. These fiber-shaped devices are obtained by rolling up the planar structure. Normally, the solar cell part and the supercapacitor part are in fiber forms and they are integrated in the core-shell or twisted configuration structure. This device has the advantages of lightness, flexibility and compatibility with weaving, which are essential properties for their use in portable and wearable electronics. In addition, fiber solar cells have the unique advantage of light incident angle-independent properties compared with planar

structure photocapacitors. Moreover, this particular fiber surface structured can increase the absorption from scattered and reflected light, expanding the adaptability of solar cells to the environment. An example of this integrated devices was reported by Wang *et al*.[166] employing a coaxial structure with a polymethyl methacrylate (PMMA) fiber as substrate. Photoanode part was fabricated of a DSSC over ZnO nanowires and a graphene counter-electrode. Storage part was composed of graphene and ZnO nanowires with a PVA/H_3PO_4 gel electrolyte.

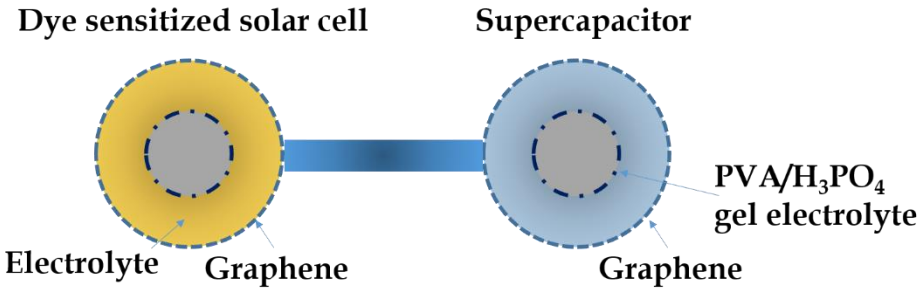

Figure 5.3. Schematic image of a wire-type dye sensitized solar cell photo-supercapacitor.

2. Evaluation of the photo-supercapacitor.

To know and to characterize a photo-supercapacitor is necessary to calculate the overall efficiency, the photovoltaic energy conversion and the storage efficiency. The overall efficiency is determined by the photovoltaic energy conversion part and the electrochemical energy-storage one, according to the following equation[167,168]:

$$\mu_{OVERALL} = \frac{E_{storage}}{E_{light}A_{solar}} \quad (5.1)$$

where $E_{storage}$ is the stored energy(Wh), E_{light} is the energy of the light illuminating the solar cell during the photocharging time and A_{solar} is the area of the solar cell.

The $E_{storage}$ and E_{light} can be calculated using the following equations:

$$E_{storage} = 0.5\, CV^2 \tag{5.2}$$

$$E_{light} = P_{in} \cdot t \tag{5.3}$$

where *C*(F) is the capacitance, *V* (V) is the potential window in the charge/discharge process, P_{in} is the incident-light power density (100 mW/cm²) and *t* is the photocharging time, respectively.

The capacitance C, and areal specific capacitance can be calculated from the charge or discharge curve according de following equations:

$$C = \frac{i\Delta t}{\Delta V} \tag{5.4}$$

$$C_A = \frac{C}{A} \tag{5.5}$$

where i (A) is the galvanostatic applied current, Δ*t* (s) is the discharge time, Δ*V* is the potential window obtained from the discharge profile excluding the voltage drop and *A* is the area of the supercapacitor.

Normally, the performance of the supercapacitors are evaluated employing different tests such as cyclic-voltammetry at different scan rates, galvanostatic charge/discharge curves at different current densities and electrochemical impedance spectroscopy measurements.

The storage efficiency of the photo-supercapacitor is calculated from the next equation:

$$\mu_{storage} = \frac{\mu_{overall}}{\mu_{conversion}} \tag{5.6}$$

where $\mu_{conversion}$ is the photovoltaic conversion efficiency that can be measured as follows.

$$\mu_{conversion} = \frac{V_{oc}J_{sc}FF}{P_{in}} \tag{5.7}$$

where V_{oc}, J_{sc}, FF and P_{in} are the open circuit voltage, short-circuit current density, fill factor and incident light power density, respectively.

Fill Factor of the solar cell can be calculated with the follow equation:

$$FF = \frac{V_{MP} I_{MP}}{V_{oc} I_{SC}} \quad (5.8)$$

where V_{MP} and I_{MP} are the voltage and current at the maximum power point, respectively. I_{SC} is the short-circuit current.

In this Chapter, it is exposed two different photosupercapacitors (PSC) of two electrodes. Initially, it is presented a PSC based on QDSSCs/FTO as photoanode, PEDOT as counter-electrode and ionic liquid as electrolyte (named PSC FTO/QDSSC-ionic liquid-PEDOT), such as it has been explained in the previous Chapter III and IV. Subsequently, it is shown a PSC whose only change with regard to previous device is the presence of GIZO as transparent conducting oxide instead of FTO and the absence of a ZnO seed layer. The elements of this device have been explained in Chapter II, III and IV (named PSC GIZO/QDSSC-ionic liquid-PEDOT). Finally, it is shown another concept of a transparent photocapacitor based on TiO_2 as photoanode, $LiFeO_2$ as counter-electrode and an ion gel as electrolyte (named PSC TiO_2-ion gel-$LiFeO_2$).

B. MATERIALS AND METHODS

The first type of PSC is based on the previous research about the transparent conductive oxide (TCO) (Chapter II), the photoanode (Chapter III) and the supercapacitor (Chapter IV) to form the final photo-supercapacitor. The explanation of this device is divided into two parts, 1.A) for the FTO as TCO and 1.B) for the GIZO as TCO. The second type of PSC is presented in last part of this section, 2).

1.A) PSC FTO/QDSSC -IONIC LIQUID- PEDOT

1.A.1) FABRICATION OF PHOTO-ANODE

The substrates used in this photoanode was commercial glass/FTO with a sheet resistance of 10 Ω/□. The size of the samples were 2 cm x 1 cm. All the substrates were properly cleaned before their first use. The substrates were immersed 15 minutes in acetone, 15 min in 2-propanol and 15 min in deionized water in an ultrasonic bath.

Spin coating was employed to grow a ZnO seed layer thin film on FTO. Zinc acetate 10 mM was dissolved in methanol and an angular velocity of 2000 rpm was used. 1 ml of solution was dropped over the sample and after waiting 40 seconds to stop finally. Then, the sample was introduced in an oven at 105˚C during 10 minutes to evaporate the solvent. This process is repeated four times and after that, a thermal treatment is carried out to the sample in the furnace during 20 minutes at 350ºC, ramp up 10ºC/min. This procedure was done twice over each sample to obtain a double seed layer of ZnO.

Subsequently, electrochemical deposition was made in a conventional electrochemical cell of three electrodes, where ZnO SL/FTO was used as working electrode; platinum (Pt) sheet as Counter electrode and a saturated calomel electrode (SCE) as a Reference electrode. Chronoamperometry was carried out at -1.0 V refers to SCE. Electrolyte was saturated bubbling O_2

about 20 min prior to ECD and during the process. After the ECD, the samples of ZnO NW´s/SL ZnO/FTO/glass were rinsed with DI water to remove impure ion and un-reacted products from the surface of ZnO nanostructures and dried in air.

ZnO nanowire arrays were sensitized with Ag_2S QDs. These were synthesized using the Succesive Ionic Layer and Adsorption Reaction (SILAR) method.
The sample was immersed in a solution of 0.05 M $AgNO_3$ dissolved in ethanol and 0.05 M Na_2S dissolved in methanol. ZnO NW´s were selected under the best condition found from the experimental design previously reported: [$ZnAc_2$] = 1 mM, T = 70 ºC, t = 60 min. ZnO NW´s were dipped into the Ag+ cationic solution for 1 min, washed with ethanol for 20 s, then dipped into S^{2-} for 1 min and finally washed with methanol. It was made during 9 cycles. Next, a thermal annealing was carried out in a furnace, during 1 hour at 400ºC with 2ºC/min of ramp up in N_2 atmosphere.

Finally, the electrode was passivated with the deposition of ZnS, this was carried out by 4 cycles of SILAR method. The photoelectrode was alternatively dipped in 0.5 M of zinc acetate ($Zn(CH_3COO)_2$) as cationic solution and 0.5 M of Na_2S as anionic aqueous solutions for 1 min, rinsing with water between both to remove the non-adsorbed/unreacted ions.
Over this structure was electrodeposited PEDOT to act as hole transporting material and as sharing electrode between photoelectrode and counter-electrode.

1.A.2) FABRICATION OF SUPERCAPACITOR

PEDOT was synthetized by electropolymerization of EDOT over commercial FTO/glass substrates. Once PEDOT was electrodeposited on one side of the FTO glass substrate, it was dipped in an ionic liquid solution composed of methanol, PVP and [HEMIm][BF_4].

1.A.3) Assembly of QDSSC with supercapacitor to form integrated Two-electrode Photo-Supercapacitor

Once the photoanode and the supercapacitor were designed, they were assembled by using a piece of a polymer separator (Solaronyx, 25 µm thickness) (size: 0.5 cm x 0.5 cm) sandwiched between the QDSSC and the Counter-electrode. Both parts were attached thanks to the high viscosity of the electrolyte. After some moment, the whole device remains totally bounded. The quantity of electrolyte was the same for all the photocapacitors. The scheme of this PSC can be seen in Figure 5.3.

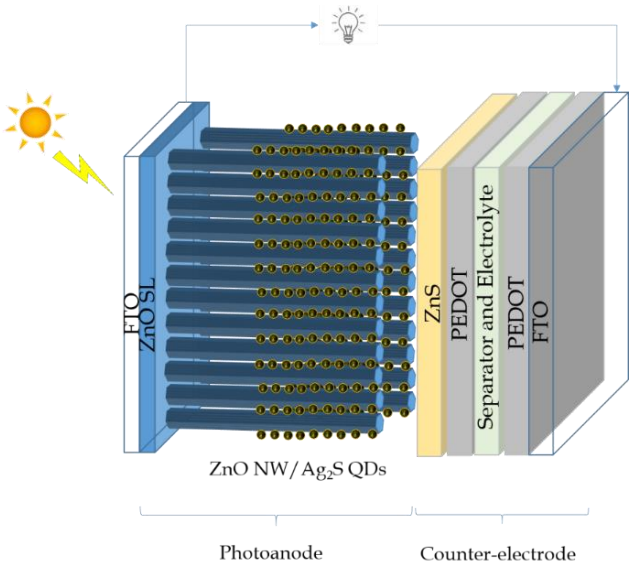

Figure 5.3. Schematic diagram of first type of photo-supercapacitor based on FTO/ZnO SL- QDSSC-Ionic Liquid- PEDOT, designed in this Thesis.

1.B) PSC GIZO/QDSSC-IONIC LIQUID- PEDOT

The next PSC presented in this Thesis is very similar to the previous one, with the only difference that the transparent conducting oxide has been home-made fabricated, being GIZO/glass thin films (see Chapter II) instead of commercial FTO/glass. Another relevant difference is this photoanode does not have a ZnO seed layer for the nanowires growth, being no necessary since GIZO possess a film of ZnO favouring the nucleation sites for the nanowires growth.

GIZO thin films substrates used in this photoanode was properly cleaned before their use and the sheet resistance was 17 Ω/□. The size of the samples were 2 cm x 1 cm. The nanowires growth and subsequent nanostructures followed the same process as explained previously for this type of PSC presented. The scheme of this PSC can be seen in the next Figure 5.4.

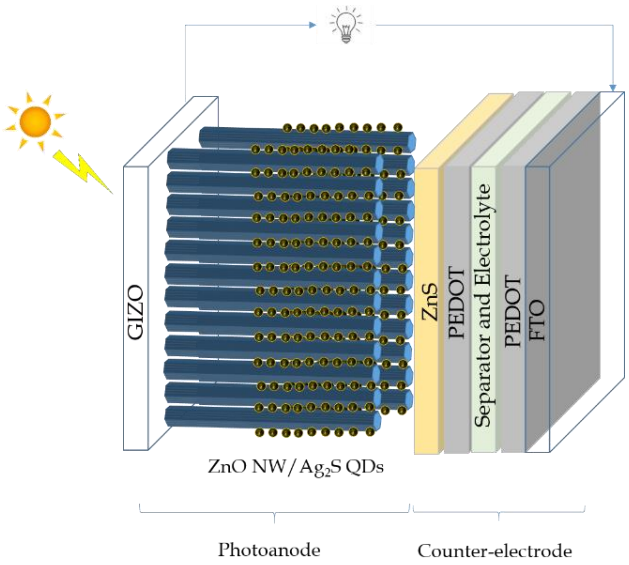

Figure 5.4. Schematic diagram of photo-supercapacitor based on GIZO/QDSSC-Ionic Liquid- PEDOT designed in this Thesis.

2) PSC TiO_2-ION GEL-$LiFeO_2$

2.1) FABRICATION OF PHOTO-ANODE

The TiO_2 photoanode films have been deposited by DC magnetron sputtering on ITO/glass substrates after being previously sequentially ultrasonically cleaned in acetone, isopropanol and finally distilled water, 5 minutes in each solvent. A titanium target (99.9%) from *AJA International, Inc.* was employed. The power was set at 300 W. The working pressure into the vacuum chamber remained constant at 3 mTorr with a high purity (5.0) Ar gas and O_2 gas, each regulated by mass flow controllers at 18 sccm and 3.23 sccm, respectively. The equipment used was a Magnetron Sputtering System ORION-5-UHV (*AJA International, Inc.*)[169].

2.2) FABRICATION OF COUNTER-ELECTRODE

The $LiFeO_2$-Ag thin film electrode was obtained by spray pyrolysis, heating at 450 ^oC during 1 hour, and using a precursor solution described in a previous work by our group[170].
There were tested two types of electrolyte in our photocapacitor. The first one was an electrolyte based on PVP/$LiClO_4$ developed by us[171] and the second one an ion gel electrolyte composed by PVP/[HEMIm][BF_4], which preparation and characterization was detailed in our previous work as well[153].

2.3) ASSEMBLY OF TiO_2 PHOTOANODE WITH $LiFeO_2$ COUNTER-ELECTRODE TO FORM INTEGRATED TWO-ELECTRODE PHOTO-SUPERCAPACITOR

Once the photoanode and the supercapacitor were designed, they were assembled by using hand pressure. Both parts were attached thanks to the high viscosity of the electrolyte. After some moment, the whole device remains totally bounded. The area of the photoanode and supercapacitor was 6 cm^2. Figure 5.5 shows the scheme of the photo-supercapacitor.

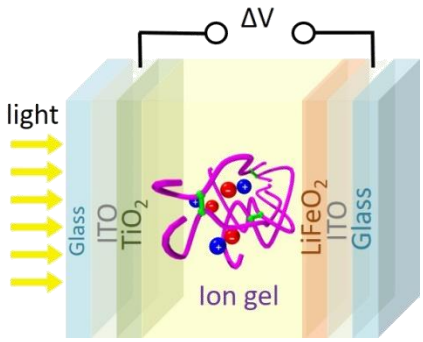

Figure 5.5. Schematic diagram of second type of PSC based on TiO_2-Ion gel-$LiFeO_2$ designed in this Thesis.

C. RESULTS AND DISCUSSION

1.A) PSC FTO/QDSSC -IONIC LIQUID- PEDOT

The operating principle of this photocapacitor based on FTO/QDSSC has been interpreted as follows: under light illumination, the Ag_2S QDs are photo-excited and the electrons from QDs are injected into ZnO nanowires flowing through the external circuit to the counter-electrode (PEDOT) where negative charge is accumulated. At the same time, the layer of PEDOT deposited by ZnO of photoanode results in partial positive charge. The BF_4^- ions are attracted to that positive charge provoking the separation of the ionic liquid electrolyte and a double layer is formed. Simultaneously, the ion gel cations $[HemIm]^+$ go to the PEDOT/FTO layer, which is negative charged as a cathode. Then, a double layer supercapacitor base is fulfilled. On the other hand, during discharging process in darkness, the double layer reorganize again itself taking place the discharge of the device.

1.A.1) PHOTOVOLTAIC CHARACTERIZATION OF QDSSCS PHOTOANODE

In order to investigate the photovoltaic performance of the photosupercapacitor, photocurrent density-voltage (J-V) characteristics were obtained under AM1.5 illumination. Figure 5.6 depicts the corresponding photocurrent density-voltage (J-V) curves of QDSSCs photoanode in dark and under illumination (100 mW cm^{-2}) solar simulator. The device represents an overall power conversion efficiency ($\eta_{CONVERSION}$) of 0.012% with a short-circuit current density (J_{sc}) of 0.042 mA cm^{-2}, open circuit voltage (V_{oc}) of 0.749 V, and fill factor (FF) of 38%.

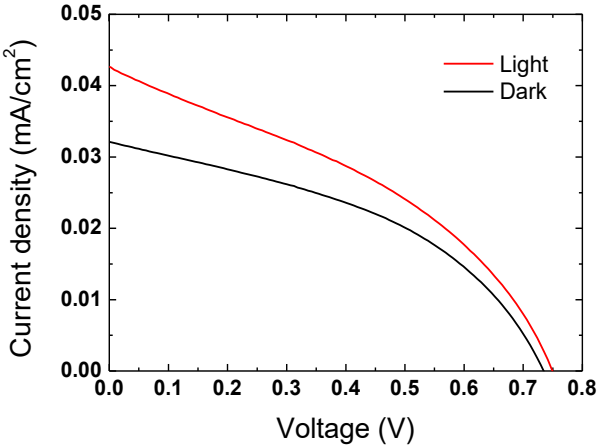

Figure 5.6. The J-V curves of the QDSSCs measured under light and dark conditions with simulated solar illumination (100 mW/cm^2).

1.A.2) Electrochemical Performance of Photo-supercapacitor

The electrochemical performance of the supercapacitor integrated in the photo-capacitor is evaluated through Cyclic voltammetries (CV) curves, Galvanostatic Charge-Discharge (GCD) curves and electrochemical spectroscopy impedance (EIS) measurements. Figure 5.7 (a) shows cyclic voltammogram curves carried out at different scan rates from 50 to 200 mV s^{-1}, obtaining higher area of the curves at higher scan rates, as expected. The shape of the curves are almost rectangular at any scan rate, indicating a low resistance and good reversibility. As shown in Figure 5.7 (b) the near triangular shape of galvanostatic charge-discharge curves different current densities indicates the good reversibility of the charging-discharging process. With the aim of testing the cyclic stability of the photocapacitor, specific capacitance and specific energy was calculated from the CV curves obtained during 1200 cycles (Fig. 5.7 (c)). The resulting values are plotted in Fig. 5.7 (d). Specific capacitances from 0.334 mF cm^{-2} to 0.339 mF cm^{-2} were achieved under dark conditions depending on the voltammetry cycle

number. On the other hand, specific energies from 7.44 μJ cm^{-2} to 7.53 μJ cm^{-2} were obtained. Both values decreased with the cycle number, but this decrease was not much relevant taking into account the number of cycles that were carried out (1200).

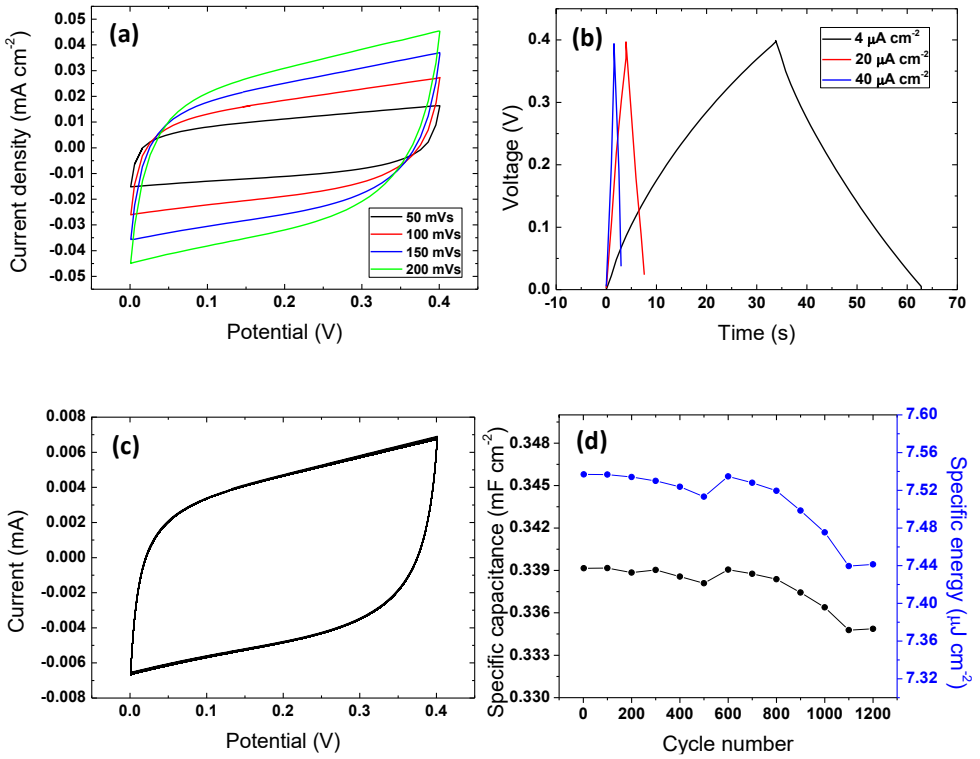

Figure 5.7. (a) Cyclic voltammetries curves at different scan rates in darkness. **(b)** Galvanostatic charge-discharge curves at different current densities. **(c)** Cyclic voltammograms measured at 100 mV s^{-1} during 1200 cycles. **(d)** Specific capacitance (black circles) and specific energy (blue circles) obtained by the CV curves for the photocapacitor.

Further insight into the photocapacitor device characteristics have been conducted by electrochemical impedance spectroscopy (EIS) measurements, which have been performed at four different applied bias potentials E= 0.0 V, 0.1 V, 0.2 V and 0.3 V under dark conditions. The obtained values are depicted in Table 5.1. Figure 5.8(a) and Figure 5.8(b) show typical Nyquist and Bode plots for the photocapacitor device under study at an applied bias

potential E=0.0 V. The fits are indicated by solid lines in the plots showing a good agreement with the data. This confirms the suitability of the equivalent circuit model used. The Nyquist plot consists of an incomplete small semicircle at the higher frequency with a nonzero intercept and a linear tail at lower frequencies. The impedance at high frequencies showed a low resistive behavior with the series resistance of 136.2 Ω at 0.0 V and it maintains constant at higher applied voltages. This series resistance (Rs) represents the sheet resistance of FTO and the contact resistance of FTO/ZnO nanowires. This resistance is related to the short circuit current in the device (see Fig.5.7). In this photocapacitor, the semicircle with linear tail showed in Nyquist plot suggests that the polarization is due to a combination of diffusion and kinetic processes. The parallel resistance (Rp) represents the resistance to the leakage currents in the photocapacitor, their values are very high and increase regarding to applied voltage. This results means a low leakage current and therefore a very low electronic conductivity of the PVP/[HEMIm][BF_4]electrolyte. Since both electrodes are not a double-layer parameter that represents an ideal capacitor. That capacitor must be replaced by a constant phase element (CPE and Q, in this case). As *n* value are nearly 1, this indicates that this QPE can be approached to a capacitance of a rough surface of 40.4 nm, which is confirmed by AFM characterization of PEDOT electrodes (see Chapter IV, Fig. 4.4). The values obtained for Rct are not very high and indicate an electron transfer reaction in the photoanode.

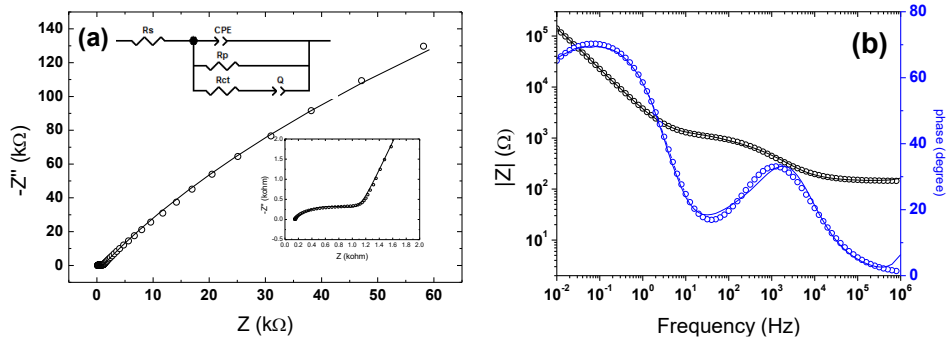

Figure 5.8. (a) Nyquist and **(b)** Bode plots recorded for the photocapacitor device under study at an applied bias potential of 0.0 V, under dark conditions. The symbols (open circle shapes) stand for experimental data; the solid lines are fitting

with electrical circuit model depicted in the inset of (a). Inset shows the high frequency region.

Table 5.1. Equivalent circuit element values obtained through a complex non-linear least- squares fitting program of the EIS spectra.

	Applied bias potential (V)			
	0	**0.1**	**0.2**	**0.3**
Rs (Ω)	136.2	157.1	155.7	154.2
CPE (S s^{α})	6.06×10^{-6}	7.5×10^{-6}	9.5×10^{-6}	1.24×10^{-5}
α	0.682	0.669	0.649	0.628
Rp (MΩ)	0.979	1.67	2.33	7.70
Rct(Ω)	1063	1582	1856	2072
Q (S s^{n})	8.74×10^{-6}	6.52×10^{-6}	6.70×10^{-6}	7.46×10^{-6}
n	0.835	0.826	0.832	0.844

1.A.3) CHARACTERIZATION OF THE INTEGRATED PHOTO-SUPERCAPACITOR

During the photo-charge process, the photo-excited electrons collected from quantum dots semiconductors of Ag_2S are transferred from the conduction band of ZnO nanowires to the counter-electrode. Figure 5.9(a) shows the photocharge and galvanostatic discharge process of the photosupercapacitor at different discharge current densities from 4 to 400 μA cm^{-2}. The device was totally photocharged until a final work potential of QDSSCs to 0.33 V in 40 s and the process was maintained for 600 s consistently. This voltage achieved is higher than another found in literature when photocapacitor is composed of two electrodes[172,173] and even for a photocapacitor of three electrodes[174]. The photocharge time is lower than another research[175] whose time is higher than 2000 s. After photocharge, the device is discharged at 4 μA cm^{-2} with a discharge time of 55 s, at 40 μA cm^{-2} in 2 s and at 400 μA cm^{-2} in 1 s. Some cycles of photocharge and galvanostatic discharge (in dark) carried out at 4 μA cm^{-2} are presented in

Fig. 5.9(b), showing the stability of the photocapacitor through the cycling process (50 cycles).

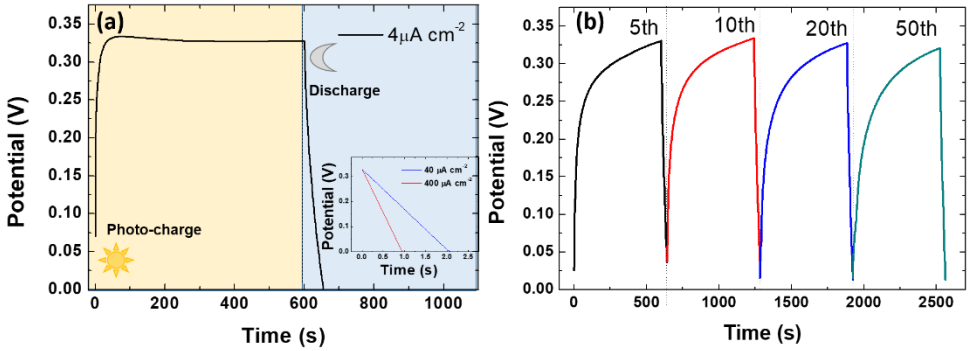

Figure 5.9. (a) Photocharge under AM1.5G simulated sunlight (100 mW/cm²) illumination and galvanostatic discharge at 4 μA cm^{-2} in dark conditions (inset shows the galvanostatic discharge at 40 μA cm^{-2} (blue line) and 400 μA cm^{-2} (red line) current densities). **(b)** Some cycles of photocharge/galvanostatic discharge at 4 μA cm^{-2}. Cycles numbers are indicated.

The performance study of the integrated photocapacitor has been evaluated through the calculations of $\eta_{overall}$ and $\eta_{storage}$ obtained from photocharge-discharge curves. The capacitance of the device resulted to be 0.667 mF cm^{-2} according to the equations (5.4) and (5.5). The stored energy was calculated to be 3.63 x 10^{-5} W obtained from equation (5.2). Finally, the integrated photocapacitor reached a maximum overall photoelectric efficiency of $\eta_{overall}$=8.25 x 10^{-4} % and a maximum storage efficiency of $\eta_{storage}$=6.83 %.

Although there exists another photocapacitors with higher efficiencies found in bibliography[176,177], this concept of photocapacitor is a promising device that exhibit a good capacitance, high photo-charge time and stability with the photocharge cycles. Furthermore, the structure of this two electrodes device is of low cost, environmentally friendly and easy of fabrication.

1.B) PSC GIZO/QDSSC-IONIC LIQUID- PEDOT

For the next device, the operating principle based on GIZO/QDSSC is very similar to the previous one with the only difference that photoelectrons flow through the external circuit by GIZO thin films as the transparent conductive oxide.

1.B.1) PHOTOVOLTAIC CHARACTERIZATION OF GIZO QDSSC PHOTOANODE

Figure 5.10. depicts the corresponding photocurrent density-voltage (J-V) curves of GIZO QDSSCs photoanode in dark and under simulated AM 1.5 illumination (100 mW cm^{-2}) solar simulator. The device represents an overall power conversion efficiency ($\eta_{CONVERSION}$) of 0.0014% with a short-circuit current density (J_{sc}) of 0.010 mA cm^{-2}, open circuit voltage (V_{oc}) of 0.622 V, and fill factor (FF) of 23%. Regarding previous PSC of FTO/QDSSC, this photoanode offers lower short-circuit current density but higher open circuit voltage, obtaining a final efficiency with one magnitude order smaller.

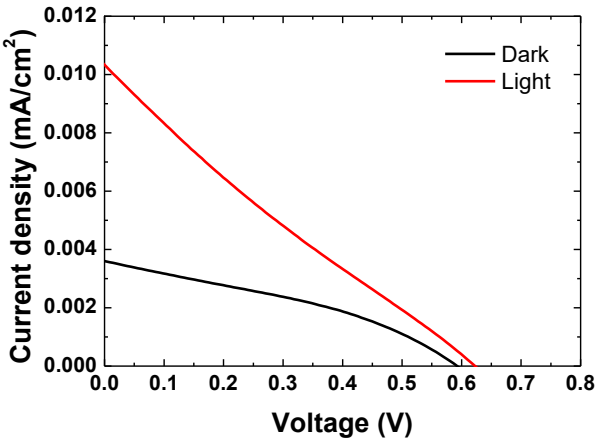

Figure 5.10. The J-V curves of the GIZO QDSSCs measured under light and dark conditions with a simulated solar illumination (100 mW/cm^2).

1.B.2) ELECTROCHEMICAL PERFORMANCE OF PHOTO-SUPERCAPACITOR

The electrochemical performance of the supercapacitor integrated in the photo-capacitor is evaluated through Cyclic voltammetries (CV) curves, Galvanostatic Charge-Discharge (GCD) curves and electrochemical spectroscopy impedance (EIS) measurements. Figure 5.11 (a) shows cyclic voltammogram curves carried out at different scan rates from 50 to 200 mV s^{-1}, obtaining higher area of the curves at higher scan rates, as expected. The shape of the curves is different with regard two previous PSC, since it is more flattened.

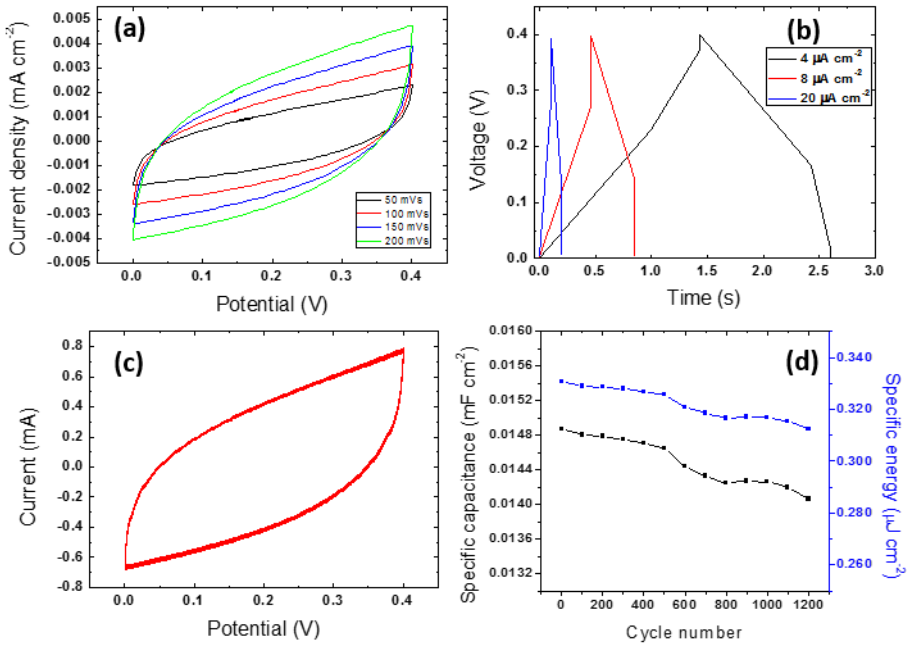

Figure 5.11. (a) Cyclic voltammetries curves at different scan rates in darkness. **(b)** Galvanostatic charge-discharge curves at different current densities. **(c)** Cyclic voltammograms measured at 100 mV s^{-1} during 1200 cycles. **(d)** Specific capacitance (black circles) and specific energy (blue circles) obtained by the CV curves for the photocapacitor.

As shown in Figure 5.11 (b) the near triangular shape of galvanostatic charge-discharge curves different current densities indicates the good reversibility of the charging-discharging process, however the lower charge-discharge time indicates a lower capacitance of this device regarding to PSC QDSSC. Furthermore, it is not possible to measure at 400 µA cm^{-2} due to it takes less than 1 s of charge and discharge. With the aim of testing the cyclic stability of the photocapacitor, specific capacitance and specific energy was calculated from the CV curves obtained during 1200 cycles.

As explained before, further insight into the photocapacitor device characteristics have been conducted by electrochemical impedance spectroscopy (EIS) measurements, which have been performed at four different applied bias potentials E= 0.2 V, 0.3 V, 0.4 V and 0.5 V under dark conditions. The obtained values are depicted in Table 5.2. Figure 5.12 (a) and (b) show typical Nyquist and Bode plots for the photocapacitor device under study at an applied bias potential E=0.2 V.

The fits are indicated by solid lines in the plots showing a good agreement with the data. This confirms the suitability of the equivalent circuit model used. In this case, Nyquist plot does not show a semicircle at higher frequencies, for this reason it is not necessary to add a series resistance to fit the impedance results. This may be due to this photocapacitor does not have a seed layer between FTO and ZnO nanowires which could add a resistance in the circuit. The parallel resistance (R_p) values are very high and decrease regarding to applied voltage. This results means again a low leakage current and therefore a very low electronic conductivity of the PVP/[HEMIm][BF_4]electrolyte. Since both electrodes are not a double-layer parameter that represents an ideal capacitor, the capacitor must be replaced by a constant phase element (CPE1 and CPE2, in this case). The values obtained for R_{ct} are very high and indicate that there is no electron transfer reaction.

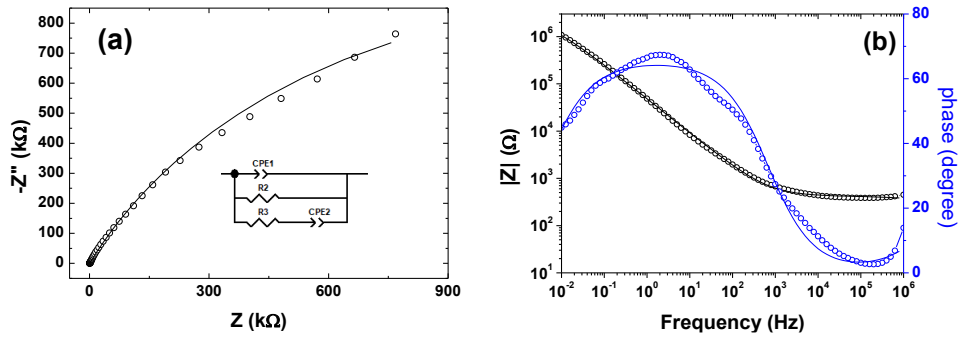

Figure 5.12. (a) Nyquist plot and equivalent circuit diagram used for fitting EIS. Inset shows the high frequency region and **(b)** Bode plot recorded for the photocapacitor device under study at an applied bias potential of 0.2 V, under dark conditions.

Table 5.2. Equivalent circuit element values obtained through a complex non-linear least- squares fitting program of the EIS spectra.

	Applied bias potential (V)			
	0.2	**0.3**	**0.4**	**0.5**
Q1 (S $s^{\alpha 1}$)	3.29×10^{-8}	4.21×10^{-8}	1.85×10^{-7}	2.22×10^{-7}
α1	0.602	0.591	0.495	0.484
R2 (Ω)	2.67×10^{6}	2.32×10^{6}	2.05×10^{6}	1.65×10^{6}
R3 (kΩ)	418.8	432.1	531.2	538.1
Q2 (S $s^{\alpha 2}$)	5.40×10^{-6}	5.44×10^{-6}	5.42×10^{-6}	5.46×10^{-6}
α2	0.727	0.729	0.733	0.734

1.B.3) CHARACTERIZATION OF THE INTEGRATED PHOTO-SUPERCAPACITOR

During the photo-charge process, the photo-excited electrons collected from quantum dots semiconductors of Ag_2S are transferred from the conduction band of ZnO nanowires and GIZO to the counter-electrode. Figure 5.13 shows the photocharge and galvanostatic discharge process of the photosupercapacitor at 4 µA cm^{-2}. The device was totally photocharged until a maximum work potential of QDSSCs to 0.35 V in 30 s and the process was maintained for 600 s consistently. After photocharge, the device is discharged at 4 µA cm^{-2} with a discharge time of 5 s.

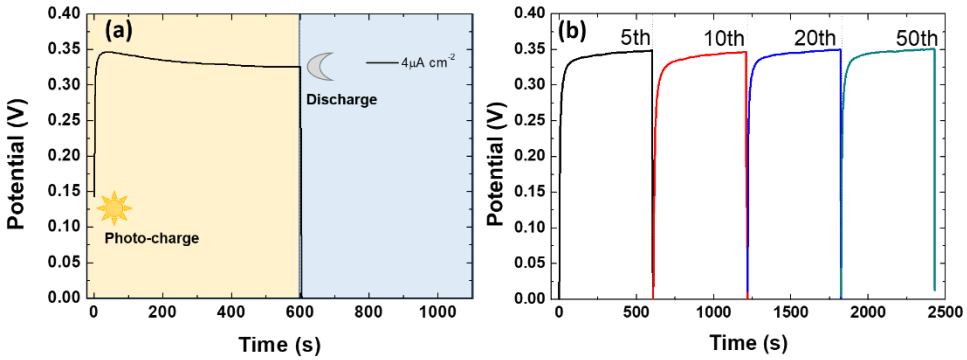

Figure 5.13. (a) Photocharge under AM1.5G simulated sunlight (100 mW/cm^2) illumination and galvanostatic discharge at 4 µA cm^{-2} in dark conditions. **(b)** Some cycles of photocharge/galvanostatic discharge at 4 µA cm^{-2}. Cycles numbers are indicated.

The performance study of the integrated photocapacitor has been evaluated through the calculations of $\eta_{overall}$ and $\eta_{storage}$ obtained from photocharge-discharge curves. The capacitance of the device resulted to be 0.056 mF cm^{-2} according to the equations (5.4) and (5.5). The stored energy was calculated to be 3.39 x 10^{-6} W obtained from equation (5.2). Finally, the integrated photocapacitor reached a maximum overall photoelectric efficiency of $\eta_{overall}$=1.13 x 10^{-4} % and a maximum storage efficiency of $\eta_{storage}$=7.83 %.

2) PSC TiO_2-Ion Gel-$LiFeO_2$

The operating principle of this second type of photocapacitor has been interpreted as follows: under light illumination, the TiO_2 film (which had rutile structure) is photo-excited resulting in partial positive charge in TiO_2-ion gel interface. The BF_4^- ions are attracted to that positive charge provoking the separation of the ion gel charge and a double layer is formed. Simultaneously, the ion gel cations $[HemIm]^+$ go to the $LiFeO_2$-ion gel interface, which is negative charged as a cathode. Then, a double layer supercapacitor base is fulfilled. On the other hand, in darkness, the double layer reorganize again itself taking place the discharge of the device.

2.1) Morphological Characterization of the electrodes by FE-SEM

The thickness of the $LiFeO_2$ and the TiO_2 electrodes was directly obtained by FESEM pictures. Fig. 5.14 shows the morphology of the films and the cross-sections carried out to measure the thickness, which was ca. 130 nm for the $LiFeO_2$ and ca. 790 nm for the TiO_2.

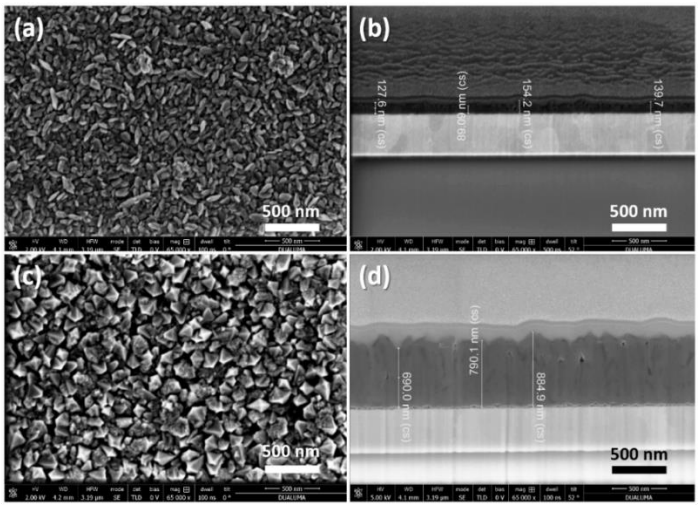

Figure 5.14. FE-SEM pictures and cross-sections of $LiFeO_2$ (a,b) and TiO_2 (c,d) thin films deposited on the ITO substrate.

2.2) CHARACTERIZATION OF THE PHOTO-ELECTRODE OF TiO_2

From the result of XRD measurement (Fig. 5.15), it was observed that the TiO_2 prepared by DC reactive sputter deposition at 623 K had rutile structure with the crystallite size of ca. 32 nm from Scherrer equation, without reflections of anatase or brookite.

XPS study was carried out to confirm the stoichiometry of TiO_2 films. In samples prepared at 200W, the XPS Ti $2p_{3/2}$ and $2p_{1/2}$ peaks of TiO_2 were shown at ca. 459.48 and 459.01 eV respectively. On the other hand, samples prepared at 300W showed more reduced, showing the XPS Ti $2p_{3/2}$ and $2p_{1/2}$ peaks of TiO_2 at ca. 459.43 and 459.04 eV.

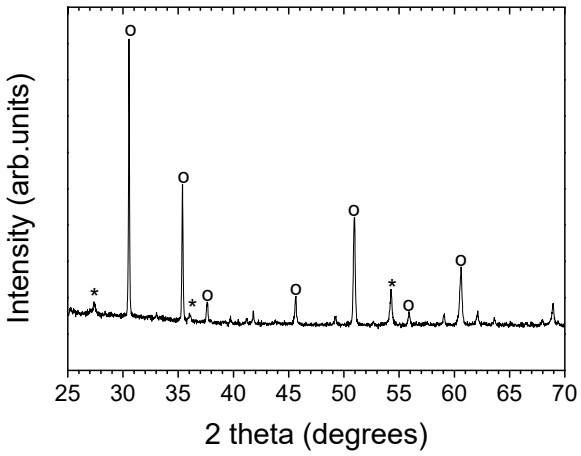

Figure 5.15. XRD pattern for the TiO_2 thin film deposited on the ITO substrate. It is shown rutile peaks (*) and ITO peaks (○).

The roughness of the $LiFeO_2$ and the TiO_2 electrodes was measured through AFM, being 14.3 nm and 31.3 nm respectively. Fig. 5.16 shows the AFM pictures for both electrodes, taking an area of 1 μm^2.

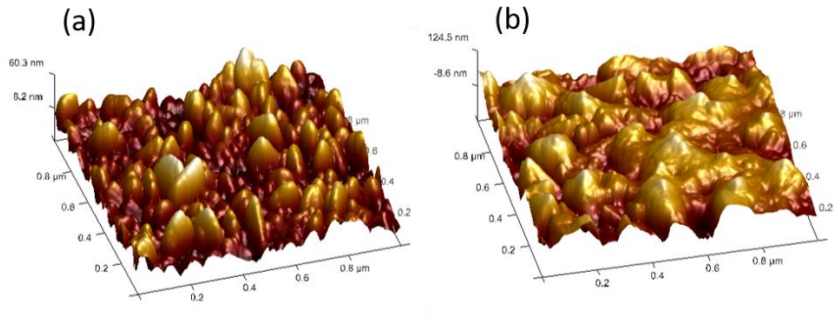

Figure 5.16. AFM for $LiFeO_2$ **(a)** and TiO_2 **(b)** thin films deposited on the ITO substrate.

2.3) OPTICAL PROPERTIES

Transmittance results for all the separated components of the photocapacitor and the photocapacitor itself are shown in Fig. 5.17. At λ= 555 nm (optical transmittance evaluated at this wavelength because the photopic eye sensitivity function has maximum sensitivity in the green spectral range at 555 nm), the transmittance of the different components of the photocapacitor was the following: 77% for the TiO_2 electrode, 67% for the $LiFeO_2$-Ag electrode and 91% for the ion gel electrolyte, being the transmittance at 555 nm for the whole device 57%.

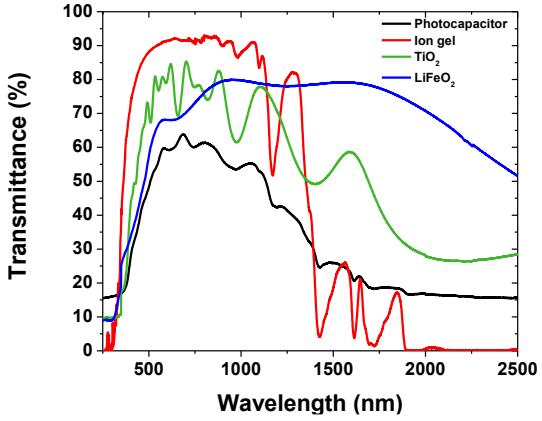

Figure 5.17. Optical transmittance of each electrode, the ion gel electrolyte and the photocapacitor itself.

2.4) PHOTOVOLTAIC CHARACTERIZATION OF TiO_2 PHOTOANODE

In order to evaluate the photovoltaic performance of the photosupercapacitor it is necessary to illuminate the photoanode with a solar simulator. Figure 5.18 depicts the corresponding photocurrent density-voltage (J-V) curves of TiO_2 photoanode in dark and under simulated AM 1.5 illumination (100 mW cm^{-2}) solar simulator. The device represents an overall power conversion efficiency ($\eta_{CONVERSION}$) of 8.1 x 10^{-5} % with a short-circuit current density (J_{sc}) of 0.43 µA cm^{-2}, open circuit voltage (V_{oc}) of 0.73 V, and fill factor (FF) of 26%.

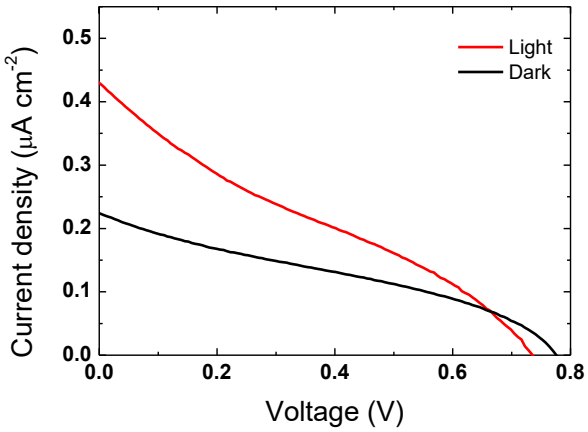

Figure 5.18. The J-V curves of the TiO_2 photoanode measured under light and dark conditions with simulated solar illumination (100 mW/cm^2).

2.5) ELECTROCHEMICAL PERFORMANCE OF PHOTO-SUPERCAPACITOR

The electrochemical performance of the supercapacitor integrated in the photo-capacitor is evaluated through Cyclic voltammetries (CV) curves, Galvanostatic Charge-Discharge (GCD) curves and electrochemical spectroscopy impedance (EIS) measurements.

Figure 5.19.(a) shows the cyclic voltammetries carried out at different scan rates from 25 to 200 mV s^{-1}, obtaining higher area of the curves at higher scan rates, as expected. As shown in Figure 5.19 (b) the triangular shape of galvanostatic charge-discharge curves at 0.17 µA cm^{-2} density indicates the good reversibility of the charging-discharging process. With the aim of testing the specific energy and specific capacitance stability of the photocapacitor, cyclic voltammetry was carried out in darkness at a scan rate of 100 mV s^{-1} during 1200 cycles (Fig. 5.19 (c)). The resulting values are plotted in Fig. 5.19 (d), being 6 cm^2 the photocapacitor area. Specific capacitances from 2.78 µF cm^{-2} to 2.98 µF cm^{-2} were achieved under dark conditions depending on the voltammetry cycle number. On the other hand, specific energies from 0.50 µJ cm^{-2} to 0.54 µJ cm^{-2} were obtained. Both values decreased with the cycle number, but this decrease was not much relevant taking into account the number of cycles that were carried out (1200).

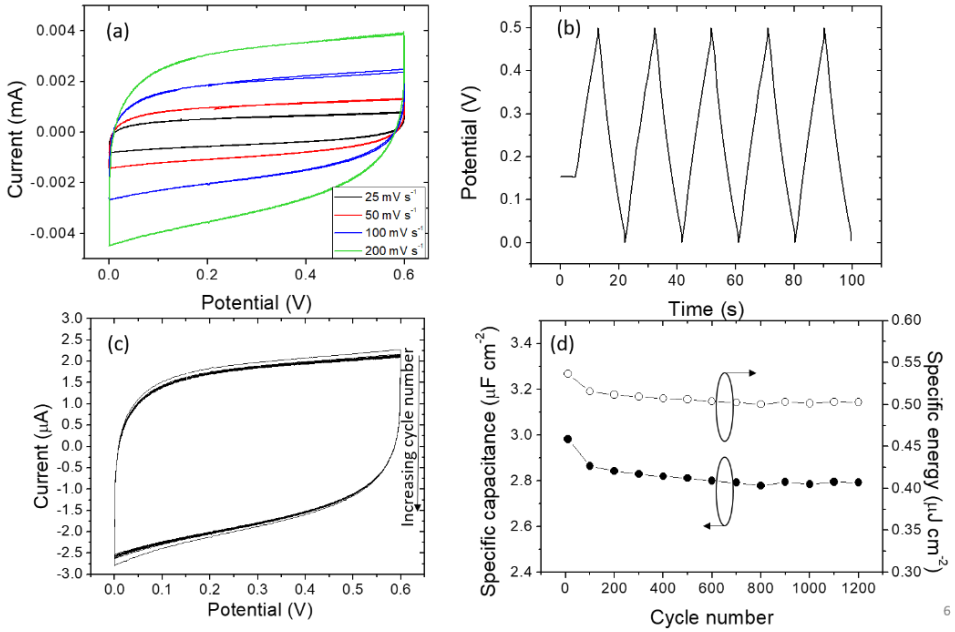

Figure 5.19. (a) Cyclic voltammetries curves at different scan rates in darkness. **(b)** Galvanostatic charge discharge at a current of +/- 0.17 µA cm^{-2}**. (c)** Cyclic voltammograms measured at 100 mV s^{-1} during 1200 cycles. (d) Specific energy (o) and specific capacitance (•) obtained by the CV curves for the photocapacitor.

Further insight into the photocapacitor device characteristics have been conducted by electrochemical impedance spectroscopy (EIS) measurements, which have been performed at four different applied bias potentials E= 0.2 V, 0.3 V, 0.4 V and 0.5 V under dark conditions. Fig. 5.20(a) and Fig. 5.20(b) show typical Nyquist and Bode plots for the photocapacitor device under study at an applied bias potential E=0.2 V.

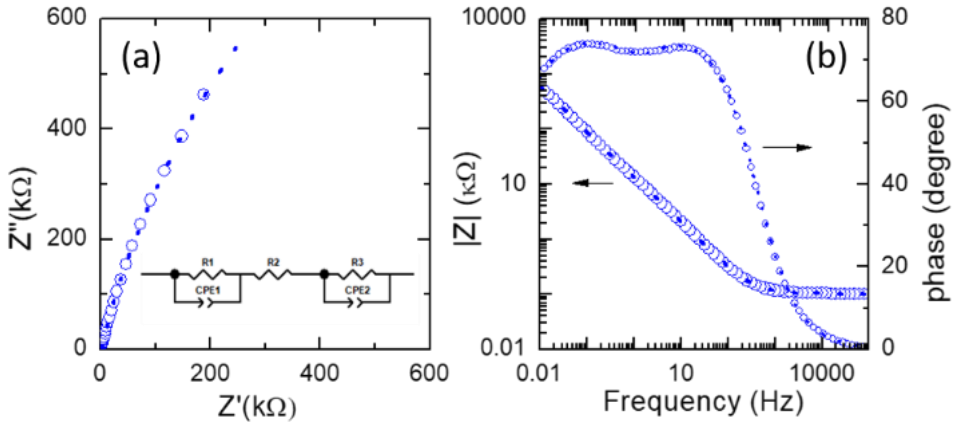

Figure 5.20. **(a)** Nyquist and **(b)** Bode plots recorded for the photocapacitor device under study at an applied bias potential of 0.2 V, under dark conditions. The symbols (open circle shapes) stand for experimental data; the dotted lines are fitting with electrical circuit model depicted in the inset of (a). Inset shows the equivalent electronic circuit model used to fit the experimental EIS data.

These EIS spectra can be simulated by the modeled equivalent circuit as illustrated in the inset of Fig. 5.20(a). In fact, the total cell impedance can be accurately modeled as the serial combination of three circuit components: (i) two parallel combinations, where one of the parallel branches in each of them is a resistance (R1 or R3), while the other one is constituted by a constant phase shift element (CPE1 or CPE2); and (ii) a serial resistance R2, denoting the electrolyte solution resistance. The fits are indicated by solid lines in the plots, and showed good agreement with the data, confirming the suitability of the equivalent circuit model used. In this way, the values of the resistive elements and the CPE parameters (Q constant phase element with power α, see note of Table 5.3), have been extracted. The obtained values for R2 for

the four different applied bias potentials are presented in Table 5.3. In the basis of both the Nyquist and Bode plots it can be inferred a significant capacitive behavior of the device, where each interface exhibited a time constant at ca. 10 Hz and 0.1 Hz, respectively. The first of them characterized by the first part of the equivalent circuit (R1‖CPE1, see inset of Fig. 5.20(a)), the obtained values are depicted in Table 5.3. As the alpha mean value is near 1, this indicates that this CPE can be approached to a capacitance of a rough surface, which is confirmed by AFM characterization, where the $LiFeO_2$ and TiO_2 electrodes exhibited roughness values of 14.3 nm and 31.3 nm, respectively (see Fig. 5.16). The second interface is also characterized by a similar equivalent circuit (R3‖CPE2, see inset of Fig. 5.20(a)), with alpha mean values also close to 1, again this CPE2 can be associated to a capacitance. However, and in spite of the symmetry of the circuit, the values of the resistances R1 and R3 (even though low), differ by three orders of magnitude, indicating low charge transfer rate processes in both interfaces. Moreover, by comparing the Bode spectra for the four different applied bias potentials, it can be concluded that the capacity values remain constant irrespective of the applied bias potential.

Table 5.3. Equivalent circuit element values obtained through a complex non-linear least- squares fitting program of the EIS spectra.[a]

	Applied bias potential (V)			
	0.2	**0.3**	**0.4**	**0.5**
R1 (MΩ)	3	3.8	3.6	3.8
Q1[b] (S $s^{\alpha 1}$)	$1.66 \cdot 10^{-5}$	$1.58 \cdot 10^{-5}$	$1.54 \cdot 10^{-5}$	$1.49 \cdot 10^{-5}$
α1	0.854	0.857	0.858	0.858
R2 (Ω)	102.2	103.5	102.6	103.5
R3 (kΩ)	1.8	2.5	3.0	3.4
Q2[b] (S $s^{\alpha 2}$)	$6.16 \cdot 10^{-5}$	$5.46 \cdot 10^{-5}$	$4.91 \cdot 10^{-5}$	$4.32 \cdot 10^{-5}$
α2	0.929	0.898	0.888	0.882

[a]See inset of Fig. 5.9(a) for the involved electrical equivalent circuit

[b]The impedance of a CPE is defined as $Z_{CPE}=1/Q(j\omega)^{\alpha}$ where α ($0<\alpha<1$) is an empirical constant with no real physical meaning.

2.6) CHARACTERIZATION OF THE INTEGRATED PHOTO-SUPERCAPACITOR

As explained before, during photo-charge process, the TiO_2 is photo-excited resulting in partial positive charge in TiO_2-ion gel interface. Electrons collected are transferred by external circuit from TiO_2 through ITO to the $LiFeO_2$ counter-electrode. In Fig. 5.21(a), the photocapacitor is illuminated under AM1.5G simulated sunlight (100 mW cm^{-2}) from 0 V during 10 min, reaching ca. 0.5 V, and then a galvanostatic discharge was carried out at 0.17 µA cm^{-2} in dark (grey shadow). The inset of Fig. 5.21 (a) shows the galvanostatic discharge at different current densities from 1.7 to 17 µA cm^{-2} in dark. As expected, the discharge time decreases with the current density applied, achieving 100 s for the lowest value of current density. This discharge time could be comparable to other photocapacitors to which the discharge current was higher[178,179]. Some cycles of photocharge and galvanostatic discharge (in dark) carried out at 0.17 µA cm^{-2} are presented in Fig. 5.21(b), showing the stability of the photocapacitor through the cycling process.

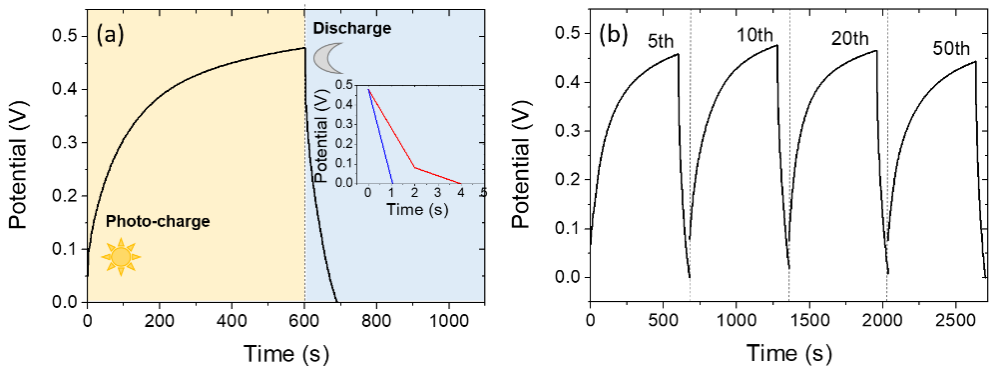

Figure 5.21. (a) Photo-charge under AM1.5G simulated sunlight (100 mW cm^{-2}) illumination and galvanostatic discharge at 0.17 µA cm^{-2} in dark conditions (inset shows the galvanostatic discharge at 1.7 µA cm^{-2} (red line) and 17 µA cm^{-2} (blue line) current densities). **(b)** Some cycles of photocharge/galvanostatic discharge at 0.17 µA cm^{-2}. Cycles numbers are indicated.

In order to study the transparency properties of the photocapacitor, optical transmittance measurements have been done for the separated components (Fig. 5.17) and the whole device before and after cycling (Fig. 5.22). Fig. 5.22 shows the visible-near IR region optical transmittance of the whole device, with the ion gel as electrolyte, exhibiting an optical transmittance of about 57% and 54% at λ= 555 nm (optical transmittance evaluated at this wavelength because the photopic eye sensitivity function has maximum sensitivity in the green spectral range at 555 nm) before and after cycling. So, a transparent photocapacitor has been obtained, considering it retains a high transmittance after the cycling. The inset of Fig. 5.22 shows a digital photography of the complete device after cycling, showing its level of transparency, letting be seen the logo of Universidad de Málaga underneath it. In literature, there are some works reporting the preparation and characterization of photocapacitor devices, but not all of them are optically transparent to the visible spectrum[165,178–180]. In the better case, Zhou *et al.*, informed the assemblage of a photocapacitor exhibiting at least a 70% of transmittance, however it darkness during the charging process[181]; so it could be said that this is the first work reporting a transparent photocapacitor device. However, a modest overall efficiency under 1% has been obtained so there is more work to do to improve this efficiency without declining the transparency of the photocapacitor.

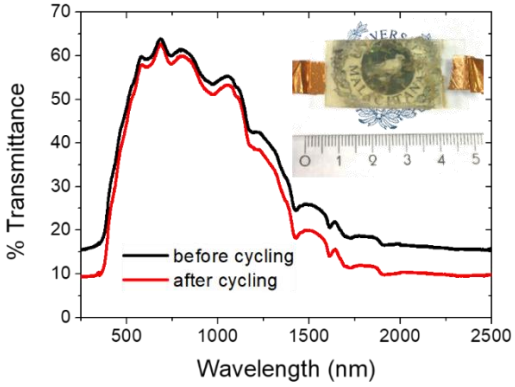

Figure 5.22. Optical transmittance spectrum of the photocapacitor with the ion gel as electrolyte, before (dark color) and after (red color) cycling. The inset shows a digital photograph of the transparent device after cycling, letting see the logo of Universidad de Málaga underneath it.

Finally, it is exposed a comparative Table 5.4. to show all the characteristics of the two types of photocapacitors studied in this Thesis.

Table 5.4. Comparative table of performance characteristics of three photocapacitors studied in this Thesis.

Photocapacitor	Maximum Voltage (V)	Conversion Efficiency (%)	Overall efficiency (%)	Storage efficiency (%)
1-TiO_2/Ion gel/$LiFeO_2$	0.48	8.1×10^{-5}	6.67×10^{-6}	8.17
2-FTO/QDSSC/Ionic Liquid/PEDOT	0.33	1.21×10^{-2}	8.25×10^{-4}	6.83
3-GIZO/QDSSC/Ionic Liquid/PEDOT	0.35	1.44×10^{-3}	1.13×10^{-4}	7.83

D. CONCLUSIONS

Three photosupercapacitors of two-electrodes planar structure have been successfully designed, developed and characterized. In this final chapter the best results of overall efficiency and storage efficiency for each type of device are presented. The TiO_2-based photosupercapacitor is a new concept of a transparent device that generates and stores electrical energy, since it has not composed of nanostructures sensitized with organic or inorganic semiconductor materials. The study of this device has recently been published in a scientific journal with a high impact index[169].

There exists an improvement in conversion and overall efficiency of QDSSC-based photosupercapacitor in comparison with the TiO_2-based. This is due to the addition of QDs supported in ZnO nanowires that produce higher photocurrents. As for the PSC based on the GIZO/QDSSC, slightly lower efficiencies have been found with regard to the FTO/QDSSC, due to the larger diameter of the nanowires, which causes a smaller surface area, a lower number of QDs deposited and therefore a smaller photocurrent. From the comparison of the three devices, it has been found the highest value of overall efficiency for the PSC based on the photoanode FTO/QDSSC with the ZnO seed layer being its value of 8.25×10^{-4} %.

VI

SUMMARY AND FINAL CONCLUSIONS

SUMMARY AND FINAL CONCLUSIONS

- Conductive and transparent GIZO thin films were successfully grown on glass substrates by magnetron sputtering. An experimental design was carried out to evaluate the influence of growth parameters on structural, morphological, optical, electrical and electrochemical properties of GIZO films, for their application as transparent conductive oxide in photoelectrodes. It has been obtained GIZO films with high conductivity, mobility, carrier density and transparency.

- New Figures of Merit (FOMs) were proposed for visible and solar region indicating the best balance between conductivity and transparency of GIZO films for visible and solar applications found for the In/Zn ratio of 0.85-0.90 range.

- Zinc Oxide (ZnO) nanowires were grown onto GIZO thin films without the employment of a seed layer, and onto FTO/glass with a deposited seed layer. It was found the optimal condition of nanowire growth regarding to deposition time, temperature and solution concentration according to the diameter, crystallite size, degree of orientation and length.

- Silver sulphide (Ag_2S) Quantum dots were deposited covering the entire nanowire, increasing the light absorption and the photoresponse of the photoanode. The highest value of efficiency was resulted to be for 0.05 M solution concentration at 9 SILAR cycles growth parameters. It was demonstrated that zinc sulphide (ZnS) thin films passivation layer improved the photoelectrochemical properties of photoanode finding the best condition at 4 coating cycles.

- There have been produced two symmetric supercapacitors based on a conducting polymer PEDOT as electrodes and an ionic liquid polymer as electrolyte. It was found that PEDOT film thickness influence in the final supercapacitor performance, resulting 5 cycles PEDOT electrodeposited the best condition.

- Two types of photosupercapacitors have been designed and developed. Photocapacitor based on TiO_2 and $LiFeO_2$ as electrodes resulted to be a new concept of two electrodes devices with high transparency having a photoconversion efficiency of 8.1×10^{-5}% and an overall efficiency of 6.67×10^{-6} %. The PSC based on FTO/QDSSC as photoanode and PEDOT as counter-electrode demonstrated an improvement of photoconversion efficiency of 0.012% and the overall efficiency was 8.25×10^{-4} %. Furthermore, it has been designed and developed a photosupercapacitor (GIZO/QDSSC) which all its parts are fabricated integrally in our laboratory, showing acceptable results of efficiencies. The effect of the conductive transparent oxide on the growth of the ZnO nanowires and the final performance of the device was analyzed.

APPENDIX A: CHARACTERIZATION TECHNIQUES

A) X-RAY DIFFRACTION (XRD)

X-ray powder diffraction (XRD) is a rapid analytical technique primarily used for phase identification of a crystalline material and can provide information on unit cell dimensions. The analyzed material is finely ground, homogenized, and average bulk composition is determined.

X-ray diffraction is based on constructive interference of monochromatic X-rays and a crystalline sample. These X-rays are generated by a cathode ray tube, filtered to produce monochromatic radiation, collimated to concentrate, and directed toward the sample.

The interaction of the incident rays with the sample produces constructive interference (and a diffracted ray) when conditions satisfy Bragg's Law:

$$n\lambda=2d\sin\theta \qquad (A.1)$$

where n is integer determined by the order given, λ is wavelengths of the inciden wave, d is the distance between layers of atoms.

This law relates the wavelength of electromagnetic radiation to the diffraction angle and the lattice spacing in a crystalline sample.

These diffracted X-rays are then detected, processed and counted. By scanning the sample through a range of 2θ angles, all possible diffraction directions of the lattice should be attained due to the random orientation of the powdered material. Conversion of the diffraction peaks to d-spacings allows identification of the mineral because each mineral has a set of unique d-spacings. Typically, this is achieved by comparison of d-spacings with standard reference patterns.

In the present work, structural characterization of all the samples such as GIZO thin films, nanostructures of photoanode and supercapacitor films. They have been performed by using a PANalytical X'Pert PRO MRD diffractometer and a PANalytical PW3050/65 (θ/2θ) goniometer.

Identification of the composition of the as-deposited GIZO coatings was carried out using X-ray diffraction (XRD) in a Bragg-Brentano configuration on a Philips X´Pert PRO MPD with monochromatic high intensity CuKα radiation (λ¼) The average crystallite size was calculated using the Scherrer equation:

$$D_{hkl} = \frac{0{,}95\,\lambda}{\beta_{hkl}\cos\theta_{hkl}} \quad \text{(A.2)}$$

where D_{hkl} is the crystallite size, λ is the wavelength used (1.54 Å), β_{hkl} is the corrected angular line width at half-maximum intensity in radians, and θ_{hkl} is Bragg's angle. The β parameter was corrected using the following formula:

$$\beta_{hkl} = \sqrt{\beta_{exp}^2 - \beta_{ins}^2} \quad \text{(A.3)}$$

where β_{exp} corresponds to the experimentally determined full width at half of the maximum intensity, FWHM, of the peak. The instrumental width was determined as β_{ins}= 0.07º by using a standard lanthanum hexaboride (LaB_6) powder pattern.

B) HIGH RESOLUTION TRANSMISSION ELECTRON MICROSCOPY (HRTEM)

Transmission electron microscopy (TEM) is a microscopy technique in which a high energy beam of electrons is shone through an ultra-thin sample, and the interactions between the electrons and the atoms can be used to observe features such as the crystal structure and features in the structure like dislocations and grain boundaries.

TEM can be used to study the growth of layers, their composition and defects in semiconductors. Also, high resolution can be employed to analyze the quality, shape, size and density of quantum wells, wires and dots.

TEM operates on the same basic principles as the light microscope but uses electrons instead of light. Because the wavelength of electrons is much smaller than that of light, the optimal resolution attainable for TEM images is many orders of magnitude better than that from a light microscope. Thus,

TEMs can reveal the finest details of internal structure - in some cases as small as individual atoms.

The equipment used in this work was a High-resolution transmission electron microscopy (HRTEM) and selected area electron diffraction (SAED) carried out with a FEI TALOS F200X microscope operated at 200 kV.

This technique has been used to obtain the orientation of the crystalline plane, QDs size, the distance between planes and a chemical elements analysis. This could be possible due to Selected Area Electron Diffraction (SAED) measurements carried out inside TEM.

C) FIELD EMISSION SCANNING ELECTRON MICROSCOPY (FESEM)

FESEM images were taken by an Helios Nanolab 650 Dual Beam from FEI company equipment, with a Tomohawk focused ion beam (FIB). This microscope is equipped with an energy dispersive spectrometer (EDS) and an electron backscatter diffraction detector (EBSD) from Oxford.

Field emission scanning electron microscopy (FESEM) provides topographical and elemental information at magnifications of 10x to 300,000x, with virtually unlimited depth of field. Compared with convention scanning electron microscopy (SEM), field emission SEM (FESEM) produces clearer, less electrostatically distorted images with spatial resolution down to 1 1/2 nanometers – three to six times better.

A field-emission cathode in the electron gun of a scanning electron microscope provides narrower probing beams at low as well as high electron energy, resulting in both improved spatial resolution and minimized sample charging and damage.

In this Thesis, it has been used FESEM to obtain top view and tilted view images of the surface material, to get thickness employing a cross section analyzes and Energy dispersive spectrometer (EDS) was used to find the atomic concentration of elements in the different nanostructures.

D) ATOMIC FORCE MICROSCOPE (AFM)

Atomic Force Microscopy is a very-high-resolution type of scanning probe microscopy, with demonstrated resolution on the order of fractions of a nanometer. In this microscope, a sharp tip is raster-scanned over a surface using a feedback loop to adjust parameters needed to image a surface. Atomic Force Microscope does not need a conducting sample and atomic forces are used to map the tip-sample interaction.

In this work, Topographic AFM examinations of GIZO thin films and electrodes of photocapacitor were performed using a Nanoscope V tapping-mode AFM (Veeco Instruments) employing sharp silicon tips, to obtain the roughness of the surface.

E) RAMAN SPECTROSCOPY

Raman spectroscopy is a spectroscopic technique that provides information about vibrational, rotational and other low-frequency modes that can be used for sample identification and quantitation. The technique involves shining a monochromatic light source (i.e. laser) on a sample and detecting the scattered light.

In Raman spectroscopy applications, intense laser beams are used to create Raman scattered light from a sample under test. The Raman finger print is measured by a spectrometer. Optical filters are critical components in Raman spectroscopy systems to prevent all undesired light from reaching the spectrometer.

In this Thesis, Raman spectroscopy has been used to analyze PEDOT thin film grown onto FTO and onto ZnO nanowires. The equipment used was a Raman JASCO NRS-5100 spectrometer-microscope employing a laser of 532 nm with a power of 2.5 mW and an objective of 100x.

F) ULTRAVIOLET - VISIBLE SPECTROMETRY (UV-VIS-NIR)

UV-Vis refers to absorption spectroscopy or reflectance spectroscopy in the ultraviolet-visible spectral region. This means it uses light in the visible and adjacent (near-UV and near-infrared [NIR]) ranges.

In the present work, it has been employed a spectrophotometer Varian Cary 5000 model with an integrating Spectralon sphere composed of a light source, a monochromator which splits the light into a continuous wavelength spectrum, and the detectors which register the intensity of transmitted or reflected light depending on the measuring mode.

The aim of the measurements was to obtain the transmittance and reflectance of the GIZO thin films and the electrodes of the photo-supercapacitor.

G) VAN der PAUW Method

The van der Pauw Method is a characterization technique used to measure the resistivity, doping type, carrier density and Hall mobility of a sample.

The van der Pauw Method employs a four-point probe placed around the perimeter of the sample, in contrast to the linear four point probe: this allows the van der Pauw method to provide an average resistivity of the sample, whereas a linear array provides the resistivity in the sensing direction.

The van der Pauw technique is applicable for an arbitrary shaped sample as long as the thickness of the sample is known and is uniform, the contact areas are small, and the contacts are all on the perimeter of the sample. In this case van der Pauw showed that:

$$e^{\left(-\frac{\pi \cdot R_{AB,CD} \cdot d}{\rho}\right)} + e^{\left(-\frac{\pi \cdot R_{BC,DA} \cdot d}{\rho}\right)} = 1 \qquad \text{(A.4)}$$

In our work, this properties have been measured in the Microelectronic Institute of Madrid (IMM-CNM-CSIC). The electrical charge carrier density and Hall mobility were measured by Hall Effect measurement using a four-

point van der Pauw method. The measurements were performed from 30K to 300K, at a current of 1 mA and 3000 Gauss of magnetic field. The system is home made, and the measurements use a conmutator Switch/Control Unit 3488A of Hewlett Packard, a current and voltage source of Keithley, electromagnet TCR Power Supply of EM Inc., Temperature controller 805 of Lake Shore Cryotronics and a vacuum system TPH 055 of Balzers Pfeiffer. The software was developed with LabView. It has been used to measure GIZO thin films whose size is 1 cm per square and the ohmic contacts were a thin film of TiAlPtAu.

H) FOUR-POINT-PROBE SHEET RESISTANCE METHOD

A four points device has been used in order to measure sheet resistance (Rsheet) of the GIZO thin films obtained. Sheet resistance is the resistivity of a material divided by its thickness, and represents the lateral resistance through a thin square of conducting/semiconducting material. This measurement uses four probes arrayed in a line, with equal spacing between each probe. A current is passed between the outer two probes, causing a reduction in voltage between the inner two probes. By measuring this change in voltage, the sheet resistance can then be calculated using the following equation:

$$R_S = \frac{\pi}{\ln(2)} \frac{\Delta V}{I} \tag{A.5}$$

where I is the applied current and ΔV is the decrease in voltage between the inner probes. The result of this equation must further be multiplied by a geometric correction factor based upon the shape, size, and thickness of the sample. This accounts for limitations to the possible current pathways through the sample, which affects the values that are measured.

Initially, sheet resistance *Rsq* and electrical resistivity ρ of GIZO films were measured in a Hewlett Packard 16055A chamber, using a Hewlett Packard 4140B as DC source and Keithley 181 as nanovoltmeter. Subsequently, these results were corroborated by using a Four-Point Probe System from Ossila.

I) CYCLIC VOLTAMMETRY

Cyclic voltammetry is one of the most used electrochemical techniques to study reaction mechanisms. This technique provides information about redox behavior of the sample, chemicals reactions where they participate and the determination of thermodynamics parameters.

The process consists on the application of a swept of potentials in a working electrode between two values at a controlled scan rate and the current response is registered at the same time. When one voltage value is reached then the potential swept is inverted as much as the cycle number is programmed. This range of potential is chosen due to the values in which the oxidation or reduction happens. The results appears as a cyclic voltammogram in a E=f(i) plot.

In this Thesis, this technique has been carried out to electropolymerize PEDOT from the monomer EDOT, and to characterize the supercapacitor and the kinetics transfer of GIZO thin films.

J) GALVANOSTATIC CHRONOPOTENCIOMETRY

Galvanostatic chronopotenciometry is an electrochemical technique based on the measure of potential in a system as a function of time, during the application of a constant current intensity.

Specially, galvanostatic charge/discharge is employed to evaluate the stability and capacitance of a supercapacitor along a large number of cycles. Usually, the capacitance of supercapacitor decrease in every cycle according to the increment of internal resistance.

This technique is very useful to evaluate the durability of the device and their commercial advantages with regard to other supercapacitors.

Ideal plot of a supercapacitor shows a perfect triangle shape, with minimal drop voltage on the top and the bottom of the slopes at the shift on every steps.

K) IMPEDANCE SPECTROSCOPY

Electrochemical impedance spectroscopy (EIS) is an electrochemical technique where the sample under investigation is excited by a small amplitude AC signal of potential or current in a wide range of frequencies and the voltage or current is measured.

This technique allows cover several magnitude orders of frequency (from MHz to μHz). It is defined like a characterization method of electrical properties of materials and their contour properties, this information is obtained with the analyze of electrochemical response of the electrodes when they are submitted to an electrical impulse.

Impedance, $\tilde{Z}(\omega)$ is defined like the relation between potential signal applied and the current intensity response of the electrochemical system, shown as:

$$\tilde{Z}(\omega) = \frac{\tilde{E}(t)}{\tilde{I}(t)} \tag{A.6}$$

Impedance can be expressed in vectorial form, dividing real and imaginary components in the complex plane:

$$\tilde{Z}(\omega) = Z' - iZ'' \tag{A.7}$$

where Z´ is the real part and Z´´ the imaginary part of impedance.

The results of impedance are depicted as Nyquist Plot, where (Z´) is in abscissas axis and (Z´´) is in ordinates axis.

Nyquist plot is formed for three areas well differences:

- High frequencies area: Imaginary part of impedance tends to zero (resistive behavior of material).
- Low frequencies area: Imaginary part increases widely (capacitive behavior of electrode).
- Intermediate frequencies area: There is a slope of impedances values respect to abscissas axis.

An ideal electrochemical capacitor is characterized by Nyquist Plot with a vertical line in the low frequencies area and a slope respect abscissas axis of a 45º. However, in the real supercapacitors are usually observed a little slope in the line at low frequencies and a semicircle in the high-intermediate frequencies, probably due to a higher resistance of device and diffusion problems of electrolyte through porous structure of electrode.

The capacity of a supercapacitor can be obtained from results of impedance spectroscopy, according the next equation:

$$C = \frac{-1}{[\omega \cdot Z''(f)]} \tag{A.8}$$

where ω is the angular frequency and Z´´(f) is the impedance value in the imaginary part for a given frequency.

In this Thesis, impedance spectroscopy has been used to determine the dynamic parameters of the supercapacitor and the photosupercapacitor.

APPENDIX B: RESUMEN EN ESPAÑOL

1. CAPÍTULO I: INTRODUCCIÓN

A. CELDAS SOLARES Y DISPOSITIVOS DE ALMACENAMIENTO

En las últimas décadas, la creciente demanda mundial de energía y el hecho de que los combustibles fósiles son limitados ha fomentado el desarrollo y la investigación de las energías renovables en muchos campos, como la energía solar, las pilas de combustible, el almacenamiento de energía o la energía eólica. Sin embargo, en el caso de las células solares, los últimos descubrimientos en celdas solares nanoestructuradas no se han comercializado a gran escala, debido al alto coste de los materiales y al bajo desarrollo de las técnicas industriales de fabricación.

Por otro lado, una buena generación de energía a partir de estos sistemas fotovoltaicos debe combinarse con un adecuado almacenamiento de energía y distribución de la electricidad. De hecho, el almacenamiento de energía es un factor crucial en la integración de las fuentes renovables y desempeña un papel importante en el mantenimiento de un sistema eléctrico moderno y fiable. Este sistema debe evitar las fluctuaciones de potencia, permitir el almacenamiento, mejorar la flexibilidad del sistema eléctrico permitiendo el suministro de energía.

Hay una amplia variedad de sistemas de almacenamiento de energía, incluyendo sistemas mecánicos, eléctricos, térmicos o electroquímicos. Los supercondensadores electroquímicos, las pilas de combustible y las baterías son tres tipos de dispositivos de almacenamiento de energía electroquímica más importantes utilizados en la actualidad. Concretamente para los sistemas fotovoltaicos, los tipos más comunes de dispositivos de almacenamiento electroquímico son las baterías, como la de níquel-cadmio, cloruro de sodio-níquel, plomo-ácido o las de ión-litio. Además, entre los dispositivos de almacenamiento eléctrico se encuentra el supercondensador electroquímico (también conocido como supercondensador), con una alta densidad de potencia y densidad de energía. Existen tres tipos de

supercondensadores, tales como condensadores de doble capa, pseudocondensadores y condensadores híbridos, cuya diferencia es el mecanismo de almacenamiento de carga.

Hoy en día, la mayoría de las células solares vendidas en el mercado están fabricadas de obleas de silicio, conocidas como tecnología de células solares de "primera generación". Debido al límite de Shockley-Queisser para dispositivos de banda única, esta tecnología ha alcanzado eficiencias récord de laboratorio del 26,7% para la tecnología basada en obleas de silicio monocristalino. Dado que existe un límite termodinámico en la conversión de la luz solar en electricidad del 93%, se espera que una nueva célula fotovoltaica (FV) emergente y menos costosa llamada de "tercera generación" supere las eficiencias de las células solares anteriores. En esta Tesis, el electrodo fotoactivo está compuesto por una "Célda Solar Sensibilizada por Puntos Cuánticos" debido a sus muchas ventajas, como se explica en el Capítulo III dedicado al foto-ánodo.

Un elemento común a ambas partes, generación de energía y almacenamiento es el óxido transparente conductor (TCO). Este elemento es esencial y funciona como sustrato siendo fundamental para el éxito del dispositivo final.

La combinación de una célula solar con un supercondensador en un solo dispositivo se conoce como foto-supercondensador, recibiendo cada vez más interés en los últimos años por sus múltiples aplicaciones en futuros dispositivos portátiles. Este dispositivo es capaz de generar y almacenar electricidad al mismo tiempo a partir de la energía solar.

B. MOTIVACIÓN

La conversión de la energía solar y el almacenamiento de la electricidad producida se están convirtiendo en estrategias clave para resolver los problemas de la crisis energética y su uso sostenible. En la actualidad, el marco conceptual y experimental del problema es la necesidad de edificios autosuficientes, lo que lleva a la utilización de la luz solar incidente en las

ventanas convirtiéndola en electricidad y la necesidad de almacenar esa energía para ser utilizada posteriormente. La célula solar transparente de capa fina cumple la primera misión y las baterías o el dispositivo de almacenamiento cumplen la segunda misión. Una parte fundamental de este problema es la posibilidad de combinar la fotogeneración con el almacenamiento de energía de una manera eficiente.

Existen algunos diseños desarrollados para combinar ambas funciones, la conversión de energía solar y el almacenamiento de energía eléctrica en un único dispositivo transparente para ventanas inteligentes.

Si se tiene en cuenta que el consumo energético de los edificios residenciales y públicos es de alrededor del 40% del total, y generalmente 2/3 de este consumo se debe a las necesidades de acondicionamiento térmico e iluminación de los edificios; es evidente la necesidad de reducir el consumo de energía en los edificios y, si es posible, lograr la autosuficiencia en los mismos. El ahorro de energía puede abordarse mediante el uso de dispositivos con un menor consumo de energía, pero el aumento de la población compensa los efectos de reducción por esta vía. El objetivo ideal es la reducción del consumo de energía a través de la autosuficiencia energética. La disminución del consumo de energía puede y debe lograrse a través de diferentes líneas de acción. El uso de la radiación solar incidente en las ventanas de los edificios mediante su conversión en energía eléctrica y la regulación de la energía que fluye a través de las ventanas son dos maneras de ahorrar energía.

Para ser autosuficiente, un edificio tiene que generar su propia energía, lo que requiere sistemas que puedan aprovechar la radiación solar incidente. Si los dispositivos se van a integrar en las superficies acristaladas, deben ser transparentes o semitransparentes. Idealmente, deben ser transparentes en la región visible y el color percibido neutro, a menos que se desee un color debido a la estética del edificio.

Lograr dispositivos estables comienza con una correcta selección y optimización de los elementos que los componen. Así, todos los dispositivos activos mencionados, fotogeneradores, acumuladores y reguladores de energía, necesitan conductores transparentes para sus contactos eléctricos y para los electrodos que forman parte de cualquiera de los dispositivos. Por lo tanto, los materiales clave en el desarrollo de este tipo de dispositivos son

los conductores transparentes y los electrolitos poliméricos transparentes. Los óxidos conductores transparentes (TCO) comprenden una clase de materiales que pueden considerarse como materiales que conjugan propiedades de interés tecnológico como la conductividad eléctrica y la transparencia.
Un dispositivo alternativo a las células y baterías solares es el fotocondensador, ya que está construido de ambos en un solo dispositivo. Un fotocondensador es un dispositivo capaz de generar energía a partir de la radiación solar y almacenarla posteriormente durante un tiempo suficiente. Las ventajas del fotocondensador son la posibilidad de ser integrados en ventanas de edificios, la rapidez de carga (foto-respuesta), la estabilidad y el aumento de la ciclabilidad.

C. OBJETIVOS

El objetivo general de la presente tesis es diseñar, desarrollar y caracterizar un fotocondensador transparente capaz de captar la energía solar, transformarla en electricidad y almacenarla de forma eficiente.

Para lograr este objetivo, se propusieron las siguientes estrategias:

1) Identificar y desarrollar un óxido conductor transparente (TCO) con propiedades optoelectrónicas adecuadas para formar parte del fotoánodo del dispositivo fotocondensador final.
2) Preparar nuevas arquitecturas de materiales semiconductores nanoestructurados en un amplio rango de morfologías, buscando la combinación sinérgica de propiedades como electrodo de fotoánodo.
3) Sintetizar polímeros conductores por electrodeposición y obtener electrolitos conductores iónicos transparentes basados en líquidos iónicos comerciales para construir un supercondensador.
4) Ensamblar y caracterizar el dispositivo fotocondensador a partir de los elementos anteriores.

D. ESQUEMA DE LA TESIS

Esta Tesis Doctoral consta de cinco capítulos; esta primera introducción explica en términos generales la situación energética de la sociedad y la necesidad de conseguir infraestructuras más eficientes energéticamente, también se da una visión global de los distintos tipos de sistemas de almacenamiento y captación de energía. La descripción de los objetivos y estrategias a seguir también son parte de este primer capítulo.

En el Capítulo II se presenta un óxido conductor transparente (TCO) emergente y de fabricación propia llamado Óxido de Zinc Indio Galio. Esta película delgada ha sido desarrollada y caracterizada para su uso como electrodo transparente.

El tercer capítulo trata de una célula solar de tercera generación (3G), centrándose en la fabricación y caracterización de células solares sensibilizadas con puntos cuánticos y nanohilos de óxido de zinc. Además, se presentan los resultados de la caracterización fotoelectroquímica.

El capítulo IV está dedicado al desarrollo de la parte de almacenamiento de todo el dispositivo, concretamente el supercondensador. Los principales resultados, materiales y metodología se discuten en este capítulo.

El fotocondensador final se presenta en el quinto capítulo, después de haber combinado los dispositivos individuales anteriores como el fotoánodo y el supercondensador.

Finalmente, una breve descripción de las técnicas de caracterización utilizadas a lo largo del proyecto se puede encontrar en el Apéndice A, junto con el resumen obligatorio en español en el Apéndice B.

2. CAPÍTULO II: ÓXIDOS TRANSPARENTES CONDUCTORES: GIZO

A. INTRODUCCIÓN

Los óxidos conductores transparentes (TCOs) son una parte muy importante en muchos dispositivos optoelectrónicos como las células solares y también en nuevos dispositivos relevantes para la generación y almacenamiento de energía como los fotocondensadores, que son dispositivos novedosos y prometedores que permitirán producir energía a partir de la luz solar y almacenarla en el mismo dispositivo. La obtención de células solares y fotocondensadores eficientes requiere un cuidadoso diseño de todas sus partes y, sin duda, los electrodos transparentes juegan un papel importante como parte activa en el desarrollo de estos dispositivos. El óxido de Zinc (ZnO) dopado con aluminio (Al) o galio (Ga), y más recientemente con indio (In), son materiales que pueden cumplir los requisitos de los dispositivos optoelectrónicos. Una oportunidad para obtener mejores materiales de TCO es utilizar compuestos de ZnO dopados con Ga e In, es decir, óxido de indio-galio-zinc (GIZO). La densidad del portador de carga y su movilidad determinan la conductividad y para obtener mejoras significativas es necesario combinar ambos adecuadamente.

En general, no existen en la bibliografía investigaciones basadas en una metodología con base estadística para llevar a cabo los experimentos de laboratorio para el crecimiento de capas delgadas. En esta Tesis, se ha elegido una planificación de los experimentos mediante un diseño experimental para el crecimiento de las películas delgadas de GIZO, para lograr películas de GIZO con conductividad eléctrica y transparencia óptimas. Se ha empleado el diseño de experimentos de superficie de respuesta Box-Behnken, para evaluar los efectos de tres factores: potencia aplicada al *target* de In_2O_3, temperatura del sustrato y tiempo de *sputtering*. El objetivo ha sido establecer el efecto de dichos factores sobre las propiedades morfológicas, estructurales, eléctricas y ópticas de las películas de GIZO, tales como la densidad del portador de carga, la movilidad, la cristalinidad, transparencia, conductividad, etc. El objetivo final es obtener películas de GIZO con un

buen compromiso entre transparencia y conductividad para ser utilizadas como electrodos transparentes. Para ello, se han definido por primera vez nuevas figuras de mérito (FOM) como una modificación de otras FOMs, propuestas por otros autores. Las FOMs se han aplicado comparativamente a las películas de GIZO obtenidas.

B. MATERIALES Y MÉTODOS

Para el crecimiento de las películas delgadas de GIZO, se eligió un proceso de evaporación mediante magnetrón por radiofrecuencia (RF). La principal ventaja de este método es la posibilidad de controlar el crecimiento de películas puras y densas variando parámetros como la temperatura, el tiempo, la potencia de RF de los *targets*, el flujo de gases en la cámara principal o la presión de evaporación. La técnica de *sputtering* es una técnica utilizada para el crecimiento de películas delgadas de un material sobre un sustrato.

En esta Tesis, los electrodos de película delgada de GIZO han sido crecidos sobre sustratos de vidrio de 1 y 2 cm^2 después de la correcta limpieza en baño de ultrasonido con isopropanol (10 min), agua desionizada (10 min), acetona (10 min) y, finalmente, secados bajo flujo de nitrógeno. Se emplearon dos tipos de *targets* cerámicos: Ga_2O_3 (2%):ZnO (98%) y In_2O_3 (99,99%).

Como se ha mencionado, se ha utilizado un diseño factorial de superficie de respuesta Box-Behnken para organizar la experimentación y determinar los efectos de tres parámetros de *sputtering*, tal como la potencia del *target* (P) de In_2O_3, el tiempo de evaporación (t) y la temperatura del sustrato (T), sobre las propiedades de las capas de GIZO y las interacciones potenciales entre estos tres factores. Los tres niveles utilizados para los factores están se recogen en la Tabla 2.1 y son, potencia de In_2O_3 de 80 W, 110 W y 140 W, y las temperaturas del sustrato son 150, 250 y 350 ^oC. Las películas fueron depositadas durante 20, 40 y 60 min. La presión de trabajo en la cámara de vacío se mantuvo constante en 1.4 x 10^{-2} mbar, y se utilizó un flujo de gas argón (Ar) de alta pureza (5N), regulado por un controlador de flujo másico a 12 sccm.

C. RESULTADOS Y DISCUSIÓN

Los valores más altos de conductividad eléctrica se obtuvieron para películas de GIZO con relación atómica In/Zn ≥ 1, siendo el mejor valor alcanzado de conductividad 1.75 x 10^3 Ω^{-1} cm^{-1}, y mejorando la conductividad de ZnO puro, Óxido de Galio y Zinc (GZO) y otras películas de GIZO depositadas por el método de *sputtering*. El resultado más alto obtenido para la movilidad electrónica fue de 45 (cm^2 V^{-1} s^{-1}). A partir del diseño se deduce que el espesor aumenta linealmente con el tiempo de evaporación y la potencia aplicada al *target* de In_2O_3, y la relación In/Zn aumenta también con la potencia aplicada. Los parámetros cristalinos de la estructura hexagonal cambian con la relación In/Zn y la densidad del portador de carga está relacionada con esos cambios y, por lo tanto, con la estequiometría de GIZO. Las películas de GIZO crecieron orientadas en el eje "c". El pequeño porcentaje de Ga produce amorfización de la estructura cristalina, lo que lleva a un aumento de la movilidad y conductividad de los portadores de carga.

El aumento de la absorbancia solar, debido al aumento de la absorbancia espectral en la región infrarrojo cercano (NIR), está relacionado con la frecuencia del plasma y, por tanto, con la densidad de portadores de carga. Se han propuesto por primera vez nuevas figuras de mérito (FOMs) que utilizan valores integrados, ponderados por funciones para la radiación visible y solar, en lugar de valores individuales de la radiación transmitida o del coeficiente de absorción. Las figuras de mérito definidas indican que el mejor balance entre conductividad y transparencia para aplicaciones visibles y solares de las películas GIZO (2% Ga/Zn) como TCOs se encuentran en el rango In/Zn de 0.85-0.90.

3. CAPÍTULO III: FOTOÁNODO

A. INTRODUCCIÓN

Las Células Solares Sensibilizadas (SSCs) han irrumpido en el campo de la energía solar en las últimas dos décadas como dispositivos fotovoltaicos de "tercera generación" muy prometedores, entre los que se encuentran las Células Solares Sensibilizadas con Colorantes (DSSCs) y las Células Solares Sensibilizadas con Puntos Cuánticos (QDSSCs). En los DSSCs, un colorante molecular orgánico y/o metálico es el material absorbente de la luz, mientras que los QDSSCs utilizan un punto cuántico semiconductor inorgánico (*QD*) para actuar como material de recolección de luz. Los QDSSCs aparecen como un nuevo concepto de SSCs, debido a sus ventajas como el bajo coste, la posibilidad de realizar la absorción de luz en regiones de amplio espectro solar, la facilidad de fabricación y la generación de múltiples excitones, lo que conlleva a una eficiencia teórica de hasta el 44%. En esta Tesis, se ha desarrollado una celda solar basada en puntos cuánticos de Ag_2S para la generación de electricidad a partir de energía solar en el dispositivo final fotocondensador.

Los puntos cuánticos se definen como un grupo de semiconductores con un ancho de banda estrecha que es una nanopartícula de dimensión cuasi-cero caracterizada por su efecto único de confinamiento cuántico. Este fenómeno ocurre cuando el diámetro del *QD* es menor que el radio de Bohr. Estas características hacen que los *QDs* posean anchos de banda modificables, generación de excitones múltiples y coeficientes de absorción más altos que las moléculas de colorante.

El principio de funcionamiento de los QDSSCs es inicialmente producir una irradiación ligera para producir una foto-excitación de los nanocristales semiconductores que lleve a una separación del excitón (pares electrón-hueco) de la Banda de Valencia (*VB*) a la Banda de Conducción (*CB*). Consecuentemente, los electrones son inyectados en el semiconductor de banda ancha, y el hueco es conducido al material transportador del hueco, para finalmente ser recogido en sus respectivos contactos.

B. MATERIALES Y MÉTODOS

Como conductor transparente se empleó GIZO, obtenido según se describe en el capítulo II, y óxido de estaño dopado con flúor (FTO) comercial con una resistencia de capa de 10 Ω/□, ambos crecidos sobre sustrato de vidrio. El tamaño de las muestras fue de 2 cm x 1 cm.

La técnica de Spin Coating se empleó para depositar una fina capa semilla de ZnO sobre sustratos de FTO para el posterior crecimiento de nanohilos de ZnO. Para el crecimiento de nanohilos de ZnO por síntesis electroquímica sobre FTO/ZnO con capa semilla, la experimentación se planificó según un diseño superficie respuesta Box-Behnken para estudiar el efecto de los parámetros de síntesis electroquímica como el tiempo de crecimiento (30, 60, 90 min), la temperatura de la solución (60, 70, 80 ^{o}C) y la concentración de la solución (0,1, 1, 1,9 mM), sobre las propiedades de los nanohilos obtenidos de ZnO. Además, los nanohilos de ZnO se crecieron sobre FTO/vidrio sin capa semilla utilizando la condición óptima encontrada para la electrodeposición para su comparación. Por otro lado, los nanohilos de ZnO se electrodepositaron sobre GIZO/vidrio sin capa semilla para obtener un foto-ánodo para el fotocondensador final.

Se ha utilizado la técnica de sucesivas inmersiones y reacciones de adsorción (SILAR) para el crecimiento de los puntos cuánticos de sulfuro de plata (Ag_2S) sobre los nanohilos de ZnO. Esta técnica consiste en la inmersión del sustrato en una solución catiónica donde son adsorbidos los iones sobre la superficie, seguidamente se sumerge en agua desionizada o solución orgánica para inmovilizar los iones adsorbidos. Posteriormente, al sumergir el sustrato sobre una solución aniónica tiene lugar la reacción entre los cationes adsorbidos y los aniones formando una primera capa delgada sólida del compuesto requerido. Se usaron distintas condiciones de crecimiento tal como, concentración de precursor y número de ciclos de SILAR para estudiar su influencia en la fotorespuesta del dispositivo. Posteriormente se realizó un tratamiento térmico en horno para mejorar la cristalinidad de las nanoestructuras. El siguiente paso ha sido el recubrimiento de los puntos cuánticos con una capa pasivante de sulfuro de zinc (ZnS) para evitar la recombinación de los pares electrón-hueco generados. Esta capa también se

ha depositado por el método SILAR y se ha estudiado la influencia del número de capas sobre las propiedades fotoelectroquímicas. Finalmente, el fotoánodo se finaliza con la síntesis de un material conductor de huecos, en nuestro caso, poli (3,4-etilendioxitiofeno) (PEDOT) sobre las nanoestructuras crecidas anteriormente.

C. RESULTADOS Y DISCUSIÓN

Se ha sintetizado y optimizado las condiciones de crecimiento del fotoánodo. Inicialmente se ha depositado una doble capa semilla de ZnO sobre el sustrato de FTO para mejorar los sitios de nucleación para los nanohilos. Se han crecido satisfactoriamente nanohilos de ZnO sobre sustratos de FTO y de GIZO comprobándose que cuando se emplea esta capa conductor transparente. Se han optimizado los parámetros de electrodeposición de los nanohilos de ZnO, encontrando las condiciones óptimas de temperatura en 70ºC, 1 hora de crecimiento y concentración de la solución de 1 mM, según el grado de orientación en el plano (0002), diámetro, longitud y densidad de los nanohilos. En un segundo paso, los parámetros del método SILAR para el crecimiento de puntos cuánticos de Ag_2S (concentración de la solución y número de ciclos) y las capas de ZnS se optimizaron con éxito en función de las propiedades fotoelectroquímicas del fotoánodo. Las mejores condiciones de crecimiento de los puntos cuánticos resultaron para una concentración de precursor de 0.05M durante 9 ciclos de SILAR. Para la capa pasivante de ZnS, el crecimiento durante 4 ciclos de SILAR resultó ser el que mayor fotorespuesta alcanzaba. Se ha electrodepositado satisfactoriamente la película del polímero PEDOT sobre las nanoestructuras anteriormente explicadas.

4. CAPÍTULO IV: SUPERCONDENSADOR SIMÉTRICO

A. INTRODUCCIÓN

El desarrollo y la implantación a gran escala de las energías renovables están estrechamente relacionados con la posibilidad de disponer de electricidad en cualquier momento del día, sin depender de las fluctuaciones debidas a los cambios meteorológicos, como la llegada de la noche o las variaciones de la velocidad del viento.

Los supercondensadores electroquímicos, las pilas de combustible y las baterías son tres ejemplos de los dispositivos de almacenamiento de energía electroquímica más importantes utilizados en la actualidad. A este respecto, el supercondensador electroquímico o también conocido como supercondensador ha despertado un gran interés en este campo de almacenamiento debido a sus notables ventajas, como su larga vida útil (>100 000 ciclos), su sencillo principio de funcionamiento, su alta densidad de potencia y su rápida velocidad de carga y descarga, si se compara con las baterías y las pilas de combustible. Este dispositivo está compuesto por dos electrodos (ánodo y cátodo) y un electrolito intermedio. Las diferentes características que debe cumplir un buen electrolito son: una amplia ventana de potencial; alto número de portadores, baja inflamabilidad, respetuoso con el medio ambiente; alta estabilidad química y electroquímica; alta conductividad iónica; amplio rango de temperaturas de funcionamiento y bajo coste.

En esta Tesis se ha elegido como cátodo un supercondensador simétrico como dispositivo de almacenamiento compuesto por un conductor polimérico (PEDOT) como electrodo y un líquido iónico como electrolito.

B. MATERIALES Y MÉTODOS

En un primer paso, el polímero PEDOT se sintetizó mediante la electropolimerización del monómero etilendioxitiofeno (EDOT) sobre sustratos comerciales de FTO/vidrio después de la limpieza ultrasónica adecuada. Se utilizó una celda electroquímica de configuración de tres electrodos, empleando una lámina de Pt como contraelectrodo, un electrodo de calomelano saturado (SCE) como electrodo de referencia y un sustrato de vidrio recubierto de FTO como electrodo de trabajo. La película delgada de PEDOT fue electrodepositada por voltamperometría cíclica de -0.8 a 2 V a 75 mV/s utilizando un potenciostato Biologic VSP, durante 5 ciclos y 10 ciclos para obtener dos supercondensadores diferentes y evaluarlos de forma comparativa.

La síntesis del electrolito basado en líquido iónico comercial y polivinilpirrolidona (PVP) se realizó mezclando proporciones definidas del polímero (PVP), metanol (CH_3OH) y líquido iónico comercial (1-hexyl-3-methylimidazolium [HEMIm][BF_4]. Una vez preparado el electrolito, se depositó sobre sustratos PEDOT/FTO por el método de inmersión (*dip coating*). Entre cada uno de los dos ciclos de inmersión, las muestras se secaron durante 10 minutos utilizando una lámpara halógena.

Finalmente, la muestra de vidrio/FTO/PEDOT/Líquido iónico-PVP recién preparada se colocó sobre el electrodo de vidrio/FTO/PEDOT por simple presión manual, empleando un separador de película de polímero entre ellos (Meltonix, 25 µm, de Solaronix). Todo el dispositivo fue calentado en una placa caliente durante 5 minutos para lograr el sellado del separador con los dos electrodos.

C. RESULTADOS Y DISCUSIÓN

Se ha sintetizado con éxito un supercondensador simétrico que utiliza PEDOT electrodepositado como electrodos y [HEMIm][BF_4]/PVP polímero líquido iónico como electrolito. Se consiguió una buena conductividad iónica de $\sigma = 1.5 \times 10^{-3}$ S cm^{-1} para el electrolito de polímero líquido iónico. El electrolito sintetizado es transparente alcanzando un máximo de transmitancia del 90 % en el intervalo del espectro visible. Se ha obtenido un valor bajo de energía de activación para el electrolito de Ea=0.28 eV, siendo un valor deseable para su aplicación en supercondensadores. El almacenamiento de energía en este dispositivo se logra a través de los mecanismos de separación de cargas y reacciones redox reversibles en el electrodo de PEDOT. Se ha estudiado la influencia del espesor de la película PEDOT en la capacitancia específica global del supercondensador, encontrándose que el supercondensador crecido durante 5 ciclos de PEDOT mostraron mejores propiedades electroquímicas que el supercondensador de 10 ciclos de PEDOT. La capacidad gravimétrica específica más alta fue de 21.04 mF g^{-1} basada en los datos de voltametría cíclica a bajas velocidades de barrido. La densidad de energía y la densidad de potencia resultaron ser 0.046 mWh/g y 59.28 mW/g, respectivamente.

5. CAPÍTULO V: FOTOCONDENSADOR

A. INTRODUCCIÓN

Como se ha comentado en los capítulos anteriores, la fluctuación de la potencia de salida de las células solares debido a la luz solar intermitente y a la necesidad de disponer de dispositivos de almacenamiento de energía adecuados hace necesaria la obtención de un nuevo y prometedor dispositivo. El fotocondensador es un innovador dispositivo de energía que combina la función de conversión fotoeléctrica de una célula solar con la capacidad de almacenamiento de energía de un supercondensador. La posibilidad de generar y almacenar energía simultáneamente en un solo dispositivo ha atraído la atención de la investigación intensiva en los últimos años. Desde que Miyasaka *et al*.[16] fabricaron por primera vez un fotocondensador en 2004, combinando un DSSC y un supercondensador, este campo de investigación se ha desarrollado rápidamente en los últimos 14 años.

Dependiendo de su estructura, el fotocondensador se puede clasificar de dos formas. Por un lado, dependiendo del número de electrodos, existen configuraciones de dos o tres electrodos y por otro lado existen dispositivos con estructura planar y en forma de fibras cilíndricas o en espiral.

En general, el principio de funcionamiento de un fotocondensador con estructura planar de dos electrodos es el siguiente: cuando el fotocondensador está iluminado, la corriente fotoeléctrica generada en el fotoánodo es conducida a través de un semiconductor de banda ancha hacia el contraelectrodo a través del circuito externo, donde se acumula en la superficie formando una carga negativa de doble capa. Una vez cargado el fotocondensador, se produce el proceso de descarga galvanostática a través del circuito externo.

En el caso de un sistema fotocondensador de tres electrodos, ocurre un procedimiento similar. Cuando el fotocondensador está iluminado se cortocircuitan el fotoánodo y el contraelectrodo. Una vez cargado el fotocondensador, se produce el proceso de descarga galvanostática a través

del circuito externo cortocircuitando en este caso, el electrodo intermedio y el contraelectrodo. Ahora, el electrodo intermedio y el contraelectrodo funcionan como electrodos cargados positivos y negativos, respectivamente.

Por otro lado, además de la tradicional estructura plana explicada anteriormente, existe un nuevo tipo de fotocondensador integrado en forma de fibra. Estos dispositivos en forma de fibra se obtienen enrollando la estructura plana. Normalmente, la parte de la célula solar y la parte de almacenamiento o supercondensador se encuentran en forma de fibra y están integradas en la estructura de configuración del núcleo o enrollada. Este dispositivo tiene las ventajas de la ligereza, la flexibilidad y la compatibilidad con los tejidos textiles. Además, las células solares de fibra tienen la ventaja única de tener propiedades independientes del ángulo de incidencia de la luz en comparación con los fotocondensadores de estructura plana.

En esta Tesis, se ha elegido una configuración de células solares sensibilizadas con puntos cuánticos para la parte fotoanódica y un supercondensador simétrico con electrodo de PEDOT para la parte de almacenamiento de energía.

B. MATERIALES Y MÉTODOS

Inicialmente, se ha diseñado y fabricado un fotocondensador durante la Tesis basado en un fotoánodo compuesto por una celda solar sensibilizada con puntos cuánticos usando como sustrato FTO comercial, habiéndose explicado su desarrollo en el capítulo III. El electrolito y el contraelectrodo empleado ha sido líquido iónico y PEDOT, respectivamente, explicados en el capítulo IV.

Seguidamente, se ha fabricado el mismo tipo de fotocondensador explicado anteriormente donde únicamente se sustituye el sustrato de FTO comercial con capa semilla por la capa delgada de GIZO conductora y transparente explicada en el capítulo II.

Finalmente, se ha caracterizado un dispositivo fabricado por nuestro grupo de investigación en el laboratorio basado en un fotoánodo de una capa delgada de TiO_2 sin ningún tipo de sensibilizante crecida por *magnetrón sputtering*, un contraelectrodo de $LiFeO_2$ depositada por spray pirólisis y un electrolito compuesto por PVP/[HEMIm][BF_4].

El ensamblaje del fotoánodo con el contraelectrodo de dichos fotocondensadores ha sido por presión mecánica una vez depositado el electrolito sobre una de las caras que funciona como agente viscoso y une ambas partes.

C. RESULTADOS Y DISCUSIÓN

Se han diseñado, desarrollado y caracterizado con éxito dos tipos de fotosupercondensadores con estructura planar de dos electrodos. En este capítulo final se presentan los mejores resultados de eficiencia global y eficiencia de almacenamiento para cada tipo de dispositivo. El fotosupercondensador transparente basado en TiO_2 es un nuevo concepto de dispositivo transparente generador y almacenador de energía eléctrica, ya que no se compone de nanoestructuras ni materiales sensibilizantes orgánicos ni inorgánicos.

Existe una mejora de la eficiencia de conversión y global entre el fotosupercondensador basado en TiO_2 y el basado en QDSSC debido a la adición de *QDs* soportados en los nanohilos de ZnO que producen mayores fotocorrientes. En cuanto al fotocondensador final basado en el QDSSC de GIZO, se han encontrado eficiencias ligeramente más bajas debido al mayor diámetro de los nanohilos, lo que provoca una menor área superficial, un menor número de *QDs* depositados y por tanto a una menor fotorespuesta. A partir de la comparación de los tres dispositivos, se ha encontrado el valor más alto de eficiencia global para el fotocondensador basado en el fotoánodo de QDSSC con capa semilla de ZnO siendo su valor de 8.25×10^{-4}%, la eficiencia de foto-conversión más alta obtenida para este dispositivo fue de 0.012% con una eficiencia de almacenamiento de 6.83%.

6. CAPÍTULO VI: RESUMEN Y CONCLUSIONES FINALES

- Las películas delgadas conductoras y transparentes de GIZO fueron crecidas con éxito sobre sustratos de vidrio mediante *magnetron sputtering*. Se realizó una planificación de los experimentos mediante un diseño experimental de superficie respuesta Box-Behnken para evaluar el efecto de los parámetros de *magnetron sputtering* sobre las propiedades estructurales, morfológicas, ópticas, eléctricas y electroquímicas de las películas de GIZO, para su aplicación como óxido conductor transparente en fotoelectrodos. Se han obtenido películas de GIZO de alta conductividad, movilidad y densidad de portadores de carga y elevada transparencia.

- Se propusieron nuevas Figuras de Mérito (FOMs) para las regiones visible y solar, obteniendo el mejor compromiso entre conductividad y transparencia de las películas de GIZO para aplicaciones visibles y solares, resultando el óptimo para la relación atómica In/Zn de 0,85-0,90.

- Los nanohilos de óxido de zinc (ZnO) se obtuvieron sobre películas delgadas de GIZO sin el empleo de una capa semilla, y sobre FTO/vidrio con una capa semilla depositada previamente. Se encontraron las condiciones óptimas de crecimiento de los nanohilos con respecto al tiempo de crecimiento, temperatura y concentración de la solución de acuerdo al diámetro, tamaño de cristal, grado de orientación y longitud.

- Los nanohilos se recubrieron completamente con *QDs* de sulfuro de plata (Ag_2S), aumentando la absorción de luz y la foto-respuesta del fotoánodo. El valor más alto de eficiencia se obtuvo para unas condiciones de concentración de 0.05 M de $AgNO_3$ y Na_2S empleando 9 ciclos de SILAR. Se demostró que la capa pasivante de películas delgadas de sulfuro de zinc (ZnS) mejoraba las propiedades

fotoelectroquímicas del fotoánodo, encontrando la mejor condición para 4 ciclos de recubrimiento.

- Se han desarrollado dos supercondensadores simétricos basados en un polímero conductor de PEDOT como electrodo y un polímero líquido iónico como electrolito (PVP/[HEMIm][BF_4]). Se encontró que el espesor de la película de PEDOT influye en el rendimiento final del supercondensador, resultando las mejores condiciones para el supercondensador con el PEDOT crecido durante 5 ciclos.

- Se han diseñado y desarrollado dos tipos de fotosupercondensadores. El fotocondensador basado en TiO_2 y $LiFeO_2$ como electrodos resultó ser un nuevo concepto de dispositivo basado en dos electrodos de alta transparencia con una eficiencia de fotoconversión de 8.1 x 10^{-5}% y una eficiencia global de 6.67 x 10^{-6}%. El fotocondensador basado en FTO/QDSSC como fotoánodo y PEDOT como contraelectrodo demostró una mejora de la eficiencia de la fotoconversión del 0.012% y la eficiencia global fue de 8.25 x 10^{-4}%. Se ha diseñado y desarrollado un fotocondensador (GIZO/QDSSC), en el cual todas sus partes han sido fabricadas íntegramente en nuestro laboratorio, mostrando resultados aceptables de eficiencia. Con ello se ha analizado el efecto que tiene el óxido transparente conductor sobre el crecimiento de los nanohilos de ZnO y el rendimiento final del dispositivo.

BIBLIOGRAPHIC REFERENCES

[1] J. Liu, G. Cao, Z. Yang, D. Wang, D. Dubois, X. Zhou, G.L. Graff, L.R. Pederson, J.G. Zhang, Oriented nanostructures for energy conversion and storage, ChemSusChem. 1 (2008) 676–697. doi:10.1002/cssc.200800087.

[2] W. Shockley, H.J. Queisser, Detailed balance limit of efficiency of p-n junction solar cells, J. Appl. Phys. 32 (1961) 510–519. doi:10.1063/1.1736034.

[3] K. Yoshikawa, H. Kawasaki, W. Yoshida, T. Irie, K. Konishi, K. Nakano, T. Uto, D. Adachi, M. Kanematsu, H. Uzu, K. Yamamoto, Silicon heterojunction solar cell with interdigitated back contacts for a photoconversion efficiency over 26%, Nat. Energy. 2 (2017). doi:10.1038/nenergy.2017.32.

[4] G. Conibeer, Third-generation photovoltaics, Mater. Today. 10 (2007) 42–50.

[5] J. Yan, B.R. Saunders, Third-generation solar cells: A review and comparison of polymer:fullerene, hybrid polymer and perovskite solar cells, RSC Adv. 4 (2014) 43286–43314. doi:10.1039/c4ra07064j.

[6] K.S. Ahn, S.J. Yoo, M.S. Kang, J.W. Lee, Y.E. Sung, Tandem dye-sensitized solar cell-powered electrochromic devices for the photovoltaic-powered smart window, J. Power Sources. 168 (2007) 533–536. doi:10.1016/j.jpowsour.2006.12.114.

[7] S.K. Deb, S.H. Lee, C. Edwin Tracy, J. Roland Pitts, B.A. Gregg, H.M. Branz, Stand-alone photovoltaic-powered electrochromic smart window, Electrochim. Acta. 46 (2001) 2125–2130. doi:10.1016/S0013-4686(01)00390-5.

[8] D. Paine, H. Hosono, D. Ginley, Handbook of Transparent Conductors ▶ Recounts dramatic progress in materials , applications anfile:///C:/Users/Dani Solís/Desktop/David S. Ginley, John D. Perkins (auth.), David S. Ginley (eds.) - Handbook of transparent conductors (2011, Springer US).pdf, 49 (2011) 6221.

[9] C.G. Granqvist, Transparent conductors as solar energy materials: A

panoramic review, Sol. Energy Mater. Sol. Cells. 91 (2007) 1529–1598. doi:10.1016/j.solmat.2007.04.031.

[10] J. Gao, K. Kempa, M. Giersig, E.M. Akinoglu, B. Han, R. Li, Physics of transparent conductors, Adv. Phys. 65 (2016) 553–617. doi:10.1080/00018732.2016.1226804.

[11] T. Miyasaka, T.N. Murakami, The photocapacitor: An efficient self-charging capacitor for direct storage of solar energy, Appl. Phys. Lett. 85 (2004) 3932–3934. doi:doi:http://dx.doi.org/10.1063/1.1810630.

[12] M. Skunik-nuckowska, K. Grzejszczyk, P.J. Kulesza, L. Yang, N. Vlachopoulos, L. Häggman, E. Johansson, A. Hagfeldt, Integration of solid-state dye-sensitized solar cell with metal oxide charge storage material into photoelectrochemical capacitor, J. Power Sources. 234 (2013) 91–99. doi:10.1016/j.jpowsour.2013.01.101.

[13] R. Romero, D. Leinen, E.A. Dalchiele, J.R. Ramos-Barrado, F. Martín, The effects of zinc acetate and zinc chloride precursors on the preferred crystalline orientation of ZnO and Al-doped ZnO thin films obtained by spray pyrolysis, Thin Solid Films. 515 (2006) 1942–1949. doi:10.1016/j.tsf.2006.07.152.

[14] R. Ayouchi, F. Martin, D. Leinen, J.R. Ramos-barrado, Growth of pure ZnO thin films prepared by chemical spray pyrolysis on silicon, J. Cryst. Growth. 247 (2003) 497–504.

[15] E.A. Dalchiele, P. Giorgi, R.E. Marotti, F. Mart, Electrodeposition of ZnO thin films on n-Si (1 0 0), Sol. Energy Mater. Sol. Cells. 70 (2001) 245–254.

[16] J. Rousset, E. Saucedo, D. Lincot, Extrinsic doping of electrodeposited zinc oxide films by chlorine for transparent conductive oxide applications, Chem. Mater. 21 (2009) 534–540. doi:10.1021/cm802765c.

[17] J. Rousset, D. Lincot, Low temperature electrodeposition of zinc oxide layers as transparent conducting oxide window layers for CIGS solar cells, Conf. Rec. IEEE Photovolt. Spec. Conf. (2009) 001246–001251. doi:10.1109/PVSC.2009.5411242.

[18] M. Gabás, P. Díaz-Carrasco, F. Agulló-Rueda, P. Herrero, A.R. Landa-Cánovas, J.R. Ramos-Barrado, High quality ZnO and Ga : ZnO thin films grown onto crystalline Si (1 0 0) by RF magnetron sputtering,

Sol. Energy Mater. Sol. Cells. 95 (2011) 2327–2334. doi:10.1016/j.solmat.2011.04.001.

[19] L. Campo, E. Navarrete-Astorga, C.J.C.J. Pereyra, A. Cuevas, R. Romero, D. Ariosa, R. Henríquez, E. Muñoz, R.E.R.E. Marotti, F. Martín, J.R.J.R. Ramos-Barrado, E.A.E.A. Dalchiele, The effect of a sputtered Al-doped ZnO seed layer on the morphological, structural and optical properties of electrochemically grown ZnO nanorod arrays, J. Electrochem. Soc. 163 (2016) 392–400. doi:10.1149/2.0611608jes.

[20] E. Muchuweni, T.S. Sathiaraj, H. Nyakotyo, Effect of gallium doping on the structural, optical and electrical properties of zinc oxide thin films prepared by spray pyrolysis, Ceram. Int. 42 (2016) 10066–10070. doi:10.1016/j.ceramint.2016.03.110.

[21] C. Lee, W. Lee, H. Kim, H.W. Kim, Influence of annealing atmosphere on the structure, resistivity and transmittance of InZnO thin films, Ceram. Int. 34 (2008) 1089–1092. doi:10.1016/j.ceramint.2007.09.053.

[22] K. Nomura, H. Ohta, A. Takagi, T. Kamiya, M. Hirano, H. Hosono, Room-temperature fabrication of transparent flexible thin-film transistors using amorphous oxide semiconductors, Nature. 432 (2004) 488–492. doi:10.1038/nature03090.

[23] M. Gabás, S. Gota, N.T. Barrett, Unraveling the conduction mechanism of Al-doped ZnO films by valence band soft x-ray photoemission spectroscopy, Appl. Phys. Lett. (2005) 2005–2007. doi:10.1063/1.1856141.

[24] B. Paul, B. Singh, S. Ghosh, A. Roy, A comparative study on electrical and optical properties of group III (Al , Ga , In) doped ZnO, Thin Solid Films. 603 (2016) 21–28. doi:10.1016/j.tsf.2016.01.044.

[25] G.K. Paul, S.K. Sen, Sol – gel preparation, characterization and studies on electrical and thermoelectrical properties of gallium doped zinc oxide films, Mater. Lett. 57 (2002) 742–746. doi:10.1016/S0167-577X(02)00865-0.

[26] D.P. Pham, H.T. Nguyen, B.T. Phan, V.D. Hoang, S. Maenosono, C.V. Tran, Influence of addition of indium and of post-annealing on structural, electrical and optical properties of gallium-doped zinc

oxide thin films deposited by direct-current magnetron sputtering, Thin Solid Films. 583 (2015) 201–204. doi:10.1016/j.tsf.2015.03.068.

[27] J.P. Wiff, Y. Kinemuchi, K. Watari, Hall mobilities of Al- and Ga-doped ZnO polycrystals, Mater. Lett. 63 (2009) 2470–2472. doi:10.1016/j.matlet.2009.08.036.

[28] N. Kimizuka, T. Mohri, Spinel, YbFe$_2$O$_4$, and Yb$_2$Fe$_3$O$_7$ types of structures for compounds in the In$_2$O$_3$ and Sc$_2$O$_3$$A_2O_3$$B$O systems [$A$: Fe, Ga, or Al; B: Mg, Mn, Fe, Ni, Cu, or Zn] at Temperatures over 1000\degree C, J. Solid State Chem. 60 (1985) 382–384. doi:10.1016/0022-4596(85)90290-7.

[29] S. Yamazaki, H. Suzawa, K. Inoue, K. Kato, T. Hirohashi, K. Okazaki, N. Kimizuka, Properties of crystalline In-Ga-Zn-oxide semiconductor and its transistor characteristics, Jpn. J. Appl. Phys. 53 (2014). doi:10.7567/jjap.53.04ed18.

[30] T. Hiramatsu, M. Nakashima, E. Kikuchi, N. Ishihara, M. Tsubuku, K. Dairiki, S. Yamazaki, Correlation between crystallinity and oxygen vacancy formation in In – Ga – Zn oxide, Jpn. J. Appl. Phys. 55 (2016) 21203. doi:10.7567/JJAP.55.021203.

[31] A.J. Leenheer, J.D. Perkins, M.F.A.M. Van Hest, J.J. Berry, R.P. O'Hayre, D.S. Ginley, General mobility and carrier concentration relationship in transparent amorphous indium zinc oxide films, Phys. Rev. B - Condens. Matter Mater. Phys. 77 (2008) 1–5. doi:10.1103/PhysRevB.77.115215.

[32] Y.H. Choi, S.H. Hong, Composition-dependent crystallization enhancing moisture-barrier performance in In-Zn-O thin films, Mater. Lett. 159 (2015) 381–384. doi:10.1016/j.matlet.2015.07.046.

[33] A.P. Rambu, N. Iftimie, V. Nica, Effect of in incorporation on the structural, electrical, and gas sensing properties of ZnO films, J. Mater. Sci. 47 (2012) 6979–6985. doi:10.1007/s10853-012-6648-z.

[34] T. Kamiya, Y. Takeda, K. Nomura, H. Ohta, H. Yanagi, M. Hirano, H. Hosono, Self-adjusted, three-dimensional lattice-matched buffer layer for growing ZnO epitaxial film: Homologous series layered oxide, InGaO3(ZnO) 5, Cryst. Growth Des. 6 (2006) 2451–2456.

doi:10.1021/cg050478k.

[35] G.H. Kim, B. Du Ahn, H.S. Shin, W.H. Jeong, H.J.H.J. Kim, H.J.H.J. Kim, Effect of indium composition ratio on solution-processed nanocrystalline InGaZnO thin film transistors, Appl. Phys. Lett. 94 (2009) 10–13. doi:10.1063/1.3151827.

[36] K. Tominaga, D. Takada, K. Shimomura, H. Suketa, K. Takita, K. Murai, T. Moriga, Influence of Ga2O3addition on transparent conductive oxide films of In2O3-ZnO, Vacuum. 83 (2008) 561–563. doi:10.1016/j.vacuum.2008.04.064.

[37] C.I. de LÉclairage, Recommendations concerning uniform colour spacing and colour differences., in: CIE Publ. 15; Tech. Rep. Color., 3rd ed., Washington, D.C., n.d.

[38] S.K. O'Leary, S.R. Johnson, P.K. Lim, The relationship between the distribution of electronic states and the optical absorption spectrum of an amorphous semiconductor: An empirical analysis, J. Appl. Phys. 82 (1997) 3334–3340. doi:10.1063/1.365643.

[39] A. Solieman, M.A. Aegerter, Modeling of optical and electrical properties of In 2 O 3 : Sn coatings made by various techniques, 502 (2006) 205–211. doi:10.1016/j.tsf.2005.07.277.

[40] A. Cuevas, R. Romero, D. Leinen, E.A. Dalchiele, J.R. Ramos-Barrado, F. Martin, Effect of the stoichiometry of CuxS thin films on the optical and electrical properties and the solar thermal performance, Sol. Energy Mater. Sol. Cells. 134 (2015) 199–208. doi:10.1016/j.solmat.2014.11.048.

[41] G. Hautier, A. Miglio, G. Ceder, G.M. Rignanese, X. Gonze, Identification and design principles of low hole effective mass p-type transparent conducting oxides, Nat. Commun. 4 (2013) 1–7. doi:10.1038/ncomms3292.

[42] A. Takagi, K. Nomura, H. Ohta, H. Yanagi, T. Kamiya, M. Hirano, H. Hosono, Carrier transport and electronic structure in amorphous oxide semiconductor, a-InGaZnO4, Thin Solid Films. 486 (2005) 38–41. doi:10.1016/j.tsf.2004.11.223.

[43] B. Kumar, H. Gong, R. Akkipeddi, High mobility undoped amorphous indium zinc oxide transparent thin films, J. Appl. Phys. 98

(2005). doi:10.1063/1.2060957.

[44] Y. Wang, W. Tang, L. Zhang, J. Zhao, Electron concentration dependence of optical band gap shift in Ga-doped ZnO thin films by magnetron sputtering, Thin Solid Films. 565 (2014) 62–68. doi:10.1016/j.tsf.2014.06.046.

[45] S.Z. Karazhanov, P. Ravindran, P. Vajeeston, A. Ulyashin, T.G. Finstad, H. Fjellvåg, Phase stability, electronic structure, and optical properties of indium oxide polytypes, Phys. Rev. B - Condens. Matter Mater. Phys. 76 (2007) 1–13. doi:10.1103/PhysRevB.76.075129.

[46] V.K. Jain, P. Kumar, D. Bhandari, Y.K. Vijay, Growth and characterization of transparent conducting nanostructured zinc indium oxide thin films, Thin Solid Films. 519 (2010) 1082–1086. doi:10.1016/j.tsf.2010.08.048.

[47] K. Ellmer, R. Mientus, Carrier transport in polycrystalline ITO and ZnO:Al II: The influence of grain barriers and boundaries, Thin Solid Films. 516 (2008) 5829–5835. doi:10.1016/j.tsf.2007.10.082.

[48] P.K. Nayak, T. Busani, E. Elamurugu, P. Barquinha, R. Martins, Y. Hong, E. Fortunato, Zinc concentration dependence study of solution processed amorphous indium gallium zinc oxide thin film transistors using high-k dielectric, Appl. Phys. Lett. 97 (2010) 1–4. doi:10.1063/1.3514249.

[49] K. Makise, B. Shinozaki, T. Asano, K. Yano, H. Nakamura, Activation like behaviour on the temperature dependence of the carrier density in In 2 O 3 -ZnO films, J. Phys. Conf. Ser. 400 (2012) 42043. doi:10.1088/1742-6596/400/4/042043.

[50] Y. Takeda, K. Nomura, H. Ohta, H. Yanagi, T. Kamiya, M. Hirano, H. Hosono, Growth of epitaxial ZnO thin films on lattice-matched buffer layer: Application of InGaO3(ZnO)6 single-crystalline thin film, Thin Solid Films. 486 (2005) 28–32. doi:10.1016/j.tsf.2004.12.045.

[51] D.B. Fraser, H.D. Cook, Highly Conductive, Transparent Films of Sputtered In[sub 2−x]Sn[sub x]O[sub 3−y], J. Electrochem. Soc. 119 (1972) 1368. doi:10.1149/1.2403999.

[52] G. Haacke, New figure of merit for transparent conductors, J. Appl. Phys. 47 (1976) 4086–4089. doi:10.1063/1.323240.

[53] R.G. Gordon, C riteria for Choosing Transparent Conductors, History. (2000) 52–57.

[54] S. Fernández, A. Martínez-Steele, J.J. Gandía, F.B. Naranjo, Radio frequency sputter deposition of high-quality conductive and transparent ZnO:Al films on polymer substrates for thin film solar cells applications, Thin Solid Films. 517 (2009) 3152–3156. doi:10.1016/j.tsf.2008.11.097.

[55] Á. Pekker, K. Kamarás, A general figure of merit for thick and thin transparent conductive carbon nanotube coatings, J. Appl. Phys. 108 (2010). doi:10.1063/1.3476278.

[56] N. Hu, H. Cai, X. Dai, G. Chen, Y. Wang, D. Zhang, Figure of merit for front electrodes of solar cells, Sol. Energy Mater. Sol. Cells. 161 (2017) 382–387. doi:10.1016/j.solmat.2016.12.014.

[57] K.U. Sim, S.W. Shin, A. V Moholkar, J.H. Yun, J.H. Moon, J.H. Kim, Effects of dopant (Al, Ga, and In) on the characteristics of ZnO thin films prepared by RF magnetron sputtering system, Curr. Appl. Phys. 10 (2010) S463–S467. doi:https://doi.org/10.1016/j.cap.2010.02.028.

[58] X.F. Chen, G. He, J. Gao, J.W. Zhang, D.Q. Xiao, P. Jin, B. Deng, Substrate temperature dependent structural, optical and electrical properties of amorphous InGaZnO thin films, J. Alloys Compd. 632 (2015) 533–539. doi:10.1016/j.jallcom.2015.01.143.

[59] H. Yabuta, M. Sano, K. Abe, T. Aiba, T. Den, H. Kumomi, K. Nomura, T. Kamiya, H. Hosono, High-mobility thin-film transistor with amorphous InGaZnO4 channel fabricated by room temperature rf-magnetron sputtering, Appl. Phys. Lett. 89 (2006) 10–13. doi:10.1063/1.2353811.

[60] J.D. Benck, B.A. Pinaud, Y. Gorlin, T.F. Jaramillo, Substrate selection for fundamental studies of electrocatalysts and photoelectrodes: Inert potential windows in acidic, neutral, and basic electrolyte, PLoS One. 9 (2014). doi:10.1371/journal.pone.0107942.

[61] C.C.P. Cid, E.R. Spada, M.L. Sartorelli, Effect of the cathodic polarization on structural and morphological proprieties of FTO and ITO thin films, Appl. Surf. Sci. 273 (2013) 603–606. doi:10.1016/j.apsusc.2013.02.085.

[62] N.D. Popovich, S.-S. Wong, S. Ufer, V. Sakhrani, D. Paine, Electron-Transfer Kinetics at ITO Films, J. Electrochem. Soc. 150 (2003) H255. doi:10.1149/1.1613672.

[63] W. Gao, S. Cao, Y. Yang, H. Wang, J. Li, Y. Jiang, Electrochemical impedance spectroscopy investigation on indium tin oxide films under cathodic polarization in NaOH solution, Thin Solid Films. 520 (2012) 6916–6921. doi:10.1016/j.tsf.2012.07.092.

[64] M.A. Martínez, J. Herrero, M.T. Gutiérrez, Electrochemical stability of indium tin oxide thin films, Electrochim. Acta. 37 (1992) 2565–2571. doi:10.1016/0013-4686(92)87053-3.

[65] A. Kraft, H. Hennig, A. Herbst, K.H. Heckner, Changes in electrochemical and photoelectrochemical properties of tin-doped indium oxide layers after strong anodic polarization, J. Electroanal. Chem. 365 (1994) 191–196. doi:10.1016/0022-0728(93)03056-U.

[66] N.R. Armstrong, A.W.C. Lin, M. Fujihira, T. Kuwana, Electrochemical and surface characteristics of tin oxide and indium oxide electrodes, Anal. Chem. 48 (1976) 741–750. doi:10.1021/ac60368a035.

[67] J.L. Anderson, N. Winograd, Film Electrodes, in: P.T. Kissinger, W.R. Heineman (Eds.), Lab. Tech. Electroanal. Chem., 2nd Ed., Marcel Dekker, Inc., 1996: p. 53.

[68] J.G.S. Moo, A. Ambrosi, A. Bonanni, M. Pumera, Inherent electrochemistry and activation of chemically modified graphenes for electrochemical applications, Chem. - An Asian J. 7 (2012) 759–770. doi:10.1002/asia.201100852.

[69] D.A.C. Brownson, C.E. Banks, The Electrochemistry of graphene, in: Handb. Graphene Electrochem., Springer US, 2014.

[70] V.H.R. Souza, S. Husmann, E.G.C. Neiva, F.S. Lisboa, L.C. Lopes, R. V. Salvatierra, A.J.G. Zarbin, Flexible, Transparent and Thin Films of Carbon Nanomaterials as Electrodes for Electrochemical Applications, Electrochim. Acta. 197 (2016) 200–209. doi:10.1016/j.electacta.2015.08.077.

[71] A. Bard, L. Faulkner, Electrochemical Methods: Fundamentals and Applications, 2001. doi:10.1016/B978-0-12-381373-2.00056-9.

[72] E. Laviron, General expression of the linear potential sweep voltammogram in the case of diffusionless electrochemical systems, J. Electroanal. Chem. 101 (1979) 19–28. doi:10.1016/S0022-0728(79)80075-3.

[73] C.X. Xu, X.W. Sun, X.H. Zhang, L. Ke, S.J. Chua, Photoluminescent properties of copper-doped zinc oxide nanowires, Nanotechnology. 15 (2004) 856–861. doi:10.1088/0957-4484/15/7/026.

[74] K.H. Kim, R.A. Wibowo, B. Munir, Properties of Al-doped ZnO thin film sputtered from powder compacted target, Mater. Lett. 60 (2006) 1931–1935. doi:10.1016/j.matlet.2005.12.055.

[75] L.M. Peter, K.G.U. Wijayantha, A.A. Tahir, Kinetics of light-driven oxygen evolution at ??-Fe 2O 3 electrodes, Faraday Discuss. 155 (2012) 309–322. doi:10.1039/c1fd00079a.

[76] T. Yoshida, T. Pauporté, D. Lincot, T. Oekermann, H. Minoura, Cathodic Electrodeposition of ZnO/Eosin Y Hybrid Thin Films from Oxygen-Saturated Aqueous Solution of ZnCl[sub 2] and Eosin Y, J. Electrochem. Soc. 150 (2003) C608. doi:10.1149/1.1598213.

[77] T. Oekermann, T. Yoshida, D. Schlettwein, T. Sugiurab, Photoelectrochemical properties of ZnO _ tetrasulfophthalocyanine hybrid thin Đlms prepared by electrochemical self-assembly, Own. Soc. 3 (2001) 3387–3392.

[78] A.J. McEvoy, M. Etman, R. Memming, Interface charging and intercalation effects on d-Band transition metal diselenide photoelectrodes., J. Electroanal. Chem. 190 (1985) 225–241.

[79] T. Yoshida, T. Pauporté, D. Lincot, T. Oekermann, H. Minoura, Cathodic Electrodeposition of ZnO/Eosin Y Hybrid Thin Films from Oxygen-Saturated Aqueous Solution of ZnCl[sub 2] and Eosin Y, J. Electrochem. Soc. 150 (2003) C608. doi:10.1149/1.1598213.

[80] K. Rajeshwar, J.B. DuBow, Photoelectrochemical devices: comparison with solid-sate solar cells and new perspectives for their design an operation, in: R.W.W. W.L. Wallace, A.J. Nozik, S.K. Deb (Ed.), Proc. Symp. Photoelectrochem. Fundam. Process. Meas. Tech., The Electrochemical Society Inc., Pennington, NJ, 1982: pp. 61–79.

[81] J. Duan, H. Zhang, Q. Tang, B. He, L. Yu, Recent advances in critical

materials for quantum dot-sensitized solar cells: a review, J. Mater. Chem. A. 3 (2015) 17497–17510. doi:10.1039/C5TA03280F.

[82] B. O'Regan, M. Gratzel, A Low-Cost, High-Efficiency Solar-Cell Based on Dye-Sensitized Colloidal TiO_2 Films, Nature. 353 (1991) 737–740. doi:10.1038/353737a0.

[83] M.C. Hanna, A.J. Nozik, Solar conversion efficiency of photovoltaic and photoelectrolysis cells with carrier multiplication absorbers, J. Appl. Phys. 100 (2006). doi:10.1063/1.2356795.

[84] S. Corer, G. Hodes, Quantum Size Effects in the Study of Chemical Solution Deposition Mechanisms of Semiconductor Films, (1994) 5338–5346.

[85] A.J. Nozik, Multiple exciton generation in semiconductor quantum dots, Chem. Phys. Lett. 457 (2008) 3–11. doi:10.1016/j.cplett.2008.03.094.

[86] W.W. Yu, L. Qu, W. Guo, X. Peng, Experimental Determination of the Extinction Coefficient of CdTe , CdSe , and CdS Nanocrystals Experimental Determination of the Extinction Coefficient of CdTe , CdSe , and CdS Nanocrystals, Chem. Mater. 15 (2003) 2854–2860. doi:10.1021/cm034081k.

[87] P. V. Kamat, Quantum Dot Solar Cells. Semiconductor Nanocrystals as Light Harvesters†, J. Phys. Chem. C. 112 (2008) 18737–18753. doi:10.1021/jp806791s.

[88] I. Mora-Seró, S. Giménez, F. Fabregat-Santiago, R. Gómez, Q. Shen, T. Toyoda, J. Bisquert, Recombination in quantum dot sensitized solar cells, Acc. Chem. Res. 42 (2009) 1848–1857. doi:10.1021/ar900134d.

[89] E.M. Barea, M. Shalom, S. Giménez, I. Hod, I. Mora-Seró, A. Zaban, J. Bisquert, Design of injection and recombination in quantum dot sensitized solar cells, J. Am. Chem. Soc. 132 (2010) 6834–6839. doi:10.1021/ja101752d.

[90] A. Tubtimtae, M. Lee, Optical and Photovoltaic Properties of CdS / Ag 2 S Quantum Dots Co-, 761 (2013) 15–18. doi:10.4028/www.scientific.net/MSF.761.15.

[91] J.H. Park, D.H. Kim, S.S. Shin, H.S. Han, M.H. Lee, H.S. Jung, J.H.

Noh, K.S. Hong, A hierarchically organized photoelectrode architecture for highly efficient CdS/CdSe-sensitized solar cells, Adv. Energy Mater. 4 (2014) 1–7. doi:10.1002/aenm.201300395.

[92] S. Ten Cate, Y. Liu, C.S. Suchand Sandeep, S. Kinge, A.J. Houtepen, T.J. Savenije, J.M. Schins, M. Law, L.D.A. Siebbeles, Activating carrier multiplication in PbSe quantum dot solids by infilling with atomic layer deposition, J. Phys. Chem. Lett. 4 (2013) 1766–1770. doi:10.1021/jz4007492.

[93] R.D. Schaller, M. Sykora, J.M. Pietryga, V.I. Klimov, Seven excitons at a cost of one: Redefining the limits for conversion efficiency of photons into charge carriers, Nano Lett. 6 (2006) 424–429. doi:10.1021/nl052276g.

[94] P. Sun, X. Zhang, L. Wang, Y. Wei, C. Wang, Y. Liu, Efficiency enhanced rutile TiO<inf>2</inf> nanowire solar cells based on an Sb<inf>2</inf>S<inf>3</inf> absorber and a CuI hole conductor, New J. Chem. 39 (2015) 7243–7250. doi:10.1039/c5nj00299k.

[95] H. Shen, X. Jiao, D. Oron, J. Li, H. Lin, Efficient electron injection in non-toxic silver sulfide (Ag2S) sensitized solar cells, J. Power Sources. 240 (2013) 8–13. doi:10.1016/j.jpowsour.2013.03.168.

[96] Y.C. Yoon, K.S. Park, S.D. Kim, Effects of low preheating temperature for ZnO seed layer deposited by sol-gel spin coating on the structural properties of hydrothermal ZnO nanorods, Thin Solid Films. 597 (2015) 125–130. doi:10.1016/j.tsf.2015.11.040.

[97] C. Zhang, High-quality oriented ZnO films grown by sol-gel process assisted with ZnO seed layer, J. Phys. Chem. Solids. 71 (2010) 364–369. doi:10.1016/j.jpcs.2010.01.001.

[98] C. Hsieh, S. Yang, J. Gu, Y. Jiang, Influence of growth parameters on texture of ZnO nanorods by using electrochemical deposition at low temperatures, Solid State Ionics. 209–210 (2012) 43–50. doi:10.1016/j.ssi.2011.12.010.

[99] M. Gabas, E. Dalchiele, J.R. Ramos-barrado, Preparation and characterization of transparent ZnO thin films obtained by spray pyrolysis, Thin Solid Films. 426 (2003) 68–77. doi:10.1016/S0040-6090(02)01331-7.

[100] H.J. Xiang, J. Yang, J.G. Hou, Q. Zhu, Piezoelectricity in ZnO nanowires: A first-principles study, Appl. Phys. Lett. 89 (2006) 87–90. doi:10.1063/1.2397013.

[101] A. Onodera, Novel ferroelectricity in II-VI semiconductor ZnO, Ferroelectrics. 267 (2002) 131–137. doi:10.1080/00150190210997.

[102] Ü. Özgür, Y.I. Alivov, C. Liu, A. Teke, M.A. Reshchikov, S. Doğan, V. Avrutin, S.J. Cho, H. Morko, A comprehensive review of ZnO materials and devices, J. Appl. Phys. 98 (2005) 1–103. doi:10.1063/1.1992666.

[103] L. Schmidt-mende, J.L. Macmanus-driscoll, defects , and devices ZnO has received much attention over the past few years because, Mater. Today. 10 (2007) 40–48. doi:10.1016/S1369-7021(07)70078-0.

[104] A.J. Behan, J.R. Neal, R.M. Ibrahim, A. Mokhtari, M. Ziese, H.J. Blythe, A.M. Fox, G.A. Gehring, Magneto-optical and transport studies of ZnO-based dilute magnetic semiconductors, J. Magn. Magn. Mater. 310 (2007) 2158–2160. doi:10.1016/j.jmmm.2006.11.024.

[105] K. Ellmer, A. Klein, B. Rech, Transparent Conductive Zinc Oxide. Basics and Applications in Thin Film Solar Cells, 2008. doi:10.1007/978-3-540-73612-7.

[106] M. Skompska, K. Zar, Electrochimica Acta Electrodeposition of ZnO Nanorod Arrays on Transparent Conducting Substrates – a Review, 127 (2014) 467–488. doi:10.1016/j.electacta.2014.02.049.

[107] W.I. Park, D.H. Kim, S.W. Jung, G.C. Yi, Metalorganic vapor-phase epitaxial growth of vertically well-aligned ZnO nanorods, Appl. Phys. Lett. 80 (2002) 4232–4234. doi:10.1063/1.1482800.

[108] K.-K. Kim, J.-H. Song, H.-J. Jung, W.-K. Choi, S.-J. Park, J.-H. Song, The grain size effects on the photoluminescence of ZnO/α-Al2O3 grown by radio-frequency magnetron sputtering, J. Appl. Phys. 87 (2000) 3573–3575. doi:10.1063/1.372383.

[109] J. Joo, B.Y. Chow, M. Prakash, E.S. Boyden, J.M. Jacobson, Face-selective electrostatic control of hydrothermal zinc oxide nanowire synthesis, Nat. Mater. 10 (2011) 596–601. doi:10.1038/nmat3069.

[110] M. Izaki, T. Omi, Transparent zinc oxide films prepared by

electrochemical reaction, Appl. Phys. Lett. 68 (1996) 2439–2440. doi:10.1063/1.116160.

[111] M. Guo, C. Yang, M. Zhang, Y. Zhang, T. Ma, X. Wang, X. Wang, Effects of preparing conditions on the electrodeposition of well-aligned ZnO nanorod arrays, Electrochim. Acta. 53 (2008) 4633–4641. doi:10.1016/j.electacta.2008.01.061.

[112] Y.F. Nicolau, Solution deposition of thin solid compound films by a successive ionic-layer adsorption and reaction process, Appl. Surf. Sci. 22–23 (1985) 1061–1074. doi:10.1016/0378-5963(85)90241-7.

[113] Y. Lee, B. Huang, H. Chien, Highly Efficient CdSe-Sensitized TiO 2 Photoelectrode for Quantum-Dot-Sensitized Solar Cell Applications, Chem. Mater. 20 (2008) 6903–6905. doi:10.1021/cm802254u.

[114] Y.L. Lee, Y.S. Lo, Highly efficient quantum-dot-sensitized solar cell based on co-sensitization of CdS/CdSe, Adv. Funct. Mater. 19 (2009) 604–609. doi:10.1002/adfm.200800940.

[115] S. Yang, C. Huang, J. Zhai, Z. Wang, L. Jiang, High photostability and quantum yield of nanoporous TiO2 thin film electrodes co-sensitized with capped sulfides, J. Mater. Chem. 12 (2002) 1459–1464. doi:10.1039/b105796k.

[116] N. Guijarro, J.M. Campiña, Q. Shen, T. Toyoda, T. Lana-Villarreal, R. Gómez, R. Go, Uncovering the role of the ZnS treatment in the performance of quantum dot sensitized solar cells w, Phys. Chem. Chem. Phys. 13 (2011) 12024–12032. doi:10.1039/c1cp20290a.

[117] V. Chakrapani, D. Baker, P. V Kamat, Understanding the role of the sulfide redox couple (S2-/S(n)2-) in quantum dot-sensitized solar cells., J. Am. Chem. Soc. 133 (2011) 9607–9615. doi:10.1021/ja203131b.

[118] P.P. Boix, G. Larramona, A. Jacob, B. Delatouche, J. Bisquert, Hole Transport and Recombination in All-Solid Sb 2 S 3 -Sensitized TiO 2 Solar Cells Using CuSCN As Hole Transporter, (2012) 1579–1587.

[119] S.J. Moon, Y. Itzhaik, J.H. Yum, S.M. Zakeeruddin, G. Hodes, M. Grätzel, Sb2S3-Based mesoscopic solar cell using an organic hole conductor, J. Phys. Chem. Lett. 1 (2010) 1524–1527. doi:10.1021/jz100308q.

[120] J. Xia, N. Masaki, M. Lira-cantu, Y. Kim, K. Jiang, S. Yanagida, Influence of Doped Anions on Poly (3 , 4-ethylenedioxythiophene) as Hole Conductors for Iodine-Free Solid-State Dye-Sensitized Solar Cells Iodine-Free Solid-State Dye-Sensitized Solar Cells, Thin Solid Films. (2008) 1258–1263. doi:10.1021/ja075704o.

[121] Q. Liu, C. Li, K. Jiang, Y. Song, J. Pei, A high-efficiency solid-state dye-sensitized solar cell with P3HT polymer as a hole conductor and an assistant sensitizer, Particuology. (2013). doi:10.1016/j.partic.2012.12.005.

[122] X. Liu, W. Zhang, S. Uchida, L. Cai, B. Liu, S. Ramakrishna, An efficient organic-dye-sensitized solar cell with in situ polymerized poly(3,4-ethylenedioxythiophene) as a hole-transporting material, Adv. Mater. 22 (2010) 150–155. doi:10.1002/adma.200904168.

[123] J. Elias, R. Tena-Zaera, C. Lévy-Clément, Electrochemical deposition of ZnO nanowire arrays with tailored dimensions, J. Electroanal. Chem. 621 (2008) 171–177. doi:10.1016/j.jelechem.2007.09.015.

[124] C. Burda, X. Chen, R. Narayanan, M.A. El-Sayed, Chemistry and properties of nanocrystals of different shapes, 2005. doi:10.1021/cr030063a.

[125] H.R. Moutinho, M.M. Al-Jassim, D.H. Levi, P.C. Dippo, L.L. Kazmerski, Effects of CdCl2 treatment on the recrystallization and electro-optical properties of CdTe thin films, J. Vac. Sci. Technol. A Vacuum, Surfaces, Film. 16 (1998) 1251–1257. doi:10.1116/1.581269.

[126] D. Bi, G. Boschloo, S. Schwarzmüller, L. Yang, E.M.J. Johansson, A. Hagfeldt, Efficient and stable CH3NH3PbI3-sensitized ZnO nanorod array solid-state solar cells, Nanoscale. 5 (2013) 11686–11691. doi:10.1039/c3nr01542d.

[127] X. Zhang, J. Liu, J. Zhang, N. Vlachopoulos, E.M.J. Johansson, ZnO@Ag2</inf>S core-shell nanowire arrays for environmentally friendly solid-state quantum dot-sensitized solar cells with panchromatic light capture and enhanced electron collection, Phys. Chem. Chem. Phys. 17 (2015) 12786–12795. doi:10.1039/c4cp06068g.

[128] G. Guerguerian, F. Elhordoy, C.J. Pereyra, R.E. Marotti, F. Martín, D. Leinen, J.R. Ramos-Barrado, E.A. Dalchiele, ZnO nanorod/CdS

nanocrystal core/shell-type heterostructures for solar cell applications, Nanotechnology. 22 (2011) 505401/1-9. doi:10.1088/0957-4484/22/50/505401.

[129] L. Campo, C.J. Pereyra, L. Amy, F. Elhordoy, R.E. Marotti, F. Martin, J.R. Ramos-Barrado, E. a. Dalchiele, F. Mart, F. Martín, J.R. Ramos-Barrado, E. a. Dalchiele, Electrochemically Grown ZnO Nanorod Arrays Decorated with CdS Quantum Dots by Using a Spin-Coating Assisted Successive-Ionic-Layer-Adsorption and Reaction Method for Solar Cell Applications, ECS J. Solid State Sci. Technol. 2 (2013) Q151–Q158. doi:10.1149/2.016309jss.

[130] D. Ramírez, G. Riveros, K. Álvarez, B. González, C.J. Pereyra, E.A. Dalchiele, R.E. Marotti, D. Ariosa, F. Martín, J.R. Ramos-barrado, Electrochemical synthesis of CuSCN nanostructures , tuning the morphological and structural characteristics : From nanorods to nanostructured layers, Mater. Sci. Semicond. Process. 68 (2017) 226–237. doi:10.1016/j.mssp.2017.06.030.

[131] L. Campo, E. Navarrete-Astorga, C.J. Pereyra, A. Cuevas, R. Romero, D. Ariosa, R. Henríquez, E. Muñoz, R.E. Marotti, F. Martín, J.R. Ramos-Barrado, E.A. Dalchiele, The Effect of a Sputtered Al-Doped ZnO Seed Layer on the Morphological, Structural and Optical Properties of Electrochemically Grown ZnO Nanorod Arrays, J. Electrochem. Soc. 163 (2016) D392–D400. doi:10.1149/2.0611608jes.

[132] S.F. Leung, Q. Zhang, F. Xiu, D. Yu, J.C. Ho, D. Li, Z. Fan, Light management with nanostructures for optoelectronic devices, J. Phys. Chem. Lett. 5 (2014) 1479–1495. doi:10.1021/jz500306f.

[133] Y.W. Chen, D. Cahen, R. Noufi, J.A. Turner, Photoelectrochemical test for photovoltaic activity of p-CuInSe2 films., 14 (1985) 109–121.

[134] C. Rama Krishna, M. Kang, Ag2S quantum dot sensitized zinc oxide photoanodes for environment friendly photovoltaic devices, Mater. Lett. 199 (2017) 188–191. doi:10.1016/j.matlet.2017.04.078.

[135] R.G. Snyder, G. Zerbi, Vibrational analysis of ten simple aliphatic ethers: Spectra, assignments, valence force field and molecular conformations, Spectrochim. Acta Part A Mol. Spectrosc. 23 (1967) 391–437. doi:10.1016/0584-8539(67)80241-1.

[136] G. Louarn, J.P. Buisson, S. Lefrant, D. Fichou, Vibrational Studies of a Series of .alpha.-Oligothiophenes as Model Systems of Polythiophene, J. Phys. Chem. 99 (1995) 11399–11404. doi:10.1021/j100029a016.

[137] W.W. Chiu, J. Travaš-Sejdić, R.P. Cooney, G.A. Bowmaker, Studies of dopant effects in poly(3,4-ethylenedioxythiophene) using Raman spectroscopy, J. Raman Spectrosc. 37 (2006) 1354–1361. doi:10.1002/jrs.1545.

[138] S. Garreau, G. Louarn, J.P. Buisson, G. Froyer, S. Lefrant, In situ spectroelectrochemical Raman studies of poly(3,4-ethylenedioxythiophene) (PEDT), Macromolecules. 32 (1999) 6807–6812. doi:10.1021/ma9905674.

[139] P. Simon, Y. Gogotsi, Materials for electrochemical capacitors, Nat. Mater. 7 (2008) 845–854. doi:10.1038/nmat2297.

[140] P. Wasserscheid, T. Welton, eds., Ionic liquids in synthesis, Wiley-VCH Verlag, Weinheim, 2011. doi:10.5772/14646.

[141] U.E.P. Nanowires, D.K. Taggart, Y. Yang, S. Kung, T.M. Mcintire, R.M. Penner, Enhanced Thermoelectric Metrics in Ultra-long Electrodeposited PEDOT Nanowires, (2011) 125–131. doi:10.1021/nl103003d.

[142] F. Di Franco, P. Bocchetta, M. Santamaria, F. Di Quarto, Electrochimica Acta Light induced electropolymerization of poly (3 , 4-ethylenedioxythiophene) on niobium oxide, Electrochim. Acta. 56 (2010) 737–744. doi:10.1016/j.electacta.2010.09.062.

[143] J. Zhong, L.Q. Fan, X. Wu, J.H. Wu, G.J. Liu, J.M. Lin, M.L. Huang, Y.L. Wei, Improved energy density of quasi-solid-state supercapacitors using sandwich-type redox-active gel polymer electrolytes, Electrochim. Acta. 166 (2015) 150–156. doi:10.1016/j.electacta.2015.03.114.

[144] G. Wang, L. Zhang, J. Zhang, A review of electrode materials for electrochemical supercapacitors, Chem. Soc. Rev. 41 (2012) 797–828. doi:10.1039/c1cs15060j.

[145] L.L. Zhang, X.S. Zhao, Carbon-based materials as supercapacitor electrodes, Chem. Soc. Rev. 38 (2009) 2520–2531. doi:10.1039/b813846j.

[146] P. Pfluger, G.B. Street, Chemical, electronic, and structural properties of conducting heterocyclic polymers: A view by XPS, J. Chem. Phys. 80 (1984) 544–553. doi:10.1063/1.446428.

[147] D.H. Han, J.W. Kim, S.M. Park, Electrochemistry of conductive polymers 38. Electrodeposited poly(3,4-ethylenedioxy-thiophene) studied by current sensing atomic force microscopy, J. Phys. Chem. B. 110 (2006) 14874–14880. doi:10.1021/jp055791b.

[148] J.S. Loring, W. Ronald Fawcett, Ion-solvent interactions in acetonitrile solutions of lithium, sodium, and tetraethylammonium perchlorate using attenuated total reflectance FTIR spectroscopy, J. Phys. Chem. A. 103 (1999) 3608–3617. doi:10.1021/jp984606+.

[149] F. X., Polymer electrolytes for electrochromic devices, in: C. Sequeira, D. Santos (Eds.), Polym. Electrolytes Fundam. Appl., Woodhead Publishing Limited, 2010: p. 3. https://books.google.com/books?hl=de&lr=&id=vHl0AgAAQBAJ&pgis=1.

[150] S. Yeon, K. Kim, S. Choi, J. Cha, H. Lee, Characterization of PVdF (HFP) Gel Electrolytes Based on 1- (2-Hydroxyethyl) -3-methyl Imidazolium Ionic Liquids, J. Phys. Chem. 109 (2005) 17928.

[151] A.L. Saroj, R.K. Singh, S. Chandra, Studies on polymer electrolyte poly(vinyl) pyrrolidone (PVP) complexed with ionic liquid: Effect of complexation on thermal stability, conductivity and relaxation behaviour, Mater. Sci. Eng. B Solid-State Mater. Adv. Technol. 178 (2013) 231–238. doi:10.1016/j.mseb.2012.11.007.

[152] J. Vila, P. Ginés, J.M. Pico, C. Franjo, E. Jiménez, L.M. Varela, O. Cabeza, Temperature dependence of the electrical conductivity in EMIM-based ionic liquids: Evidence of Vogel-Tamman-Fulcher behavior, Fluid Phase Equilib. 242 (2006) 141–146. doi:10.1016/j.fluid.2006.01.022.

[153] E. Navarrete-astorga, J. Rodríguez-moreno, E.A. Dalchiele, R. Schrebler, P. Leyton, J.R. Ramos-barrado, F. Martín, A transparent solid-state ion gel for supercapacitor device applications, J. Solid State Electrochem. (2017). doi:10.1007/s10008-016-3494-y.

[154] K.H. Lee, S. Zhang, T.P. Lodge, C.D. Frisbie, Electrical impedance of

spin-coatable ion gel films, J. Phys. Chem. B. 115 (2011) 3315–3321. doi:10.1021/jp110166u.

[155] J.O. Bockris, A.K.N. Reddy, Ionic Liquids, in: Mod. Electrochem., 2nd ed., Plenum Press, New York, 1998: pp. 601–753.

[156] J. Tang, R. Muchakayala, S. Song, M. Wang, K.N. Kumar, Effect of EMIMBF4ionic liquid addition on the structure and ionic conductivity of LiBF4-complexed PVdF-HFP polymer electrolyte films, Polym. Test. 50 (2016) 247–254. doi:10.1016/j.polymertesting.2016.01.023.

[157] R. Nadimicherla, R. Kalla, R. Muchakayala, X. Guo, Effects of potassium iodide (KI) on crystallinity, thermal stability, and electrical properties of polymer blend electrolytes (PVC/PEO:KI), Solid State Ionics. 278 (2015) 260–267. doi:10.1016/j.ssi.2015.07.002.

[158] C.A. Vincent, Polymer electrolytes, Prog. Solid State Chem. 17 (1987) 145–261. doi:10.1016/0079-6786(87)90003-3.

[159] J.E. Weston, B.C.H. Steele, Thermal history - conductivity relationship in lithium salt-poly (ethylene oxide) complex polymer electrolytes, Solid State Ionics. 2 (1981) 347–354. doi:10.1016/0167-2738(81)90038-2.

[160] T. Miyamoto, K. Shibayama, Free-volume model for ionic conductivity in polymers, J. Appl. Phys. 44 (1973) 5372–5376. doi:10.1063/1.1662158.

[161] G. Hirankumar, S. Selvasekarapandian, M.S. Bhuvaneswari, R. Baskaran, M. Vijayakumar, Ag+ion transport studies in a polyvinyl alcohol-based polymer electrolyte system, J. Solid State Electrochem. 10 (2006) 193–197. doi:10.1007/s10008-004-0612-z.

[162] G.Z. Chen, Understanding supercapacitors based on nano-hybrid materials with interfacial conjugation, Prog. Nat. Sci. Mater. Int. 23 (2013) 245–255. doi:10.1016/j.pnsc.2013.04.001.

[163] Y. Sun, X. Yan, Recent Advances in Dual-Functional Devices Integrating Solar Cells and Supercapacitors, Sol. RRL. 1 (2017) 1700002. doi:10.1002/solr.201700002.

[164] R. Narayanan, P.N. Kumar, M. Deepa, A.K. Srivastava, Combining Energy Conversion and Storage: A Solar Powered Supercapacitor,

Electrochim. Acta. 178 (2015) 113–126. doi:10.1016/j.electacta.2015.07.121.

[165] T.N. Murakami, N. Kawashima, T. Miyasaka, A high-voltage dye-sensitized photocapacitor of a three-electrode system, Chem. Commun. (2005) 3346–3348. doi:10.1039/b503122b.

[166] J. Bae, Y.J. Park, M. Lee, S.N. Cha, Y.J. Choi, C.S. Lee, J.M. Kim, Z.L. Wang, Single-fiber-based hybridization of energy converters and storage units using graphene as electrodes, Adv. Mater. 23 (2011) 3446–3449. doi:10.1002/adma.201101345.

[167] Y. Fu, H. Wu, S. Ye, X. Cai, X. Yu, S. Hou, H. Kafafy, D. Zou, Integrated Power Fiber for Energy Conversion and Storage Stystem, Energy Environ. Sci. 6 (2013) 805–812. doi:10.1039/b000000x.

[168] J. Xu, H. Wu, L. Lu, S.F. Leung, D. Chen, X. Chen, Z. Fan, G. Shen, D. Li, Integrated photo-supercapacitor based on Bi-polar TiO2 nanotube arrays with selective one-side plasma-assisted hydrogenation, Adv. Funct. Mater. 24 (2014) 1840–1846. doi:10.1002/adfm.201303042.

[169] E. Navarrete-Astorga, D. Solís-Cortés, J. Rodríguez-Moreno, E.A. Dalchiele, R. Schrebler, F. Martín, J.R. Ramos-Barrado, A new concept of a transparent photocapacitor, Chem. Commun. 54 (2018) 10762–10765. doi:10.1039/C8CC06112B.

[170] F. Martín, E. Navarrete, J. Morales, C. Roldán, J.R. Ramos-Barrado, L. Sanchez, High-energy, efficient and transparent electrode for lithium batteries, J. Mater. Chem. 20 (2010) 2847–2852. doi:10.1039/b920466k.

[171] J. Rodríguez-Moreno, E. Navarrete-Astorga, E.A. Dalchiele, L. Sánchez, J.R. Ramos-Barrado, F. Martín, Polyvinylpyrrolidone-LiClO4 solid polymer electrolyte and its application in transparent thin film supercapacitors, J. Power Sources. 237 (2013) 270–276. doi:10.1016/j.jpowsour.2013.03.043.

[172] X. Zhang, X. Huang, C. Li, H. Jiang, Dye-Sensitized Solar Cell with Energy Storage Function through PVDF / ZnO Nanocomposite Counter Electrode, (2013) 1–4. doi:10.1002/adma.201301088.

[173] P.J. Kulesza, M. Skunik-Nuckowska, K. Grzejszczyk, N. Vlachopoulos, L. Yang, L. Haggman, A. Hagfeldt, Development of Solid-State Photo-Supercapacitor by Coupling Dye-Sensitized Solar

Cell Utilizing Conducting Polymer Charge Relay with Proton-Conducting Membrane Based Electrochemical Capacitor, ECS Trans. 50 (2013) 235–244. doi:10.1149/05043.0235ecst.

[174] P.A. Mini, S. V Nair, K.R. V Subramanian, Design and development of an integrated device consisting of an independent solar cell with electrical, 2 (2012). doi:10.1002/pip.

[175] A. Takshi, H. Yaghoubi, T. Tevi, S. Bakhshi, Photoactive supercapacitors for solar energy harvesting and storage, J. Power Sources. 275 (2015) 621–626. doi:10.1016/j.jpowsour.2014.10.110.

[176] X. Huang, X. Zhang, H. Jiang, Energy Storage via Polyvinylidene Fluoride Dielectric on the Counterelectrode of Dye-Sensitized Solar Cells, J. Power Sources. (2013). doi:10.1016/j.jpowsour.2013.09.094.

[177] Y. Wang, J. Tang, Z. Peng, Y. Wang, D. Jia, B. Kong, A.A. Elzatahry, D. Zhao, G. Zheng, Fully Solar-Powered Photoelectrochemical Conversion for Simultaneous Energy Storage and Chemical Sensing, (2014).

[178] S.C. Lau, H.N. Lim, T.B.S.A. Ravoof, M.H. Yaacob, D.M. Grant, R.C.I. MacKenzie, I. Harrison, N.M. Huang, A three-electrode integrated photo-supercapacitor utilizing graphene-based intermediate bifunctional electrode, Electrochim. Acta. 238 (2017) 178–184. doi:10.1016/j.electacta.2017.04.003.

[179] J. Xu, Z. Ku, Y. Zhang, D. Chao, H.J. Fan, Integrated Photo-Supercapacitor Based on PEDOT Modified Printable Perovskite Solar Cell, Adv. Mater. Technol. 1 (2016) 1–5. doi:10.1002/admt.201600074.

[180] C.Y. Hsu, H.W. Chen, K.M. Lee, C.W. Hu, K.C. Ho, A dye-sensitized photo-supercapacitor based on PProDOT-Et2 thick films, J. Power Sources. 195 (2010) 6232–6238. doi:10.1016/j.jpowsour.2009.12.099.

[181] F. Zhou, Z. Ren, Y. Zhao, X. Shen, A. Wang, Y.Y. Li, C. Surya, Y. Chai, Perovskite Photovoltachromic Supercapacitor with All-Transparent Electrodes, ACS Nano. 10 (2016) 5900–5908. doi:10.1021/acsnano.6b01202.

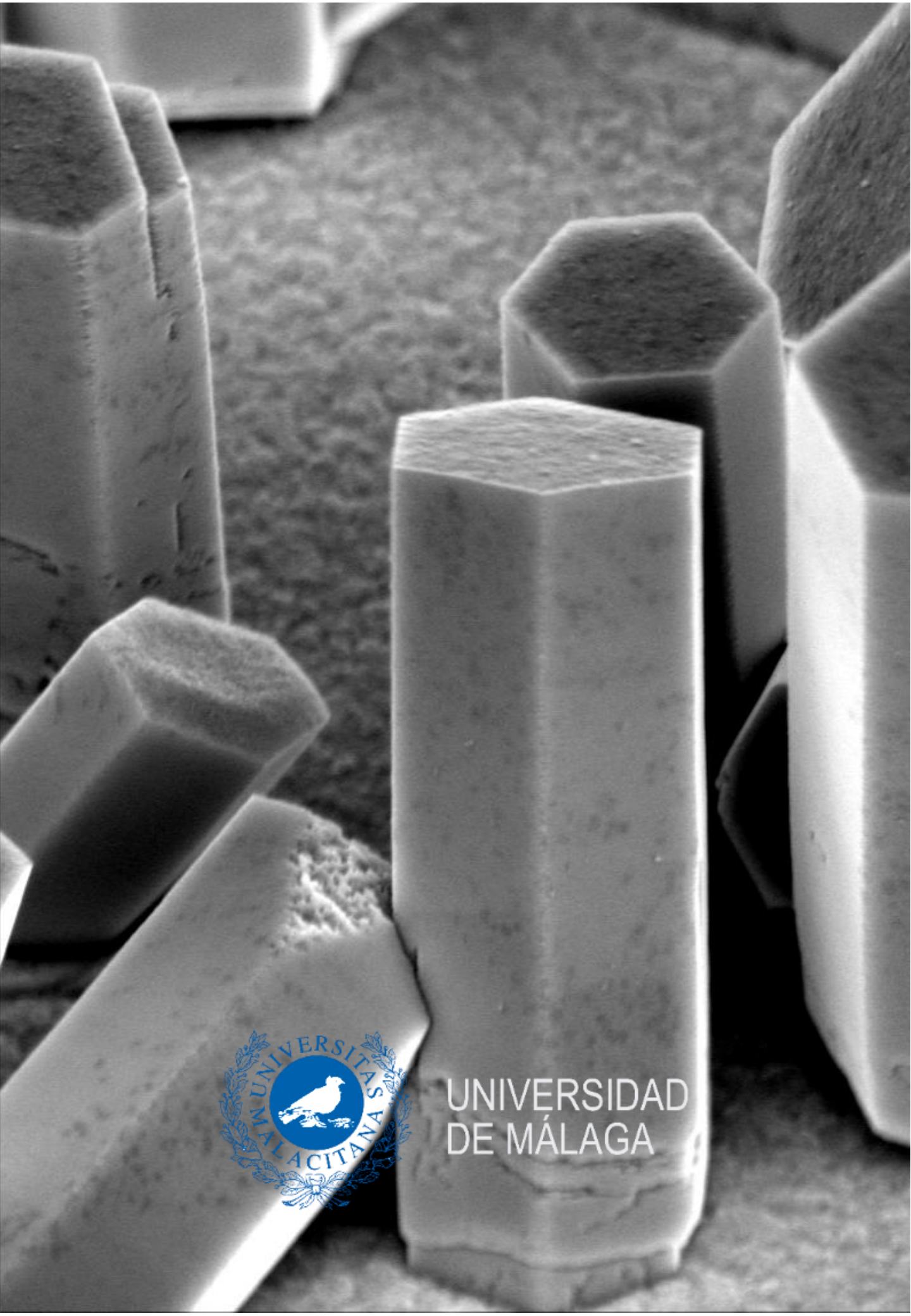
UNIVERSITAS MALACITANA
UNIVERSIDAD
DE MÁLAGA